Statistical signal processing for multiple sources separation on antennas

Benjamin Poste

UNIVERSITÉ D'ORLÉANS

ÉCOLE DOCTORALE MATHÉMATIQUES, INFORMATIQUE, PHYSIQUE THÉORIQUE ET INGÉNIERIE DES SYSTÈMES
LABORATOIRE PRISME

THÈSE présentée par :

Benjamin POSTE

soutenue le : 13 novembre 2024

pour obtenir le grade de : Docteur de l'Université d'Orléans

Discipline/ Spécialité : Sciences et Technologies industrielles/Traitement du signal

STATISTICAL SIGNAL PROCESSING FOR MULTIPLE SOURCES SEPARATION ON ANTENNAS

THÈSE dirigée par :

M. ABED-MERAIM Karim	Professeur, Université d'Orléans
M. CHARBIT Maurice	Professeur émerite, MJCC
M. LE PICHON Alexis	Docteur, CEA

RAPPORTEURS :

M. CHONAVEL Thierry	Professeur, IMT Atlantique
M. PICHERAL José	HdR, CentraleSupélec

JURY :

Mme MARCOS Sylvie	Directrice de recherche, CNRS, Présidente du jury
M. ABED-MERAIM Karim	Professeur, Université d'Orléans
M. CHARBIT Maurice	Professeur émerite, Institut Mines Telecom, Paris
M. LE PICHON Alexis	HdR, CEA, DAM, DIF
M. CHONAVEL Thierry	Professeur, Institut Mines Telecom Atlantique
M. PICHERAL José	HdR, CentraleSupélec
M. ROUEFF François	Professeur, Institut Mines Telecom, Paris
M. NAESHOLM Peter	Professeur assistant, NORSAR, Université d'Oslo, Norvège

Quand on s'est trompé, il faut persévérer. Et l'on finit toujours par avoir raison.

Napoleon I^{er}

Remerciements

Lorsqu'on débute l'écriture des remerciements, c'est qu'on est plutôt sur la bonne voie pour finir la rédaction. Je profite donc d'une accalmie entre deux corrections pour dire merci à toutes les personnes auxquelles je pense en ce moment. Cette thèse a débuté il y a trois ans, après mon alternance. Cette dernière a été rendue possible grâce tout d'abord à Alexis Le Pichon et à Nicolas Lardjane qui m'ont donné ma chance au CEA malgré quelques questionnements dont nous rigolons encore parfois, et tout cela sous le regard toujours bienveillant et avisé d'Eleonore Stutzmann qui m'a soutenu lors de mes choix. Lors de cette alternance, puis maintenant de cette thèse, j'ai pu compter non seulement sur le soutien et les conseils toujours pertinents d'Alexis, mais aussi ceux de mes directeurs de thèse bien évidemment. C'est pourquoi je tiens à remercier infiniment Karim Abed-Meraim et Maurice Charbit pour les connaissances qu'ils m'ont apportées pendant ces trois ans. Je suis toujours aussi admiratif de l'étendue des connaissances en traitement du signal que vous avez acquises au fil de vos carrières. Si seulement cela pouvait se transmettre d'un claquement de doigt... Bien que cette thèse soit terminée, je continuerai à me former activement sur le sujet en espérant atteindre un jour un bon pourcentage de ce que vous avez en tête. Bel objectif en perspective, et cela avant même l'introduction de la thèse...

C'est aussi grâce à notre travail que j'ai pu être embauché dans cette entreprise dont le rayonnement et les missions me rendent fier. Cette embauche a aussi été rendue possible grâce à Julien, avec qui le travail en commun sur l'interprétation des résultats des algorithmes de détection a été vital pour évaluer la qualité physique de nos résultats. Merci beaucoup à toi et vive les « stone crushers » ! Dans la même veine, j'aimerais remercier Samuel qui m'a beaucoup aidé lors de mes recherches et a relu ce manuscrit, j'espere ne pas avoir trop massacré la langue de Shakespeare. Je tiens aussi à remercier Alice, avec qui j'ai énormément travaillé sur l'intelligence artificielle pour l'estimation du nombre de sources. Travailler avec toi a été très enrichissant. Je pense également à Olivier avec qui j'ai travaillé sur l'aspect sismique de ce travail. Merci beaucoup pour ton aide et ta gentillesse. Je tiens aussi à remercier Constantino et Amaury pour leurs conseils avisés et leur bienveillance durant ces trois années de recherche. Je ne peux pas non plus oublier Charly dont la bonne humeur rayonne dans le laboratoire. À jamais les premiers vainqueurs de la Coupe du Bardifoot! Rémy rejoint ces remerciements, plein de bonne humeur, mais avec un niveau au babyfoot encore loin derrière de celui des poussins. Je remercie également Philippe pour son humour ironique et pour son talent de skipper hors pair. Merci de ne nous avoir pas fait couler dans la baie de Quiberon... Je remercie aussi tous les permanents, doctorants, post-doctorants ainsi que les stagiaires pour votre bonne humeur, votre soutien et les soirées passées avec vous : Pierre (mister Infrason et mister Tsunami), Alice, Nicolas, Manon, Aurélie, Samuel, Grégoire, Vincent, Maxime, Gonzalo, Fanny, les Paul (tant celui qui ramène ces interactions sociales à un combat en octogone sans règle que celui avec qui j'ai passé des heures à la salle de sport et quelques dignes apéros). Plus généralement, j'aimerais remercier tout le BARD qui m'a accueilli : Constantino, Philippe, Alexis, Amaury, Damien, Olivier, Charly, Laurent, Clara, Michaël, Anne, Audrey, Aurélien, Pascal, Gilles, Bruno, Sylvia, Caroline ainsi que les opérateurs du CENALT et du CSEM. Je tiens également à remercier mon nouveau laboratoire pour son accueil chaleureux : Yoann, Johann, Aurélie, Séverine, Julien, Mikaël, Stéphanie, Claire, Denis, Sophie, François qui ont tout fait pour que mon arrivée se passe bien, ainsi que Stéphane (les deux !), Nicolas, Christian, Philippe, Isabelle, Daphné, Yannick, Ronan, Benoit et Olivier. Je souhaite également une bonne retraite à Pascal ! Bref, un grand merci au CEA ! Je remercie aussi infiniment l'université d'Orléans et le laboratoire PRISME pour leur accueil. Je pense notamment certes à Karim, mais aussi à Nacim Ramdani, Philippe Ravier, Rodolphe Weber, Meryem Jabloun, Sylvie Plessard, Guanglie Ouyang, Trung Thanh Le, dit « Mister Le » et Zuokun Ouyang.

Je souhaite également remercier ma famille, à commencer par mes parents, pour leur soutien tout au long de mes études. Je repense avec humour (et nostalgie!) à l'époque où ma mère pouvait m'aider en mathématiques. Il y a eu du chemin depuis. Je compte sur toi pour tout lire et résumer à Papa qui ne comprendra pas l'anglais! Un grand merci également à mes grands-parents Michel et Christiane, une pensée pour mon autre grand-mère à qui j'aurais aimé montrer le résultat final. Merci aussi à ma cousine Amandine qui attend toujours patiemment que je parte à l'autre bout du monde pour m'accompagner, ainsi qu'à mes oncles et tantes, cousins et cousines. Une petite aparté pour mon oncle qui me poussait à faire une thèse en me disant que ça serait bête de ne pas tenter l'aventure. Tu as eu infiniment raison. Je ne peux pas ne pas remercier mes amis Ben, Gaël, Loïc, Adrien, Vince et les autres intenables zozos pour

chaque moment passé avec vous. Merci à toi aussi Léane pour ton soutien ces derniers mois. Dominus vobiscum !

Enfin, un dernier grand merci à l'école publique, à l'IPGP à qui je dois tant, ainsi qu'à tous mes professeurs et aux personnes que j'y ai rencontrées. Je remercie d'avance les rapporteurs qui liront et corrigeront ce manuscrit, ainsi que tout éventuel futur lecteur.

Commençons !

Contents

List of Figures

List of Tables

List of Acronyms

AIC	Akaike Information Criterion
ACI	Analyse en Composantes Indépendantes
ARISE	Atmospheric Dynamics Research InfraStructure in Europe
AUC	Area Under the Curve
BIC	Bayesian Information Criterion
BIDS	Blind Identification via Decorrelating Subchannels
CEA	Commissariat à l'énergie atomique et aux énergies alternatives
CID	Centre International de Données
CMA-ES	Covariance Matrix Adaptation - Evolution Strategy
CND	Centre National de Données
CRB	Cramer-Rao Bound
CSSM	Coherent Signal Subspace Method
CTBT	Comprehensive Nuclear Test-Ban Treaty
CTBTO	Comprehensive Nuclear Test-Ban Treaty Organisation
DBSCAN	Density-Based Spatial Clustering of Applications with Noise
DOA	Direction Of Arrival
EAUC	Empirical Area Under the Curve
EM	Expectation Maximisation
EROC	Empirical Receiver Operating Characteristic
FIR	Finite Impulse Response
F-K	Frequency-Wavenumber
GLR	Generalized Likelihood Ratio
GLRT	Generalized Likelihood Ratio Test
GMM	Gaussian Mixture Model
HyMeX	HYdrological cycle in Mediterranean EXperiment
ICA	Independent Component Analysis
IDC	International Data Centre
ISSM	Incoherent Signal Subspace Method

IMS International Monitoring System

IMT Institut Mines-Telecom

JADE Joint Approximate Diagonalization of Eigenmatrices

KDE Kernel Density Estimation

LASSO Least Absolute Shrinkage and Selection Operator

LOC Loss Of Coherency

LSBB Low-noise underground laboratory

LTS Least Trimmed Squares

MCCM Mean of Cross Correlation Maximum

MCML Multi-Channel Maximum Likelihood

MLE Maximum Likelihood Estimation

MLP Multi-Layer Perceptron

MRE Mutually Referenced Equalizers

MUSIC MUltiple SIgnal Classification

MVDR Minimum Variance Distortionless Response

NDC National Data Centre

OHP Haute Provence Observatory

OLS Ordinary Least Squares

OMP Orthogonal Matching Pursuit

OTICE Organisation du Traité d'Interdiction Complète des Essais nucléaires

PCA Principal Component Analysis

PMCC Progressive Multi-Channel Correlation

POSM Parameter Of Stochastic Model

LTBT Limited Test Ban Treaty

RMS Root Mean Square

ROC Receiver Operating Characteristic

RSS Rotational Signal Subspace

SNR Signal to Noise Ratio

SOBI Second-Order Blind Identification

SOI Signal Of Interest

SSI Systeme de Surveillance International

TDOA Time Difference of Arrivals

TICE Traité d'Interdiction Complète des Essais nucléaires

TOPS Test of Orthogonality of Projected Subspaces

TS Test Statistic

VIS Volcanic Information System

List of symbols

$\hat{(.)}$	The estimation of the parameter
$(.)^\star$	The true value of the parameter
$\mathbb{E}\{(.)\}$	The expectation
$(.)^H$	The conjugate transpose
$(.)^\#$	The Moore-Penrose pseudoinverse
$(.)^T$	The transpose
$\mathbf{A}$	The steering matrix
$a(\theta, v)$	The steering vector
B	The bandwidth
$\mathbf{B}$	The whitening matrix
$\mathbf{C}$	The density spectral matrix
$\mathbf{C}_{ss}$	The density spectral matrix of the sources
$\mathbf{C}_{focussing}$	The density spectral matrix resulted of the focussing method
ϵ	The error on the true delay estimation
f_0	The central frequency
f_i	The frequency i in the bandwidth
Fs	The frequency sampling
η	Threshold of the Test Statistic
H_0	The null hypothesis
H_1	The alternative hypothesis
$\mathbf{I}$	The identity matrix
K	The number of frequency bin
L	The window length
λ_i	The eigenvalue i
M	The number of sensor for an array
$\overline{m}$	The mean of a distribution m
μ	The Parameter Of Stochastic Model
$n(t)$	The additive noise
$n_m(t)$	The additive noise at the sensor m
$\mathbf{N}$	The noise matrix for the array
$\mathbf{N_{t_l}}$	The matrix of the noise at a time t_l
N	The number of sources
N_e	The number of samples
$p(t)$	The in-phase signal
p_n	The slowness vector of the n-th source
$q(t)$	The in-quadrature signal
r_m	The location of the sensor m in an arbitrary orthogonal 2D coordinate system
$\mathbf{R_{nn}}$	The covariance matrix of the noise
$\mathbf{R_{ss}}$	The covariance matrix of the source
$\mathbf{R_{zz}}$	The theoretical covariance matrix of the observed signal
$\widehat{\mathbf{R_{zz}}}$	The estimated covariance matrix of the observed signal
$s(t)$	The SOI
$s_n(t)$	The n-th SOI
$\mathbf{S}$	The matrix of the SOI
$\mathbf{S_{t_l}}$	The matrix of the SOI at a time t_l
$\sigma^2_{s_n}$	The power of the n-th source
σ^2	The power of the noise
$\mathbf{T}$	The focussing matrix
T_e	The period sampling
t_l	A time t in the time window

θ	The angle of arrival of a wavefront
θ_n	The angle of arrival of the n-th source
τ	The delay of the wavefront between the referenced sensor and other sensor of the array
τ_m	The delay of the wavefront between the referenced sensor and the sensor m
v	The horizontal trace velocity
v_n	The horizontal trace velocity of the n-th source
v_{pi}	The eigenvector i
$\mathbf{V}$	The rotation matrix allowing diagonalisation
$\mathbf{W}$	The demixing matrix
$x(t)$	The complex envelop of $s(t)$
$\mathbf{X}$	The 2D matrix of the difference positions between each sensor pairs
$z(t)$	The observed signal at the array
$z_m(t)$	The observed signal at the sensor m
$\mathbf{Z}$	The matrix of the observed signals
$\mathbf{Z_{t_1}}$	The matrix of the observed signals at a time t_l

Part I

Introduction

Chapter I.1

General introduction about infrasound

I.1.1 What is infrasound?

We usually speak about acoustic waves in reference to audible sounds for humans but refer, more generally, to pressure waves. Indeed, acoustic waves are longitudinal elastic waves, which means that the particles set in motion by the wave move in the same direction as the wave itself [Leisure, 2017]. The process of compression and rarefaction involves a periodic alternation between the closest and farthest particle positions, with the particles themselves occupying intermediate positions between these extremes. The restoring force is the ambient air pressure, which acts to drive the pressure back to this equilibrium pressure. Acoustic waves are divided into several categories, with reference to the audible range for humans (figure I.1.1).

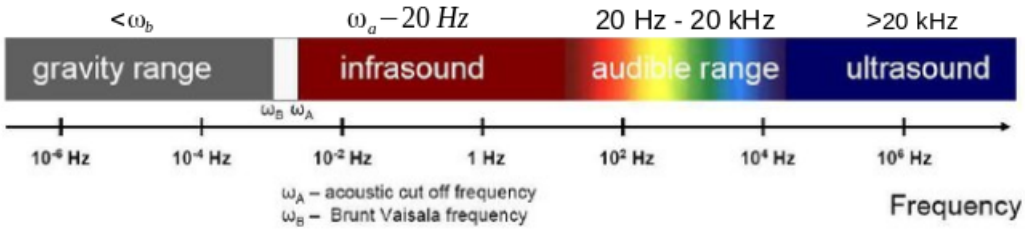

Figure I.1.1: Schematic view of the different acoustic sections and their frequency boundaries (extracted and modified from Bittner et al. [2010]).

The audible section for humans is characterised by a frequency range between 20 Hz and 20 kHz. This section is bounded by ultrasound, at frequencies higher than 20 kHz and by infrasound at frequencies lower than 20 Hz. Infrasound spans from the acoustic cut off frequency at about 3.3 mHz to the audible section at 20 Hz. The acoustic cut off frequency is the frequency where acoustic waves begin to propagate. Frequencies below the acoustic cut-off frequency and the Brunt-Väisälä frequency (i.e., 2.9 mHz in the lower atmosphere) are associated with gravity waves [Hines, 1960]. Because of their low frequencies and correspondingly long wavelengths, as well as the low absorption by the atmosphere, infrasounds are poorly attenuated and can travel thousands of kilometres. To create them, however, a high amount of energy is needed to set in motion a sufficient portion of the atmosphere.

I.1.2 Infrasound-generating sources

The sources of infrasound must be large and powerful to create infrasound. Infrasound sources have different frequency content (i.e., broadband or narrowband spectrum) and time duration (i.e., impulsive or quasi-permanent signals), which allows us to distinguish between them. Two main types of sources can be described: natural and anthropogenic sources.

Natural sources of infrasound are numerous due to the wide variety of existing natural phenomena. Indeed, auroras, for example, produce infrasound by moving a large volume of atmosphere through the interaction of the upper atmosphere and the solar wind [Wilson, 1969]. Debris flows such as landslides or avalanches, can also generate infrasound due to the large displacement of material [Belli et al., 2022]. These signals can be used for civil applications, such as early warning of avalanches [Belli et al., 2024]. Earthquakes generate infrasound by shaking the ground, which can be detected at arrays [Mutschlecner and Whitaker, 2005] and by ionospheric observations due to the large power of such events [Artru et al., 2001]. Weather phenomena, particularly storms, are sources of infrasound due to their turbulent structure, shear winds and also tornadoes [Schecter et al., 2008]. This has led to storm tracking activity in order to better understand the phenomenon (Pásztor et al. [2021]; Listowski et al. [2022]). The lightnings generated during thunderstorms are a high frequency infrasound source. They are formed by the sudden thermal expansion of the atmosphere leading to shock waves [Few, 1969]. A large part of the frequency content is in the infrasound frequency range. A better understanding of thunderstorms by lightning reconstruction is an important task due to climate change challenges and the increasing of unstable meteorological events (Farges and Blanc [2010]; Farges et al. [2019]). The colliding of oceanic waves incoming from opposite directions and the interactions with the seafloor generates a very low frequency infrasound content called microbaroms [De Carlo, 2020]. Meteors are able to produce infrasound by the supersonic velocity of the bolide when entering the atmosphere creating shock waves. The fragmentation of the meteor or its explosion also creates infrasound [Edwards, 2009]. These bolides can be detected and analysed. The first detection of such event was the Tungunska meteor in 1908 [Chyba et al., 1993]. Since this event many studies were done on other bolides entering the atmosphere like the Chelyabinsk meteor in 2013 [Le Pichon et al., 2013] or more recently the fireball which flew over the south Atlantic ocean [Hupe et al., 2024]. Last natural examples of this overview are volcanic eruptions which produce infrasound and seismic activity. Numerous studies about volcanic eruptions (Symons [1888]; Vergoz et al. [2022]) and processes [Perttu et al., 2020] have been carried out by using infrasound technology. Recent research is ongoing in order to warn nearby citizens about dangerous volcanic activity (Marchetti et al. [2019]; Métaxian et al. [2024]) or aviation about ash clouds [Gheri et al., 2024].

Humans are also able to produce infrasound through our activities. First of all, airplanes can be detected with subsonic velocities when the conditions of recording are appropriate. These kind of events are still detected up to 30 km before being attenuated [Evers, 2008]. However supersonic flights, by the generated shock waves, can be detected up to hundred of kilometres away. Indeed, the Concorde has been the target of several infrasound studies [Balachandran et al., 1977]. Rockets can also be detected very far from the launching site [Pilger et al., 2021b]. Industrial activities (Smirnov et al. [2015]; Pilger et al. [2018]) and wind farms [Marcillo et al., 2015] can be detected and can be used as ground truth information. Finally, sufficiently large explosions generate infrasound from simple quarry blasts [Bondár et al., 2022] or ammunition explosions as the events of Hukkakero in Finland [Blixt et al., 2019] to large industrial accidents [Vergoz et al., 2021] or nuclear explosions (Che et al. [2009]; Che et al. [2022]). The largest nuclear test was conducted by the Soviet Union in 1961 with the Tsar Bomba. The power liberated was 57 megatons of TNT, equivalent to 4000 times the energy of the Bomb which devastated Hiroshima [Sakharov, 1990]. These events produce infrasound that can travel several times around the globe. The following table I.1.1 summarises the characteristics of infrasound sources of interest, including their frequency content, maximum measured amplitude, and maximum distance of detection. This summary is adapted from a table in Campus and Christie [2009]. The table also shows how the amplitudes of the recorded phenomena are low relative to the atmospheric pressure of around 10^5 Pa, leading to a need for very sensitive sensors.

Table I.1.1: Different natural and anthropogenic sources and their characteristics in frequency, maximum recorded amplitude and maximum estimated detection range.

Infrasound sources and references	Frequency range (Hz)	Maximum observed amplitude (Pa)	Estimated maximum detection range (km)
Auroras [Wilson, 1971]	0.008 - 20	2	4000
Landslides [Bedard, 1993]	0.1 - 20	1	1000
Earthquakes [Le Pichon et al., 2003]	0.005 - 10	4	>10 000
Storms (Bedard et al. [2000]; Listowski et al. [2022])	0.01 - 10	0.5	>1500
Tornadoes [Bedard Jr et al., 2004]	0.5 - 20	0.5	300
Lightnings [Few, 1970]	0.5 - 20	2	50
Meteors [ReVelle, 1976]	0.01 - 20	>10	>20000
Microbaroms [Donn and Rind, 1972]	0.12 - 0.35	5	10000
Volcanoes (Donn and Balachandran [1981]; Vergoz et al. [2022])	0.003 - 20	>20	>20000
Subsonic aircraft [Fee et al., 2013]	0.03 - 20	2	<100
Supersonic aircraft [Liszka and Waldemark, 1995]	0.3 - 20	10	5000
Rocket launches [Pilger et al., 2021b]	0.01 - 20	5	3000
Mining activity/Quarry blast (Bondár et al. [2022]; Mitterbauer et al. [2024])	0.05 - 20	5	>5000
Chemical explosions [Vergoz et al., 2021]	0.05 - 20	10	>5000
Atmospheric nuclear explosion [Mutschlecner et al., 1999]	0.003 - 20	>20	>20000
Underground nuclear explosion [Whitaker, 2008]	1 - 20	1	>20000

I.1.3 The impact of atmospheric conditions on infrasound propagation

The atmosphere is composed of several layers as illustrated in the figure I.1.2. These layers can be defined based on how mixed the atmosphere is in each portion. Below 100 km, the atmosphere is mixed by turbulent eddies, and this portion is called the homosphere. Above 100 km up to 500 km, the mix is done by diffusion, and this portion is called the heterosphere. However, infrasound propagation is particularly impacted by temperature and wind. Infrasound follows the path of decreasing effective speed of sound. The effective sound speed can be expressed as

$$C_{eff} = \sqrt{\gamma_g RT} + \hat{n} \cdot u \tag{I.1.1}$$

where γ_g is the specific heat of dry air, R is the gas constant for air, T is the temperature and $\hat{n} \cdot u$ is the projection from the source to the receiver $\hat{n}$ of the wind speed u. When the effective sound speed in the atmosphere is greater than at the ground, infrasound wavefronts are refracted to the ground following the Snell–Descartes law at the first order (i.e because it also depends on the launch angle of the infrasound, as well as the effective speed of sound profile. Additionally, small scale phenomena, such as gravity waves, can cause diffraction, resulting in a partial reflection of the acoustic energy). Thus four different layers can be described due to the temperature gradients. The first one is troposphere from ground to 8 to 15 km depending on the latitude and the season. The troposphere contains 90% of the atmosphere by mass. The temperature is constantly decreasing from the ground to the limit of the troposphere, the tropopause, where the temperature remains approximately constant. The jet stream is

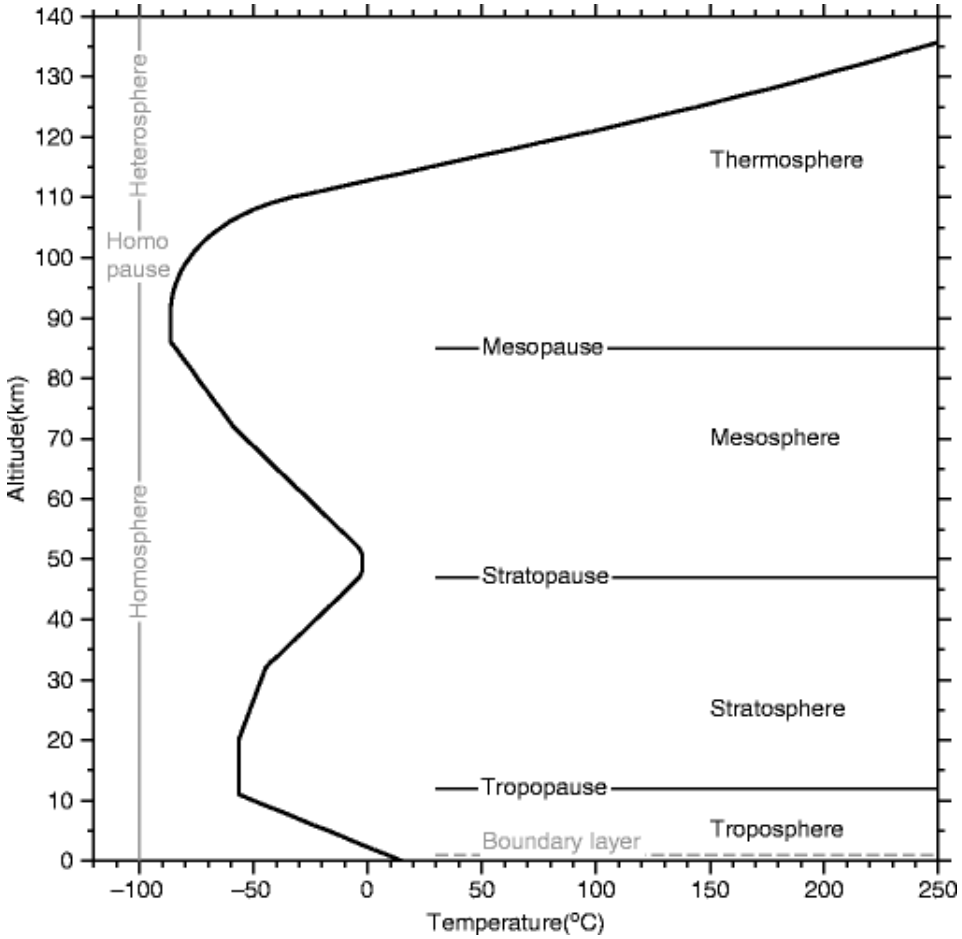

Figure I.1.2: Atmospheric layers according to the mixing of the atmosphere or its temperature gradient as a function of the altitude. Figure extracted from US-Standard [1976].

just below the tropopause. It should be noted that in the troposphere a small temperature inversion can occur in first 100 m due to, for example, a warm front passing over a cold front, or by a larger amount radiation emitted by surface than the incident solar radiation. Temperature is then increasing in the stratosphere due to ozone up to around 50 km, which is called the stratopause. If winds are favourable for a propagation a waveguide can be formed at this altitude. However, a sudden stratospheric warming characterised by an increased temperature and, for major warmings, a wind inversion can destroy the waveguide. Often this sets up summertime conditions during the winter and this means that the typically westerly guide is destroyed, but there is usually an easterly guide that forms in its place [Charlton and Polvani, 2007]. Then infrasound can travel up to the mesosphere where the temperature is decreasing again until the mesopause. A waveguide is possible if strong winds occur. Finally temperature increases in the thermosphere due the absorption of highly energetic solar radiation. This results in a thermospheric waveguide, however, the strong attenuation at these altitudes means that these signals (particularly at high frequency) are not detected at the surface. The attenuation is small for low-frequency infrasound, which is why strong sources with low-frequency content, such as microbaroms or mountain associated waves [Wilson et al., 2009], can be easily detected anywhere on Earth if the recording conditions are favourable. The following figure I.1.3.b is a ray tracing simulation of stratospheric and thermospheric paths. The thermospheric path is due to the high temperature specific to this layer leading to a high effective sound speed. The stratospheric arrival is due to high temperature of the stratopause combined with the high winds towards the observer from the source, as shown in graph (a); the temperature alone is not large enough to cause the waves to refract back to the ground. Therefore, wind is needed to increase the effective sound speed and produce a stratospheric waveguide. It can be seen that there are no arrivals in the first 200 km from the source and between the last stratospheric arrival and the first thermospheric

arrival; these are what we call a shadow zones. It should be noted that shadow zones are less pronounced for low frequency signals because energy refraction happens continuously through out the path due to the diffraction of these longer wavelengths. That is also why microbaroms are often detected. Ongoing research is being done in order to quantify the impact of gravity waves on infrasound propagation at high altitude (Chunchuzov and Kulichkov [2019]; Listowski et al. [2024]).

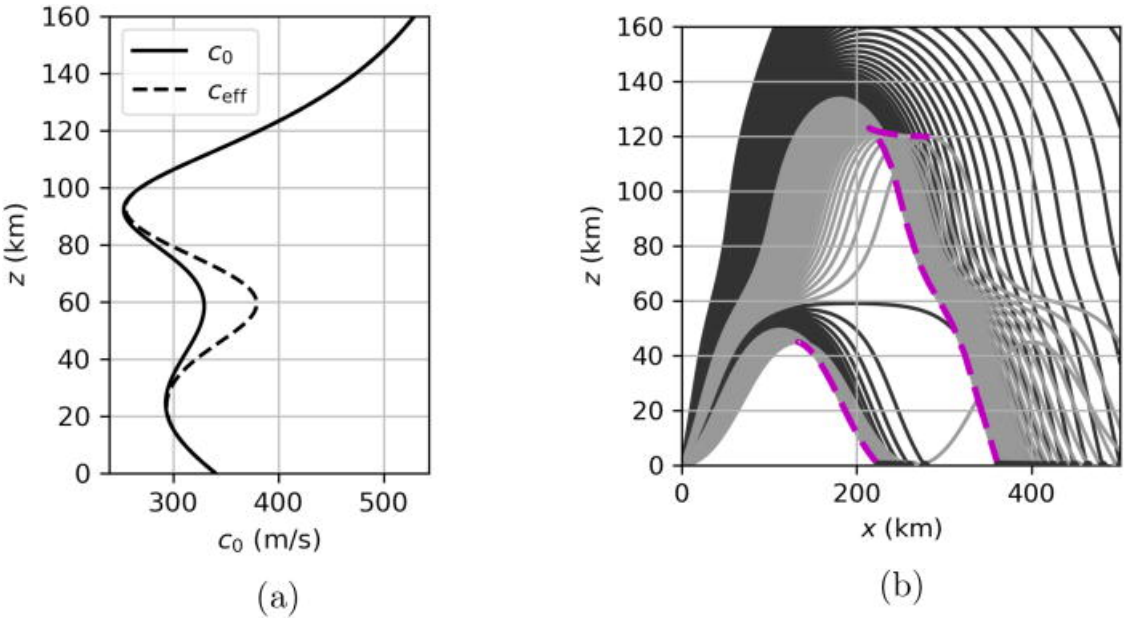

Figure I.1.3: The figure (a) is made up of the sound speed profile c_0 (solid line) [Lingevitch et al., 1999] and the effective sound speed profile c_{eff} (dashed line) according to a Gaussian wind profile [Blom, 2019], (b) is the illustration of real rays obtained with ray tracing method [Zelias et al., 2022] for a launch angle varying from 0 to 60 deg. The stratospheric and thermospheric caustics are indicated by the thick purple dashed lines. Extracted from Zelias et al. [2022].

A final impact on propagation must be described, which is the loss of coherency of the signal during the propagation. The loss of coherency for the signal between sensors is generated by atmospheric heterogeneities, such as temperature gradients and wind. These heterogeneities cause wave diffraction and generate wave packets with back azimuth and trace velocity variances, $\Delta\theta$ and Δv, with respect to the source waves. θ and v represent the back azimuth and trace velocity (i.e the apparent horizontal speed of a wave) of the plane wave, respectively [Mack and Flinn, 1971].

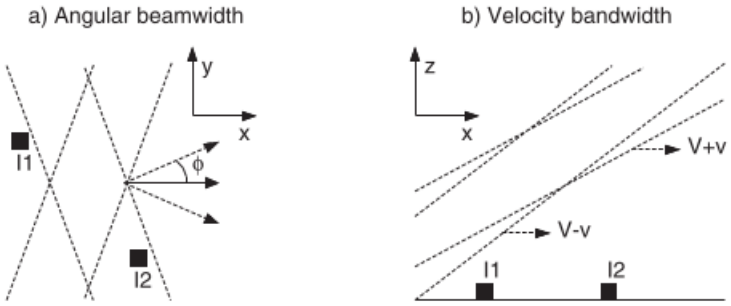

Figure I.1.4: A representation of the beam decoherence as shown in Gossard and Hooke [1975]. The average direction of horizontal propagation of this set of wavefronts is along the x-axis. Individual wavefronts with small deviations from this direction are represented by ϕ on graph (a). The average apparent velocity of all the wavefronts through the array is designated as V. The individual components of the wavefronts with small deviations from this value are shown on graph (b) [Green, 2015].

The aforementioned decoherence is even more pronounced when

- the distance between the source and the receiver is considerable, since there will be a decrease in the correlation with increasing distance. This phenomenon is discussed in detail in Green [2015]. In event where the inter-sensor distance is in kilometres, an approximation of the coherence loss may be expressed as $\gamma^2 = exp(-\alpha z)$ where α is the attenuation coefficient and z is the distance between sensors [Green, 2015].
- this is a late arrival in the signal of interest, which is likely due to a diffraction effect [Green, 2015].
- the pair of sensors under consideration is parallel to the wavefront arrival, given that, the coherence loss is anisotropic. This is in accordance with the findings in Mack and Flinn [1971].

The coherency can be calculated as a function of the period using the following formula [Christie et al., 2007]

$$\gamma^2(r,T) = \left| \frac{sin(2\pi x sin(\Delta\theta)/\overline{v}T)}{2\pi x sin(\Delta\theta)/\overline{v}T} \right|^2 \cdot \left| \frac{sin(2\pi y \Delta v/(\overline{v}T(\overline{v}+\Delta v)))}{2\pi y \Delta v/(\overline{v}T(\overline{v}+\Delta v))} \right|^2 \tag{I.1.2}$$

where T is the period under consideration, $\overline{v}$ is the mean phase velocity, x and y are the components of the inter sensor distance vector r, $\Delta\theta$ and Δv are back azimuth and trace velocity distributions, respectively. It can also be calculated by a Gaussian approximation [Green, 2015]

$$\gamma_{12}^2(w) = \left| exp\left(-\frac{k^2}{4} \left[x^2 \left(\frac{\Delta v}{\overline{v}} \right) + y^2 \Delta\theta \right] \right) \right|^2 \tag{I.1.3}$$

where k is the magnitude of the horizontal angular wave number in the direction of propagation. Experimental estimates of $\Delta\theta$ and Δv are consistent between models from Mack and Flinn [1971] and from Christie et al. [2007] providing respectively on average $\Delta\theta = 5^\circ$ for $\Delta v = 15\ m/s$ and $\Delta\theta = 4.5^\circ$ for $\Delta v = 14\ m/s$. On the other hand, by analysing the coherence of signals from reference events, Green [2015] showed that a wider range of values existed, from $\Delta\theta = 0.4^\circ$ to $\Delta\theta = 7^\circ$ and $\Delta v = 2\ m/s$ to $\Delta v = 40\ m/s$ whose median was $\Delta\theta = 3.1^\circ$ for a $\Delta v = 12\ m/s$. The individual wavefronts are specific to each frequency band of the signal.

Chapter I.2

Context of infrasound monitoring

I.2.1 Why recording infrasound is important

As explained in the previous sections, due to the low attenuation of infrasound in the atmosphere, they are able to travel long distances. This leads to the interest of monitoring infrasound for both source characterisation and atmospheric studies up to the thermosphere. Indeed early warning applications for avalanches [Marchetti et al., 2015], volcanic eruptions like the Volcanic Information System (VIS) whose aim is to monitor volcanic activity and provide early warnings, are developed for civilian protection from natural hazards. Other source characterisations involving the localisation, the energy estimation (for example chemical explosions [Pilger et al., 2021a], military intelligence like firearms use [Glaser et al., 2017] or earthquakes [Macpherson et al., 2023]) can be done by infrasound studies. But infrasound can be also used for atmospheric studies, for weather predictions or climate research. This is the objective of several studies on lightning like the HYdrological cycle in Mediterranean EXperiment (HyMeX) in which electrically active and highly precipitating events over southeastern France that often lead to severe flash floods are studied [Defer et al., 2015]. Other atmospheric studies about sudden stratospheric warmings are conducted in order to better understand the climate [Smets, 2018]. Major international projects like Atmospheric Dynamics Research InfraStructure in Europe (ARISE) have used infrasound technology as a tool to describe the middle-atmosphere. This can be done using known sources to develop remote sensing methods by inference, like for example ammunition explosions in Hukkakero, Finland [Vera Rodriguez et al., 2020]. Finally one of the major use of infrasound is the detection of nuclear tests by the International Monitoring System (IMS) in the context of the Comprehensive Nuclear Test-Ban Treaty (CTBT).

I.2.2 The development of the International Monitoring System (IMS)

After the second world war, the cold war progressively took place between the United State, the Soviet Union and their respective allies. This led to the nuclear arms race competition for supremacy in nuclear warfare. In addition to the American and Soviet nuclear stock expansion, other countries developed nuclear weapons. The culmination of tensions was reached after two events, the Tsar bomba test (1961), previously described as the most powerful nuclear test ever conducted and the Cuban Missile Crisis (1962). In a gesture of easing of relations between the United States and the USSR, the Limited Test Ban Treaty (LTBT) was signed between these two countries in Moscow on 5 August 1963 then it was opened for signature by other countries. The treaty formally went quickly into effect on 10 October 1963. Since then, 123 other states have become party to the treaty. This treaty prohibits all tests except those done underground. Then with a total of more than 2000 nuclear tests after the end of the second world war, another treaty was shaped, the Comprehensive Nuclear Test-Ban Treaty (CTBT). This one is a multilateral treaty banning nuclear test explosions in all environments including underground. It was adopted by the United Nations General Assembly on 10 September 1996, but has not entered yet into force, as nine specific nations have not ratified the treaty (United States, Russia which withdrew its ratification in 2023, China, India, Pakistan, Democratic People's Republic of Korea, Iran, Egypt and Israel). However, since the opening for signature and ratification, 178 countries across the world have signed and

ratified the treaty. The Comprehensive Nuclear Test-Ban Treaty Organisation (CTBTO), which hosts the International Data Centre (IDC), was established to promote the ratification of the treaty in order to put it into force and to verify its application by the member nations.

With this in mind, a monitoring system has been developed by the organisation and the member states. The International Monitoring System (IMS) consists of four different technologies : seismic, infrasound, hydroacoustic monitoring the different media (underground, atmospheric and under water) and radionuclide laboratories in order to detect radioactive particulates or noble gases produced by a nuclear explosions. There is a total number of 337 facilities including 50 primary seismic stations and 120 auxiliary seismic stations, 11 hydroacoustic stations, 60 infrasound stations, 80 radionuclide stations associated to 16 radionuclide laboratories. Figure I.2.1 shows the IMS map of all the facilities across the world. The IMS has been designed at the Conference on Disarmament in Geneva in 1996 in order to efficiently cover the globe. At this moment, 90% of the IMS stations are operational and France is the first country of the Permanent Five (P5) of the United Nations Security Council who has set up all the stations on its territory.

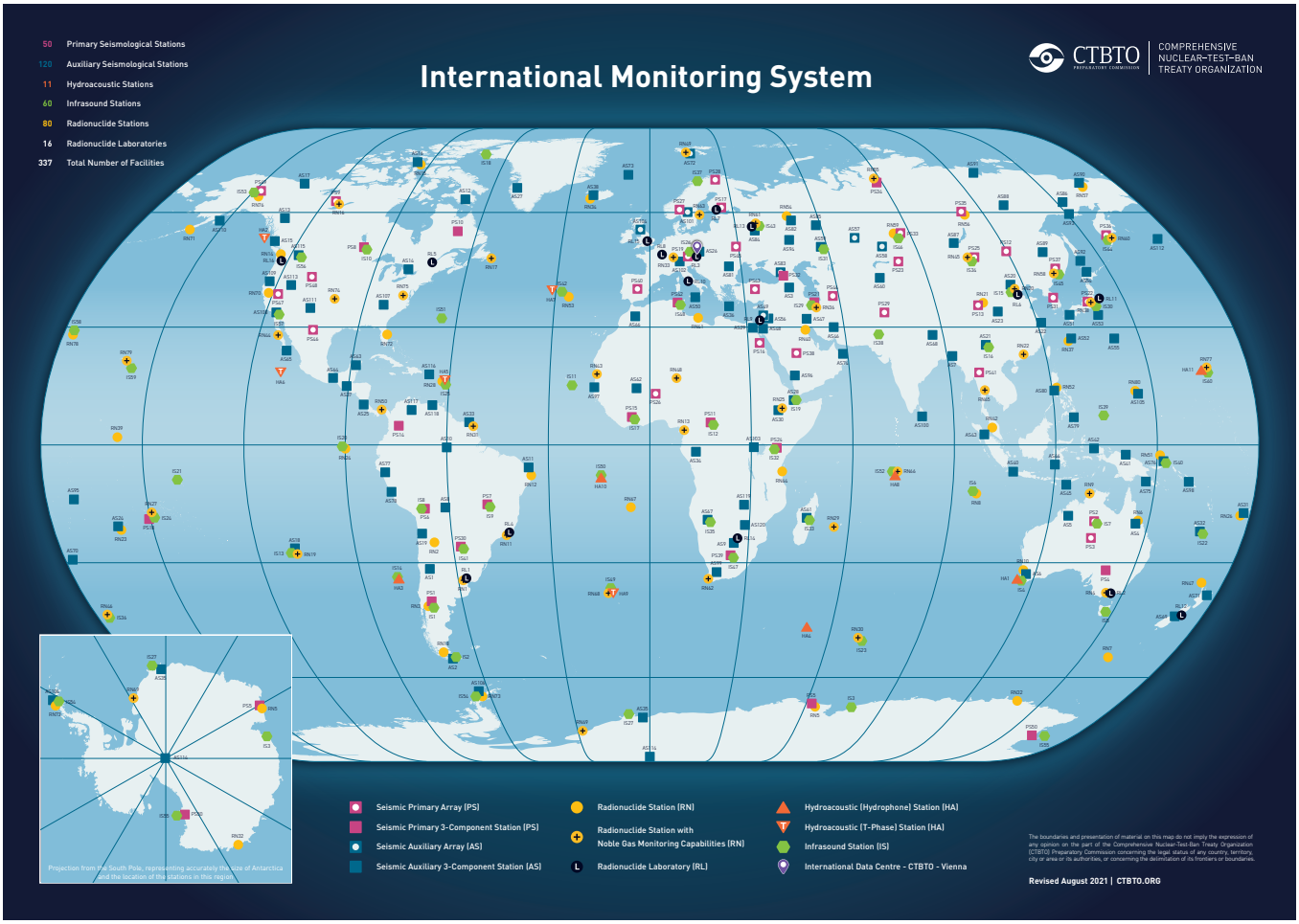

Figure I.2.1: The International Monitoring System (IMS) spans the globe with a network that, when complete, will consist of 321 monitoring stations and 16 laboratories hosted by 89 countries around the world. Extracted from the CTBTO website (https://www.ctbto.org).

I.2.3 Infrasound array design

A total of 60 infrasound stations are planned as part of the IMS global network, with nearly uniform spacing despite the lack of emerged land in the southern hemisphere. This configuration was proposed

with the intention of detecting explosions with a yield of around 1 kiloton equivalent of TNT and to localise it with at least two stations. An infrasound station consists of several microbarometers that measure the atmospheric pressure fluctuations. Several sensors were developed for the purpose of the IMS requirements namely having a self noise measurements lower than the low noise model [Bowman et al., 2005]. The model MB2000/2005, developed at the Commissariat à l'énergie atomique et aux énergies alternatives (CEA) hosting the French National Data Centre (NDC), and the Chaparral 5 designed by Chaparral Physics were manufactured [Marty, 2019]. MB2000/2005, for example has a self noise over the low noise model at frequencies higher than 1 Hz [Alcoverro et al., 2005]. It is not the case of the Chaparral 5 which however has a response and a self noise sensitive to the environment. Due to their low sensitivity to environmental conditions the MB2000/2005 were deployed at over more than 90% of the network in 2012. To manage their own issues, new developments led to the MB3a [Merchant and McDowell, 2014], the Chaparral 50 A [Hart and Rembold, 2010] and then the Hyperion 5113/A [Merchant, 2015]. Due to the respect of the IMS requirements, the low sensitivity to the environment and the new advantage of the MB3 (i.e smaller power consumption, integrated calibration coil) the MB2000/2005 and the MB3 represented more than 80 % of the sensors of the network in 2017. Previously we showed that the fluctuation of the atmospheric pressure was around ones to tens of Pascals, compared to the 1000 hPa of the atmospheric pressure at the surface, indicating how sensitive the sensors must be in order to detect an event. However, the capability of the station to detect an event depends on several parameters. The first one is the capability to reduce the noise that can mask signals of interest. For this aim the sensors are installed in quiet places with reduced exposition to local wind turbulences. Wind noise reduction systems are also added to each sensor in order to average the signal and reduce incoherent wind noise [McDonald et al., 1971]. Figure I.2.2 represents a microbarometer setup within a vault connected to a pipe system, a summing manifold and inlet ports. Infrasound waves pass through the ports and propagate through the pipes to the manifold. The manifold is connected to a microbarometer located in the centre of the element and itself is connected to a digitizer, a GPS, meteorological equipment and a data transmission system. This experimental design yields improvement of the signal to noise ratio when averaging coherent signal amplitude and incoherent noise at the scale of the filtering system.

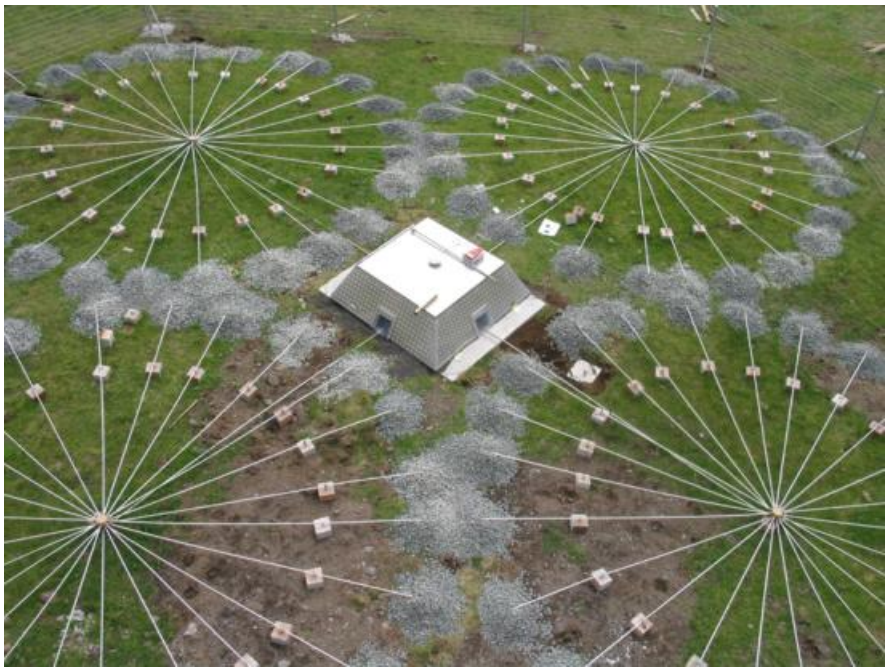

Figure I.2.2: Illustration of the pipe array connected to the manifold where the microbarometers is contained. Extracted from the CTBTO website (https://www.ctbto.org).

The other parameters that affect the capability of the station to detect an event include the sensitivity of the sensor to a particular range of frequencies, atmospheric conditions at the station, the data processing algorithm, and the array design. The array design refers to the geometry of the station, including the spacing, distribution and the number of sensors. A way to study the geometry of the station and to

improve its ability to detect a signal is to study the array manifold, which is the sum over 360° of the array response [Christie and Campus, 2009]. The goal is, of course, to be isotropic that means that the desired design must have a response that is independent from the direction of arrival of the incident signal. The distance between the sensors will govern the frequency sensitivity of the station. The initial array design was with four sensors forming a triangle with the fourth sensor located in the centre; typical apertures were between 1 and 3 km. However this kind of array was sensitive to spatial decoherence at high frequency. That is why most stations are now comprised of, at minimum, 8 sensors with a small aperture sub-array. The following figures I.2.3 and I.2.4 show the impact of the array design of the Kazakhstani station IS31 on the response for an infrasound arrival at 50° and 340 m/s at 1 Hz. It is worth noting that there are a large number of side lobes with high amplitude when only four sensors are used with a large aperture, resulting in spatial aliasing. Nevertheless, the impact of the side lobes has been significantly reduced by incorporating additional sensors and a sub-array adapted for high-frequency estimation. Thus, these additional sensors allow more accurate signal processing. Although this aliasing is important for plane waves, much of the aliasing issue can be reduced due to the non-dispersive nature of infrasound. That is that the group and phase velocities are approximately equal at all frequencies.

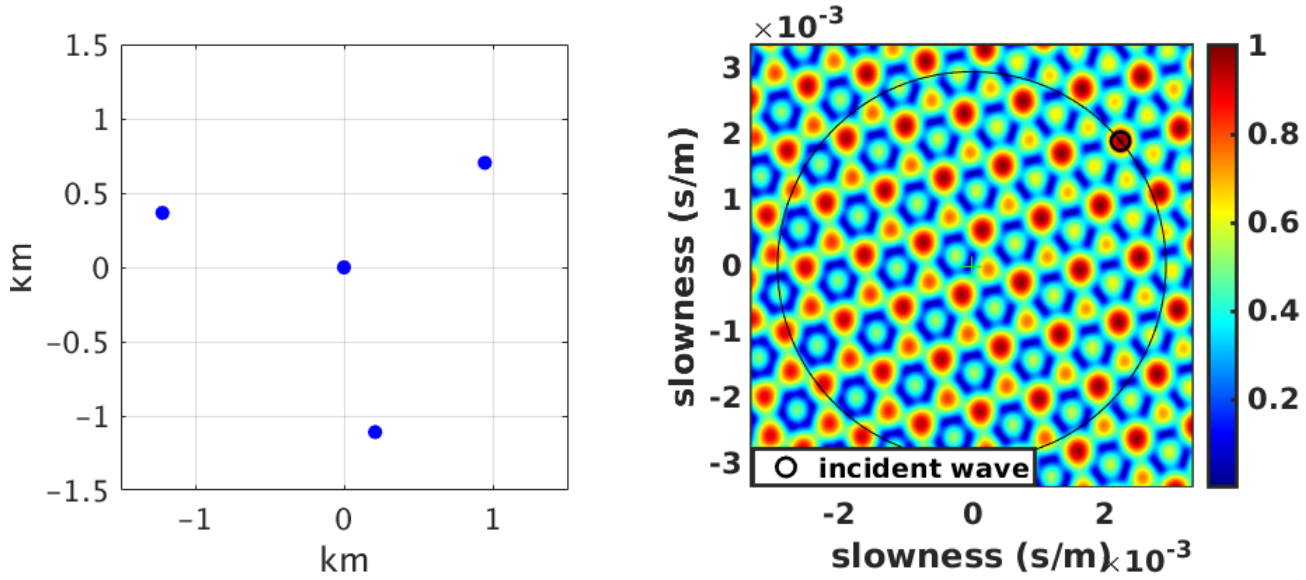

Figure I.2.3: Illustration of the relative position of the four sensors at the IS31 station and the corresponding response of the array to an infrasound arrival at 50° and 340 m/s at 1 Hz. The side lobes are numerous and have high amplitudes. The large black circle represents the sound speed at 340 m/s and the little black circle the position in the slowness space of the incident wave.

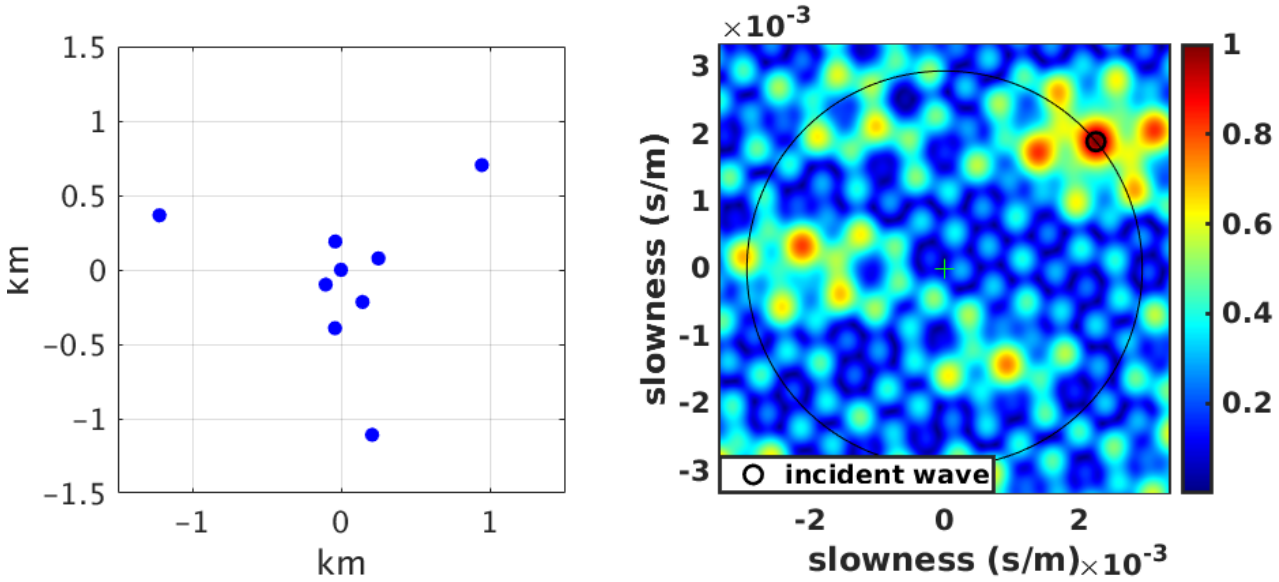

Figure I.2.4: Illustration of the relative position of the nine sensors at the IS31 station and the corresponding response of the array to an infrasound arrival at 50° and 340 m/s at 1 Hz. The side lobes are fewer and have lower amplitudes. The large black circle represents the sound speed at 340 m/s and the little black circle the position in the slowness space of the incident wave.

Chapter I.3

Signal processing and objectives

I.3.1 Signal models

Once the signal is recorded, we need to process it. Different signal models can be used. In many problems the signals observed can be written as

$$z(t) = s(t;\tau) + n(t) \tag{I.3.1}$$

where $z(t)$ is the observed signal, $s(t;\tau)$ is the Signal Of Interest (SOI) as a function of time, τ is the parameter to estimate and $n(t)$ the additive noise considered to be white and Gaussian. Both $s(t;\tau)$ and $n(t)$ are assumed to be stationary.

Two types of signal exist in the literature for this model: a broadband signal model and a narrowband one. A narrowband signal is characterised by a bandwidth at least a hundred times smaller than the central frequency. It means that the frequency band of the signal does not exceed the coherency of the frequency band of the channel. The frequency response is considered to be flat over the narrow bandwidth. In contrast, a broadband signal is composed of a large amount of frequency content and, therefore, significantly exceeds the channel bandwidth. As a result, the frequency response of a broadband signal is not flat and depends of the frequency content of the signal. Figure I.3.1 illustrates the frequency content of a narrowband signal and a broadband signal with background noise in a passband filter. The two models are explained in the following subsections, assuming multiple sources.

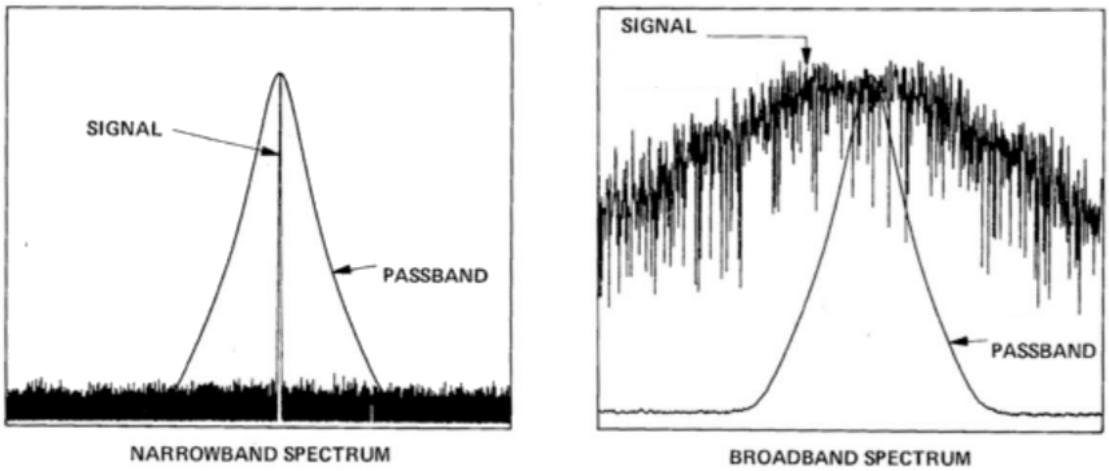

Figure I.3.1: Illustration of a narrowband and broadband spectra. The spectrum of the narrowband signal is hundred times smaller than the passband. The bandwidth of the broadband signal is much broader than the passband (extracted and modified from Wyatt).

I.3.1.1 Narrowband model

Let's consider an infrasound array of M microbarometers on a horizontal plane [Nouvellet et al., 2014]. The infrasound-generating source is supposed to be far enough to assume a planar wavefront. As previously stated, the SOI, $s(t)$, is a narrowband signal if the spectrum extends over a bandwidth, B, much smaller than the central frequency, f_0. Graphically, such a signal can be represented as in figure I.3.2 where the section of the signal in the black box can be approximated to a sinusoidal function with frequency f_0. The pseudo-period of variations of the signal envelope is of order $1/B$.

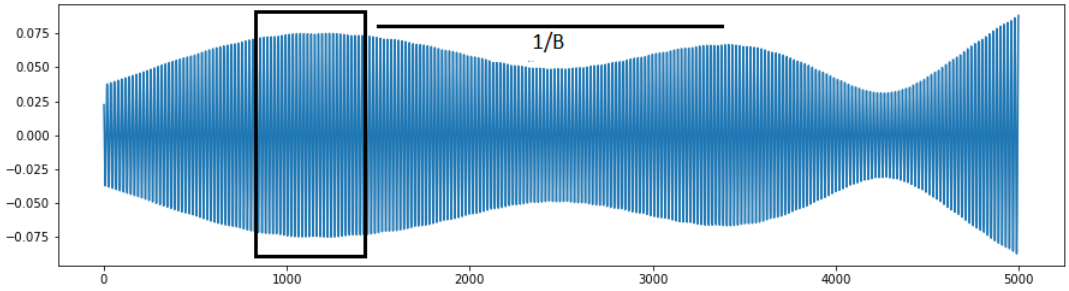

Figure I.3.2: The signal portion in a black box is a quasi-sinusoid of frequency f_0. The period of the envelope fluctuations is of order of $1/B$.

Thus, we can express the signal $s(t)$ by its in-phase and quadrature-phase components:

$$s(t) = p(t)cos(2\pi f_0 t) - q(t)sin(2\pi f_0 t) = Real\{(p(t) + iq(t))e^{2i\pi f_0 t}\} \tag{I.3.2}$$

where $p(t)$ and $q(t)$ are respectively in-phase and quadrature signals with regard to f_0 which vary slowly relative to $1/f_0$. The complex envelope of $s(t)$ is:

$$x(t) = (p(t) + iq(t))e^{2i\pi f_0 t} \tag{I.3.3}$$

which is easily related to the equation I.3.1 by z(t)=Real{x(t)}+n(t). Considering now $\frac{1}{f_0} << B$, it comes that the complex envelope of the signal can be written as:

$$\begin{aligned} x(t-\tau) &= (p(t-\tau) + iq(t-\tau))e^{2i\pi f_0 t - \tau} \\ &\approx (p(t) + iq(t))e^{2i\pi f_0 t}e^{-2i\pi f_0 \tau} = x(t)e^{-2i\pi f_0 \tau} \end{aligned} \tag{I.3.4}$$

It comes finally that, in a narrowband model, the observed signal is a sum of several sources with a phase shift for each sensor, such that:

$$z_m(t) = \sum_{n=1}^{N} s_n(t)a_m(\theta_n, v_n) + n_m(t) \tag{I.3.5}$$

where z_m is the observed signal assumed centred (i.e the mean has been removed) at sensor m, N is the number of sources that has to be estimated, $s_n(t)$ is the n-th SOI, a spatially coherent signal at the sensor m, $n_m(t)$ is the additive noise of the m-th environment. The vector $a(\theta_n, v_n) = [1, e^{-2i\pi f_0 \tau_1(\theta_n, v_n)}, ..., e^{-2i\pi f_0 \tau_{M-1}(\theta_n, v_n)}]^T$ represents the phase shift of the SOI for each sensor at the central frequency, f_0, characterised by the delay between sensor m and the reference sensor. The M signals are sampled with the sampling period $T_e = 1/Fs$, according with the Nyquist condition where Fs is the sampling frequency. Thus $z_t = z(tT_e)$ but for the sake of simplicity we will denote $z(t)$ for z_t thereafter. The notation of the equation I.3.5 can be simplified using matrices for a time window of length L with N_e samples:

$$\mathbf{Z} = \mathbf{AS} + \mathbf{N} \tag{I.3.6}$$

where $\mathbf{Z}$ $(M \times N_e)$ is the observation matrix for all the sensors for N_e samples, and $\mathbf{A}$ $(M \times N)$ is the steering matrix which contains N steering vectors, $a(\theta, v)$. $\mathbf{S}$ is the source matrix containing amplitude/phase

information ($N \times N_e$) and $\mathbf{N}$ ($M \times N_e$) is the additive noise of each sensor. This new equation leads to the covariance matrix formula related to the model at a time t_l [Guérard, 2016]:

$$\mathbf{R_{zz}} = \mathbb{E}\{\mathbf{Z_{t_l}}\mathbf{Z_{t_l}}^H\} = \mathbf{A}\mathbb{E}\{\mathbf{S_{t_l}}\mathbf{S_{t_l}}^H\}\mathbf{A}^H + \mathbb{E}\{\mathbf{N_{t_l}}\mathbf{N_{t_l}}\} = \mathbf{A}\mathbf{R_{ss}}\mathbf{A}^H + \mathbf{R_{nn}} \tag{I.3.7}$$

The matrix $\mathbf{R_{zz}}$ is hermitian and is related to the observed signal received at the array sensors for a time t_l including both the SOI and the noise. The matrix $\mathbf{R_{ss}}$ and $\mathbf{R_{nn}}$ correspond to the covariance matrix of the source and the noise, respectively. Finally, the matrix $\mathbf{R} = \mathbf{A}\mathbf{R_{ss}}\mathbf{A}^H$ is the covariance matrix of the observed signals received by the sensors without the noise. In general the $\mathbf{R_{zz}}$ can be estimated over a N_e-sized time window for a better precision as:

$$\widehat{\mathbf{R_{zz}}} = \frac{1}{N_e}\mathbf{Z}\mathbf{Z}^H \tag{I.3.8}$$

I.3.1.2 Broadband model

While in a narrowband model the propagation delay can be related to a phase shift because of the considerably smaller bandwidth compared to the central frequency, the propagation delay in a broadband model is related to a time shift. Then, in the time domain, the observed centred signal at the sensor m is

$$z_m(t) = \sum_{n=1}^{N} s_n(t - \tau_m(\theta_n, v_n)) + n_m(t) \tag{I.3.9}$$

where $\tau_m(\theta_n, v_n)$ represents the delay of n-th wavefront at the sensor m with respect to the referenced sensor. These wavefront are characterised by the back-azimuth θ_n and the trace velocity v_n of the slowness vector p_n. Let r_m be the location of sensor m in an arbitrary orthogonal 2D coordinate system. The delay $\tau_m(\theta_n, v_n)$ for sensor m of the n-th source can be described as :

$$\tau_m(\theta_n, v_n) \quad = \quad r_m^T p_n \tag{I.3.10}$$

where the slowness vector in two dimensions is

$$p_n \quad = \quad -v_n^{-1}\begin{bmatrix}\sin(\theta_n)\\ \cos(\theta_n)\end{bmatrix} \tag{I.3.11}$$

with v_n and θ_n the wavefront parameters of the n-th source.

By vectoring the equation I.3.9 it gives:

$$z(t) \quad = \quad \sum_{n=1}^{N} s(t - \tau(\theta_n, v_n)) + n(t) \tag{I.3.12}$$

where $z(t)$, $\tau(\theta_n, v_n)$ and $n(t)$ are of size M. One approximation is made here: the wave reaches all sensors with the same amplitude. This simplification can be justified by the fact that the distance between the sources and the array is much larger than the distance between the sensors at the array station. Moreover, IMS stations are designed to detect such sources. Indeed the distances between sensors are adapted to the wavelength of infrasound sources, therefore, the relative gain at each sensor is approximately equal.

When applying a Fourier transform on the discrete signal $z(t)$, it becomes:

$$\begin{bmatrix}Z_1(f_i)\\ Z_2(f_i)\\ \vdots\\ Z_M(f_i)\end{bmatrix} = \begin{bmatrix}a(f_i,\theta_1,v_1) & a(f_i,\theta_2,v_2)\dots a(f_i,\theta_N,v_N)\end{bmatrix}\begin{bmatrix}S_1(f_i)\\ S_2(f_i)\\ \vdots\\ S_N(f_i)\end{bmatrix} + \begin{bmatrix}N_1(f_i)\\ N_2(f_i)\\ \vdots\\ N_M(f_i)\end{bmatrix} \tag{I.3.13}$$

where $Z(f_i)$ ($M \times 1$) is the Fourier transform of the discrete signal $z(t)$ at the frequency f_i, $\mathbf{A}(f_i, \theta, v)$ ($M \times N$) is the steering matrix which contains N steering vectors $a(f_i, \theta, v)$, $S(f_i)$ ($N \times 1$) is the spectrum of the N sources containing amplitude/phase information and $N(f_i)$ ($M \times 1$) is the spectrum of the noise

recorded by the M sensors at the frequency f_i. Thus, in this case a spectral density matrix can be written as

$$\mathbf{C}(f_i) = \sum_{n}^{N} a(f_i, \theta_n, v_n)\sigma^2_{s_n} a^H(f_i, \theta_n, v_n) + \sigma^2\mathbf{I} \tag{I.3.14}$$

where $\sigma^2_{s_n}$ is the power of the signal, σ^2 is the power of the noise and $\mathbf{I}$ is the identity matrix $(M \times M)$. In general, the spectral density matrix is estimated by a periodogram [Brockwell and Davis, 1991] that writes

$$\mathbf{C}_{per}(f_i) = \frac{1}{Ne} Z(f_i) Z^H(f_i) \tag{I.3.15}$$

A smoothing kernel over frequencies is used to better estimate the spectral density matrix. For a better estimation, $\mathbf{C}(f_B)$ can be defined as the mean of all the $\mathbf{C}(f_i)$ calculated in the band.

The broadband model is classically used for infrasound monitoring by the NDC and the CTBTO for operational purposes due to the broadband nature of infrasound sources. Moreover, a narrowband model would require extremely narrow filters around each frequency of interest. For example around the frequency of 0.1 Hz, a narrowband processing would require a [0.0999 - 0.101] Hz frequency band. In addition, the number of frequency bands to process would be huge and would increase the computational cost considerably.

I.3.2 Principle of detection

The previous section describes the signal models when the SOIs are present. But the first question to answer is: Is any SOI present or not? In statistics, such a question is called detection or hypothesis testing. This method consists of checking the validity of a statistical assumption with the data. At first we need to specify the two classical hypotheses in signal processing:

- The null hypothesis, H_0, assuming that the signal is random, thus no SOI is present and only noise is recorded by the array. It can be related to the white and Gaussian structure of the noise.
- The alternative hypothesis, H_1, which assumes a particular structure in the signal, meaning the presence of coherent signals crossing the array. It can be related to the structure of the covariance matrix or the spectral matrix according to the signal models explained in the section I.3.1.

The hypotheses set aims to reject or accept the null hypothesis, H_0, with a certain degree of confidence. If the hypothesis H_0 is rejected, then the hypothesis H_1 is verified with a degree of confidence. However, if the null hypothesis is not rejected, it only means that no evidence of a coherent signal has been found. The H_0 assumption is not verified in this case.
Mathematically, the problem of the presence of one SOI (i.e N=1) is related to the presence or not of the variable $s(t)$, such that

$$\begin{cases} H_0 & : & s(t) = 0 \\ H_1 & : & s(t) \neq 0 \end{cases} \tag{I.3.16}$$

In a multisource problem, the hypotheses have to be redefined iteratively after each test when the previous null hypothesis has been rejected.

$$\begin{cases} H_0 & : & s_n(t) = 0, \quad \forall n \in \{1, \dots, N\} \\ H_1 & : & s_n(t) \neq 0, \quad \forall n \in \{1, \dots, N\} \end{cases} \tag{I.3.17}$$

Another approach would be a non-binary test with M hypotheses. After the careful choice of the hypotheses, the appropriate statistics must be selected in order to discriminate between the two hypotheses with respect to the distributions of the TS. The Test Statistic (TS) used to resolve the problem leads to errors represented in figure I.3.3 when selecting a threshold to discriminate between the two hypotheses. They are of two types, the first type of error (error α) occurs when the null hypothesis H_0 is rejected even though it is true. The second type (error β) occurs when the null hypothesis H_0 is accepted even though it is false. In a detection problem, the α error leads to a false positive while the β error leads

to a false negative. It is important to note that the two errors cannot be minimised at the same time. That is why the choice of the threshold has to be set depending on the type of error to be minimised. A commonly approach for binary hypotheses testing (H_0 against H_1) is to compute a real-valued TS and compare the result to a given threshold. If we are above the threshold we choose H_0, or else, we choose H_1. When the distribution of TS under H_0 is estimated, the p-value can be calculated and used as a threshold [Gibbons and Pratt, 1975]. Typically, if the p-value is less than 0.01, it is likely that H_0 is false, therefore we reject H_0 and accept H_1. It is the TS value that fixes the value of the α error for which the hypothesis H_0 is rejected. Usually, a p-value of 1% is set, it means that the false positive probability is 1%. Alternatively, if the H_1 distribution is estimated, a threshold based on the β error can be fixed, the goal here is to minimise the false negative probability.

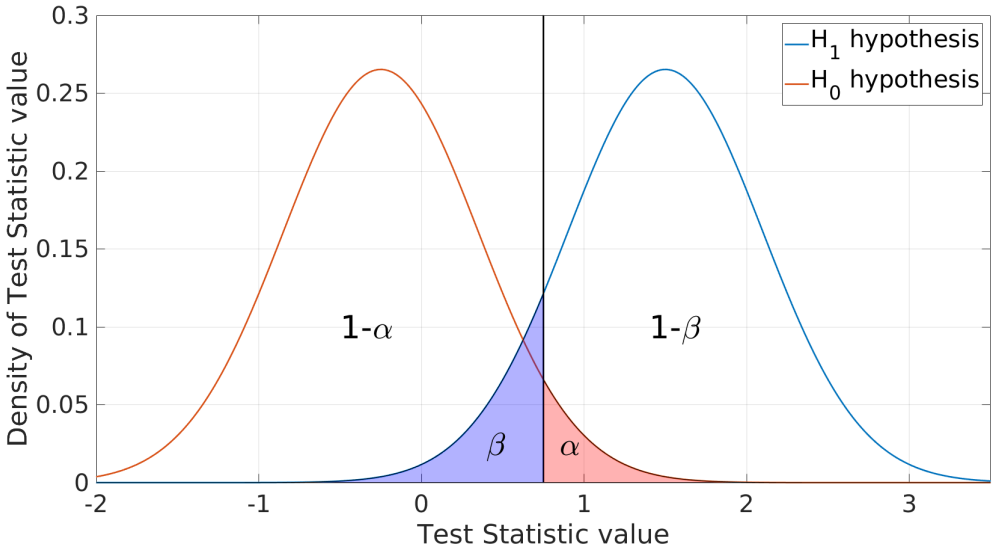

Figure I.3.3: Illustration of the probability density of the null and alternative hypotheses, respectively in red and blue, in a "simple" problem. The threshold in black leads to the error of type one α and type two β represented by areas under the curves.

Each TS method has its own performance and it is important to know if a TS method is appropriate to discriminate between the two hypotheses. For this purpose, we use the Receiver Operating Characteristic (ROC) curves approach that measures the capacity of a binary classifier to distinguish between two assumptions which have to be synthetically modelled (Arrowsmith et al. [2009]; Atapattu et al. [2010]; Park et al. [2017]; Marcillo et al. [2019]). We denote for the TS function, F :

- $F_1^0, \ldots, F_i^0$ the i maximum values of the TS function, F, under H_0.
- $F_1^1, \ldots, F_j^1$ the j maximum values of the TS function, F, under H_1.

The two probability densities are modelled in order to accurately calculate the true positive (i.e $1-\beta$) and the false positive (i.e α) for each possible threshold value separating the both distributions, η. The true positive (TPR) and the false alarm rates (FAR) are defined with respect to η

$$\begin{cases} \text{FAR}(\eta) &= i^{-1} \sum_{k=1}^{i} \mathbb{1}(F_k^0 > \eta) \\ \text{TPR}(\eta) &= j^{-1} \sum_{l=1}^{j} \mathbb{1}(F_l^1 > \eta) \end{cases} \tag{I.3.18}$$

When all the true positive and false positive of the ground truth database are calculated, an Empirical Receiver Operating Characteristic (EROC) curve can be generated as we can see in figure I.3.4. The closer a curve is to the point (0,1) the better the detector. An easier way to interpret the result is to

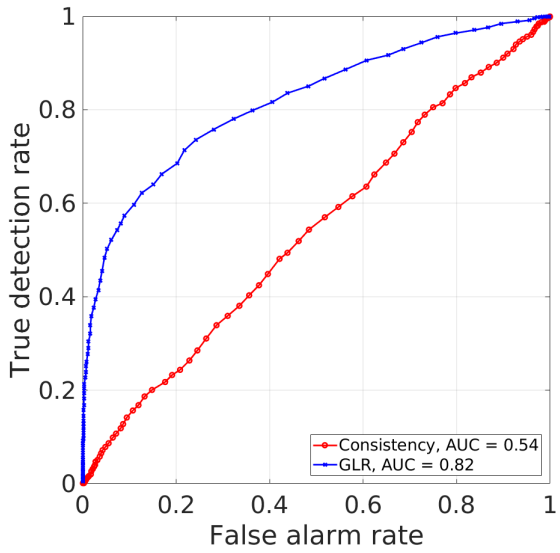

Figure I.3.4: Illustration of Receiver Operating Characteristic (ROC) curves for two detectors. The closer the curve is to the point (0,1) the better the detector is. The Area Under the Curve (AUC) approaches one if the detector distinguishes perfectly the two hypotheses H_0 and H_1.

focus on the Empirical Area Under the Curve (EAUC) of the EROC curve.
The EAUC is obtained by the Wilcoxon-Mann-Whitney statistic [Hanley and McNeil, 1982] defined as :

$$\text{EAUC} = \frac{\sum_{k=1}^{i}\sum_{l=1}^{j} S(F_k^0, F_l^1)}{ij} \tag{I.3.19}$$

$$\text{with} \quad S(X,Y) = \begin{cases} 1 & \text{if} \quad Y < X \\ 1/2 & \text{if} \quad Y = X \\ 0 & \text{if} \quad Y > X \end{cases} \tag{I.3.20}$$

It comes that the closer to one the EAUC, the better the TS method is.

Several kinds of TS based on different approaches are developed in the literature. The F-detector is one of the most used detector and applied by several NDCs (Evers and Haak [2005]; Arrowsmith et al. [2009]). It can be implemented either in the time or frequency domain and estimates the ratio between the variance of a hypothetical SOI with a specific Direction Of Arrival (DOA) and the variance of the noise. It can also be used to measure the Signal to Noise Ratio (SNR). This ratio can be compared to a threshold based on the Fisher distribution in order to make a decision between H_0 and H_1. This method will be developed in detail later. Another similar method named the Generalized Likelihood Ratio Test (GLRT) is constructed by calculating the ratio of the log likelihood of the probability density function of H_1 and H_0 (Kay [2013]; Charbit [2017]). Here, the test is performed using the Neyman-Pearson criteria adjusted by the desired false alarm rate. The Generalized Likelihood Ratio (GLR) derived from this method will be used in this thesis as a key TS from the state-of-the-art. Finally, correlation methods based detectors, such as the Mean of Cross Correlation Maximum (MCCM) [Lee et al., 2013] and the consistency [Cansi and Pichon, 2008] are widely used. They are built upon the estimation of the time delay between pairs of sensors by maximising the cross correlation function. The consistency is applied by Progressive Multi-Channel Correlation (PMCC) which is detailed in the following and used by the French NDC and the IDC.

I.3.3 Signal processing workflow

Currently, the received signal $z(t)$ is splitted into the time-frequency domain. It allows the source separation in both time and frequency space by the use of sliding window and filter over the entire period of

analysis. The time-frequency domain is generated, here, by a third octave decomposition. A type one, order two Chebychev filter is used. This kind of filter is applied due to the steep roll-off. It allows an almost constant filter response in the wanted frequency band despite an equiripple behaviour due to the ripple of the filter in the passband. The phase change is, however, important due to the transfer function of the filter. Figure I.3.5 shows the window length used for each frequency band. The window length used for each frequency band ensures the observation of ten times the mean wavelength of the filtered signal. The second graph shows the used filters between 0.1 and 4 Hz. The main characteristic of these filters are that they are flat in the frequency band of interest, with no gain. Finally, the third one is about the phase change in function of frequency. This phase change is not a problem because the filter is applied equally to all the sensors.

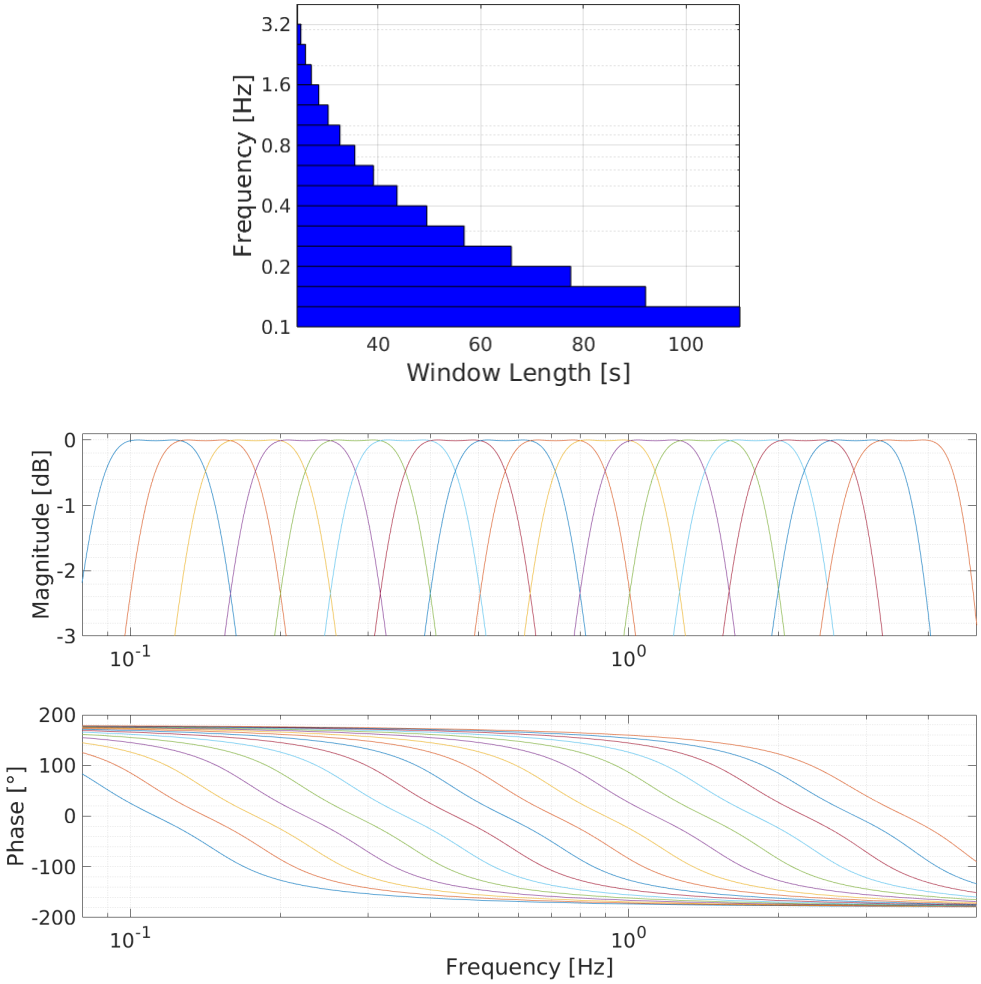

Figure I.3.5: Example of a third octave decomposition showing the duration of a time window as a function of frequency band (top). Filter response in magnitude and phase of each filter in function of frequency (bottom).

The processing is thus performed in the time frequency domain using a filter and windowing of the time series. Finally, the results are graphically represented as in the figure I.3.6 where each parameter of interest (θ, v) is illustrated by a pixel. The length of the pixel is proportional to the window length, the height is proportional to the bandwidth, and the colour depends on the parameter of interest. This representation allows for a better interpretation, as sources are isolated by their frequency content and time duration.

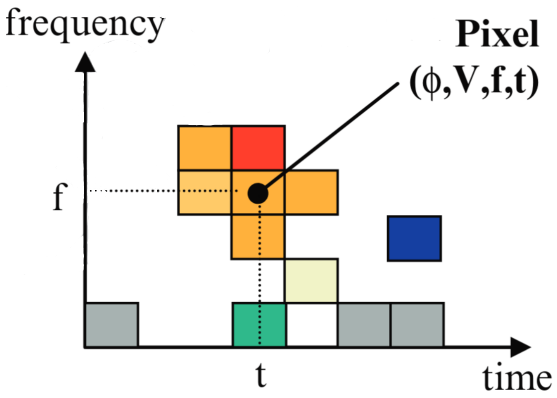

Figure I.3.6: Graphical representation of estimates in the time-frequency domain. The color of each pixel represents the value of the parameter of interest. Illustration extracted and modified from Brachet et al. [2010].

I.3.4 Motivations of the thesis

The CEA is a research centre and also the French NDC which exploits and analyses the seismic, radionuclide, hydroacoustic and infrasound data in view of the development of the IMS being set up by the CTBTO. So far, the correlation-based method (Progressive Multi-Channel Correlation (PMCC)) is used by the CTBTO to analyse signals recorded within the different stations of the IMS. This detection method has been essentially developed to detect and localise a single coherent source signal within a given time-frequency cell. To ensure the single source hypothesis, in practice, the signal received is split into the time-frequency domain by, for example, a third octave decomposition [Brachet et al., 2010]. This allows the separation of multiple sources with different frequency content. Thus, this multi-band setting leads to a finer estimate of the coherent infrasound energy from a wide variety of natural and artificial sources. It allows better characterisation of environmental coherent noise and discrimination of events of interest [Matoza et al., 2013]. However feedbacks on the use of PMCC show erroneous detections and inaccurate estimates in degraded recording conditions [Nouvellet et al., 2014]. One of the reasons for this is the degradation of the capacities with low SNR, another reason is that the algorithm was developed and optimised to detect a single source of coherent signals in the same time-frequency cell. Under realistic recording conditions, the stations detect multiple sources and the current processing is not suitable. Rather than assuming the presence of a single source of interest at most, it is relevant to consider the presence of several signals of interest crossing the sensor array at the same time and same frequency. This thesis project involves developing and testing high-resolution methods for separating multiple infrasound sources in the same frequency band on controlled bases of synthetic and real signals.

The thesis will first introduce the current monosource processing method used at the NDC and the IDC as well as recent developments in the part II. This part consists of two chapters. The chapter II.1 describes Progressive Multi-Channel Correlation (PMCC), the current algorithm used by the CEA and the CTBTO for operational monitoring. Recent developments are discussed in chapter II.2, which covers the Multi-Channel Maximum Likelihood (MCML) algorithm, a new method based on the likelihood. This chapter includes methods and accuracy results on synthetic and real data. Real data from the infrasound IMS are analysed but also seismic data from a national network.

Then, high resolution state-of-the-art estimation approaches are detailed in the part III which consists of four chapters. It involves the description of subspace decomposition approaches like the MUltiple SIgnal Classification (MUSIC) in chapter III.1, spectrum approaches like the F-K spectrum or the Capon spectrum in chapter III.2, statistical approaches like the F-ratio already in used in several NDC or CLEAN, a new developed method in chapter III.3 and finally robust regression techniques in which the least trimmed squares based on a improved least squares method in chapter III.4. Several methods from these different

chapters are implemented to compare their estimation capabilities.

The part IV is about developed multisource processing to find out if better methods compared to the state-of-the-art could be implemented. This part consists of five chapters. In which, the different extensions of the MCML method for multisource processing are investigated in the chapter IV.1 in order to capitalise on recent developments. Other methods are investigated, like the ICA approach for wideband source separation in chapter IV.2 and a dictionary coding strategy on the likelihood function of the MCML method or on the delay between sensors pairs in chapter IV.3. A comparison of the performances in accuracy of the developed estimators is presented in chapter IV.4 in order to quantify the accuracy of each implemented method compared to the state-of-the-art algorithms. This comparison is carried out on synthetic signals with ground truth controlled parameters first and on real data afterwards. The post processing of the estimations is characterised by the clustering of results with similar parameters, which is crucial for event analysis. A new method based on a Gaussian Mixture Model (GMM) is presented for better event building in chapter IV.5.

Finally, the part V covers the conclusion of the whole study and the future work to improve the results.

Chapter I.4

Introduction générale sur les infrasons (français)

I.4.1 Qu'est-ce que les infrasons?

Nous parlons généralement d'ondes acoustiques en référence aux sons audibles pour les êtres humains, mais nous faisons référence, plus généralement, aux ondes de pression. En effet, les ondes acoustiques sont des ondes élastiques longitudinales, ce qui signifie que les particules mises en mouvement par l'onde se déplacent dans la même direction que l'onde elle-même [Leisure, 2017]. Le processus de compression et de raréfaction implique une alternance périodique entre les positions des particules les plus proches et les plus éloignées, les particules occupant elles-mêmes des positions intermédiaires entre ces extrêmes. La force de restauration est la pression atmosphérique ambiante, qui agit pour ramener la pression à cette pression d'équilibre. Les ondes acoustiques sont divisées en plusieurs catégories, en référence à la plage audible pour les êtres humains (figure I.4.1).

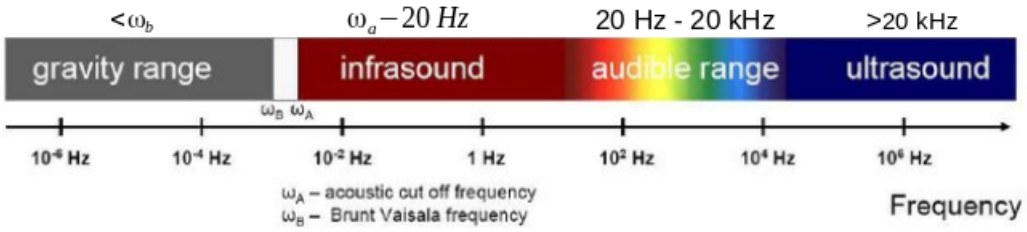

Figure I.4.1: Vue schématique des différentes sections acoustiques et de leurs limites en fréquence (extrait et modifié de Bittner et al. [2010]).

La section audible pour les êtres humains est caractérisée par une plage de fréquences allant de 20 Hz à 20 kHz. Cette section est délimitée par des ultrasons, à des fréquences supérieures à 20 kHz, et par des infrasons à des fréquences inférieures à 20 Hz. L'infrason s'étend de la fréquence de coupure acoustique d'environ 3,3 mHz à la section audible à 20 Hz. La fréquence de coupure acoustique est la fréquence à laquelle les ondes acoustiques commencent à se propager. Les fréquences inférieures à la fréquence de coupure acoustique et à la fréquence de Brunt-Väisälä (c'est-à-dire 2,9 mHz dans la basse atmosphère) sont associées aux ondes de gravité [Hines, 1960]. En raison de leurs basses fréquences et de leurs larges longueurs d'onde correspondantes, ainsi que de la faible absorption par l'atmosphère, les infrasons sont peu atténués et peuvent parcourir des milliers de kilomètres. Cependant, pour les créer, une grande quantité d'énergie est nécessaire pour mettre en mouvement une portion suffisante de l'atmosphère.

I.4.2 Les sources génératrices d'infrasons

Les sources d'infrasons doivent être grandes et puissantes pour créer des infrasons. Les sources d'infrasons ont un contenu de fréquence différent (c'est-à-dire un spectre large ou étroit) et une durée temporelle différente (c'est-à-dire des signaux impulsifs ou quasi-permanents), ce qui nous permet de les distinguer. Deux types principaux de sources peuvent être décrits : les sources naturelles et les sources anthropiques.

Les sources naturelles d'infrasons sont nombreuses en raison de la grande variété de phénomènes naturels existants. En effet, les aurores polaires, par exemple, produisent des infrasons en déplaçant un grand volume d'atmosphère grâce à l'interaction entre la haute atmosphère et le vent solaire [Wilson, 1969]. Les coulées de débris telles que les glissements de terrain ou les avalanches peuvent également générer des infrasons en raison du déplacement important de matériel [Belli et al., 2022]. Ces signaux peuvent être utilisés pour des applications civiles, telles que l'alerte précoce des avalanches [Belli et al., 2024]. Les tremblements de terre génèrent des infrasons en secouant le sol, qui peuvent être détectés par des stations [Mutschlecner and Whitaker, 2005] et par des observations ionosphériques en raison de la grande puissance de tels événements [Artru et al., 2001]. Les phénomènes météorologiques, en particulier les tempêtes, sont des sources d'infrasons en raison de leur structure turbulente, des vents cisaillants et également des tornades [Schecter et al., 2008]. Cela a conduit à des activités de suivi des tempêtes afin de mieux comprendre ce phénomène (Pásztor et al. [2021] ; Listowski et al. [2022]). Les éclairs générés lors des orages sont une source d'infrasons à haute fréquence. Ils se forment par l'expansion thermique soudaine de l'atmosphère, entraînant des ondes de choc [Few, 1969]. Une grande partie du contenu en fréquence se situe dans la gamme des infrasons. Une meilleure compréhension des orages par la reconstruction des éclairs est une tâche importante en raison des défis liés au changement climatique et à l'augmentation des événements météorologiques instables (Farges and Blanc [2010] ; Farges et al. [2019]). La collision des vagues océaniques venant de directions opposées couplée à l'interaction avec le fond marin génère un contenu infrasonore à très basse fréquence appelé houle [De Carlo, 2020]. Les météores peuvent produire des infrasons par sa vitesse supersonique lorsqu'il pénètre dans l'atmosphère, créant des ondes de choc. La fragmentation du météore ou son explosion crée également des infrasons [Edwards, 2009]. Ces objets peuvent être détectés et analysés. La première détection d'un tel événement fut le météore de Tunguska en 1908 [Chyba et al., 1993]. Depuis cet événement, de nombreuses études ont été réalisées sur d'autres bolides entrant dans l'atmosphère, comme le météore de Tcheliabinsk en 2013 [Le Pichon et al., 2013] ou plus récemment le météore qui a survolé l'océan Atlantique sud [Hupe et al., 2024]. Les derniers exemples naturels de cet aperçu sont les éruptions volcaniques qui produisent des infrasons et une activité sismique. De nombreuses études sur les éruptions volcaniques (Symons [1888] ; Vergoz et al. [2022]) et leurs processus [Perttu et al., 2020] ont été réalisées en utilisant la technologie infrason. Des recherches récentes sont en cours afin d'avertir les citoyens à proximité d'activités volcaniques dangereuses (Marchetti et al. [2019] ; Métaxian et al. [2024]) ou l'aviation concernant les nuages de cendres [Gheri et al., 2024].

Nous sommes également capables de produire des infrasons par nos activités. Tout d'abord, les avions peuvent être détectés à des vitesses subsoniques lorsque les conditions d'enregistrement sont appropriées. Ces types d'événements sont détectés jusqu'à 30 km avant d'être atténués [Evers, 2008]. Cependant, les vols supersoniques, en raison des ondes de choc générées, peuvent être détectés jusqu'à des centaines de kilomètres de distance. En effet, le Concorde a été l'objet de plusieurs études par la technologie infrason [Balachandran et al., 1977]. Les fusées peuvent également être détectées très loin du site de lancement [Pilger et al., 2021b]. Les activités industrielles (Smirnov et al. [2015] ; Pilger et al. [2018]) et les parcs éoliens [Marcillo et al., 2015] peuvent être détectés et peuvent servir d'informations de vérité terrain de référence. Enfin, des explosions suffisamment puissantes génèrent des infrasons que ce soit de simples explosions de carrière [Bondár et al., 2022] ou des explosions de munitions comme les événements de Hukkakero en Finlande [Blixt et al., 2019], mais aussi de grands accidents industriels [Vergoz et al., 2021] ou des explosions nucléaires (Che et al. [2009] ; Che et al. [2022]). Le plus grand essai nucléaire a été réalisé par l'Union soviétique en 1961 avec la Tsar Bomba. La puissance libérée était de 57 mégatonnes de TNT, équivalente à 4000 fois l'énergie de la bombe qui a dévasté Hiroshima [Sakharov, 1990]. Ces événements produisent des infrasons qui peuvent faire plusieurs fois le tour du globe. Le tableau suivant I.4.1 résume les caractéristiques des sources d'infrasons d'intérêt, dont leur contenu fréquentiel, l'amplitude maximale mesurée et la distance maximale de détection. Ce résumé est adapté d'un tableau de Campus

and Christie [2009]. Le tableau montre également comment les amplitudes des phénomènes enregistrés sont faibles par rapport à la pression atmosphérique d'environ 10^5 Pa, ce qui nécessite des capteurs très sensibles.

Table I.4.1: Différentes sources naturelles et anthropiques et leurs caractéristiques en termes de fréquence, d'amplitude maximale enregistrée et de portée de détection maximale estimée.

Sources d'infrasons et références	Bande de fréquence (Hz)	Amplitude maximale observée (Pa)	Distance de détection maximum estimée (km)
Aurores polaires [Wilson, 1971]	0.008 - 20	2	4000
Mouvements de terrain [Bedard, 1993]	0.1 - 20	1	1000
Séismes [Le Pichon et al., 2003]	0.005 - 10	4	>10 000
Tempêtes (Bedard et al. [2000] ; Listowski et al. [2022])	0.01 - 10	0.5	>1500
Tornades [Bedard Jr et al., 2004]	0.5 - 20	0.5	300
Éclairs [Few, 1970]	0.5 - 20	2	50
Météores [ReVelle, 1976]	0.01 - 20	>10	>20000
Houle [Donn and Rind, 1972]	0.12 - 0.35	5	10000
Volcans (Donn and Balachandran [1981] ; Vergoz et al. [2022])	0.003 - 20	>20	>20000
Avions subsoniques [Fee et al., 2013]	0.03 - 20	2	<100
Avions supersoniques [Liszka and Waldemark, 1995]	0.3 - 20	10	5000
Lancers de fusée [Pilger et al., 2021b]	0.01 - 20	5	3000
Activités minières/Tirs de carrière (Bondár et al. [2022] ; Mitterbauer et al. [2024])	0.05 - 20	5	>5000
Explosions chimiques [Vergoz et al., 2021]	0.05 - 20	10	>5000
Explosions nucléaires atmosphériques [Mutschlecner et al., 1999]	0.003 - 20	>20	>20000
Explosions nucléaires souterraines [Whitaker, 2008]	1 - 20	1	>20000

I.4.3 L'impact des conditions atmosphériques sur la propagation des infrasons

L'atmosphère est composée de plusieurs couches comme l'illustre la figure I.4.2. Ces couches peuvent être définies en fonction de la manière dont l'atmosphère est mélangée. En dessous de 100 km, l'atmosphère est mélangée par des vents turbulents, et cette partie est appelée l'homosphère. Au-dessus de 100 km jusqu'à 500 km, le mélange se fait par diffusion, et cette portion est appelée l'hétérosphère. Cependant, la propagation des infrasons est particulièrement influencée par la température et le vent. Les infrasons suivent le chemin de la vitesse effective du son la plus basse. La vitesse du son effective peut être exprimée par

$$C_{eff} = \sqrt{\gamma_g RT} + \hat{n} \cdot u \tag{I.4.1}$$

où γ_g est le coefficient adiabatique de l'air sec, R est la constante universelle des gaz parfaits, T est la température et $\hat{n} \cdot u$ est la projection de la source vers le capteur $\hat{n}$ de la vitesse du vent u. Lorsque la vitesse du son effective dans l'atmosphère est supérieure à celle au sol, les fronts d'ondes infrasonores sont réfractés vers le sol selon la loi de Snell-Descartes au premier ordre (car cela dépend également de l'angle d'arrivée de l'onde, ainsi que du profil de la vitesse effective du son). De plus, des phénomènes à petite échelle, tels que les ondes gravitationnelles, peuvent provoquer une diffraction, entraînant une réflexion partielle de l'énergie acoustique. Ainsi, quatre couches différentes peuvent être décrites en raison des gradients de température. Le premier est la troposphère, qui s'étend du sol jusqu'à 8 à 15 km selon la latitude et la saison. La troposphère contient 90 % de la masse de l'atmosphère. La température diminue constamment du sol jusqu'à la limite de la troposphère, la tropopause, où la température reste approximativement constante. Le courant-jet (jet stream) se situe juste en dessous de la tropopause. Il convient de noter qu'une légère inversion de température peut se produire dans la troposphère au cours des 100 premiers mètres, en raison, par exemple, d'un front chaud passant au-dessus d'un front froid, ou d'une quantité de rayonnement émis par la surface supérieure à celle du rayonnement solaire incident. La température augmente dans la stratosphère en raison de l'ozone jusqu'à environ 50 km, limite appelée la stratopause. Si les vents sont favorables à une propagation, un guide d'onde peut se former à cette altitude. Cependant, un réchauffement stratosphérique soudain caractérisé par une augmentation de la température et, pour les réchauffements majeurs, une inversion de vent peut détruire ce guide d'ondes. Souvent, cela crée des conditions estivales pendant l'hiver, ce qui signifie que le guide généralement occidental est perturbé, mais il y a généralement un guide oriental qui se forme à sa place [Charlton and Polvani, 2007]. Les infrasons peuvent voyager jusqu'à la mésosphère où la température diminue à nouveau jusqu'à la mésopause. Un guide d'ondes est possible si des vents forts se produisent. Enfin, la température augmente dans la thermosphère en raison de l'absorption de radiations solaires hautement énergétiques. Cela crée un guide d'ondes thermosphérique, cependant, la forte atténuation à ces altitudes signifie que ces signaux (particulièrement à haute fréquence) ne sont pas détectés à la surface. L'atténuation est faible pour les infrasons de basse fréquence, c'est pourquoi les sources puissantes avec un contenu de basse fréquence, telles que la houle ou les ondes orographiques [Wilson et al., 2009], peuvent être facilement détectées partout sur Terre si les conditions d'enregistrement sont favorables.
La figure suivante I.4.3.b est une simulation de lancer de rayons des trajectoires stratosphériques et thermosphériques. Le chemin thermosphérique est dû à la température élevée propre à cette couche, ce qui entraîne une vitesse du son effective élevée. L'arrivée stratosphérique est due à la haute température de la stratopause combinée aux vents forts en direction de l'observateur depuis la source, comme le montre le graphique (a) ; la température à elle seule n'est pas suffisamment élevée pour provoquer la réfraction des ondes vers le sol. Par conséquent, le vent est nécessaire pour augmenter la vitesse du son effective et produire un guide d'ondes stratosphérique. On peut constater qu'il n'y a pas d'arrivées dans les 200 premiers kilomètres depuis la source et entre la dernière arrivée stratosphérique et la première arrivée thermosphérique ; ce sont des zones d'ombre. Il convient de noter que les zones d'ombre sont moins prononcées pour les signaux de basse fréquence, car la réfraction de l'énergie se produit en continu tout au long du trajet en raison de la diffraction de ces longueurs d'onde plus longues. C'est aussi pourquoi la houle est souvent détectée. Des recherches en cours sont menées afin de quantifier l'impact des ondes gravitationnelles sur la propagation des infrasons à haute altitude (Chunchuzov and Kulichkov [2019] ; Listowski et al. [2024]).
Un dernier impact sur la propagation doit être décrit, à savoir la perte de cohérence du signal durant

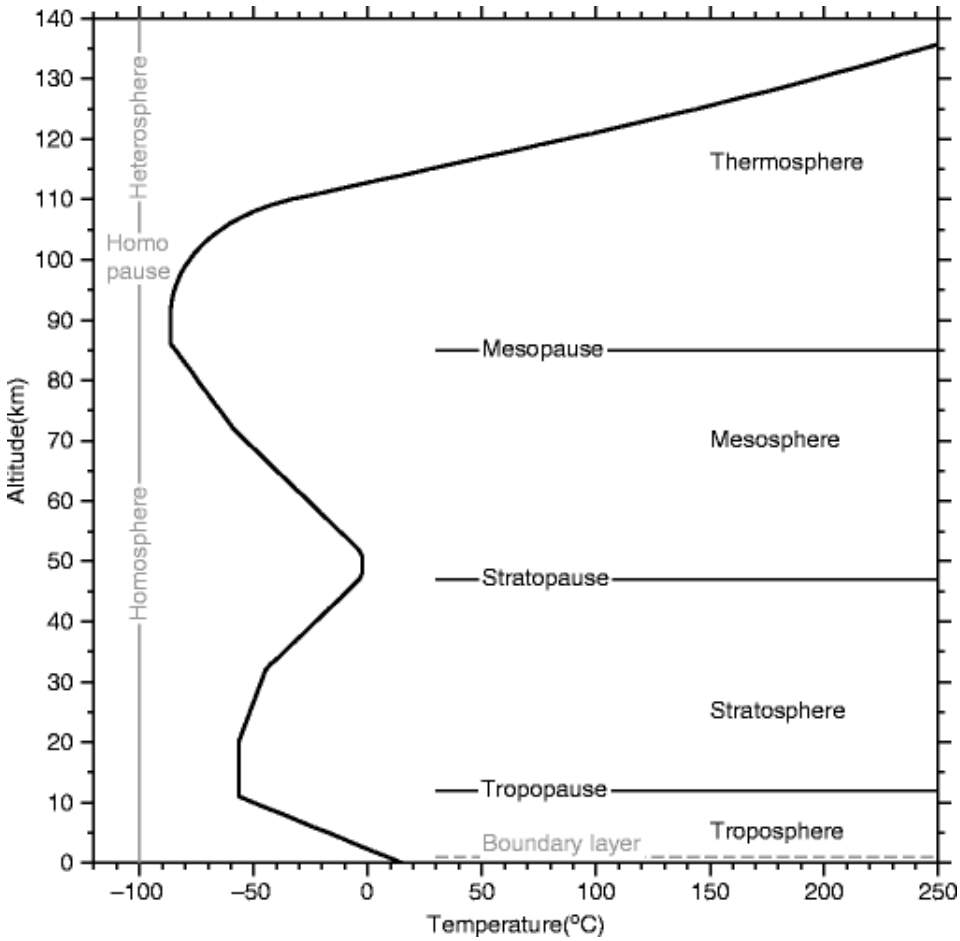

Figure I.4.2: Les couches atmosphériques selon le mélange de l'atmosphère ou son gradient de température, en fonction de l'altitude. Figure extraite de US-Standard [1976].

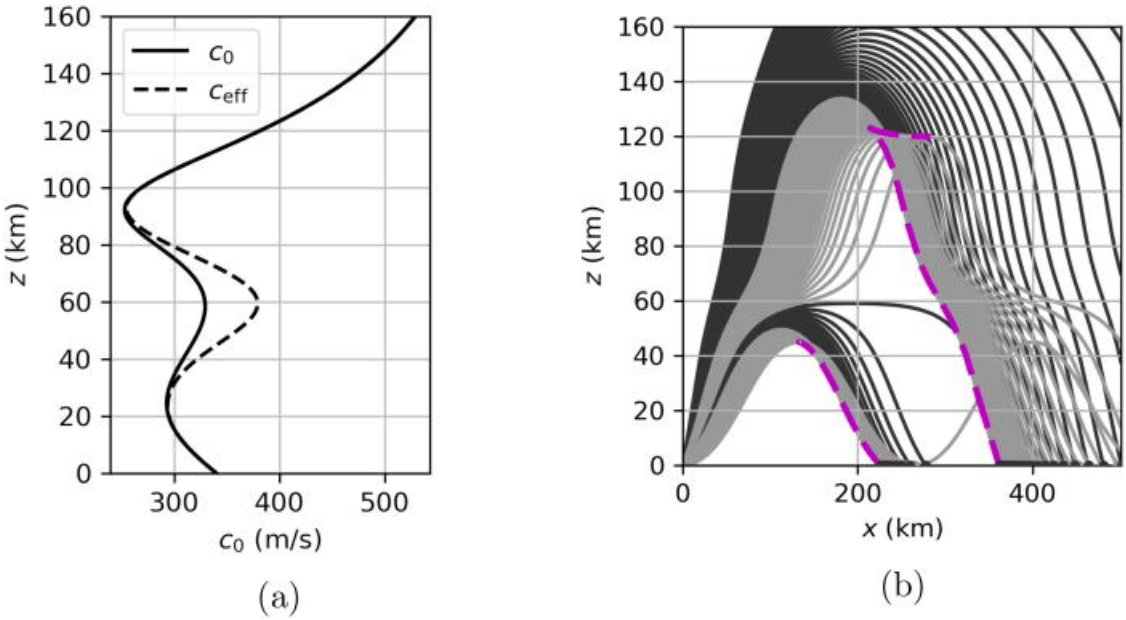

Figure I.4.3: La figure (a) représente le profil de vitesse du son c_0 (ligne pleine) [Lingevitch et al., 1999] et le profil de la vitesse du son effective c_{eff} (ligne en pointillés) selon un profil de vent gaussien [Blom, 2019], (b) est l'illustration des rayons réels obtenus par la méthode de traçage de rayons [Zelias et al., 2022] pour un angle de lancement variant de 0 à 60 degrés. Les caustiques stratosphériques et thermosphériques sont indiquées par les épais traits en pointillés violets. Extraite de Zelias et al. [2022].

la propagation. La perte de cohérence du signal entre les capteurs est générée par des hétérogénéités atmosphériques, telles que les gradients de température et le vent. Ces hétérogénéités provoquent une diffraction des ondes et génèrent des paquets d'ondes avec des variances d'azimut et de vitesse horizontale, $\Delta\theta$ et Δv, par rapport aux ondes sources. θ et v représentent l'azimut et la vitesse horizontale de l'onde plane, respectivement [Mack and Flinn, 1971].

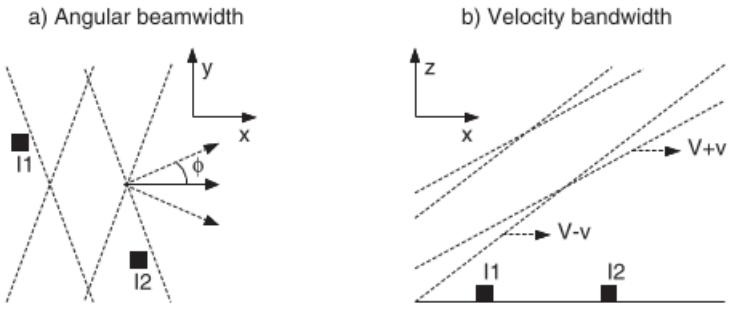

Figure I.4.4: Une représentation de la décohérence de l'onde, comme montré dans Gossard and Hooke [1975]. La direction moyenne de propagation horizontale de cet ensemble de fronts d'onde est le long de l'axe des x. Les fronts d'onde individuels avec de petites déviations par rapport à cette direction sont représentés par ϕ sur le graphique. (a). La vitesse apparente moyenne de tous les fronts d'onde à travers l'ensemble est désignée par V. Les composants individuels des fronts d'onde avec de petites déviations par rapport à cette valeur sont montrés sur le graphique (b) [Green, 2015].

La décohérence mentionnée ci-dessus est encore plus prononcée lorsque

– La distance entre la source et le récepteur est grande, car il y aura une diminution de la corrélation

avec l'augmentation de la distance. Ce phénomène est discuté en détail dans Green [2015]. Dans le cas où la distance entre les capteurs est en kilomètres, une approximation de la perte de cohérence peut être exprimée comme $\gamma^2 = exp(-\alpha z)$ où α est le coefficient d'atténuation et z est la distance entre les capteurs [Green, 2015].

- il s'agit d'une arrivée tardive dans le signal d'intérêt, probablement due à un effet de diffraction [Green, 2015].
- Le couple de capteurs en question est parallèle à l'arrivée de l'onde, ce qui fait que la perte de cohérence est anisotrope. Ceci est conforme aux résultats dans Mack and Flinn [1971].

La cohérence peut être calculée en fonction de la période en utilisant la formule suivante [Christie et al., 2007]

$$\gamma^2(r,T) = \left| \frac{sin(2\pi x sin(\Delta\theta)/\overline{v}T)}{2\pi x sin(\Delta\theta)/\overline{v}T} \right|^2 \cdot \left| \frac{sin(2\pi y \Delta v/(\overline{v}T(\overline{v}+\Delta v)))}{2\pi y \Delta v/(\overline{v}T(\overline{v}+\Delta v))} \right|^2 \tag{I.4.2}$$

où T est la période considérée, $\overline{v}$ est la vitesse de phase moyenne, x et y sont les composantes du vecteur de distance intercapteurs r, $\Delta\theta$ et Δv sont respectivement les distributions de l'azimut et de la vitesse horizontale. Cela peut également être calculé par une approximation gaussienne [Green, 2015]

$$\gamma_{12}^2(w) = \left| exp\left(-\frac{k^2}{4} \left[x^2 \left(\frac{\Delta v}{\overline{v}} \right) + y^2 \Delta\theta \right] \right) \right|^2 \tag{I.4.3}$$

où k est la magnitude du nombre d'onde angulaire horizontal dans la direction de la propagation. Les estimations expérimentales de $\Delta\theta$ et Δv sont cohérentes entre les modèles de Mack and Flinn [1971] et de Christie et al. [2007] fournissant respectivement en moyenne $\Delta\theta = 5^\circ$ pour $\Delta v = 15\ m/s$ et $\Delta\theta = 4.5^\circ$ pour $\Delta v = 14\ m/s$. D'autre part, en analysant la cohérence des signaux provenant d'événements de référence, Green [2015] a montré qu'une plus large gamme de valeurs existait, allant de $\Delta\theta = 0.4^\circ$ à $\Delta\theta = 7^\circ$ et de $\Delta v = 2\ m/s$ à $\Delta v = 40\ m/s$, dont la médiane était $\Delta\theta = 3.1^\circ$ pour un $\Delta v = 12\ m/s$. Les fronts d'onde individuels sont spécifiques à chaque bande de fréquence du signal.

Chapter I.5

Contexte de la surveillance par méthode infrasonore (français)

I.5.1 Pourquoi l'enregistrement des infrasons est important

Comme expliqué dans les sections précédentes, en raison de la faible atténuation des infrasons dans l'atmosphère, ceux-ci peuvent parcourir de longues distances. Cela conduit à l'intérêt de les surveiller pour à la fois la caractérisation des sources et les études atmosphériques jusqu'à la thermosphère. En effet, des applications d'alerte précoce pour les avalanches [Marchetti et al., 2015], ainsi que pour les éruptions volcaniques comme le Volcanic Information System (VIS), dont l'objectif est de surveiller l'activité volcanique et de fournir des alertes précoces, sont développées pour la protection civile contre les risques naturels. D'autres caractérisations de sources impliquant la localisation, l'estimation de l'énergie (par exemple, les explosions chimiques [Pilger et al., 2021a], le renseignement militaire tel que l'utilisation d'armes à feu [Glaser et al., 2017] ou les tremblements de terre [Macpherson et al., 2023]) peuvent être réalisées par des études sur les infrasons. Mais les infrasons peuvent également être utilisés pour des études atmosphériques, pour des prévisions météorologiques ou des recherches climatiques. C'est l'objectif de plusieurs études sur la foudre, comme le HYdrological cycle in Mediterranean EXperiment (HyMeX), dans lesquelles des événements orageux avec de fortes précipitations sur le sud-est de la France, menant souvent à de graves inondations par des crues éclair, sont étudiés [Defer et al., 2015]. D'autres études atmosphériques sur les réchauffements stratosphériques soudains sont menées afin de mieux comprendre le climat [Smets, 2018]. Des projets internationaux majeurs comme Atmospheric Dynamics Research InfraStructure in Europe (ARISE) ont utilisé la technologie infrason comme un outil pour décrire la stratosphère. Cela peut être réalisé en utilisant des sources connues pour développer des méthodes de télédétection par inférence, comme par exemple les explosions de munitions à Hukkakero, en Finlande [Vera Rodriguez et al., 2020]. Enfin, l'un des principaux usages des infrasons est la détection des essais nucléaires par le Systeme de Surveillance International (SSI) dans le cadre du Traité d'Interdiction Complète des Essais nucléaires (TICE).

I.5.2 Le développement du Systeme de Surveillance International (SSI)

Après la Seconde Guerre mondiale, la guerre froide s'est progressivement installée entre les États-Unis, l'Union soviétique et leurs alliés respectifs. Cela a conduit à la course aux armements nucléaires pour la suprématie. En plus de l'expansion des stocks nucléaires américains et soviétiques, d'autres pays ont développé des armes nucléaires. La culmination des tensions a été atteinte après deux événements : le test de la Tsar Bomba (1961), précédemment décrit comme le test nucléaire le plus puissant jamais réalisé, et la crise des missiles de Cuba (1962). Dans un geste d'apaisement des relations entre les États-Unis et l'URSS, le Limited Test Ban Treaty (LTBT) a été signé entre ces deux pays à Moscou le 5 août 1963, puis il a été ouvert à la signature d'autres pays. Le traité est officiellement entré en vigueur le 10 octobre 1963. Depuis lors, 123 autres États sont devenus parties au traité. Ce traité interdit tous les essais sauf ceux

effectués sous terre. Puis, après un total de plus de 2000 essais nucléaires après la fin de la Seconde Guerre mondiale, un autre traité a été élaboré, le Traité d'Interdiction Complète des Essais nucléaires (TICE). Il s'agit d'un traité multilatéral interdisant les essais nucléaires dans tous les environnements, y compris souterrains. Il a été adopté par l'Assemblée générale des Nations Unies le 10 septembre 1996, mais n'est pas encore entré en vigueur, car neuf nations nucléaires n'ont pas ratifié le traité (États-Unis, Russie qui a retiré sa ratification en 2023, Chine, Inde, Pakistan, République populaire de Corée, Iran, Égypte et Israël). Cependant, depuis l'ouverture à la signature et à la ratification, 178 pays à travers le monde ont signé et ratifié le traité. L'Organisation du Traité d'Interdiction Complète des Essais nucléaires (OTICE), qui abrite le Centre International de Données (CID), a été créé pour promouvoir la ratification du traité afin de le mettre en vigueur et de vérifier son application par les nations membres. Dans cette optique, un système de surveillance a été développé par l'organisation et les États membres. Le Systeme de Surveillance International (SSI) se compose de quatre technologies différentes : la surveillance sismique, infrason, hydroacoustique qui surveillent les différents milieux (souterrain, atmosphérique et sous-marin) et des laboratoires de radionucléides afin de détecter les particules radioactives ou les gaz nobles produits par des explosions nucléaires. Il y a un total de 337 installations, comprenant 50 stations sismiques principales et 120 stations sismiques auxiliaires, 11 stations hydroacoustiques, 60 stations infrasons, 80 stations de radionucléides associées à 16 laboratoires de radionucléides. La figure I.5.1 montre la carte du SSI de toutes les installations à travers le monde. Le SSI a été conçu lors de la Conférence sur le désarmement à Genève en 1996 afin de couvrir efficacement le globe. En ce moment, 90 % des stations du SSI sont opérationnelles et la France est le premier pays des cinq membres permanents du conseil de sécurité des Nations unies (P5) à avoir mis en place toutes les stations sur son territoire.

Figure I.5.1: Le Systeme de Surveillance International (SSI) s'étend à travers le monde avec un réseau qui, une fois complété, comptera 321 stations de surveillance et 16 laboratoires accueillis par 89 pays à travers le globe. Extrait du site web de l'OTICE (https://www.ctbto.org).

I.5.3 Conception d'une station infrason

Un total de 60 stations infrasons sont prévus dans le cadre du réseau mondial du SSI, avec un espacement presque uniforme malgré le manque de terres émergées dans l'hémisphère sud. Cette configuration a été proposée dans l'intention de détecter des explosions d'une puissance d'environ 1 kilotonne équivalent TNT et de les localiser avec au moins deux stations. Une station infrason se compose de plusieurs microbaromètres qui mesurent les fluctuations de la pression atmosphérique. Plusieurs capteurs ont été développés dans le but de répondre aux exigences du SSI, à savoir avoir des mesures de bruit propre inférieures à celles du modèle à faible bruit [Bowman et al., 2005]. Le modèle MB2000/2005, développé au CEA accueillant le Centre National de Données (CND) français, et le Chaparral 5 conçu par Chaparral Physics ont été fabriqués [Marty, 2019]. Le MB2000/2005, par exemple, présente un bruit propre supérieur à celui du modèle à faible bruit à des fréquences supérieures à 1 Hz [Alcoverro et al., 2005]. Ce n'est pas le cas du Chaparral 5 qui, cependant, a une réponse et un bruit propre sensibles à l'environnement. En raison de leur faible sensibilité aux conditions environnementales, les MB2000/2005 ont été déployés sur plus de 90 % du réseau en 2012. Pour résoudre leurs problèmes respectifs, de nouveaux développements ont conduit au MB3a [Merchant and McDowell, 2014], au Chaparral 50 A [Hart and Rembold, 2010] et ensuite à l'Hyperion 5113/A [Merchant, 2015]. En raison du respect des exigences du SSI, de la faible sensibilité à l'environnement et du nouvel avantage du MB3 (c'est-à-dire une consommation d'énergie réduite, une bobine de calibration intégrée), les MB2000/2005 et le MB3 représentaient plus de 80 % des capteurs du réseau en 2017. Auparavant, nous avons montré que la fluctuation de la pression atmosphérique était d'environ une à plusieurs dizaines de Pascals, par rapport aux 1000 hPa de la pression atmosphérique à la surface, ce qui indique à quel point les capteurs doivent être sensibles pour détecter un événement. Cependant, la capacité de la station à détecter un événement dépend de plusieurs paramètres. Le premier est la capacité de réduire le bruit qui peut masquer les signaux d'intérêt. À cet effet, les capteurs sont installés dans des endroits calmes avec une exposition réduite aux turbulences de vent locales. Des systèmes de réduction du bruit du vent sont également ajoutés à chaque capteur afin de moyenner le signal et de réduire le bruit incohérent du vent [McDonald et al., 1971]. La figure I.5.2 représente un dispositif de microbaromètre installé dans un caveau, relié à un système de tuyaux appelé rosette, un collecteur et des ports d'entrée. Les ondes infrasonores passent par les ports et se propagent à travers les tuyaux jusqu'au collecteur. Le collecteur est relié à un microbaromètre situé au centre de l'élément, qui est lui-même connecté à un numériseur, un GPS, un équipement météorologique et un système de transmission de données. Ce design expérimental permet d'améliorer le rapport signal sur bruit en moyennant l'amplitude du signal cohérent et le bruit incohérent à l'échelle du système de filtrage.

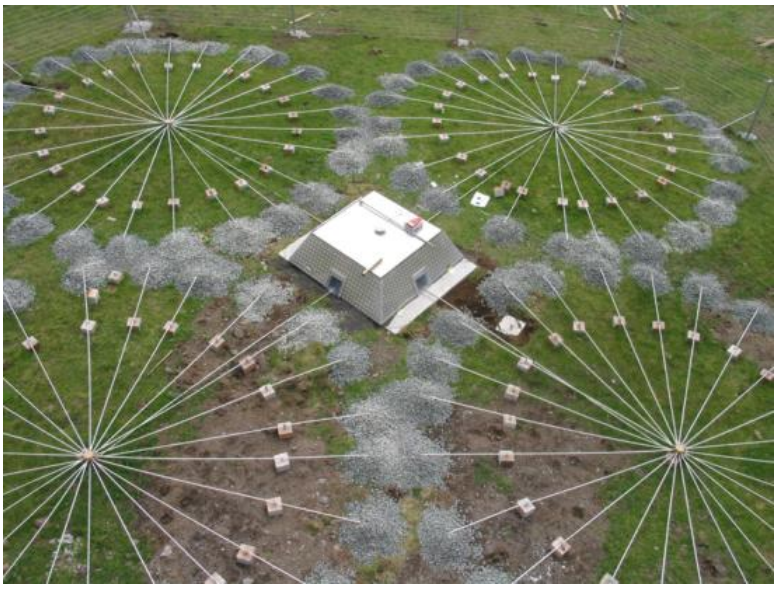

Figure I.5.2: Illustration de l'ensemble de la rosette connectée au collecteur où se trouve le microbaromètre. Extraite du site web de l'OTICE (https://www.ctbto.org).

Les autres paramètres qui affectent la capacité de la station à détecter un événement incluent la sensibilité du capteur à une certaine plage de fréquences, les conditions atmosphériques à la station, l'algorithme de traitement des données et la conception de la station. La conception de la station fait référence à sa géométrie, comprenant l'espacement, la distribution et le nombre de capteurs. Une façon d'étudier la géométrie de la station et d'améliorer sa capacité à détecter un signal est d'examiner le manifold de l'antenne, qui est la somme sur 360° de la réponse de l'antenne [Christie and Campus, 2009]. L'objectif est, bien sûr, d'être isotrope, ce qui signifie que le design souhaité doit avoir une réponse qui est indépendante de la direction d'arrivée du signal incident. La distance entre les capteurs déterminera la sensibilité en fréquence de la station. La conception initiale de la station comportait quatre capteurs formant un triangle, avec le quatrième capteur situé au centre ; les ouvertures typiques variaient entre 1 et 3 km. Cependant, ce type de station était sensible à la décohérence spatiale à haute fréquence. C'est pourquoi la plupart des stations sont désormais composées, au minimum, de 8 capteurs avec un sous-ensemble à petite ouverture. Les figures suivantes I.5.3 et I.5.4 montrent l'impact de la conception de la station kazakhe IS31 sur la réponse à une arrivée infrason à 50° et 340 m/s à 1 Hz. Il convient de noter qu'il y a un grand nombre de lobes secondaires avec une amplitude élevée lorsque seuls quatre capteurs sont utilisés avec une grande ouverture, ce qui entraîne un aliasing spatial. Néanmoins, l'impact des lobes secondaires a été considérablement réduit grâce à l'incorporation de capteurs supplémentaires et d'un sous-ensemble adapté à l'estimation haute fréquence. Ainsi, ces capteurs supplémentaires permettent un traitement du signal plus précis. Bien que cet aliasing soit important pour les ondes planes, une grande partie du problème d'aliasing peut être réduite en raison de la nature non dispersive des infrasons. C'est à dire que les vitesses de groupe et de phase sont approximativement égales pour toutes les fréquences.

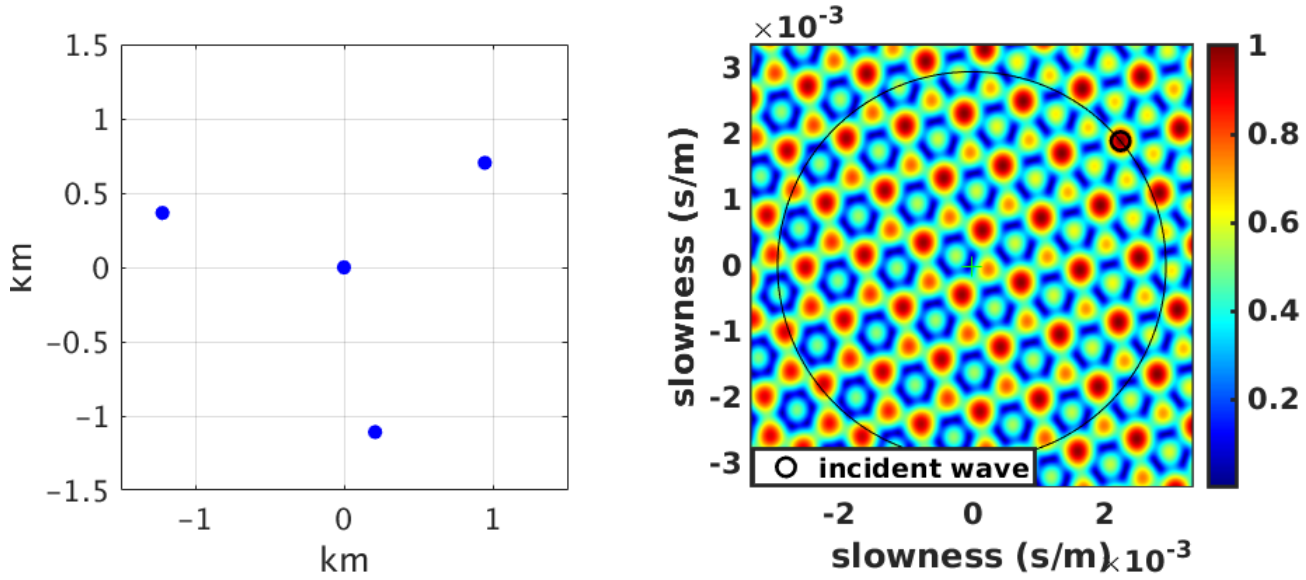

Figure I.5.3: Illustration de la position relative des quatre capteurs à la station IS31 et de la réponse correspondante à une arrivée infrason à 50° et 340 m/s à 1 Hz. Les lobes secondaires sont nombreux et ont des amplitudes élevées. Le grand cercle noir représente la vitesse du son à 340 m/s et le petit cercle noir la position dans l'espace de lenteur de l'onde incidente.

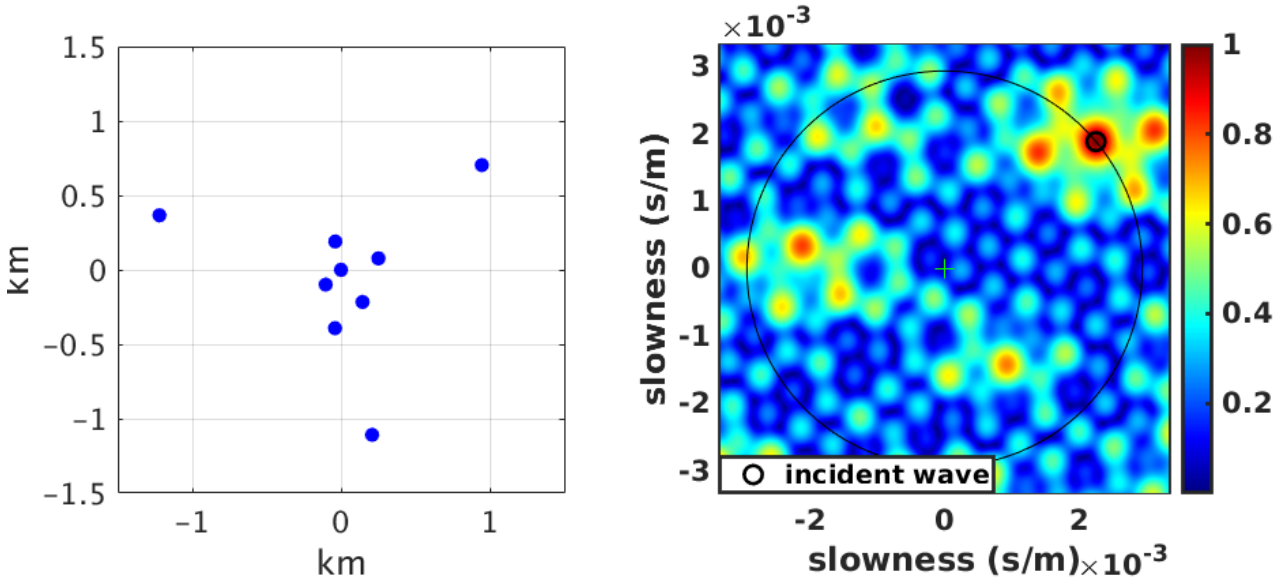

Figure I.5.4: Illustration de la position relative des neuf capteurs à la station IS31 et de la réponse correspondante à une arrivée infrason à 50° et 340 m/s à 1 Hz. Les lobes secondaires sont moins nombreux et ont des amplitudes plus faibles. Le grand cercle noir représente la vitesse du son à 340 m/s et le petit cercle noir la position dans l'espace de lenteur de l'onde incidente.

Chapter I.6

Traitement du signal et objectifs (français)

I.6.1 Modèles de signaux

Une fois le signal enregistré, nous devons le traiter. Différents modèles de signaux peuvent être utilisés. Dans de nombreux problèmes, les signaux observés peuvent être écrits comme

$$z(t) = s(t;\tau) + n(t) \tag{I.6.1}$$

où $z(t)$ est le signal observé, $s(t;\tau)$ est le Signal Of Interest (SOI) en fonction du temps, τ est le paramètre à estimer et $n(t)$ est le bruit additif considéré comme blanc et gaussien. On suppose que $s(t;\tau)$ et $n(t)$ sont stationnaires.

Deux types de signaux existent dans la littérature pour ce modèle : un modèle de signal large bande et un modèle de signal bande étroite. Un signal à bande étroite est caractérisé par une largeur de bande au moins cent fois plus petite que la fréquence centrale. Cela signifie que la bande de fréquence du signal ne dépasse pas la cohérence de la bande de fréquence du canal. La réponse en fréquence est considérée comme plate sur la bande. En revanche, un signal à large bande est composé d'un grand contenu fréquentiel et dépasse donc de manière significative la largeur de bande du canal. En conséquence, la réponse en fréquence d'un signal large bande n'est pas plate et dépend du contenu fréquentiel du signal. La figure I.6.1 illustre le contenu en fréquence d'un signal à bande étroite et d'un signal à large bande avec du bruit de fond dans un filtre passe-bande. Les deux modèles sont expliqués dans les sous-sections suivantes, en supposant plusieurs sources.

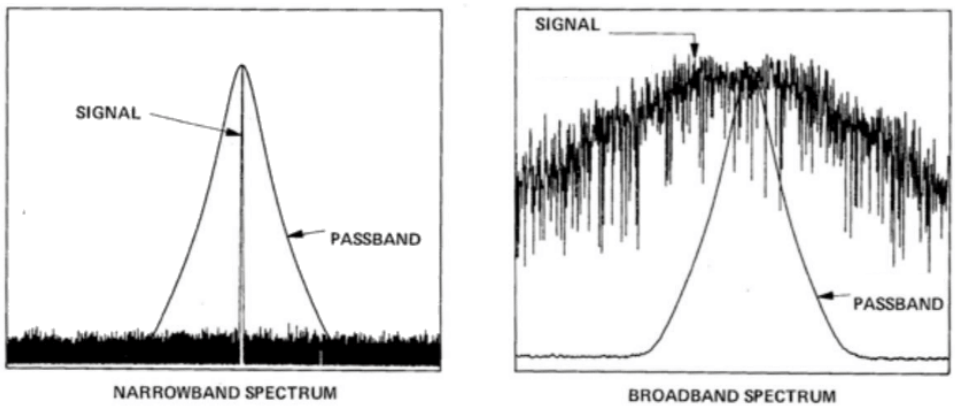

Figure I.6.1: Illustration des spectres à bande étroite et large. Le spectre du signal à bande étroite est cent fois plus petit que le filtre passe-bande. La bande du signal à large bande est beaucoup plus large que le filtre passe-bande (extraite et modifiée de Wyatt).

I.6.1.1 Modèle à bande étoite

Considérons un réseau de M microbaromètres sur un plan horizontal [Nouvellet et al., 2014]. La source génératrice d'infrasons est supposée être suffisamment éloignée pour considérer un front d'onde plan. Comme indiqué précédemment, le SOI, $s(t)$, est un signal à bande étroite si le spectre s'étend sur une largeur de bande, B, beaucoup plus petite que la fréquence centrale, f_0. Graphiquement, un tel signal peut être représenté comme dans la figure I.6.2 où la section du signal dans la boîte noire peut être approximée par une fonction sinusoïdale de fréquence f_0. Le pseudo-période des variations de l'enveloppe du signal est de l'ordre de $1/B$.

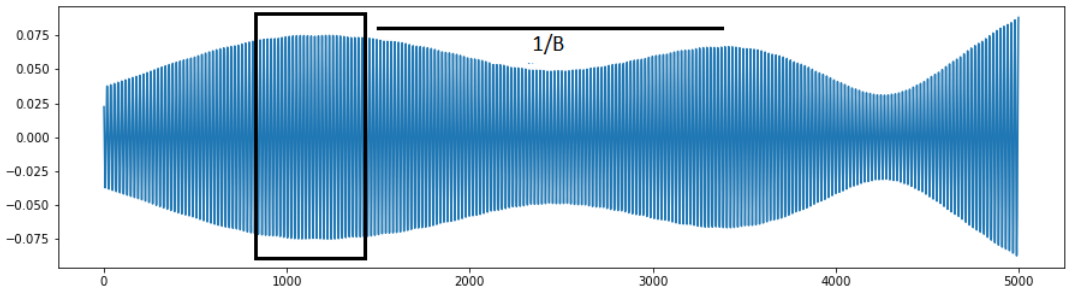

Figure I.6.2: La portion du signal dans une boîte noire est une quasi-sinusoïde de fréquence f_0. La période des fluctuations de l'enveloppe est de l'ordre de $1/B$.

Ainsi, nous pouvons exprimer le signal $s(t)$ par ses composants en phase et en quadrature :

$$s(t) = p(t)cos(2\pi f_0 t) - q(t)sin(2\pi f_0 t) = Real\{(p(t) + iq(t))e^{2i\pi f_0 t}\} \tag{I.6.2}$$

où $p(t)$ et $q(t)$ sont respectivement des signaux en phase et en quadrature de phase par rapport à f_0 qui varient lentement par rapport à $1/f_0$. L'enveloppe complexe de $s(t)$ est :

$$x(t) = (p(t) + iq(t))e^{2i\pi f_0 t} \tag{I.6.3}$$

qui est facilement lié à l'équation I.6.1 par z(t)=Real{x(t)}+n(t). En considérant maintenant que $\frac{1}{f_0} << B$, il en résulte que l'enveloppe complexe du signal peut être écrite comme :

$$\begin{aligned} x(t-\tau) &= (p(t-\tau) + iq(t-\tau))e^{2i\pi f_0 t - \tau} \\ &\approx (p(t) + iq(t))e^{2i\pi f_0 t}e^{-2i\pi f_0 \tau} = x(t)e^{-2i\pi f_0 \tau} \end{aligned} \tag{I.6.4}$$

Il arrive finalement que, dans un modèle à bande étroite, le signal observé soit une somme de plusieurs sources avec un décalage de phase pour chaque capteur, de sorte que :

$$z_m(t) = \sum_{n=1}^{N} s_n(t)a_m(\theta_n, v_n) + n_m(t) \tag{I.6.5}$$

où z_m est le signal observé au capteur m supposé centré (c'est-à-dire que la moyenne a été retirée), N est le nombre de sources à estimer, $s_n(t)$ est le n-ième SOI, un signal spatialement cohérent au capteur m, et $n_m(t)$ est le bruit additif dû à l'environnement du capteur m. Le vecteur $a(\theta_n, v_n) = [1, e^{-2i\pi f_0 \tau_1(\theta_n, v_n)}, \ldots, e^{-2i\pi f_0 \tau_{M-1}(\theta_n, v_n)}]^T$ représente le changement de phase du SOI pour chaque capteur à la fréquence centrale, f_0, caractérisé par le retard entre le capteur m et le capteur de référence. Les M signaux sont echantillonnés avec une période d'échantillonnage $T_e = 1/Fs$ où Fs est la fréquence d'échantillonnage respectant la condition de Nyquist. Ainsi $z_t = z(tT_e)$ mais pour des raisons de simplicité on denotera par la suite $z(t)$ pour z_t. La notation de l'équation I.6.5 peut être simplifiée en utilisant des matrices pour une fenêtre temporelle de longueur L avec N_e échantillons :

$$\mathbf{Z} = \mathbf{AS} + \mathbf{N} \tag{I.6.6}$$

où $\mathbf{Z}$ $(M \times N_e)$ est la matrice d'observation de tous les capteurs pour N_e échantillons, et $\mathbf{A}$ $(M \times N)$ est la matrice des directions contenant N vecteurs directionnels, $a(\theta, v)$. $\mathbf{S}$ est la matrice des sources contenant

les informations d'amplitude/phase ($N \times N_e$) et $\mathbf{N}$ ($M \times N_e$) le bruit additif pour chaque capteur. Cette nouvelle équation conduit à la formule de la matrice de covariance liée au modèle à un moment donné t_l [Guérard, 2016]:

$$\mathbf{R_{zz}} = \mathbb{E}\{\mathbf{Z_{t_l}}\mathbf{Z_{t_l}}^H\} = \mathbf{A}\mathbb{E}\{\mathbf{S_{t_l}}\mathbf{S_{t_l}}^H\}\mathbf{A}^H + \mathbb{E}\{\mathbf{N_{t_l}}\mathbf{N_{t_l}}\} = \mathbf{A}\mathbf{R_{ss}}\mathbf{A}^H + \mathbf{R_{nn}} \tag{I.6.7}$$

La matrice $\mathbf{R_{zz}}$ est hermitienne et est liée au signal observé reçu par les capteurs de la station à un instant t_l, incluant à la fois le SOI et le bruit. La matrice $\mathbf{R_{ss}}$ et la matrice $\mathbf{R_{nn}}$ correspondent respectivement à la matrice de covariance de la source et du bruit. Enfin, la matrice $\mathbf{R} = \mathbf{A}\mathbf{R_{ss}}\mathbf{A}^H$ est la matrice de covariance des signaux observés reçus par les capteurs sans le bruit. En général, $\mathbf{R_{zz}}$ peut être estimée sur une fenêtre temporelle de taille N_e pour une meilleure précision comme suit :

$$\widehat{\mathbf{R_{zz}}} = \frac{1}{N_e}\mathbf{Z}\mathbf{Z}^H \tag{I.6.8}$$

I.6.1.2 Modèle à large bande

Alors que dans un modèle à bande étroite, le délai de propagation peut être lié à un décalage de phase en raison de la bande considérablement plus petite par rapport à la fréquence centrale, le délai de propagation dans un modèle à large bande est lié à un décalage temporel. Alors, dans le domaine temporel, le signal centré observé au capteur m est

$$z_m(t) = \sum_{n=1}^{N} s_n(t - \tau_m(\theta_n, v_n)) + n_m(t) \tag{I.6.9}$$

où $\tau_m(\theta_n, v_n)$ représente le retard du n-ième front d'onde au capteur m par rapport au capteur de référence. Ces fronts d'onde sont caractérisés par l'azimut θ_n et la vitesse apparente v_n du vecteur de lenteur p_n. Soit r_m la position du capteur m dans un système de coordonnées 2D orthogonal arbitraire. Le délai $\tau_m(\theta_n, v_n)$ pour le capteur m de la n-ième source peut être décrit comme suit :

$$\tau_m(\theta_n, v_n) \quad = \quad r_m^T p_n \tag{I.6.10}$$

où le vecteur de lenteur en deux dimensions est

$$p_n \quad = \quad -v_n^{-1}\begin{bmatrix}\sin(\theta_n)\\ \cos(\theta_n)\end{bmatrix} \tag{I.6.11}$$

avec v_n et θ_n les paramètres d'onde de la n-ième source.

En vectorisant l'équation I.6.9, on obtient :

$$z(t) \quad = \quad \sum_{n=1}^{N} s(t - \tau(\theta_n, v_n)) + n(t) \tag{I.6.12}$$

où $z(t)$, $\tau(\theta_n, v_n)$ et $n(t)$ sont de taille M. Une approximation est faite ici : l'onde atteint tous les capteurs avec la même amplitude. Cette simplification peut être justifiée par le fait que la distance entre les sources et la station est beaucoup plus grande que la distance entre les capteurs de la station. De plus, les stations du SSI sont conçues pour détecter de telles sources. En effet, les distances entre les capteurs sont adaptées à la longueur d'onde des sources infrasonores, par conséquent, le gain relatif à chaque capteur est à peu près égal.

En appliquant une transformée de Fourier sur le signal discret $z(t)$, il devient :

$$\begin{bmatrix}Z_1(f_i)\\ Z_2(f_i)\\ \vdots\\ Z_M(f_i)\end{bmatrix} = \begin{bmatrix} a(f_i,\theta_1,v_1) & a(f_i,\theta_2,v_2)\dots a(f_i,\theta_N,v_N)\end{bmatrix}\begin{bmatrix}S_1(f_i)\\ S_2(f_i)\\ \vdots\\ S_N(f_i)\end{bmatrix} + \begin{bmatrix}N_1(f_i)\\ N_2(f_i)\\ \vdots\\ N_M(f_i)\end{bmatrix} \tag{I.6.13}$$

où $Z(f_i)$ $(M \times 1)$ est la transformée de Fourier du signal discret $z(t)$ à la fréquence f_i, $\mathbf{A}(f_i, \theta, v)$ $(M \times N)$ est la matrice de direction qui contient N vecteurs de direction $a(f_i, \theta, v)$, $S(f_i)$ $(N \times 1)$ est le spectre des N sources contenant les informations d'amplitude/de phase et $N(f_i)$ $(M \times 1)$ est le spectre du bruit enregistré par les M capteurs à la fréquence f_i. Ainsi, dans ce cas, la matrice de densité spectrale s'écrit

$$\mathbf{C}(f_i) = \sum_{n}^{N} a(f_i, \theta_n, v_n)\sigma_{s_n}^2 a^H(f_i, \theta_n, v_n) + \sigma^2\mathbf{I} \tag{I.6.14}$$

où $\sigma_{s_n}^2$ est la puissance du signal, σ^2 est la puissance du bruit et $\mathbf{I}$ est la matrice identité $(M \times M)$. En générale, la matrice de densité spectrale est estimée par un périodogramme [Brockwell and Davis, 1991] qui se définit comme

$$\mathbf{C}_{per}(f_i) = \frac{1}{Ne} Z(f_i) Z^H(f_i) \tag{I.6.15}$$

Un noyau de lissage sur les frequences est utiliosé pour une meilleure estimation de la matrice de densité spectrale. Pour une meilleure estimation, $\mathbf{C}(f_B)$ peut être défini comme la moyenne de tous les $\mathbf{C}(f_i)$ calculées dans la bande.

Le modèle à large bande est classiquement utilisé pour la surveillance infrason par le Centre National de Données (CND) et l'OTICE à des fins opérationnelles en raison de la nature à large bande des sources infrasons. De plus, un modèle à bande étroite nécessiterait des filtres extrêmement étroits autour de chaque fréquence d'intérêt. Par exemple, autour de la fréquence de 0,1 Hz, un traitement en bande étroite nécessiterait une bande de fréquence de [0,0999 - 0,101] Hz. De plus, le nombre de bandes de fréquence à traiter serait important et augmenterait considérablement le coût en calcul.

I.6.2 Principe de la détection

La section précédente décrit les modèles de signaux lorsque des SOI sont présents. Mais la première question à laquelle répondre est : Y a-t-il un SOI présent ? En statistique, une telle question est appelée détection ou test d'hypothèse. Cette méthode consiste à vérifier la validité d'une hypothèse statistique avec les données. Tout d'abord, nous devons préciser les deux hypothèses classiques en traitement du signal :

- L'hypothèse nulle, H_0, supposant que le signal est aléatoire, donc qu'aucun SOI n'est présent et que seul du bruit est enregistré par la station. Cela peut être lié à la structure blanche et gaussienne du bruit.
- L'hypothèse alternative, H_1, suppose une structure particulière dans le signal, signifiant la présence de signaux cohérents traversant la station. Cela peut être lié à la structure de la matrice de covariance ou de la matrice de densité spectrale selon les modèles de signaux expliqués dans la section I.6.1.

L'objectif des hypothèses formulées est de rejeter ou d'accepter l'hypothèse nulle, H_0, avec un certain degré de confiance. Si l'hypothèse H_0 est rejetée, alors l'hypothèse H_1 est vérifiée avec un certain degré de confiance. Cependant, si l'hypothèse nulle n'est pas rejetée, cela signifie seulement qu'aucune preuve d'un signal cohérent n'a été trouvée. L'hypothèse H_0 n'est pas vérifiée dans ce cas.
Mathématiquement, le problème de la présence d'un SOI (c'est-à-dire N=1) est lié à la présence ou non de la variable $s(t)$, de sorte que

$$\begin{cases} H_0 & : & s(t) = 0 \\ H_1 & : & s(t) \neq 0 \end{cases} \tag{I.6.16}$$

Dans un problème multisource, les hypothèses doivent être redéfinies de manière itérative après chaque test lorsque l'hypothèse nulle précédente a été rejetée.

$$\begin{cases} H_0 & : & s_n(t) = 0, \quad \forall n \in \{1, \ldots, N\} \\ H_1 & : & s_n(t) \neq 0, \quad \forall n \in \{1, \ldots, N\} \end{cases} \tag{I.6.17}$$

Une autre approche serait un test non binaire avec M hypothèses. Après un choix minutieux des hypothèses, il est nécessaire de sélectionner les statistiques appropriées afin de distinguer les deux hypothèses dans les distributions du TS. Le TS utilisé pour résoudre le problème entraîne des erreurs lors de la sélection d'un seuil pour distinguer les deux hypothèses représentées dans la figure I.6.3. Ils sont de deux types, le premier type d'erreur (erreur α) se produit lorsque l'hypothèse nulle H_0 est rejetée alors qu'elle est vraie. Le deuxième type (erreur β) se produit lorsque l'hypothèse nulle H_0 est acceptée alors qu'elle est fausse. Dans un problème de détection, l'erreur α entraîne un faux positif tandis que l'erreur β entraîne un faux négatif. Il est important de noter que les deux erreurs ne peuvent pas être minimisées en même temps. C'est pourquoi le choix du seuil doit être déterminé en fonction du type d'erreur à minimiser. Une approche courante pour le test d'hypothèses binaires (H_0 contre H_1) consiste à calculer un TS à valeur réelle et à comparer le résultat à un seuil donné. Si nous sommes au-dessus du seuil, nous choisissons H_0, sinon, nous choisissons H_1. Lorsque la distribution du TS sous H_0 est estimée, la valeur-p peut être calculée et utilisée comme seuil [Gibbons and Pratt, 1975]. Typiquement, si la valeur-p est inférieure à 0,01, il est probable que H_0 soit faux, donc nous rejetons H_0 et acceptons H_1. C'est la valeur du TS qui fixe la valeur de l'erreur α pour laquelle l'hypothèse H_0 est rejetée. En général, un seuil de p-value de 1 % est établi, ce qui signifie que la probabilité de faux positifs est de 1 %. Alternativement, si la distribution H_1 est estimée, un seuil basé sur l'erreur β peut être fixé, l'objectif ici étant de minimiser la probabilité de faux négatifs. Chaque méthode de TS a ses propres performances et il est important

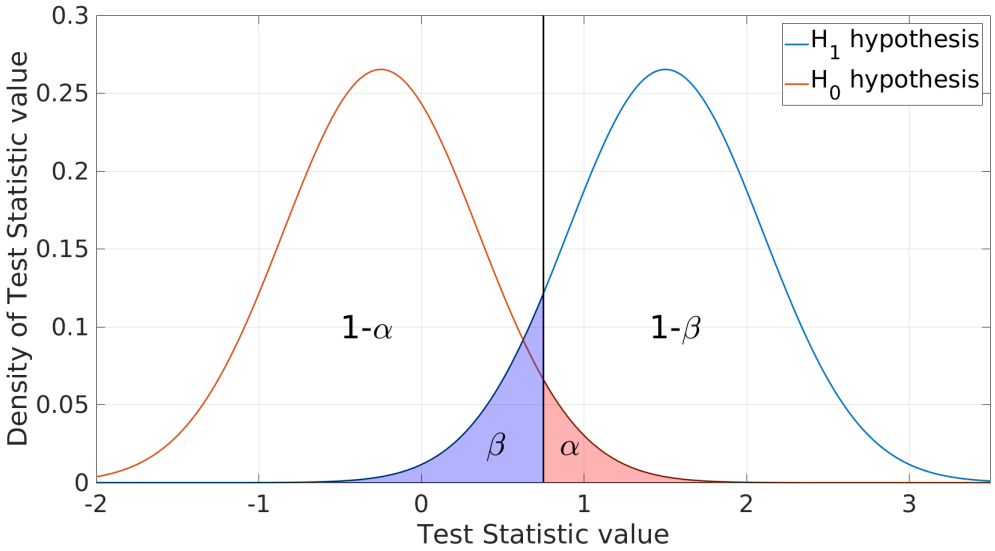

Figure I.6.3: Illustration de la densité de probabilité des hypothèses nulle et alternative, respectivement en rouge et en bleu, dans un problème "simple". Le seuil en noir conduit à l'erreur de type un α et à l'erreur de type deux β, représentées par les zones sous les courbes.

de savoir si un TS est approprié pour discriminer deux hypothèses. À cette fin, nous utilisons l'approche des courbes Receiver Operating Characteristic (ROC) qui mesure la capacité d'un classificateur binaire à distinguer deux hypothèses qui doivent être modélisées de manière synthétique (Arrowsmith et al. [2009] ; Atapattu et al. [2010] ; Park et al. [2017] ; Marcillo et al. [2019]). Nous désignons pour la fonction TS, F :

- $F_1^0, \ldots, F_i^0$ les i valeurs maximales de la fonction de TS, F, sous H_0.
- $F_1^1, \ldots, F_j^1$ les j valeurs maximales de la fonction TS, F, sous H_1.

Les deux densités de probabilité sont modélisées afin de calculer avec précision le vrai positif (c'est-à-dire $1-\beta$) et le faux positif (c'est-à-dire α) pour chaque valeur seuil possible séparant les deux distributions, η. Le taux de vrais positifs (TVP) et les taux de fausses alarmes (TFA) sont définis par rapport à η.

$$\begin{cases} \text{TFA}(\eta) &= i^{-1} \sum_{k=1}^{i} \mathbb{1}(F_k^0 > \eta) \\ \text{TVP}(\eta) &= j^{-1} \sum_{l=1}^{j} \mathbb{1}(F_l^1 > \eta) \end{cases} \tag{I.6.18}$$

Lorsque tous les vrais positifs et faux positifs de la base synthétique (données de vérité de terrain) sont calculés, une courbe Empirical Receiver Operating Characteristic (EROC) peut être générée comme nous pouvons le voir dans la figure I.6.4. Plus une courbe est proche du point (0,1), meilleur est le détecteur.

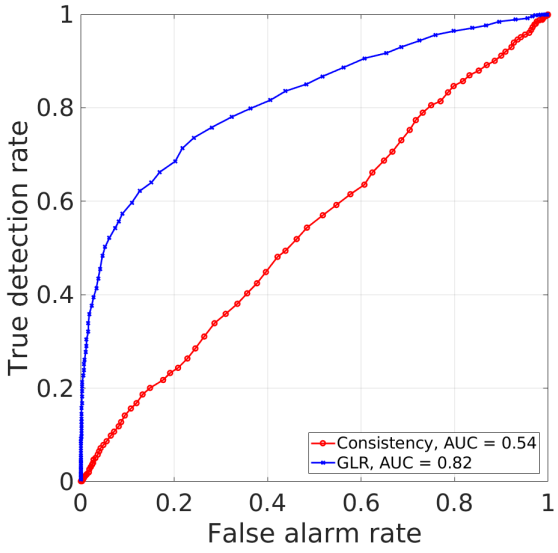

Figure I.6.4: Illustration des courbes Receiver Operating Characteristic (ROC) pour deux détecteurs. Plus la courbe est proche du point (0,1), meilleur est le détecteur. L'Area Under the Curve (AUC) approche un si le détecteur distingue parfaitement les deux hypothèses H_0 et H_1.

Une manière plus simple d'interpréter le résultat est de se concentrer sur l'Empirical Area Under the Curve (EAUC) de la courbe EROC.
L'EAUC est obtenue par la statistique de Wilcoxon-Mann-Whitney [Hanley and McNeil, 1982] définie comme :

$$\text{EAUC} = \frac{\sum_{k=1}^{i}\sum_{l=1}^{j} S(F_k^0, F_l^1)}{ij} \tag{I.6.19}$$

$$\text{avec} \quad S(X,Y) = \begin{cases} 1 & \text{si} \quad Y < X \\ 1/2 & \text{si} \quad Y = X \\ 0 & \text{si} \quad Y > X \end{cases} \tag{I.6.20}$$

Ainsi, plus l'EAUC se rapproche de un, meilleure est le TS.

Plusieurs types de TS basés sur différentes approches ont été développés dans la littérature. Le détecteur F est l'un des détecteurs les plus utilisés et appliqué par plusieurs CND (Evers and Haak [2005] ; Arrowsmith et al. [2009]). Il peut être mis en œuvre soit dans le domaine temporel, soit dans le domaine fréquentiel et estime le rapport entre la variance d'un SOI hypothétique avec une Direction Of Arrival (DOA) spécifique et la variance du bruit. Il peut également être utilisé pour mesurer le Signal to Noise Ratio (SNR). Ce rapport peut être comparé à un seuil basé sur la distribution de Fisher afin de prendre une décision entre H_0 et H_1. Cette méthode sera développée en détail plus tard. Une autre méthode similaire appelée le Generalized Likelihood Ratio Test (GLRT) est construite en calculant le rapport des log-vraisemblances des fonctions de densité de probabilité de H_1 et H_0 (Kay [2013] ; Charbit [2017]). Ici, le test est effectué en utilisant les critères de Neyman-Pearson ajustés par le taux de fausse alarme souhaité. Le Generalized Likelihood Ratio (GLR) dérivé de cette méthode sera utilisé dans cette thèse comme un TS clé provenant de l'état de l'art. Enfin, les détecteurs basés sur des méthodes de corrélation, tels que le Mean of Cross Correlation Maximum (MCCM) [Lee et al., 2013] et la consistance [Cansi and Pichon, 2008], sont largement utilisés. Ils sont basés sur l'estimation du retard temporel entre des paires de capteurs en maximisant la fonction de corrélation croisée. La consistance est appliquée par PMCC, qui est détaillé dans la prochaine partie et utilisé par le CND français ainsi que le CID.

I.6.3 Déroulement du traitement des signaux

Actuellement, le signal reçu $z(t)$ est divisé dans le domaine temps-fréquence. Cela permet la séparation des sources à la fois dans le temps et en fréquence grâce à l'utilisation d'une fenêtre glissante et d'un filtre sur l'ensemble de la période d'analyse. Le domaine temps-fréquence est généré, ici, par une décomposition en tiers d'octave. Un filtre de Chebychev de type un, d'ordre deux, est utilisé. Ce type de filtre est appliqué en raison de la pente abrupte du filtre. Cela permet une réponse de filtre presque constante dans la bande de fréquence souhaitée, malgré un comportement ondulatoire en raison des ondulations du filtre dans la bande. Le changement de phase est cependant important en raison de la fonction de transfert du filtre. La figure I.6.5 montre la longueur de la fenêtre utilisée pour chaque bande de fréquence. La longueur de la fenêtre utilisée pour chaque bande de fréquence garantit l'observation de dix fois la longueur d'onde moyenne du signal filtré. Le deuxième graphique montre les filtres utilisés entre 0,1 et 4 Hz. La principale caractéristique de ces filtres est qu'ils sont plats dans la bande de fréquence d'intérêt, sans gain. Enfin, le troisième concerne le changement de phase en fonction de la fréquence. Ce changement de phase n'est pas un problème car le filtre est appliqué de manière égale à tous les capteurs. Le traitement s'effectue donc

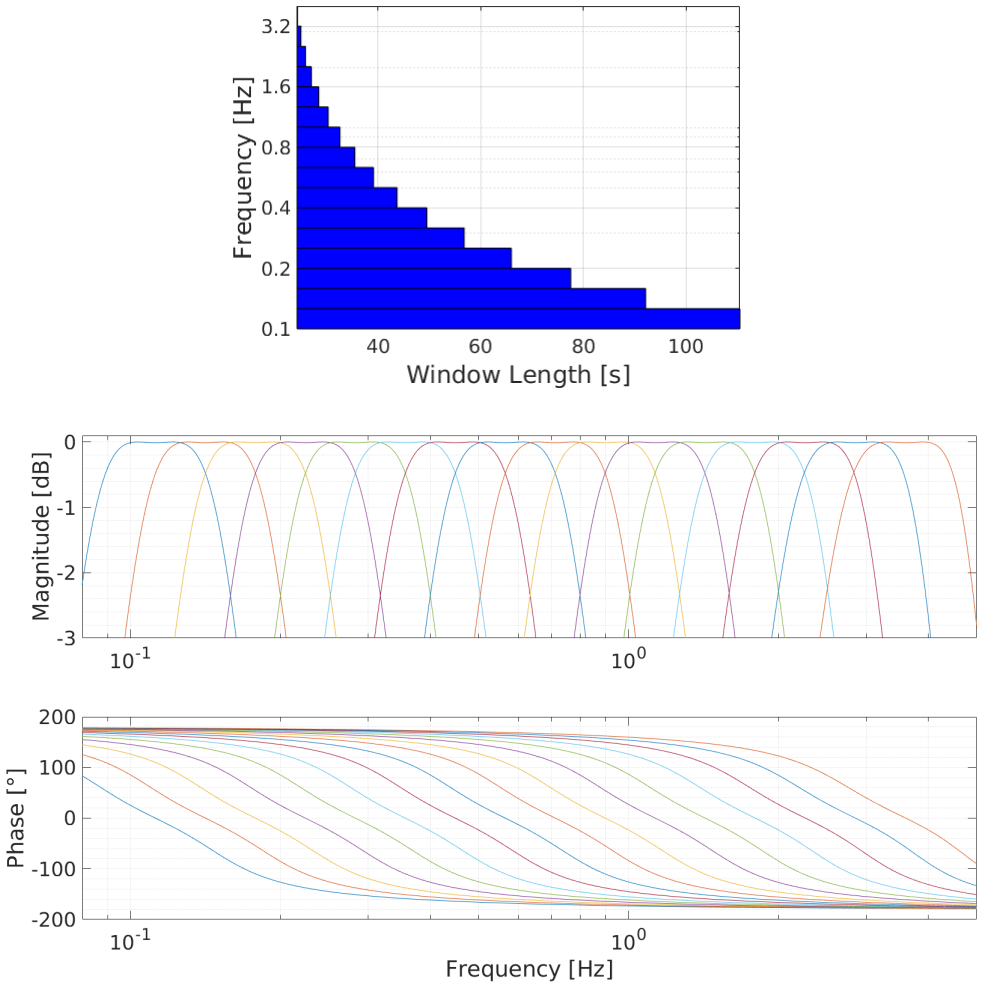

Figure I.6.5: Exemple d'une décomposition en tiers d'octave montrant la durée d'une fenêtre temporelle en fonction de la bande de fréquence (haut). Réponse du filtre en magnitude et en phase de chaque filtre en fonction de la fréquence (bas).

dans le domaine temps-fréquence en utilisant un filtre et un fenêtrage de la série temporelle. Enfin, les résultats sont représentés graphiquement comme dans la figure I.6.6 où chaque paramètre d'intérêt (θ, v) est illustré par un pixel. La longueur du pixel est proportionnelle à la longueur de la fenêtre, la hauteur est proportionnelle à la bande passante, et la couleur dépend du paramètre d'intérêt. Cette représentation

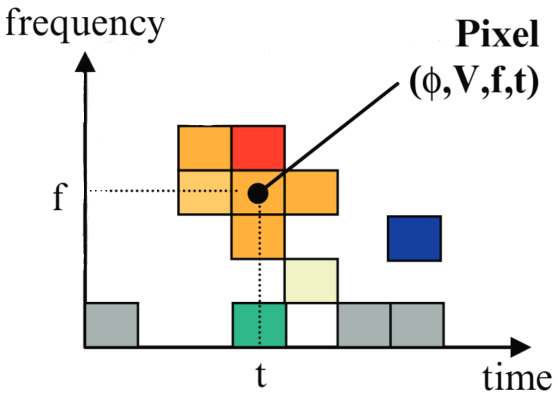

Figure I.6.6: Représentation graphique des estimations dans le domaine temps-fréquence. La couleur de chaque pixel représente la valeur du paramètre d'intérêt. Illustration extraite et modifiée de Brachet et al. [2010].

permet une meilleure interprétation, car les sources sont isolées par leur contenu fréquentiel et leur durée temporelle.

I.6.4 Motivations de la thèse

Le CEA est un centre de recherche et également le CND français qui exploite et analyse les données sismiques, de radionucléides, hydroacoustiques et infrasons en vue du développement du SSI mis en place par l'OTICE. Jusqu'à présent, la méthode basée sur la corrélation (Progressive Multi-Channel Correlation (PMCC)) est utilisée par l'OTICE pour analyser les signaux enregistrés au sein des différentes stations du SSI. Cette méthode de détection a été essentiellement développée pour détecter et localiser un signal cohérent de source unique au sein d'une cellule temps-fréquence donnée. Pour garantir l'hypothèse de source unique, en pratique, le signal reçu est divisé dans le domaine temps-fréquence avec, par exemple, une décomposition en tiers d'octave [Brachet et al., 2010]. Cela permet la séparation de plusieurs sources avec un contenu fréquentiel différent. Ainsi, ce réglage multi-bande permet une estimation plus précise de l'énergie infrasonore cohérente provenant d'une grande variété de sources naturelles et artificielles. Cela permet une meilleure caractérisation du bruit environnemental cohérent et une discrimination des événements d'intérêt [Matoza et al., 2013]. Cependant, les retours sur l'utilisation de PMCC montrent des détections erronées et des estimations inexactes dans des conditions d'enregistrement dégradées [Nouvellet et al., 2014]. L'une des raisons est la dégradation des capacités avec un faible SNR, une autre raison est que l'algorithme a été développé et optimisé pour détecter une seule source de signaux cohérents dans la même cellule temps-fréquence. Dans des conditions d'enregistrement réalistes, les stations détectent plusieurs sources et le traitement actuel n'est pas adapté. Plutôt que de supposer la présence d'une seule source d'intérêt au maximum, il est pertinent de considérer la présence de plusieurs signaux d'intérêt traversant le réseau de capteurs en même temps et à la même fréquence. Ce projet de thèse consiste à développer et tester des méthodes à haute résolution pour séparer plusieurs sources d'infrasons dans la même bande de fréquence, sur des bases contrôlées de signaux synthétiques et réels.

La thèse présentera d'abord la méthode de traitement monosource actuellement utilisée au CND et au CID, ainsi que les développements récents dans la partie II. Cette partie se compose de deux chapitres. Le chapitre II.1 décrit PMCC, l'algorithme actuel utilisé par le CEA et l'OTICE pour la surveillance opérationnelle. Les développements récents sont abordés dans le chapitre II.2, qui couvre l'algorithme Multi-Channel Maximum Likelihood (MCML), une nouvelle méthode basée sur la vraisemblance. Ce chapitre comprend les méthodes et les résultats sur des données synthétiques et réelles. Des données infrasons réelles provenant du SSI sont analysées, mais également des données sismiques d'un réseau national. Ensuite, des approches d'estimation à l'état de l'art et de haute résolution sont détaillées dans la partie III, qui se compose de quatre chapitres. Cela implique la description des approches de décomposi-

tion de sous-espace comme MUltiple SIgnal Classification (MUSIC) dans le chapitre III.1, des approches spectrales comme le spectre F-K ou le spectre de Capon dans le chapitre III.2, des approches statistiques comme le ratio de Fisher déjà utilisé dans plusieurs CND ou CLEAN, une méthode récemment développée dans le chapitre III.3, et enfin des techniques de régression robuste dans lesquelles les moindres carrés tronqués sont basés sur une méthode des moindres carrés améliorée dans le chapitre III.4. Plusieurs méthodes de ces différents chapitres sont mises en œuvre pour comparer leurs capacités d'estimation.

La partie IV concerne le développement de traitements multisources afin de déterminer si de meilleures méthodes par rapport à l'état de l'art pourraient être mises en œuvre. Cette partie se compose de cinq chapitres. Dans laquelle, les différentes extensions de la méthode MCML pour le traitement multisource sont examinées dans le chapitre IV.1 afin de tirer parti des développements récents. D'autres méthodes sont explorées, comme l'approche d'Analyse en Composantes Indépendantes (ACI) pour la séparation de sources à large bande dans le chapitre IV.2 et une stratégie de *dictionary coding* sur les fonctions de vraisemblance de la méthode MCML ou sur les retards entre les paires de capteurs dans le chapitre IV.3. Une comparaison des performances en termes de précision des estimateurs développés est présentée dans le chapitre IV.4 afin de quantifier la précision de chaque méthode mise en œuvre par rapport aux algorithmes de l'état de l'art. Cette comparaison est d'abord réalisée sur des signaux synthétiques avec des paramètres contrôlés de vérité terrain, et sur des données réelles par la suite. Le post-traitement des estimations se caractérise par le regroupement des résultats avec des paramètres similaires, ce qui est crucial pour l'analyse des événements. Une nouvelle méthode basée sur un Gaussian Mixture Model (GMM) est présentée pour améliorer la construction d'événements dans le chapitre IV.5.

Enfin, la partie V couvre la conclusion de l'ensemble de l'étude et les travaux futurs pour améliorer les résultats.

Part II

Current processing methods

Abstract

Two methods for calculating the wavefront parameters developed at the CEA are presented in this part. The first, Progressive Multi-Channel Correlation (PMCC), was developed starting in the 1995s [Cansi, 1995], and is used operationally at the French NDC and both at the IDC and partner NDCs. The detector (consistency) and the estimator (Time Difference of Arrivals (TDOA)) based on the calculation of the maximum inter-sensor correlation are studied before defining the covariance of this estimator. In order to characterise the detected events, the development of a post-processing system to group the detections proved to be necessary. Finally, an analysis of the infrasound signals generated by the Amatrice earthquake (Italy) on August 24, 2016, is conducted [Hernandez et al., 2018].

The second method is Multi-Channel Maximum Likelihood (MCML), developed since 2022 as part of a collaboration between CEA and Institut Mines-Telecom (IMT) to address the limitations of PMCC in degraded recording conditions [Poste et al., 2023b]. This new approach is based on the likelihood function derived from a multi sensors stochastic model. Using the likelihood function, for the detection problem, the GLR is established, and for the estimation of the slowness vector, the Maximum Likelihood Estimation (MLE). Simulations on synthetic signals show that MCML outperforms multichannel correlation algorithms such as PMCC in terms of false alarm rate and detection probability at low SNR and in the presence of coherence loss. The contribution of this new method is demonstrated using real data from the IMS, illustrating the performance of MCML for conducting refined analyses of events of interest.

Résumé

Deux méthodes de calcul du vecteur d'onde élaborées au CEA sont présentées dans cette partie. La première, Progressive Multi-Channel Correlation (PMCC), a été développée à partir des années 1995 [Cansi, 1995], et est utilisée en opérationnel tant au CND français qu'au CID et aux CND partenaires. Le détecteur (consistance) et l'estimateur (Time Difference of Arrivals (TDOA)) basés sur le calcul du maximum de corrélation inter capteurs sont étudiés avant de définir la covariance de cet estimateur. Afin de caractériser les événements détectés, le développement d'un post-traitement regroupant les détections s'est révélé nécessaire. Enfin, une analyse des signaux infrasons générés par le séisme d'Amatrice (Italie) du 24 août 2016 est réalisée [Hernandez et al., 2018].

La seconde méthode est Multi-Channel Maximum Likelihood (MCML) développée depuis 2022 dans le cadre d'une collaboration entre le CEA et l'IMT afin de pallier les limites de PMCC en situations d'enregistrement dégradées [Poste et al., 2023b]. Cette nouvelle approche repose sur la fonction de vraisemblance dérivée d'un modèle stochastique multicapteurs. En utilisant la fonction de vraisemblance, pour le problème de détection, le GLR est établi et, pour l'estimation du vecteur de lenteur, le MLE. Des simulations sur des signaux synthétiques montrent que MCML est plus performant que les algorithmes de corrélation multicanaux tels que PMCC en termes de taux de fausse alarme et de probabilité de détection à faible SNR et en présence de perte de cohérence. L'apport de cette nouvelle méthode est démontré sur des données réelles du SSI, illustrant les performances de MCML pour réaliser des analyses affinées d'événements d'intérêt.

Chapter II.1

The Progressive Multi-Channel Correlation (PMCC)

The Progressive Multi-Channel Correlation (PMCC) is an algorithm used to estimate the DOA and the trace velocity of the wavefront. This algorithm was first developed by the CEA firstly for seismic signal processing [Cansi, 1995]. However, the need to estimate the various wave parameters leads to the use of PMCC on infrasound data. PMCC is comprised of a detector which determines whether a wavefront is present or not and an estimator which determines, if there is a coherent wavefront, the parameters θ and v. This is a state-of-the-art monosource algorithm used in operational survey mission at many NDC and at the IDC.

II.1.1 Methods

II.1.1.1 Detection: the consistency

Detectors discriminate between two hypothesis, the H_0 hypothesis when there is no signal, $s = 0$ and the H_1 hypothesis when $s \neq 0$. The detector used by PMCC is the consistency. Let i, j and k be a subnetwork of three sensors, the algebraic sum of the propagation delays between sensor pairs of the triplet is

$$\tau_{ijk} = \tau_{ij} + \tau_{jk} + \tau_{ki} \tag{II.1.1}$$

where

$$\tau_{ij} \quad = \quad \arg\max_{u} \int_{L} z_i(t) z_j(t-u) dt \tag{II.1.2}$$

is determined by maximum of correlation between the sensor i and j by the TDOA method on a time window of length L. Then the consistency is the mean of τ_{ijk}^2 over all the possible triplet ijk of the array for $1 \leq k < j < i \leq M$:

$$C_M \quad = \quad \frac{6}{M(M-1)(M-2)} \sum_{1 \leq k < j < i \leq M} \tau_{ijk}^2 \tag{II.1.3}$$

Theoretically, when a SOI is present with no noise, $C_M = 0$, however in practice, there is always noise, that is why an arbitrary threshold, close to zero, based on experimental observations is set. When the consistency is lower than the threshold then the H_0 hypothesis is rejected. If so, a new sensor is added and the consistency is recalculated. This is called the *Progressivity*, it allows a better estimation including more and more sensors avoiding noisy ones.

II.1.1.2 Estimation: the Time Difference of Arrivals (TDOA)

The estimator used by PMCC is the Time Difference of Arrivals (TDOA) (equation II.1.2) which calculates the delay by maximum of correlation between the $P = M(M-1)/2$ sensors pairs.

The model derived from the TDOA expression is:

$$\tau = \mathbf{X}p + \epsilon \tag{II.1.4}$$

where τ is all the different entries of τ_{ij}, $\mathbf{X}$ the 2D matrix of the difference in position between each sensor pairs where $r_{m,i}$ denotes the ith coordinate of the mth sensor,

$$\mathbf{X} = \begin{bmatrix} r_{1,1} - r_{2,1} & r_{1,2} - r_{2,2} \\ \vdots & \vdots \\ r_{M-1,1} - r_{M,1} & r_{M-1,2} - r_{M,2} \end{bmatrix} \tag{II.1.5}$$

and ϵ the errors on the estimation of the true delays. It is a random vector of dimension P of mean zero and of covariance $\mathbf{\Gamma} = \sigma^2\mathbf{I}$.

Then to estimate the slowness vector p, the TDOA is based on the Ordinary Least Squares (OLS), the slowness vector is:

$$\hat{p} = (\mathbf{X}^T\mathbf{X})^{-1}\mathbf{X}^T\tau \tag{II.1.6}$$

From the slowness vector, we can calculate the azimuth and the velocity of the wavefront by:

$$\begin{cases} v &= \frac{1}{||\hat{p}||_2} \\ \theta &= arctan\left(\frac{\hat{p}_x}{\hat{p}_y}\right) \end{cases} \tag{II.1.7}$$

An improvement of PMCC has been implemented in the decades following its creation in order to overcome delay estimation errors due to sampling. Indeed when the sampling rate becomes non negligible compared to propagation time through the array then the errors on the estimation are increasing. The correction method involves the interpolation of the inter correlation function around the found maximum [Charbit et al., 2012]. The interpolation of the inter correlation function to search for the real maximum is represented by the figure II.1.1. The equation of the parabolic interpolation is

$$p(t) = \alpha t^2 + \beta t + \gamma \tag{II.1.8}$$

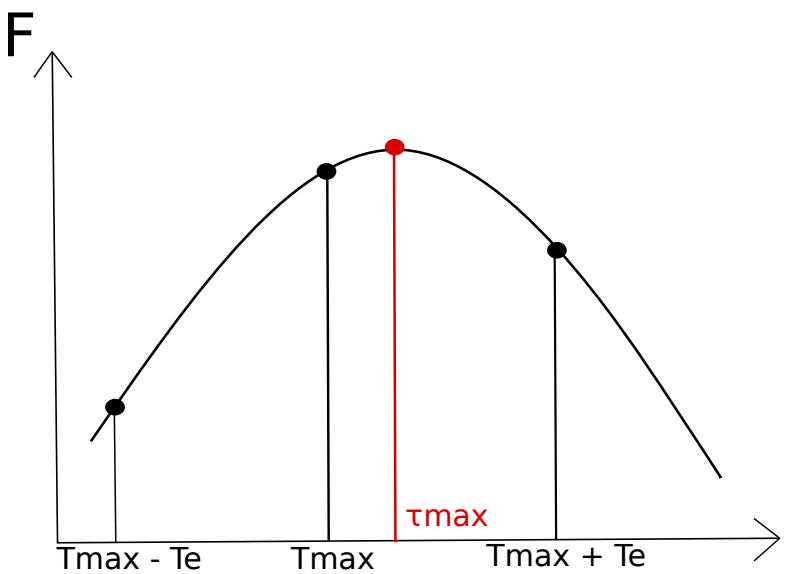

Figure II.1.1: Parabolic interpolation of the discrete inter correlation function taking into account three points: the found maxima and the two adjacent points, T_e denotes the time period sampling.

It comes that τ_{max} expresses the maximum of the parabola passing through the three chosen points

$$\tau_{max} = -\frac{\beta}{2\alpha} \tag{II.1.9}$$

The parabolic interpolation enables a significant improvement of the result in particular for small aperture array stations as if the sampling rate was ten times larger with minimal supplementary calculation cost.

The Root Mean Square (RMS) amplitude of the signal is calculated as follows, as a function of the number of samples N_e and sensors M

$$\text{RMS} = \frac{1}{M}\sum_{m=1}^{M}\sqrt{\sum_{t=1}^{N_e}\frac{z_m(t)^2}{N_e}} \tag{II.1.10}$$

II.1.1.3 Covariance of the estimator

Recall equation II.1.4 of the model derived from TDOA expression

$$\tau = \mathbf{X}p + \epsilon \tag{II.1.11}$$

where ϵ is a zero mean random vector of length P representing the errors on the estimation of the true delays. When τ is calculated by maximum of correlation, as in TDOA, the covariance matrix $\mathbf{\Gamma}$ has a complex expression identified in Cheung et al. [2008]. However, as a first approximation, we take $\mathbf{\Gamma} = \sigma^2\mathbf{I}$ with $\sigma^2 = \frac{3}{8\pi^2 B^3 T \text{SNR}}$ where B is the filter bandwidth and T is the time window [Carter, 1987].

The slowness vector is estimated by the ordinary least square

$$\begin{aligned}\hat{p} &= (\mathbf{X}^T\mathbf{X})^{-1}\mathbf{X}^T\tau \\ \hat{p} &= (\mathbf{X}^T\mathbf{X})^{-1}\mathbf{X}^T(\mathbf{X}p+\epsilon) \\ \hat{p} &= p + (\mathbf{X}^T\mathbf{X})^{-1}\mathbf{X}^T\epsilon\end{aligned} \tag{II.1.12}$$

We thus have

$$\hat{p} - p = (\mathbf{X}^T\mathbf{X})^{-1}\mathbf{X}^T\epsilon \tag{II.1.13}$$

The estimator is unbiased because $\mathbb{E}\{\hat{p}-p\} = 0$ and, in addition

$$\begin{aligned}\mathbf{Cov}\{\hat{p}\} &= (\mathbf{X}^T\mathbf{X})^{-1}\mathbf{X}^T\mathbf{Cov}\{\epsilon\}\mathbf{X}(\mathbf{X}^T\mathbf{X})^{-1} \\ \mathbf{Cov}\{\hat{p}\} &= \sigma^2(\mathbf{X}^T\mathbf{X})^{-1}\end{aligned} \tag{II.1.14}$$

If we assume that ϵ is Gaussian centred in zero, then this is Cramer-Rao Bound (CRB) [Cramér, 1999], it means that among all unbiased estimators, it has minimum variance.

II.1.1.4 Post processing into families

Once all the time window has been processed and the time frequency cells filled by wavefront estimations (figure I.3.6), the aim is to characterise an event by its wavefront parameters over time and frequency, in order to reconstruct the sequence of the event or how weather conditions impact the wave propagation. It comes that the need of detection agglomeration to statistically characterise the event becomes relevant. To do this, a nearest-neighbour search method based on a weighted distance in the (t, f, θ, v) domain is used [Cansi and Klinger, 1997]. This distance between two pixels can be expressed as :

$$d(p_1,p_2) = \sqrt{\left(\frac{t_2-t_1}{\sigma_t}\right)^2 + \left(\frac{f_2-f_1}{\sigma_f}\right)^2 + \left(\frac{v_2-v_1}{\sigma_v v_2}\right)^2 + \left(\frac{\theta_2-\theta_1}{\sigma_\theta}\right)^2} \tag{II.1.15}$$

The weights can be adapted to each parameter. The weights represent the maximum difference (in time, frequency band, trace velocity and back-azimuth) acceptable between a pixel and a family. The distance

is calculated for each detection forming a family to all the other detections. One pixel can be clustered with a family if the distance between the pixel and the mean parameters of the family pixels is below the threshold defined as the maximum acceptable dimensionless Euclidean distance in the (t, f, θ, v) domain [Le Pichon et al., 2010]. If it is not the case, the pixel will form a new family. The family is also controlled by a maximum and minimum amount of pixels. The minimum amount of pixels required allows the post processing to suppress isolated detections resulting of possible errors. Moreover, another post processing to group the family called the metafamily clustering. This allows the families to be grouped and event characterisation to be built, in particular when the event is a quasi-permanent one (i.e microbaroms [Le Pichon et al., 2011]).

II.1.2 Real data from the IMS infrasound network

PMCC is used at the French NDC but also at the IDC for monitoring purposes. This monitoring includes CTBT compliance monitoring but also civilian and scientific monitoring. Here, an example of a scientific monitoring of the Amatrice earthquake that struck central Italy on 24 August 2016 of moment magnitude 6.2 is shown [Hernandez et al., 2018]. This earthquake happened at a shallow depth of 4 km and around 45 km north of L'Aquila in central Italy. The mechanism occurred on a normal fault segment along the Apennines [Chiaraluce et al., 2017]. This event was followed by an aftershock of moment magnitude of 5.5 [Michele et al., 2016]. This kind of event can also radiate pressure waves when topographic conditions are favourable. Indeed, seismic waves that are shaking prominent topographic points in the area of the epicentre may induce infrasound wavefront from this point [Green et al., 2009]. These infrasounds can be registered and processed by PMCC, as here with the Haute Provence Observatory (OHP) station composed of four sensors and located in Provence, France at 623 km from the earthquake epicentre. Figure II.1.2 shows, from top to bottom, the azimuth, the trace velocity detection, respectively as functions of the time and the frequency band. Plotted below the PMCC detections are the four signals of the station filtered between 0.2 and 4 Hz are plot below the detection. Three main arrivals are identifiable on the figure. The arrival A has a high trace velocity greater than 3 km/s, these are in good agreement with theoretical seismic arrival delay. Thus this arrival can be linked to microbarometer response to local seismically coupled air waves [Ponceau and Bosca, 2009]. The two other arrivals correspond in time and trace velocity to infrasound. The back azimuths of arrival B increase from 70° to 125° whereas the back azimuths of the arrival C have a lower range from 100° to 110°. These two arrivals are thus linked to the mainshock and the aftershock of the Amatrice earthquake. The large azimuth variation from the first arrival suggests the presence of spatially extended sources of infrasound from the Po Valley to the Gulf of Naples [Hernandez et al., 2018]. This shows how an earthquake event can radiate acoustic energy by the shaking of the topography far from the epicentre. Here PMCC detects, with a high accuracy, this event, proving how robust this algorithm can be.

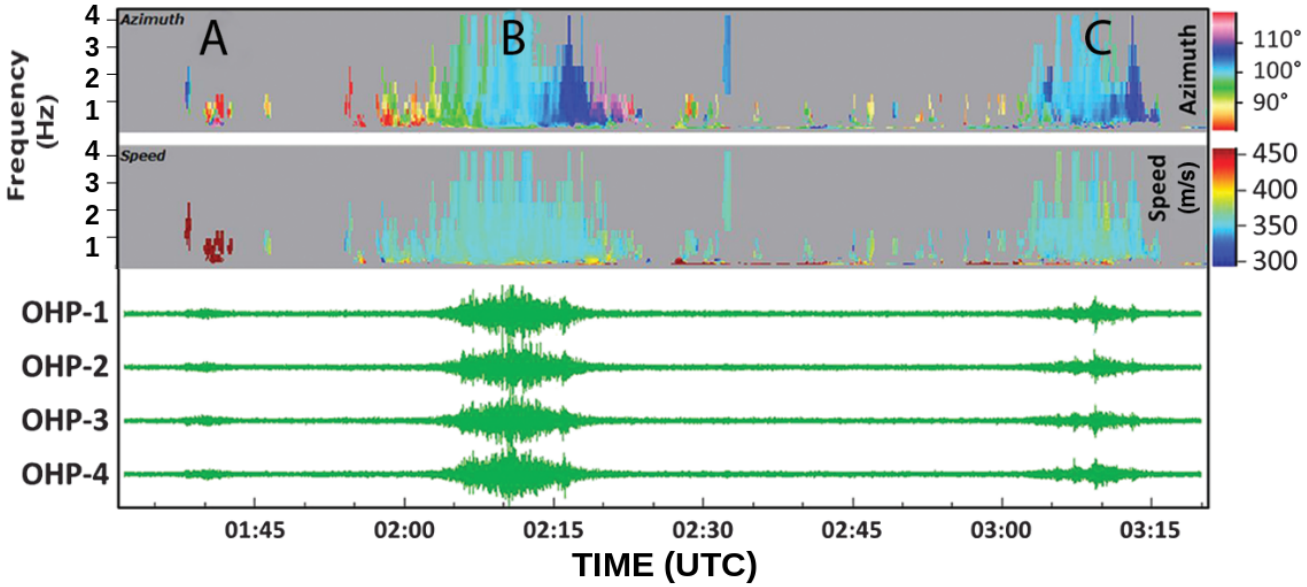

Figure II.1.2: Illustration of the back azimuth and trace velocity detection in function of the time (UTC) and frequency. The four sensors are also plotted below the detection. Three main arrivals can be detected by PMCC at the Haute Provence Observatory (OHP) station. The first one is the local seismically coupled air waves at the station at around 01h40 UTC and the two following arrival B located at 02h00 and C at 03h05 are linked to the mainshock and aftershock of the Amatrice event. Extracted and modified from Hernandez et al. [2018].

Chapter II.2

The Multi-Channel Maximum Likelihood (MCML)

Feedback from the IDC of the current PMCC algorithm have sometime shown erroneous detections and estimations in degraded recording conditions. That is why the CEA, in partnership with the IMT, developed a likelihood-based algorithm, Multi-Channel Maximum Likelihood (MCML) [Poste et al., 2023b]. This new approach relies on the likelihood function derived from a multi-sensor stochastic model. Using the likelihood function, for the detection problem, the Generalized Likelihood Ratio (GLR) is set and, for the estimation of the slowness vector, the MLE. We establish new asymptotic results for the TS under the null hypothesis leading to the computation of the corresponding p-value threshold and for the MLE by focusing on two wave parameters, the back-azimuth and the trace velocity. The MCML method is implemented in the same environment as PMCC, the time-frequency domain, in order to avoid the presence of interfering signals. Simulations on synthetic signals show that MCML outperforms the state-of-the-art multi-channel correlation algorithms like PMCC in terms of false alarm rate and detection probability in poor SNR and coherency loss conditions. The use of this new method is also shown on real data from the IMS and reveal how the improved performances of MCML lead to a refined analysis of events in accordance with expert knowledge.

II.2.1 Methods

II.2.1.1 Expression of the likelihood

Let's suppose a broadband model signal with a single coherent source

$$z_m(t) = s(t - \tau_m(\theta, v)) + n_m(t) \tag{II.2.1}$$

as expressed in the equation I.3.9 but with $N = 1$ source. We assumed that $z(t)$ is centred (i.e the mean has been removed). As previously stated, it is assumed that only a single source is present in each frequency band of the third octave band. The SOI is assumed to be Gaussian and temporally white while the noise is assumed simultaneously Gaussian, temporally white, spatially white and independent from $s(t)$.

$$\begin{cases} \mathbb{E}\{n(t)n(t')^T\} &= \sigma^2 \mathbf{I}_M \delta(t-t') \text{ noise temporally and spatially white} \\ \mathbb{E}\{s(t)s(t')^T\} &= \sigma_s^2 \delta(t-t') \quad \text{SOI temporally white} \end{cases} \tag{II.2.2}$$

where δ represents the dirac distribution. Let $\mu = (\theta, v, \sigma_s^2, \sigma^2)$ be defined as the Parameter Of Stochastic Model (POSM). In the case of a deterministic model, the parameter σ_s^2 should be replaced by the unknown deterministic sequence $s(t)$ to estimate $s(1), ..., s(N_e)$ where $N_e = F_s \times L$ the number of samples proportional to the sampling rate and the window length.

If $\tau^\star$ denotes the true delay then the m-th sensor signal is

$$z_m(t + \tau_m^\star) = s(t) + n_m(t + \tau_m^\star) \tag{II.2.3}$$

Because $n_m(t)$ is Gaussian, temporally white, spatially white and independent from $s(t)$, $n_m(t+\tau^\star)$ also has these properties with the same variance σ^2. Consequently, $z_m(t+\tau^\star)$ is a Gaussian, centred process of covariance matrix

$$\mathbf{R}_0(\sigma_{s\star}^2, \sigma_\star^2) = \sigma_{s\star}^2 \mathbb{1}_M \mathbb{1}_M^T + \sigma_\star^2 \mathbf{I}_M \tag{II.2.4}$$

with $\mathbb{1}$ a vector of length M whose components are set to 1. Thus the probability density function of the sequence $\tilde{z}_{1:N_e} = z_{1:N_e}(\theta^\star, v^\star)$, where $1{:}N_e$ is a short-hand notation for $1, \cdots, N_e$, is

$$p(\tilde{z}_{1:N_e}; \mu^\star) = \prod_{n=1}^{N_e} (2\pi)^{-M/2} \det \mathbf{R}_0{}^{-1/2} \exp\left(-\frac{1}{2}\tilde{z}_n^T \mathbf{R}_0^{-1} \tilde{z}_n\right)$$

Let us note that $\tilde{z}_n^T \mathbf{R}_0^{-1} \tilde{z}_n = trace(\mathbf{R}_0^{-1} \tilde{z}_n \tilde{z}_n^T)$. It is possible then to express the log-likelihood by taking the logarithm of the probability density function

$$\mathcal{L}(\mu^\star) = -\frac{MN}{2}\log(2\pi) - \frac{N}{2}\log(\det \mathbf{R}_0) - \frac{N}{2}\text{trace}\left(\mathbf{R}_0^{-1}\mathbf{R}_{\mathbf{zz}}(\theta^\star, v^\star)\right) \tag{II.2.5}$$

where $\mathbf{R}_{\mathbf{zz}}$ is the covariance matrix of the signals, accounting for delays. The expression of $\det \mathbf{R}_0$ and $\mathbf{R}_0^{-1}$ is given in appendix A.1. Injecting the expression of the equation A.5 and A.6 in the likelihood expression II.2.5 we obtain

$$\begin{aligned}\mathcal{L}(\mu^\star) &= -\frac{MN}{2}\log(2\pi) - \frac{NM}{2}\log(\sigma_\star^2) - \frac{N}{2}\log(1+\rho^{2\star}) - \frac{N}{2}\frac{T_N(\theta^\star, v^\star)}{\sigma_\star^2} + \frac{N}{2\sigma_\star^2}\frac{\rho^{2\star}}{1+\rho^{2\star}}\frac{1}{M}S_N(\theta^\star, v^\star) \\ &= -\frac{MN}{2}\log(2\pi) - \frac{NM}{2}\log(\sigma_\star^2) - \frac{N}{2}\log(1+\rho^{2\star}) - \frac{N}{2\sigma_\star^2}\left(T_N(\theta^\star, v^\star) + \frac{\rho^{2\star}}{1+\rho^{2\star}}\frac{1}{M}S_N(\theta^\star, v^\star)\right)\end{aligned} \tag{II.2.6}$$

where

$$\rho^{2\star} = \frac{M\sigma_{s\star}^2}{\sigma_\star^2} \geq 0 \tag{II.2.7}$$

$$S_N(\theta^\star, v^\star) = \mathbb{1}_M^T \mathbf{R}_{\mathbf{zz}}(\theta^\star, v^\star)\mathbb{1}_M = \frac{1}{N}\sum_{n=1}^{N_e}\left(\sum_{m=1}^{M}\tilde{z}_{n,m}\right)^2 \tag{II.2.8}$$

$$T_N(\theta^\star, v^\star) = \text{trace}\left(\mathbf{R}_{\mathbf{zz}}(\theta^\star, v^\star)\right) = \frac{1}{N}\sum_{n=1}^{N_e}\sum_{m=1}^{M}\tilde{z}_{n,m}^2 \tag{II.2.9}$$

The parameter set of the POSM μ is

$$\mathcal{P} = \left\{(0° - 360°) \times (v_{\min} - v_{\max}) \times \mathbb{R}^+ \times \mathbb{R}^+\right\} \tag{II.2.10}$$

II.2.1.2 Detection: Generalized Likelihood Ratio

We denote $H_0 = \{\mu \text{ such that } \rho = 0\} \subset \mathcal{P}$ as the null hypothesis of the test, referring to the definition at the equation I.3.16.

The function used for testing the null hypothesis is the GLR

$$GLR = 2\left(\max_{\mathcal{P}}\mathcal{L} - \max_{H_0}\mathcal{L}_0\right) \tag{II.2.11}$$

The first term represents the maximisation of the likelihood in a context where $\rho^2 \neq 0$ (i.e a SOI is present) and the second term represents the maximisation of the likelihood with respect to σ^2 with the constraint that $\rho^2 = 0$ (i.e only noise is present).

In order to maximise the log-likelihood function we first derive the function with respect to σ^2 with (θ, v) fixed. The function is maximised with

$$\sigma^2 = \frac{1}{M}\left(T_N(\theta, v) - \frac{1}{M}\frac{\rho^2}{1+\rho^2}S_N(\theta, v)\right) \tag{II.2.12}$$

The maximisation of σ^2 is proved by the Cauchy–Schwarz inequality

$$\left(\sum_{m=1}^{M} \tilde{z}_{n,m}\right)^2 \leq \sum_{m=1}^{M} \tilde{z}_{n,m}^2 \sum_{m=1}^{M} 1^2 = M \sum_{m=1}^{M} \tilde{z}_{n,m}^2 \tag{II.2.13}$$

It means that we have

$$0 \leq S_N \leq T_N \tag{II.2.14}$$

Replacing the expression of σ^2 in the equation II.2.6, the log-likelihood is then

$$\frac{-2}{N_e}\mathcal{L} - M(1 + \log(2\pi)) = M \log(T_N + \rho^2(T_N - \frac{S_N}{M})) - (M-1)\log(1+\rho^2) - M\log(M) \tag{II.2.15}$$

Setting $\rho^2 = 0$ it is possible to express $\mathcal{L}_0^\star$ in the subset H_0

$$\frac{-2}{N_e}\mathcal{L}_0^\star = M \log \frac{T_N}{M} + M(1 + \log(2\pi)) \tag{II.2.16}$$

The expression of ρ^2 can be expressed deriving the previous equation II.2.15 with respect to ρ^2 also with (θ, v) fixed

$$\rho^2 = \frac{S_N - T_N}{T_N - \frac{S_N}{M}} \tag{II.2.17}$$

This equation is valid for $S_N > \frac{T_N}{M}$, $\rho^2 = 0$ otherwise.

The log likelihood in the parameter set of the POSM μ can be expressed as

$$\frac{-2}{N_e}\mathcal{L}^\star = \log \frac{S_N}{M} + (M-1)\log \frac{T_N - \frac{S_N}{M}}{M-1} + M(1 + \log(2\pi)) \tag{II.2.18}$$

It is then possible to express the GLR of the equation II.2.11 as

$$\text{GLR} = 2\left(\max_{\theta,v} \mathcal{L}^\star - \max_{\theta,v} \mathcal{L}_0^\star\right) \tag{II.2.19}$$

It is worth to notice that $\mathcal{L}_0^\star$ does not depend on (θ, v) because T_N does not depend on these parameters for a large number of N_e (equation II.2.16). Indeed for all points in the subset of H_0 the couple back-azimuth/trace velocity does not modify the likelihood. It means that the likelihood is not χ^2 distributed and that the Wilks' theorem fails in our case [Wilks, 1938]. Up to an edge effect the GLR can be redefined as

$$\text{GLR} = 2\max_{\theta,v}(\mathcal{L}^\star - \mathcal{L}_0^\star) \tag{II.2.20}$$

Injecting the expression of $\mathcal{L}_0^\star$ and $\mathcal{L}^\star$ in the equation of the GLR it can be seen that the detection function depends on

$$\frac{2}{N_e}(\mathcal{L}^\star - \mathcal{L}_0^\star) = \log \frac{T_N}{S_N} + (M-1)\log \frac{(M-1)T_N}{M(T_N - \frac{S_N}{M})} \tag{II.2.21}$$

If $S_N > \frac{T_N}{M}$, $\mathcal{L}^\star - \mathcal{L}_0^\star = 0$ otherwise. Setting the following variable

$$F = \left(\frac{S_N}{T_N} - 1\right)_+ \leq M - 1 \tag{II.2.22}$$

It follows that the variation of the GLR is

$$\frac{2}{N_e}(\mathcal{L}^\star - \mathcal{L}_0^\star) = -\log(1+F) - (M-1)\log\left(1 - \frac{F}{M-1}\right) \tag{II.2.23}$$

It is easy to show that the previous equation can be written as $-\log(1+x) - (M-1)\log(1-\frac{x}{M-1})$ and that it is an monotonically increasing function on $[0, M-1)$. When x is close to zero then this function acts as $\frac{M}{2}x^2 + o(x^2)$. Thus to test H_1 against H_0, the GLR statistic is equivalent to

$$\text{GLR} = \frac{M}{2} \sup_{(\theta,v)} F(\theta,v)^2(1 + o_P(1)) \tag{II.2.24}$$

where $\sup_{(\theta,v)}$ is the supremum if the maximum does not exist and $o_P(1)$ is the probability order in the stochastic model.

To discriminate between the null hypothesis, H_0, and the alternative hypothesis, H_1, the method used is the p-value. The p-value is used to quantify the statistical significance of the null hypothesis. The main idea is to determine if the null hypothesis is true. The *statistically significant result* is defined by a result that verifies H_0 but would be improbable. Then the studied case differs significantly from the H_0 hypothesis and it does not apply to the observation. The observation is then related to the alternative hypothesis H_1.

A way of calculating the p-value for a TS has been developed in Arrowsmith [2018] with synthetics and is based on Kernel Density Estimation (KDE) [Scott, 2014]. For each time window L the likelihood is maximised to find the optimal parameters of the wavefront. In addition to the maximum likelihood, it is also possible to calculate the variance of the found DOA on a couple of time windows, αL, where α is superior to two. These two variables reflect different properties of the ambient noise, thus they can vary independently. We can now consider the total signal length and the histogram of the distributed parameters. The KDE allows the fit of these values into two separate distribution functions as follows

$$f(x) = \frac{1}{hN_e}\sum_{i=1}^{N_e} K\left(\frac{x - x_i}{h}\right) \tag{II.2.25}$$

where x_i is the observation, N_e is the number of observations in the total signal, h is the smoothing parameters for adapted distribution representation and K is the kernel function (Rosenblatt [1956]; Parzen [1962]). The kernel function is a non-negative function that can be uniform, normal (mostly used), triangular, weighted or Epanechnikov which is optimal in a mean square error sense [Epanechnikov, 1969]. Thanks to this distribution, a p-value can be calculated without any prior knowledge of the statistical property of the noise

$$p - \text{value} = \int_F^{+\infty} f(x)dx \ \in [0,1] \tag{II.2.26}$$

where F is the value of the individual TS (here the maximum likelihood and then the DOA variance) and $f(x)$ is the obtained kernel function. The Fisher's method can be applied [Arrowsmith, 2018] to combine the TS

$$\chi^2 = -2\sum_{i=1}^{k} \ln p - \text{value}_i \tag{II.2.27}$$

where k is the number of independent distributions used, in this case equal to two. This p-value can be calculated for every time windows of length L by resampling the variance for each time window.

However, this method is not used here because of the prior knowledge of the noise property made by the stochastic model. Indeed we model the distribution of the GLR under the H_0 hypothesis. As stated in equation II.2.24, it is necessary to determine the asymptotic behaviour of F under H_0 when the time T is going to infinity, which in turn follows from that of the empirical covariance matrix R_N of the white Gaussian noise. However, the closed form expression of the distribution of the GLR under H_0 is unknown. To circumvent this problem, we replace the maximisation of equation II.2.24, which assumes a continuous set

of values, by a maximisation over a fine, finite 2D grid over the domain $[0, 360] \times [v_{min}, v_{max}]$ m/s where the two last values are given by the field of study (i.e range of velocities different for infrasound or seismic).

It can be established (i.e after a demonstration given in the appendix A.2) that the asymptotic behaviour of the TS under the H_0 hypothesis is

$$\left(\frac{S_N}{T_N} - 1\right)_{(\theta,v)} \xrightarrow{T\to+\infty} (\boldsymbol{\mathcal{R}}(\theta, v))_{\theta,v} \tag{II.2.28}$$

where the $\mathcal{R}$ is a centred Gaussian process of covariance

$$\boldsymbol{\xi}((\theta, v), (\theta', v')) = 2 \times \frac{\int |H(f)|^4 \sum_{k=1}^{M} \sum_{k'=1}^{M} e^{2i\pi f(\tau_k(\theta,v) - \tau_{k'}(\theta',v'))} df}{\left(\int |H(f)|^2 df\right)^2} \tag{II.2.29}$$

where $H(f)$ denotes the frequency response of the selected filter of the filter bank. In a coarse calculation, we assume that $H(f) = 1$ in the frequency bandwidth $(F_{\min}, F_{\max})$ and 0 outside. In a finer approach, an appropriate algorithm can be used to perform expression (II.2.29) directly from the coefficients of the transfer function, for example, with a Chebyschev filter. This behaviour can be illustrated by the following vector

$$G = (\boldsymbol{\xi}((\theta, v), (\theta', v')))_{((\theta,v),(\theta',v'))} \in \mathcal{P} \tag{II.2.30}$$

However, the distribution of the maximum among the components of a zero-mean Gaussian vector, when the covariance matrix is not diagonal, has no closed form expression. That is why a Monte Carlo approach was used to generate a large number of vectors, G, in order to make statistics. The maximum is then selected from this vector to construct the distribution of the maximum of the GLR under the H_0-hypothesis. Indeed, the log-log cumulative function of F under H_0 can be constructed using the Fisher-Tippet theorem [Embrechts et al., 1997] that states that the maximum of a sample of independent and identically distributed Gaussian variables converges to the Gumbel distribution $x \mapsto f = e^{-e^{(b-x)/a}}$ or equivalently $\log(-\log(f)) = (b - x)/a$. In our case, the independent and identically distributed assumption fails due to the maximum selection of the vectors G, we replace the linear argument $(b - x)/a$ by a cubic spline function. The cubic spline, associated to the n knots $x_1 < x_2 < \cdots < x_n$, is a degree 3 polynomial piecewise function on interval (x_k, x_{k+1}) with $1 < k < n$ and linear on interval $(-\infty, x_1]$ and interval $[x_n, +\infty)$.

Once the distribution F under H_0 is estimated, the p-value is similar to equation II.2.26

$$p - \text{value} = \int_F^{+\infty} p_{F|H_0}(t)dt \ \in [0, 1] \tag{II.2.31}$$

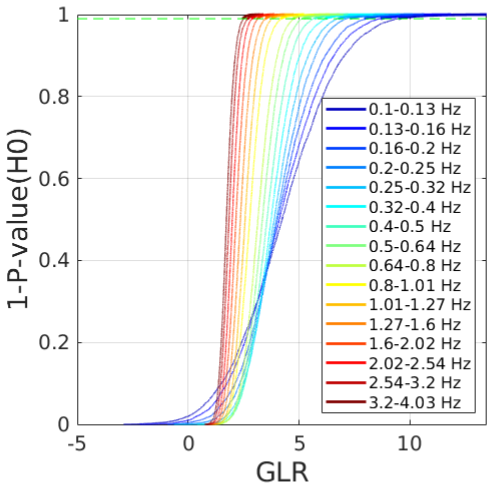

Figure II.2.1: $1-p-$value function as the complement to 1 of the cumulative function of F under H_0, for different log-scaled filter bands and for a 1 km aperture geometry (IS31). The above green dotted line indicates GLR values corresponding to a false alarm rate of 1%.

where $p_{F|H_0}(t)$ is the distribution of F under the null hypothesis approximated by the spline function. As an example, figure II.2.1 shows, from 0.1 Hz to 4 Hz, the complement to 1 of the cumulative function of F under the null hypothesis for the IMS station IS31 in Kazakhstan. These functions allow a direct calculation of the $p-$value from the observed value F given by the equation II.2.22.

II.2.1.3 Estimation: Maximum Likelihood Estimator

The maximisation of the likelihood function $\mathcal{L}(\mu)$ with respect to (σ_s^2, σ^2) leads to the closed form solution for σ_s and σ related to the equation II.2.18. The maximisation of (θ, v) can be performed as

$$(\hat{\theta}, \hat{v})_{\text{MLE}} = \underset{(\theta,v)}{arg\max} \left(-\log \frac{S_N(\theta,v)}{M} - (M-1)\log \frac{T_N(\theta,v) - \frac{S_N(\theta,v)}{M}}{M-1} - M(1+\log(2\pi)) \right) \quad \text{(II.2.32)}$$

From the maximum likelihood approach, the SNR can be estimated thanks to the expression of ρ^2 (equations II.2.7 and II.2.17)

$$\widehat{\text{SNR}} = \frac{S_N(\hat{\theta}_{\text{MLE}}, \hat{v}_{\text{MLE}}) - T_N(\hat{\theta}_{\text{MLE}}, \hat{v}_{\text{MLE}})}{MT_N(\hat{\theta}_{\text{MLE}}, \hat{v}_{\text{MLE}}) - S_N(\hat{\theta}_{\text{MLE}}, \hat{v}_{\text{MLE}})} \quad \text{(II.2.33)}$$

The Root Mean Square (RMS) amplitude of the SOI is also calculated by MCML using the equation II.2.7, II.2.12 and II.2.17

$$\text{RMS} = \sqrt{\sigma_s^2} = \sqrt{\frac{S_N - T_N}{M(M-1)}} \quad \text{(II.2.34)}$$

Asymptotically (i.e when the observation time goes to infinity) the MLE is unbiased and thus the central limit theorem is satisfied. This property can be can be explicitly described by

$$\sqrt{T}\left((\hat{\theta}, \hat{v})_{\text{MLE}} - (\theta^\star, v^\star)\right) \xrightarrow{T\to+\infty} \mathcal{N}(0, \mathbf{R}_{MLE}^{\theta,v}) \quad \text{(II.2.35)}$$

where $\mathbf{R}_{MLE}^{\theta,v}$ is the inverse of the Fisher Information matrix with respect to the parameter (θ, v)

$$\mathbf{R}_{MLE}^{\theta,v} = \mathbf{J}\boldsymbol{\Gamma}_0\mathbf{J}^T, \quad \text{(II.2.36)}$$

$\mathbf{J}$ is the Jacobian matrix of the transformation for the true parameters,

$$\mathbf{J} = \begin{bmatrix} -v^\star\cos(\theta^\star) & v^\star\sin(\theta^\star) \\ v^{2\star}\sin(\theta^\star) & v^{2\star}\cos(\theta^\star) \end{bmatrix} \quad \text{(II.2.37)}$$

with

$$\boldsymbol{\Gamma}_0 = \frac{\int 4\pi^2 f^2 |H(f)|^4 \ (M \times SNR^\star + 1)\, df}{\left(\int 4\pi^2 f^2 M \times SNR^\star \times |H(f)|^2 df\right)^2} \times \left(\mathbf{X}_{MLE}^T \boldsymbol{\Pi}_M^\perp \mathbf{X}_{MLE}\right)^{-1} \quad \text{(II.2.38)}$$

where $\mathbf{X}_{MLE}$ is the position matrix of the sensors in an arbitrary orthogonal 2-D coordinate system (different from the inter sensor distance matrix $\mathbf{X}$ of PMCC). $\boldsymbol{\Pi}_M^\perp = \mathbf{I}_M - M^{-1}\mathbb{1}_M\mathbb{1}_M^T$ is the orthogonal projector onto the orthogonal space of the vector $\mathbb{1}_M$.

It is worth noting that the expression (II.2.36) depends on the true unknown values of the POSM (back azimuth, trace velocity and SNR). In practice, to define a confidence region around the estimates, the true values are replaced by MLE estimates that are consistent. It also depends on the chosen filter and the antenna geometry.

It is also possible to calculate the estimation uncertainty for a recording condition without any prior estimation in order to study the impact of the geometry and filter. To mitigate this dependence on the POSM, the covariance matrix (II.2.36) is integrated over the full set of the couple (θ, v). The integrated expression is

$$\overline{\mathbf{R}}_{MLE} = \int_0^{360} \int_{v_{\min}}^{v_{\max}} \mathbf{R}_{MLE}^{\theta,v} \, d\theta dv \tag{II.2.39}$$

The dependence on the SNR is defined by a multiplicative weight. Therefore, we can derive the impact of the station geometry, assuming the SNR is 0 dB.

Finally the back azimuth and the trace velocity uncertainties are given by

$$\begin{cases} \sigma_\theta = \sqrt{\mathbf{R}_{MLE}(1,1)} \\ \sigma_v = \sqrt{\mathbf{R}_{MLE}(2,2)} \end{cases} \tag{II.2.40}$$

II.2.1.4 Computation time optimisation

Both the GLR and the MLE are obtained through a maximisation over a set of parameters μ of the likelihood function, which can be explicitly solved with respect to σ_s^2 and σ^2. The maximisation with respect to (θ, v) however needs to be carried out numerically over a finite regular grid for $(\theta, v) \in (0° - 360°) \times (v_{\min} - v_{\max})$ m/s. This grid search is made for each time-frequency cell of the signal and thus the calculation can be parallelised for each cell, making it faster.

The grid step has to be cleverly chosen to avoid any undesired computational load, for this purpose, we choose a grid step based on the error made by the antenna configuration at each frequency band. Indeed it is useless to set a grid much finer than the actual accuracy of the estimator. For this aim, we first calculate the integrated covariance matrix $\overline{\mathbf{R}}_{MLE}$ and then the error. The chosen grid step is equal to $\frac{\sigma_\theta}{2}$ for the back azimuth grid and $\frac{\sigma_v}{4}$ for the trace velocity grid. A maximum and a minimum grid step is, however, set based on physically realistic values for infrasound:

$$\begin{cases} 0.5° < a_\theta < 5° \\ 5 \; m/s < a_v < 50 \; m/s \end{cases} \tag{II.2.41}$$

The maximum resulting from this grid search can then be refined. This optimisation can be done in two different ways:

- Using the genetic algorithm Covariance Matrix Adaptation - Evolution Strategy (CMA-ES).
- Using the paraboloid interpolation algorithm.

The Covariance Matrix Adaptation - Evolution Strategy (CMA-ES) is a genetic algorithm designed to solve non-linear and non-convex numerical problems. Starting with a preliminary solution, it samples a population of potential solutions in the space of parameters to be estimated [Varelas et al., 2018] using a multivariate Gaussian distribution $\mathcal{N}$ whose parameters are the mean, standard deviation and covariance matrix. For each individual in this population, the algorithm evaluates a cost function in relation to its distance from maximum likelihood. It then selects the best individuals from this population, which will be called parents, in order to update the parameters of the $\mathcal{N}$ distribution [Loshchilov and Hutter, 2016]. The new iteration is expressed as follows

$$x_k^{g+1} \simeq \mathcal{N}(\overline{m}^g, (\sigma^g)^2, \mathbf{R}^g) \simeq \overline{m}^g + \sigma^g \mathcal{N}(0, \mathbf{R}^g) \tag{II.2.42}$$

where x_k^{g+1} is the k-th individual of generation $g+1$, $\overline{m}^g$ is the mean of the best elements of generation g, σ^g and $\mathbf{R}^g$ are the mean standard deviation and the covariance matrix of generation g, respectively [Hansen and Ostermeier, 1997]. In other words, the new generation of population $g+1$ is constructed with the mean of the best parents of the old generation g added to the associated multivariate distribution. The strength of this algorithm is that it calculates, in parallel, the path p_c taken by the successive generations g, by correlating the different steps [Hansen, 2006]. If the same direction has been taken in several stages, this can be taken into account when updating the covariance matrix to increase the

variance of individuals in the future generation in order to move faster towards the solution [Hansen and Ostermeier, 1997]. When the cost function converges and the population values no longer change below a given threshold, CMA-ES stops and returns the solution found [Sigaud and Stulp, 2013]. In this case, the algorithm refines the maximum likelihood from the results of the grid search. Once it has been reached, the algorithm returns the coordinates of this maximum. These coordinates are the back azimuth and the trace velocity.

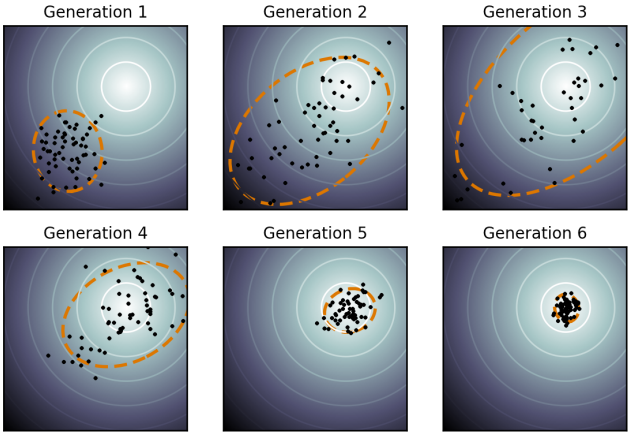

Figure II.2.2: This is the optimum to be found in the light area. The population represented by the dots will evolve thanks to the selection of the parents and will tend towards this optimum. The path p_c allows the variance of the generations $n+1$ to vary more strongly if the previous populations take the same direction. This is achieved by correlating the path of the previous generations. Extracted from [RandOpt-INRIA].

A second approach to refine the grid search solution is based on a parabolic interpolation method. This method involves interpolating the likelihood function, which is assumed to be derivable at any order, with a paraboloid around the maximum found on the grid. Nine points on the grid, including the maximum, are used to fit the paraboloid. The equation of this paraboloid is

$$z = ax^2 + by^2 + 2cxy + dx + ey + f \tag{II.2.43}$$

In matrix form, the previous equation II.2.43 is expressed as

$$z = \begin{pmatrix} x & y \end{pmatrix} \times \mathbf{R} \times \begin{pmatrix} x & y \end{pmatrix}^T + M \times \begin{pmatrix} x & y \end{pmatrix}^T + f \tag{II.2.44}$$

with

$$\mathbf{R} = \begin{pmatrix} a & c \\ c & b \end{pmatrix} \quad \text{and} \quad M = \begin{pmatrix} d & e \end{pmatrix}$$

The six coefficients of the paraboloid are determined by the ordinary least squares method, that is by minimising an overdetermined system of nine equations.

We are looking for the maximum in Z of this paraboloid, which is the maximum likelihood related to the back azimuth and trace velocity parameters (x, y). The maximum is reached when the sum of the derivatives in x and y are zero

$$\begin{pmatrix} x & y \end{pmatrix} \times 2\mathbf{R} + M = 0 \tag{II.2.45}$$

The wavefront parameters of interest are expressed by

$$\begin{pmatrix} x \\ y \end{pmatrix} = -\frac{1}{2} M \times \mathbf{R}^{-1} \tag{II.2.46}$$

Due to the speed of the parabolic interpolation calculation and the similar results obtained, this algorithm has been adopted. In fact, the gain in calculation time is significant, with a reduction of around a factor of 100 compared to CMA-ES.

A last optimisation on the computational cost is about how the matrix $\mathbf{R_{zz}}$ is calculated. As said previously $\mathbf{R_{zz}}$ is the covariance matrix of the signals accounting for delays. During the process this matrix is computed for each grid nodes which is time consuming. This is why, the covariance matrix of the signals, after compensation for the delays $\mathbf{R_{zz}}$, is estimated outside the estimation loop. This is done by estimating the $M(M-1)/2$ intercovariances:

$$\rho_{i,j}(\tau_{i,j}(\theta,v)) = \frac{1}{N_e - p} \sum_{n=1}^{N_e - p} z_i(n) z_j(n+p)$$

We consider a back azimuth/trace velocity grid (θ, v) and the intercovariance $\rho_{i,j}(\tau_{ij}(\theta,v))$. The matrix rewrites outside of the loop as

$$\mathbf{R_{zz}}(\theta,v) = \begin{bmatrix} \rho_{1,1}(\tau_{1,1}(\theta,v)) & \dots & \rho_{1,M}(\tau_{1,M}(\theta,v)) \\ \vdots & & \\ \rho_{M,1}(\tau_{M,1}(\theta,v)) & \dots & \rho_{M,M}(\tau_{M,M}(\theta,v)) \end{bmatrix} \tag{II.2.47}$$

For similar results the computational cost has been reduced to 70% maximum depending on the frequency band and thus the grid step.

II.2.2 Results on simulated data

Both algorithms, PMCC and MCML, are compared for the two tasks of detection and estimation. For this purpose, the consistency without the progressivity is compared to the GLR and the TDOA is compared to the MLE, respectively. The progressivity is first not taken into account in order to compare the same geometry between the two detectors and estimators. Indeed if taken into account, the estimator and detector would be better but some sensors could be not taken in order to build the estimation. The geometry would be thus changed. In absence of enough real data with ground truth information, synthetic data are generated in order to make statistics as follow

- The SOI is generated randomly and delayed in accordance with the considered DOA, trace velocity and the M sensor locations of the chosen geometry as reported in Figure II.2.3.
- SOI of the M sensors are then filtered in the selected frequency band with an order 2 Chebychev filter and windowed according to the bandwidth (ten times the central period of the bandwidth).
- The source of noise is either a white Gaussian noise or randomly extracted from a long record of pressure measurement background noise in a windy situation. (>10 m/s).
- The Loss Of Coherency (LOC) is modelled in order to observe which algorithm deals better with this physical effect [Green, 2015].

II.2.2.1 Detection results

The Receiver Operating Characteristic (ROC) and the associated Area Under the Curve (AUC) are used to quantify the performance of the consistency and the GLR. Here, we have considered different situations. Indeed several SNR levels (from 20 dB to -15 dB) and different station geometries are used to represent the variability of IMS station configurations, varying from 4 sensors (IS46) to 10 sensors (IS37) represented in figure II.2.3. The LOC is also implemented to quantify the impact of this physical effect on both detectors with parameters of coherency loss of $\sigma_\theta = 5°$ and $\sigma_v = 15$ m/s. These parameters has been chosen to be in the high range of the values already measured as for example the Chelyabinsk meteor recorded at IS34 at the central frequency of 0.8 Hz [Green, 2015].
To produce statistics, samples of 1000 events under the H_0 hypothesis and samples of 2000 events under the H_1 hypothesis are constructed. To avoid bias effect under H_1, couples are uniformly and randomly distributed within (θ, v) $(0° - 360°) \times (300 - 800)$ m/s. Moreover, to compare the impact of the geometry on the detection, the same grid is applied (steps of 5° in azimuth and 20 m/s in trace velocity).

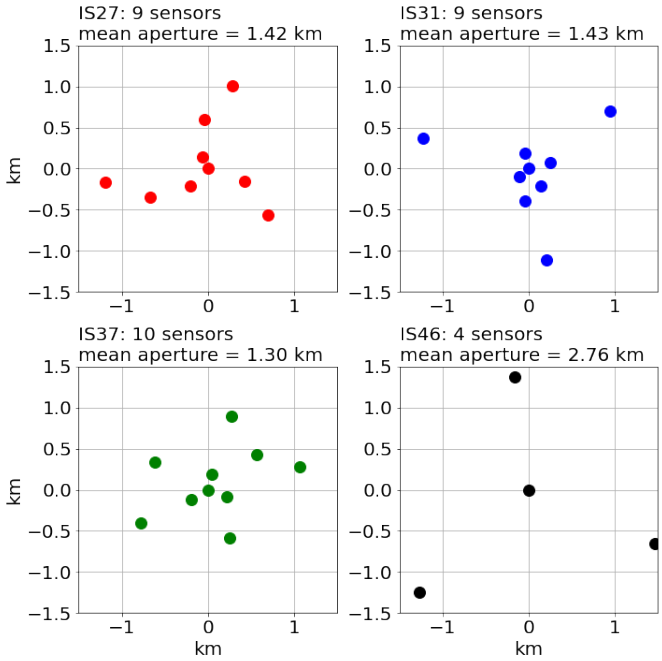

Figure II.2.3: IMS array configurations used to generate synthetic data (https://www.ctbto.org).

Without loss of coherency

Table II.2.1 indicates the EAUC values obtained using the consistency (in red) and the GLR (in blue) for different SNR ranging from -10 dB to 0 dB. Real wind noise extracted from windy records and different station geometries are considered. The arrays are chosen to reflect the variability in IMS station's geometry.
The first observation that can be made for both detectors is the decreasing of the EAUC when lowering SNR, increasing station aperture and decreasing number of sensors.

Table II.2.1: EAUC for different SNRs from -10 to 0 dB with real wind noise and different array configurations. In blue : EAUC of the GLR; in red : EAUC of the consistency.

Stations	M sensors	mean aperture	0 dB	-2 dB	-5 dB	-8 dB	-10 dB
IS27	9	1.42 km	1.00 1.00	1.00 0.95	1.00 0.72	0.91 0.55	0.69 0.51
IS31	9	1.43 km	1.00 0.99	1.00 0.92	1.00 0.67	0.92 0.56	0.73 0.53
IS37	10	1.30 km	1.00 1.00	1.00 0.96	1.00 0.74	0.95 0.58	0.77 0.53
IS46	4	2.76 km	0.98 0.89	0.93 0.71	0.69 0.57	0.52 0.51	0.50 0.48

For low SNR, the GLR performs better than the consistency. Averaging all geometries, the consistency's EAUC drops below 0.7 at around -5 dB whereas the GLR maintains a high EAUC. The GLR's EAUC drops below 0.7 at around -10 dB except for the 4-sensor station IS46 where the EAUC drops below 0.7 at -5 dB. As expected, for the both algorithms, the lowest EAUC are obtained with the 4-sensor, 2.76 km aperture array, demonstrating the importance of a sufficiently high density of sensors for signal detection, at least, for this frequency band. As a last observation, it can be seen that the choice of noise type does not significantly impact the detection (see Table II.2.2). Indeed, the results are very similar, although a slightly better result can be observed for the GLR at -10 dB for the first three stations and from -5 dB for IS46.
The figure II.2.4 shows the variations of EAUC for the consistency (i.e dotted lines) and the GLR (i.e solid lines) versus SNR for the four stations IS27, IS31, IS37 and IS46 with real wind noise. The effect of both the array aperture and SNR decay on the EAUC, but also the higher performance of the GLR relative to the consistency in all cases are confirmed. Finally, this figure allows us to verify that the

Table II.2.2: EAUC for different SNR from −10 dB to 0 dB with Gaussian white noise and different array configurations. In blue the EAUC of GLR; in red the EAUC of the consistency.

Stations	M sensors	mean aperture	0 dB	-2 dB	-5 dB	-8 dB	-10 dB
IS27	9	1.42 km	1.00 1.00	1.00 0.96	1.00 0.71	0.94 0.57	0.76 0.51
IS31	9	1.43 km	1.00 0.99	1.00 0.94	1.00 0.69	0.94 0.54	0.77 0.54
IS37	10	1.30 km	1.00 1.00	1.00 0.97	1.00 0.76	0.97 0.56	0.82 0.54
IS46	4	2.76 km	0.99 0.92	0.96 0.74	0.75 0.55	0.57 0.50	0.52 0.50

consistency has same results as the GLR for SNR above 0 dB.

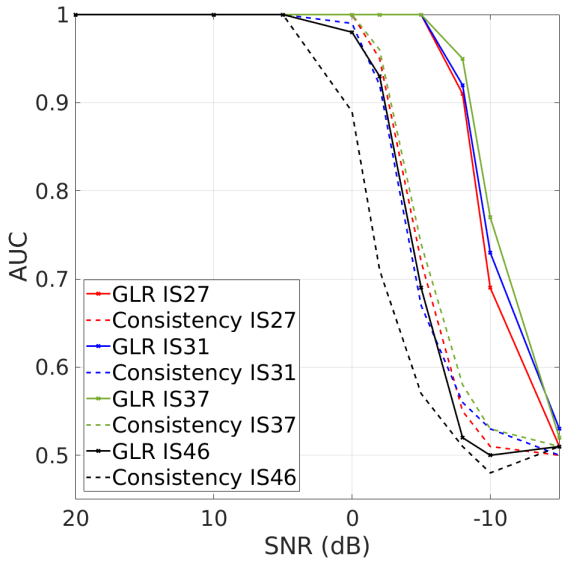

Figure II.2.4: EAUC as a function of the SNR for the consistency and the GLR with four different array geometries. The solid and dotted lines represent the EAUC for the GLR and the consistency, respectively.

With loss of coherency

To model the LOC, the slowness vector p is defined as a normally distributed random variable with mean $\overline{p}$ and covariance matrix $\mathbf{\Sigma}_p$ including the loss of coherency parameters (here of $\sigma_\theta = 5°$ and $\sigma_v = 15$ m/s) [Nouvellet et al., 2014]. As a reminder, the coherency between two sensors m and l is

$$Coh_{m,l}(f) = e^{-2\pi^2 f^2 (r_m - r_l)^T \mathbf{\Sigma}_p (r_m - r_l)} \tag{II.2.48}$$

Let $s(t)$ be a random source with zero mean and spectral density $C_{ss}(f) = \gamma_s$ constant for all the K frequencies. According to [Brillinger et al., 1982], for a stationary signal the distribution of the Fourier transform of $z(t)$ can be approximated for large amount of samples by a centred circular complex Gaussian distribution of covariance $\mathbf{W}_k$

$$\mathbf{W}_k = \gamma_s \mathbf{D}_k(\overline{p}) \mathbf{G}_k(\mathbf{\Sigma}_p) \mathbf{D}_k^H(\overline{p}) \tag{II.2.49}$$

Where $\mathbf{G}_k(\mathbf{\Sigma}_p)$ is a $M \times M$ matrix in which the element at the line m and column l is $Coh_{m,l}(f_k)$ and $\mathbf{D}_k(\overline{p})$ is the $M \times M$ diagonal matrix filled by the pure delays function of $\overline{p}$. Then the inverse Fourier transform of $\mathbf{W}_k^{-\frac{1}{2}} s_k$ allows us to obtain the signals $z(t)$ with the associated coherency loss.

Here again, the results show that the EAUC has the same trend as previously observed with the decreasing of the SNR (table II.2.3). However, it can be seen that the EAUC of the consistency is much

lower from 0 dB, reaching an EAUC of around 0.8 for stations with the highest number of sensors and the smallest aperture (i.e IS27, IS31 and IS37). Thus, the consistency becomes inefficient at around -5 dB. However, the GLR, at -5 dB reaches an EAUC of 0.8 being roughly that of the consistency at 0 dB. Thus, in summary, the GLR also performs better when the LOC effect is applied; the consistency seems to be more sensitive to this physical phenomenon. The impact of the LOC is a function of the mean aperture. Indeed the stations array with the higher EAUC are the stations with the highest number of sensors and the smallest aperture. In contrast, the array IS46 has a very low EAUC because of its wide mean aperture of 2.76 km. Thus, with the LOC the detection of events would be very degraded while both the GLR and the consistency are reliable without this effect (i.e EAUC of 0.98 and 0.89 for the GLR and consistency respectively, see table II.2.1).

Table II.2.3: EAUC for different SNRs from -10 to 0 dB with real wind noise, Loss Of Coherency (LOC) effect and different array configurations. In blue : EAUC of GLR; in red : EAUC of the consistency.

Stations	M sensors	mean aperture	0 dB	-2 dB	-5 dB	-8 dB	-10 dB
IS27	9	1.42 km	1.00 0.81	1.00 0.72	0.97 0.56	0.75 0.53	0.60 0.52
IS31	9	1.43 km	1.00 0.76	1.00 0.66	0.99 0.56	0.83 0.54	0.63 0.50
IS37	10	1.30 km	1.00 0.83	1.00 0.74	0.97 0.60	0.77 0.53	0.61 0.51
IS46	4	2.76 km	0.64 0.54	0.56 0.51	0.50 0.51	0.51 0.51	0.49 0.50

The difference of noise model suggests small differences, especially at very low SNR, as previously stated. Indeed an EAUC difference between 0.04 and 0.08 can be observed at -8dB and -10 dB.

Table II.2.4: EAUC for different SNRs from -10 to 0 dB with Gaussian white noise, Loss Of Coherency (LOC) effect and different array configurations. In blue : EAUC of GLR; in red : EAUC of the consistency.

Stations	M sensors	mean aperture	0 dB	-2 dB	-5 dB	-8 dB	-10 dB
IS27	9	1.42 km	1.00 0.81	1.00 0.72	0.99 0.57	0.81 0.53	0.65 0.51
IS31	9	1.43 km	1.00 0.77	1.00 0.67	1.00 0.56	0.87 0.52	0.71 0.50
IS37	10	1.30 km	1.00 0.82	1.00 0.75	0.98 0.57	0.81 0.52	0.65 0.51
IS46	4	2.76 km	0.72 0.53	0.65 0.50	0.54 0.52	0.52 0.51	0.50 0.51

The figures II.2.5 and II.2.6 are more visual representations of how the GLR is more robust to the LOC than the consistency. Indeed for the GLR the different curves are really close to each other, a little slope break can be observed around -8 dB for the GLR. However, for the consistency, the EAUC is lower from 20 dB where the noise is very low indicating a clear degradation of the detection due to the coherency loss. Here adding the progressivity should enhance the detection capability. The station IS46 is, as previously stated, the worst station due to the number of sensors and the large aperture. The station seems to be inefficient from around 0 dB for the GLR with an EAUC of 0.6, but with the consistency the station seems almost useless at 20 dB indicating a clear need of additional sensors.

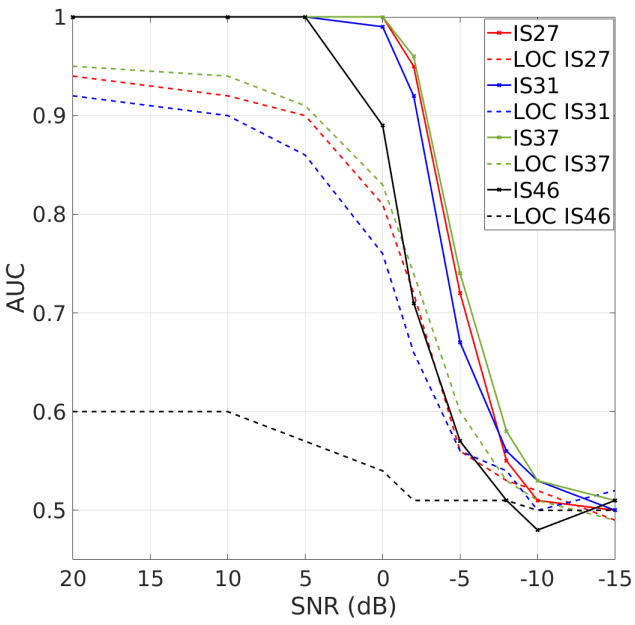

Figure II.2.5: EAUC as a function of the SNR for the consistency with four different array geometries. The solid and dotted lines represent the EAUC without and with Loss Of Coherency (LOC), respectively.

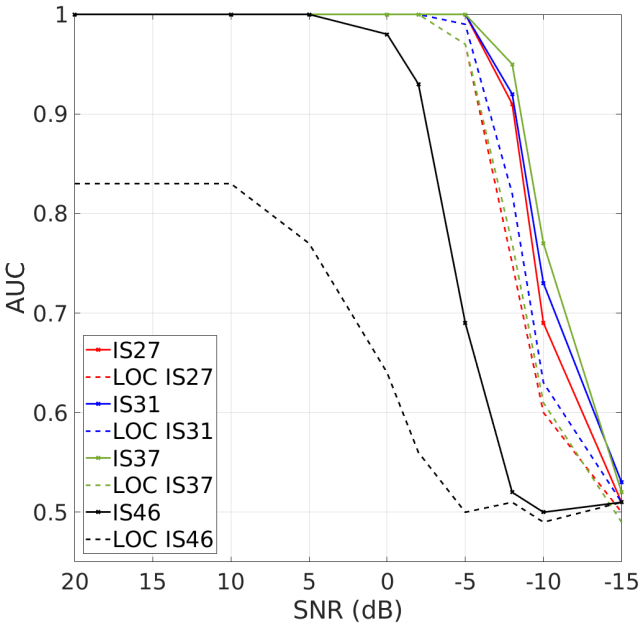

Figure II.2.6: EAUC as a function of the SNR for the GLR with four different array geometries. The solid and dotted lines represent the EAUC without and with Loss Of Coherency (LOC), respectively.

II.2.2.2 Estimation results

When an infrasound event is detected then the estimation of the back-azimuth and the trace velocity can be done. Here, we provide numerical results of the asymptotic standard deviations of these estimations derived from expressions (II.2.36) and (II.1.14). We also show numerical results of the SNR estimation. Finally, we use the expression (II.2.36) to evaluate how the performance of the estimator evolves with number of sensors and array aperture.

The figure II.2.7 illustrates the asymptotic covariance of both estimators (i.e MLE and TDOA) estimating the couple $(\hat{\theta}, \hat{v})$ for a SNR of 0 dB with the station of IS31. For MLE, values are in good agreement with the theoretical confidence ellipse at 95%. Only 1.5% of the estimated $(\hat{\theta}, \hat{v})$ couples are outside of the ellipse. For TDOA, however, we observe a large variance of the estimated parameters with 65.5% of values outside of the confidence ellipse associated with the MLE. It should be noted that, for the figure illustrating the distribution of $(\hat{\theta}, \hat{v})_{\text{TDOA}}$ (Figure II.2.7 at the right), we focus on a limited range of values for better readability. These results can be explained because TDOA is a low breakdown point number algorithm (i.e. a small number of outliers will biais the results), that is why the progressivity is added in PMCC for better results.

The figure II.2.8 shows the ratio of the standard deviations of the back-azimuth and the trace velocity derived from the TDOA approach with respect to the standard deviation of the back-azimuth and the trace velocity derived from the MLE as a function of the SNR. A ratio above 1 indicates that MLE has less variance than TDOA, particularly at low SNRs. It is worth noting that, from expressions (II.2.36) and (II.1.14), this ratio does not depend on the true DOA (i.e. they are averaged), nor the frequency band (i.e. the bandwidth). It can be observed, that even at high SNR, the ratio is not 1.00 but 1.25 due to the fact that the TDOA is not asymptotically equal to the MLE.

The Figure II.2.9 shows the SNR estimation for different SNR values at IS31 using the MLE and the TDOA estimators. The back-azimuth and trace velocity are randomly distributed in order to miti-

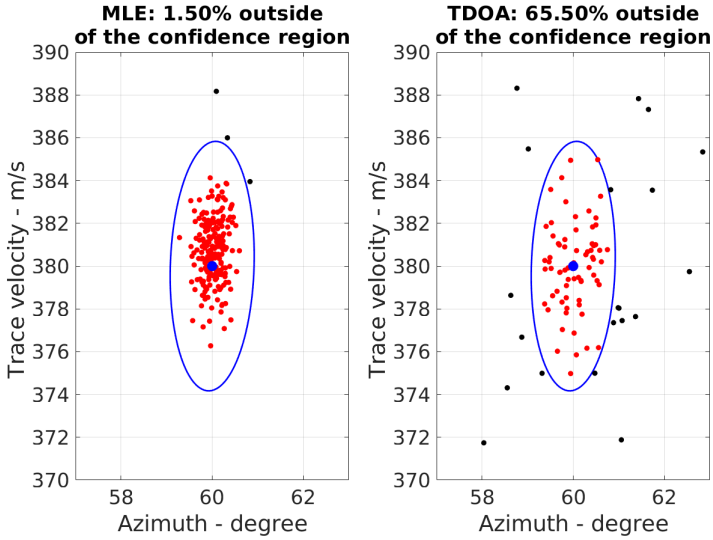

Figure II.2.7: Zoom around the distribution of the estimated couple $(\hat{\theta}, \hat{v})_{\text{MLE}}$ (left) derived from expression (II.2.32) and $(\hat{\theta}, \hat{v})_{\text{TDOA}}$ (right) derived from the expression II.1.6 for 200 simulations in the frequency band $[0.8 - 1]$ Hz.

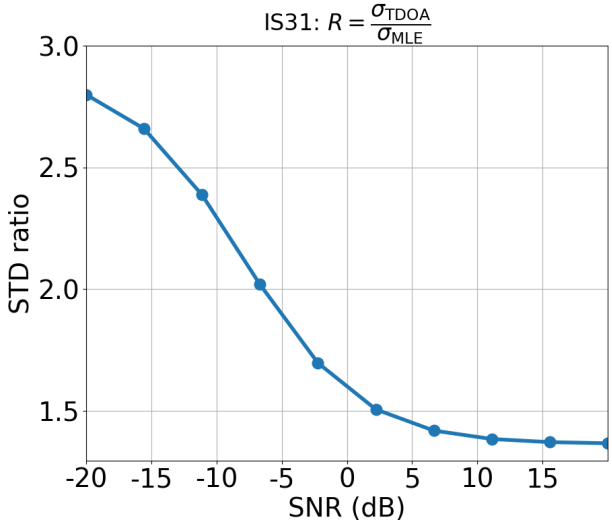

Figure II.2.8: Ratio between standard deviation estimates of back-azimuth/trace velocity using TDOA and MLE as a function of the SNR for IS31.

gate the orientation of the station. The results are consistent with the true solutions for all SNR values for MLE and can be used to calculate the asymptotic covariance matrix of $(\hat{\theta}_{\text{MLE}}, \hat{v}_{\text{MLE}})$. The MLE estimator given by equation (II.2.33) performs better than TDOA. Indeed, TDOA seems to systematically overestimate the SNR by one order of magnitude.

The overestimation of the SNR by the TDOA is confirmed by the Root Mean Square (RMS) power amplitude of the SOI estimation illustrated on the figure II.2.10. Indeed 20 RMS values between -10 dB and 30 dB are estimated. For each value, a mean of 100 estimations is made for statistics. The theoretical value RMS* is represented by the black dotted line whose expression is $RMS^\star = 10^{\frac{SNR^\star}{20}}\sigma_\star^2$. The parameter $\sigma_\star$ is fixed to one during the simulation. Then the RMS parameter is estimated by PMCC and MCML thanks to the expressions II.1.10 and II.2.34 respectively. The two curves represent the means of the 100 estimations and they are bounded by $\pm 2\sigma$. It can be seen that above 10 dB the estimations of the both algorithms are very similar but progressively with decreasing SNR while MCML asymptotically

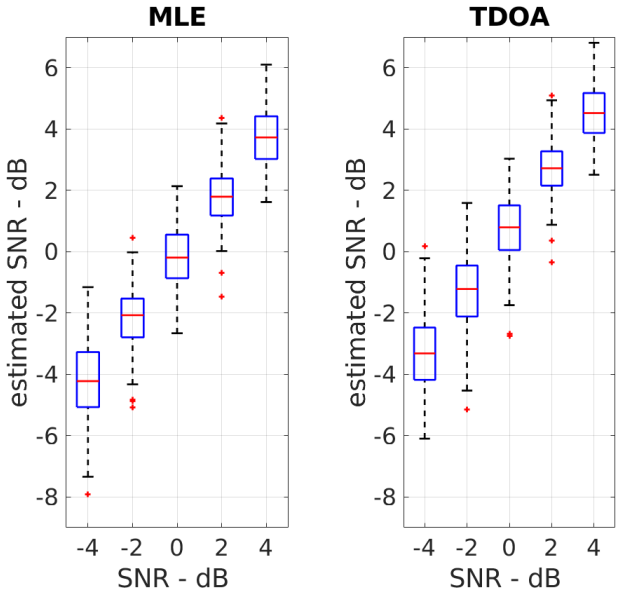

Figure II.2.9: Boxplots for different estimates of the SNR (200 simulations) for IS31 (Figure II.2.3). Left: MLE estimation; right: TDOA estimation.

tends to the true value with increasing standard deviation, the PMCC estimation tends to the value of the noise parameter $\sigma_\star$, thus overestimating the RMS amplitude of the SOI.

The figure II.2.11 shows the log-scaled standard deviation of the back-azimuth (top) and the trace

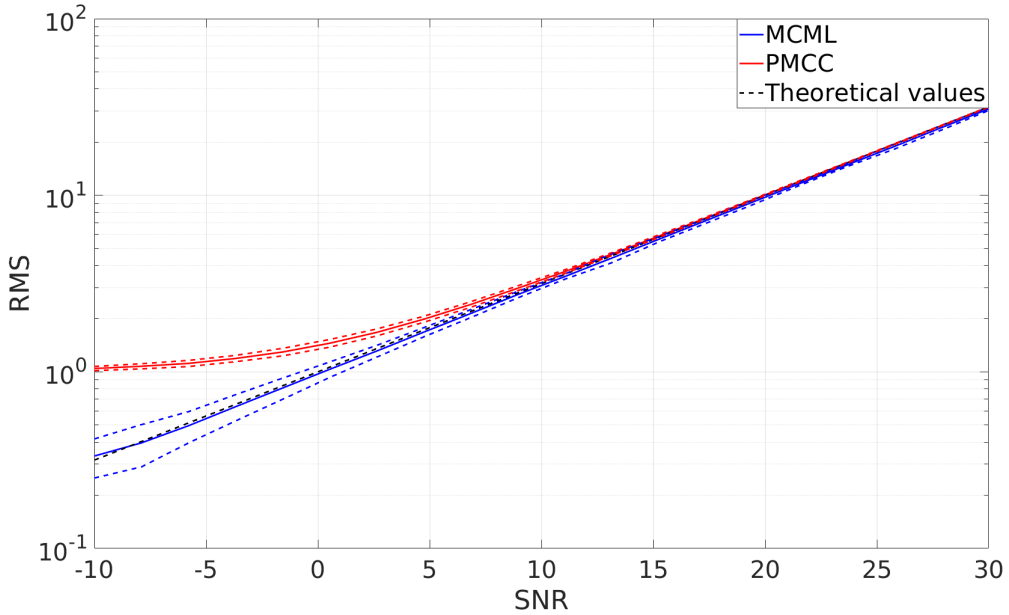

Figure II.2.10: RMS amplitude estimation for PMCC in red and MCML in blue. The theoretical values are represented by the black dotted line. The blue and red dotted line represent the maximum deviation from the average of $\pm 2\sigma$. It can be seen that the estimation of MCML asymptotically tends to the true value whereas the estimation of PMCC asymptotically tends to the noise parameter $\sigma_\star$.

velocity (bottom) according to the station radius and the number of sensors at an SNR of 0 dB. Indeed the red, green, blue and black curves correspond respectively to a radius of 100 m, 200 m, 400 m and 1000 m. It becomes evident that increasing the size of the array aperture results in a decrease in errors.

Furthermore, the errors do not decrease significantly when more than twelve sensors are added. These results are taken into account when calculating the back-azimuth and trace velocity grid resolutions of MCML as explained in the subsection II.2.1.4.

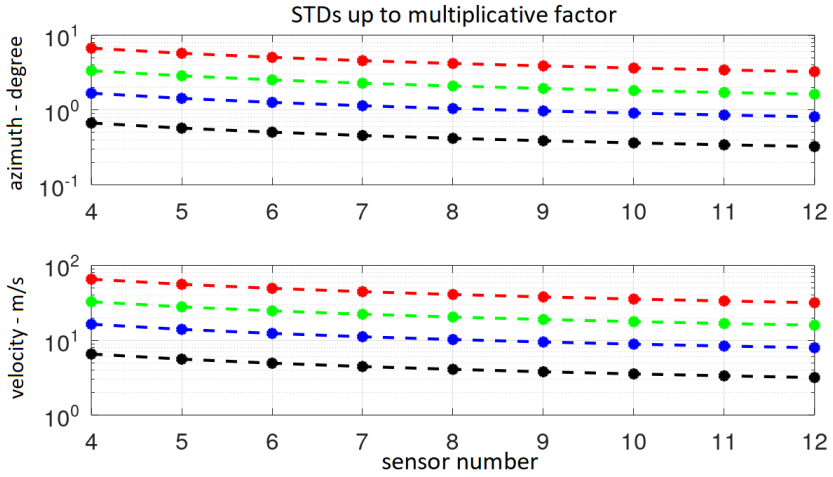

Figure II.2.11: Standard deviations of the back-azimuth and the trace velocity as a function of the number of sensors for different apertures and an SNR of 0 dB. The red, green, blue and black curves correspond, respectively, to a radius of 100 m, 200 m, 400 m and 1000 m. For other SNRs, values are to be divided by the square root of the SNR.

II.2.3 Revisiting real data from the IMS (infrasound) network

After evaluating the detectors and estimators using a controlled synthetic dataset of noise and SOI sequences, we compare the performance of MCML (which includes MLE with GLR and the associated $p-$value as detection criteria) and PMCC (which includes TDOA as estimator and consistency as detector with progressivity [Cansi, 1995]) on real data. This evaluation includes the post-processing in family described in the subsection II.1.1.4 that aims at clustering individual detections (pixels) in the time-frequency domain into homogeneous groups (families) to be associated with infrasound arrivals from events [Brachet et al., 2010]. One day of data at the station IS31 (array configuration shown in figure II.2.3) is processed (figure II.2.12 and figure II.2.13). Signals and detections associated with the Beirut explosion of August 2020 recorded at IS42 (Azores) and IS48 (Tunisia), a low and high SNR condition, are shown in Figure II.2.15 and Figure II.2.16, respectively.

II.2.3.1 A typical soundscape at IS31

Figure II.2.12 shows the detections at IS31 on 27 November 2021 in the frequency band $[0.1 - 4]$ Hz made by PMCC and MCML. Each coloured pixel represents a detection associated to an estimated back-azimuth or trace velocity for a given time-frequency cell. The wind speed is recorded at the central element and is illustrated by the superimposed black curve. Using MCML, five different sources are clearly identified and are characterised by different back azimuths. Above 0.7 Hz, quasi-permanent sources dominate at ∼41° and 56° (in orange-yellow). The associated trace velocities around 320-330 m/s are in accordance with the temperature ranging from -7°C to -15°C during this day. These detections are related with the Badamsha wind farms located at around ∼20 km away from the station. For these detections, PMCC provides fewer pixels than MCML probably because of interfering sources making it harder to correlate. Another permanent source detected around 312° below 0.7 Hz corresponds to the North Atlantic microbaroms [Smirnov et al., 2021] with a higher trace velocity than the Badamsha source explained by an incidence angle of 20-30° typical of stratospheric arrivals. The number of pixels reduces from 06:00 to 08:00 UTC due to the increase of the wind speed to 8 m/s. Indeed, PMCC does not provide both microbaroms and wind farm detections, whereas MCML captures both sources. In such windy conditions, MCML detections can be explained by the performance of GLR in low SNR situations and snow cover effects which reduce the wind generated noise. Finally, a new source is detected from 20:00 to 22:00 UTC using MCML, with continuous detections, whereas PMCC provides only a weak number of pixels. This source is detected at around 264° and is likely linked to a stone crusher (A. Smirnov, personal communication).

Between 07:30 UTC and 12:30 UTC, a total of six events at around 256° are detected both by PMCC and MCML (Figure II.2.13). These sources are most likely linked to quarry blasts. The increase of the trace velocity (from 340 to 380 m/s) is evident for each event and indicates the appearance of six individual events. This increase is likely explained by propagation effects as investigated by Vergoz et al. [2019]. The wave parameters are well constrained by both PMCC and MCML. However, compared to PMCC, MCML captures more pixels of the other interfering sources (i.e wind farms, stone crusher and microbarom).

The figure II.2.14 illustrates the log-scaled polar histograms of PMCC and MCML pixels and indicates the counts of the main sources identified. It can be noticed that the number of MCML pixels linked to the quarry blasts are superior by a factor 1.65 to PMCC (MCML : $\sim$ 2080 pixels, PMCC: $\sim$ 1260 pixels). However, for interfering sources, such as the Badamsha wind farms, North Atlantic microbaroms and especially the stone crusher, better detection by MCML are observed by filling the time-frequency domain. Indeed this algorithm has almost twice as many pixels for the microbaroms, between two and three times as many pixels for the wind farms and eight times more for the stone crusher. The GLR performs better than the consistency, derived from TDOA even with the progressivity. One explanation is that the sensor location is an integral part of the likelihood function whereas it is not involved in the TDOA estimation (i.e. it is however involved in the progressivity).

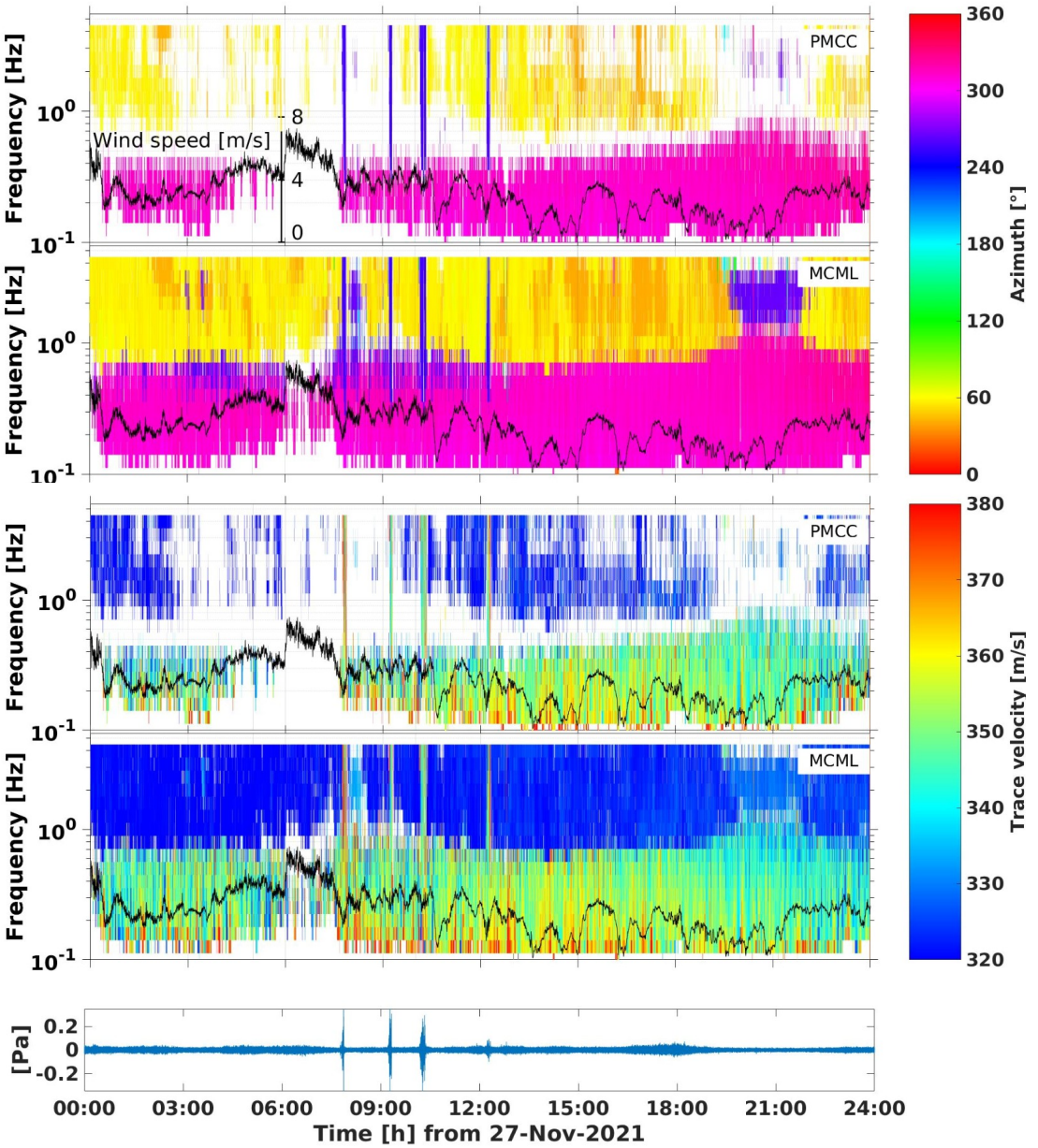

Figure II.2.12: Results of PMCC and MCML processing at IS31 on November 27, 2021. 16 adjacent frequency bands are log-scaled between 0.1 and 4 Hz. The two upper graphs show the back-azimuth detections using PMCC and MCML after applying the grouping post-processing procedure explained in subsection II.1.1.4. The two graphs below display the trace velocity detections using PMCC and MCML. The black curve shows the wind speed variation recorded at the central element of the station (see top plot for an indication on the wind speed scale). The last plot shows the waveform recorded at the central element band-pass filtered from 1 to 4 Hz.

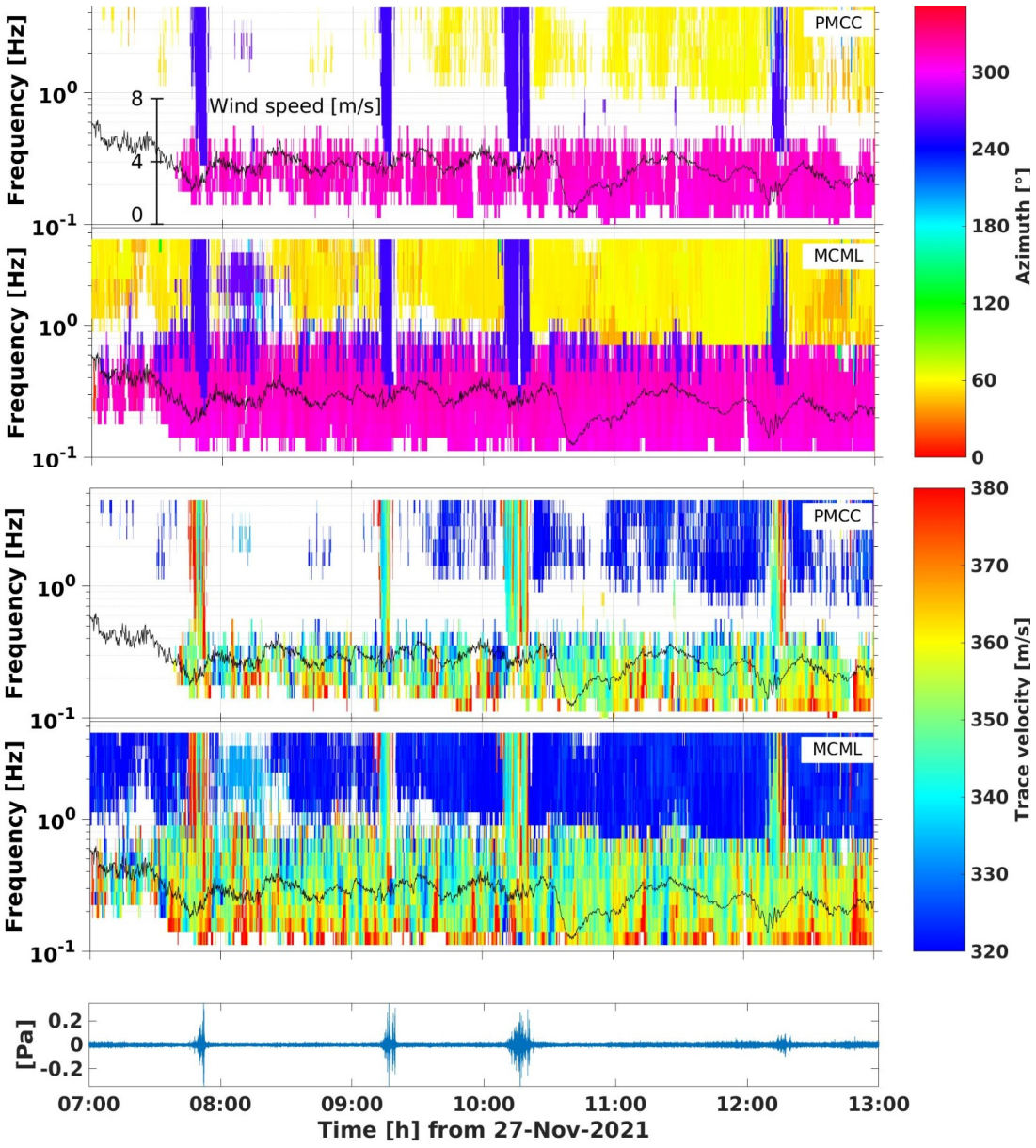

Figure II.2.13: PMCC and MCML quarry shot detections at IS31, which characterise the typical soundscape of the station. The black curve shows the wind speed variation recorded at the central element of the station as in Figure II.2.12. Back-azimuth and trace velocity estimates are presented as for Figure II.2.12.

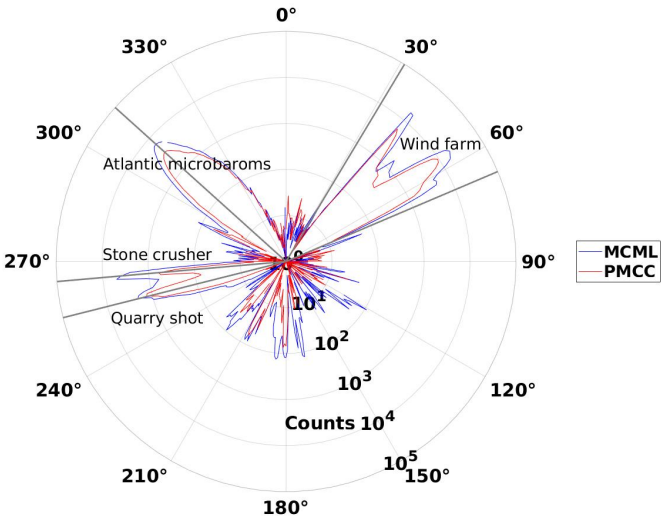

Figure II.2.14: Polar histograms of PMCC and MCML detections at IS31 on November 27, 2021 in red and blue, respectively. Counts are in logarithmic scale. Gray lines represents the DOA of sources discussed.

II.2.3.2 The Beirut explosion recorded at IS48 and IS42

Figures II.2.15 and II.2.16 show the accidental explosion that struck the city of Beirut, Lebanon, on August 4, 2020 observed at the stations IS48 (Tunisia, 2455 km) and IS42 (Azores, 5431 km) [Pilger et al., 2021a] and processed by PMCC and MCML. At IS48, a clear feature of the records is the signal separation between consecutive arrivals associated to multiple stratospheric propagation paths from the source to the receiver. An increase of the trace velocity (from 340 to $\sim$ 370 m/s) is noticed for the first arrivals and can be explained by refraction in the stratosphere (40-50 km altitude) which affects the incidence angle of the ray paths. For many arrivals, the SNR is large enough ($>$ 10 dB) to allow clear detection for both PMCC and MCML algorithms. MCML however, detects additional pixels at lower frequencies (below 0.5 Hz) where the SNR is lower due to the increase of the background noise in moderate wind noise conditions (gusts reach 5 m/s at most) [Marty, 2019]. From this station, the true DOA of Beirut is around 87.4°. The mean DOA estimates obtained using MCML and PMCC between 17h20 and 17h25 UTC at frequencies between 0.4 Hz and 1.4 Hz are 88.4 $\pm$ 0.4° and 88.4 $\pm$ 0.5°, respectively. The difference between the DOA estimated and the true DOA may be partly explained by uncorrected wind effect along the propagation path [Pilger et al., 2021a].

At IS42 however, wind noise is moderate to high, with a maximum of 5 m/s due to the island environment. In such degraded observational conditions, only few PMCC pixels can be linked to the event because of the heavy interaction of the incoherent wind noise with the SOI. On the other hand, MCML provides a long duration detection with homogeneous pixel families. From this station the true DOA of Beirut is around 75.0°. The mean DOA estimation obtained using MCML and PMCC between 20h20 and 20h25 UTC are 81.0 $\pm$ 1.6° and 80.7 $\pm$ 1.6° respectively. The trace velocity (340-370 m/s) and arrival times of these detections are suitable with long-range propagation of stratospheric phases explained by prevailing easterly stratospheric winds [Pilger et al., 2021a].

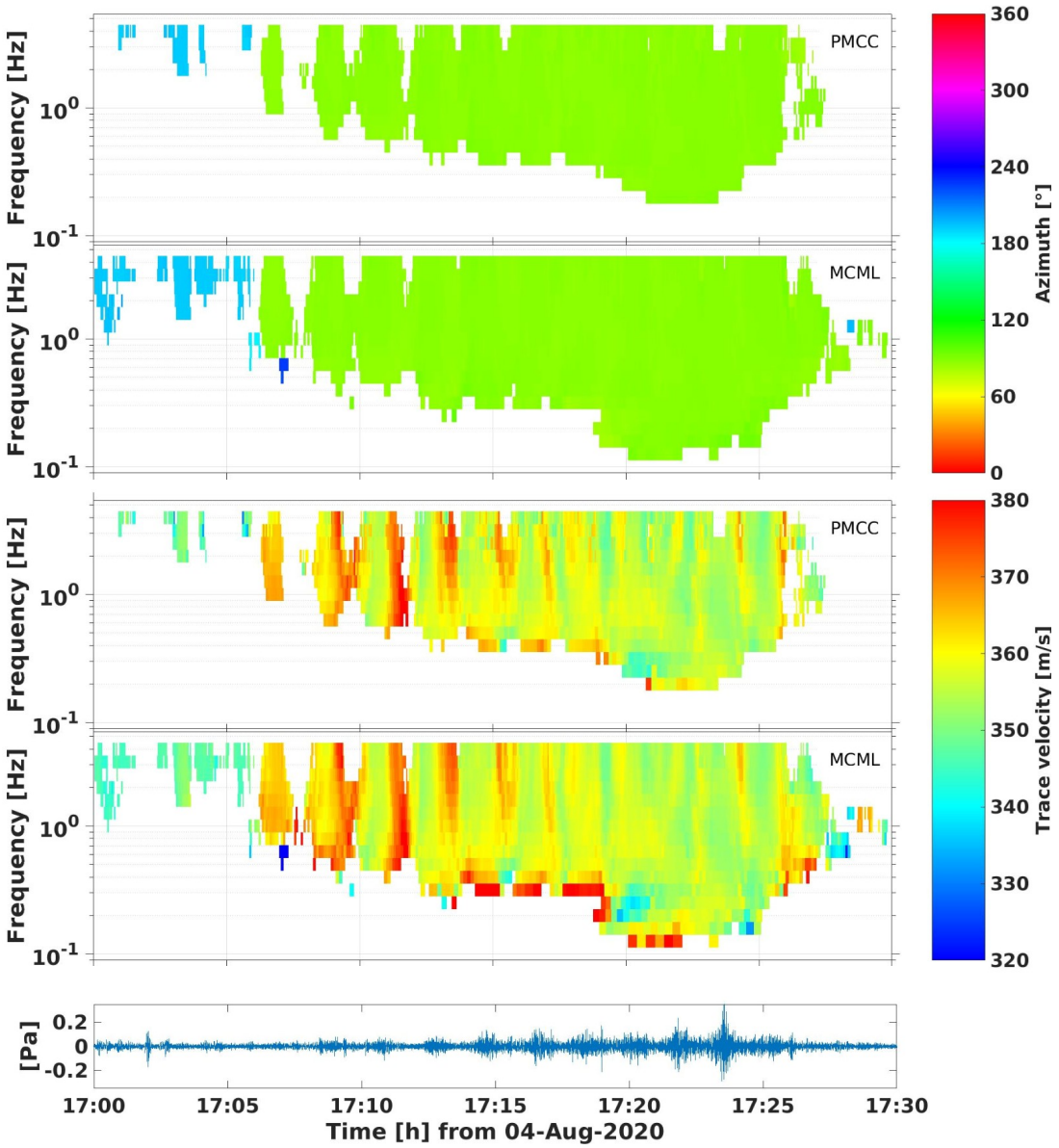

Figure II.2.15: PMCC and MCML detections at IS48 (Tunisia, 2455 km) of the Beirut explosion on August 4, 2020. The different arrivals are detected by PMCC and MCML but the latter provides additional pixels at lower frequency. The blue curve shows the waveform recorded at the central element band-pass filtered from 1 to 4 Hz.

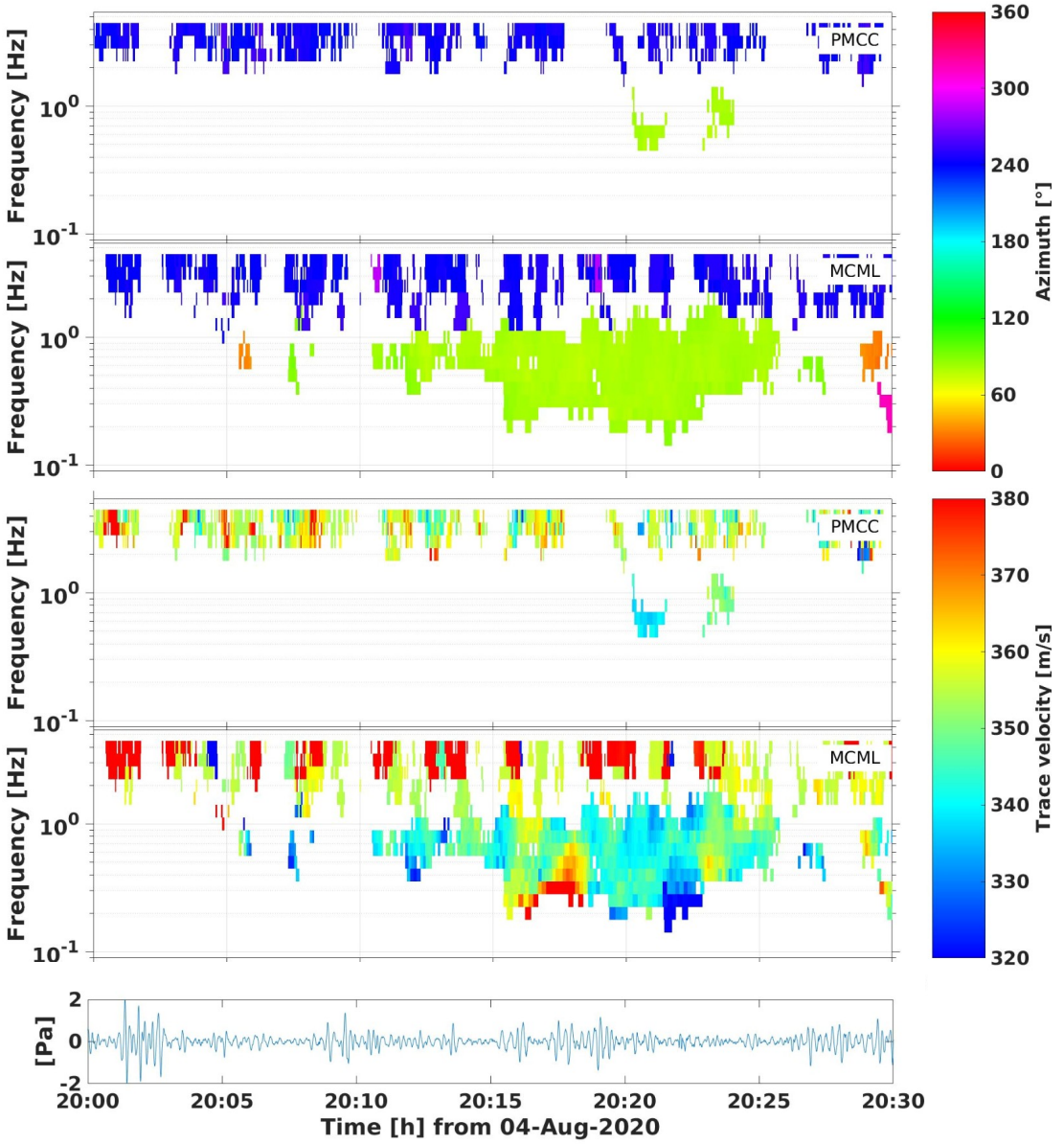

Figure II.2.16: PMCC and MCML detections at IS42 (Azores, 5431 km) of the Beirut explosion on August 4, 2020. The blue curve shows the waveform recorded at the central element band-pass filtered from 0.2 to 1 Hz. The event is better characterised by MCML with long lasting homogeneous pixels.

II.2.4 The use of MCML on seismic data, the example of Le Teil earthquake

The novel method was also used on seismic data in order to compare the ability of MCML to PMCC on a technology other than infrasound. The example used here is the Le Teil earthquake recorded at the LSBB (https://lsbb.cnrs.fr) with the four sensors on the top of the hill. This event occurred in close vicinity of Le Teil on 11 November 2019 at 10:52 UTC (figure II.2.17). This event greatly damaged the epicentre's surroundings (intensity of VII and VIII EMS98) with an associated moment magnitude of 4.8–4.9 [Vallage et al., 2021]. This is the largest event recorded in the last 16 years in metropolitan France that has been detected and localised, with a local magnitude estimated by 145 stations from national and international networks. This earthquake was provoked by the La Rouvière fault belonging to the Cevennes fault system [Causse et al., 2021]. The main objective here is to estimate, as well as possible, the different wavefront parameters in order to characterise the wave propagation and their source. This is thus done by PMCC and then MCML. The figure II.2.18 illustrates the detections done by PMCC on 11 November 2019 between 10:45 and 11:15 UTC. The P and S waves of the event can be detected as early as 10:53 UTC with associated apparent velocity of around 7.4 ± 0.2 km/s and 3.8 ± 0.2 km/s. The measured back azimuths are 297 ± 1.9° and 302 ± 7.0°, while the true back azimuth is around 315° indicating a small deviation of the wavefront. The signal is then followed by a seismic coda caused by dispersion between the source and the receiver with angle ranging between 240° and 300°. Those secondary seismic arrivals are interfering with a permanent source coming from 160-180° which affect the PMCC detections. The figure II.2.19 shows the event in the same context as previously but processed by MCML. The P and S waves of the event are estimated with a trace velocity of 7.53 km/s ± 0.7 and 3.4 ± 0.4 km/s, respectively with back azimuth of 298 ± 3.8° and 301 ± 2.8. The global detections of the body waves from MCML are similar to PMCC with the same directions of arrival and trace velocities indicating a deviation of the true DOA (315°). Fewer detections can be seen on MCML compared to PMCC at high frequency, due to the use of the progressivity by PMCC. Indeed the latter only use three sensors for a large amount of the estimation above 1 Hz. Thus, this is an advantage for PMCC. However, it seems that the estimations in the coda show better results with MCML due to the more continuous grouping of pixels suitable for analysis. Indeed, the estimation of the coda can be compared thanks to figures II.2.20 and II.2.21.

It is worth noting than PMCC has more detections of the coda waves than MCML due to the progressivity of PMCC, which detects high frequency content thanks to a sub-array of three sensors but with degraded estimation. The detection of PMCC are, however, isolated and not continuous as for the MCML which provides continuous detections until 2.5 Hz related to the aperture of the used four sensors station. To characterise the coda, we chose detections above 1 Hz to avoid, as much as possible, the permanent source at low frequency and at around 160°. The detections with apparent velocities above 20 km/s are also removed because they are inconsistent with real values. PMCC detections are plotted in the polar histogram II.2.22 on the left and the MCML detections are plotted on the right. The global distribution of the detections of the coda are in the range 240°-300° for the both algorithms, with more detections by PMCC (i.e of the coda and permanent source) as previously stated. This deviation of the coda back azimuth could be explained by a strong scattering of the seismic waves on the heterogeneities of the Rhone's sedimentary basin. The important role of the scattering in the coda late arrivals is also supported by the lower deviation observed for the direct P and S arrivals. The array processing analysis of the Le Teil event, seems to reveal two kinds of waves deviations: a systematic one related to the regional propagation properties of the seismic rays and a second stronger and more random associated with the coda waves. The figure II.2.23 shows the dispersion curves for the both algorithms where the left plot is the PMCC one while the right plot is the dispersion curve of MCML. They show the mean of the apparent velocities as a function of the frequency. The probability density distribution of the detection in the frequency-velocity domain is superimposed on the graph. Both curves show a decreasing velocity with increasing frequency. This systematic observation of a wave dispersion with frequency, combined with an estimated apparent velocity ranging between 2.5 km/s and 4 km/s, are in agreement with the main properties expected for the seismic surface waves travelling along the earth surface (i.e. horizontally). Moreover, it is worth noting that the distribution of the velocities in MCML is centred with a small error around the expected values for surface waves at the LSBB where the S wave velocity is around 2.5-3.5

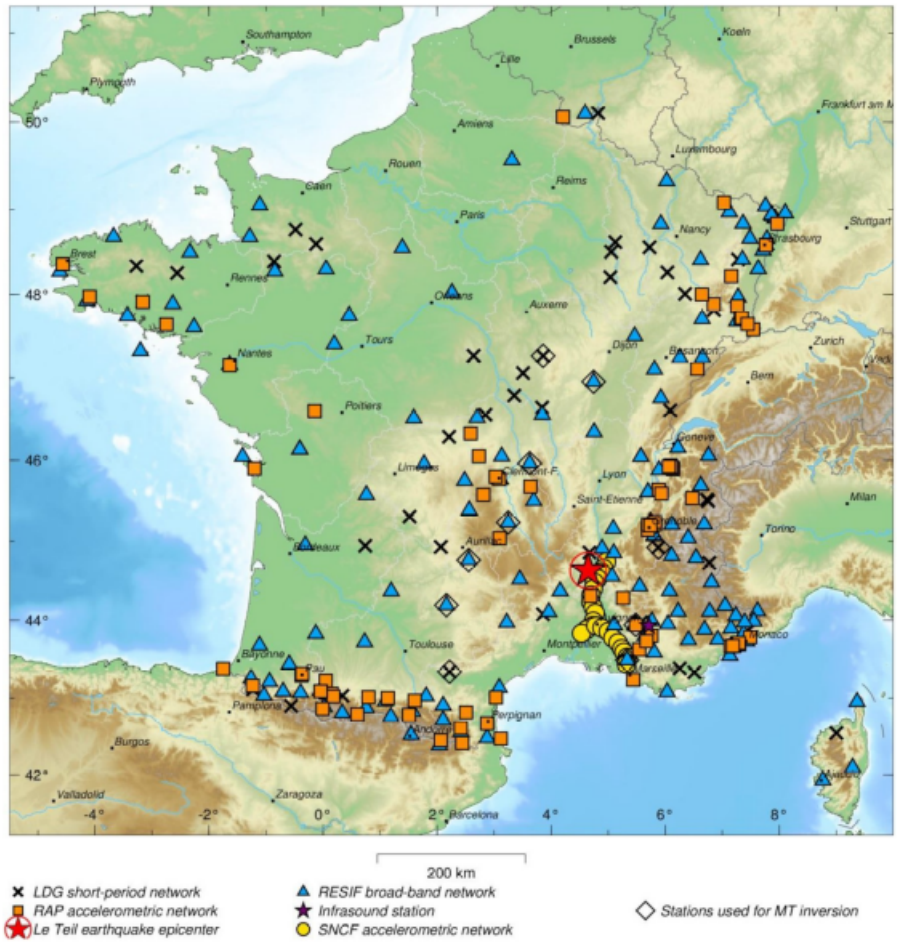

Figure II.2.17: Geophysical networks in France used to characterise the Le Teil earthquake. Extracted from Vallage et al. [2021].

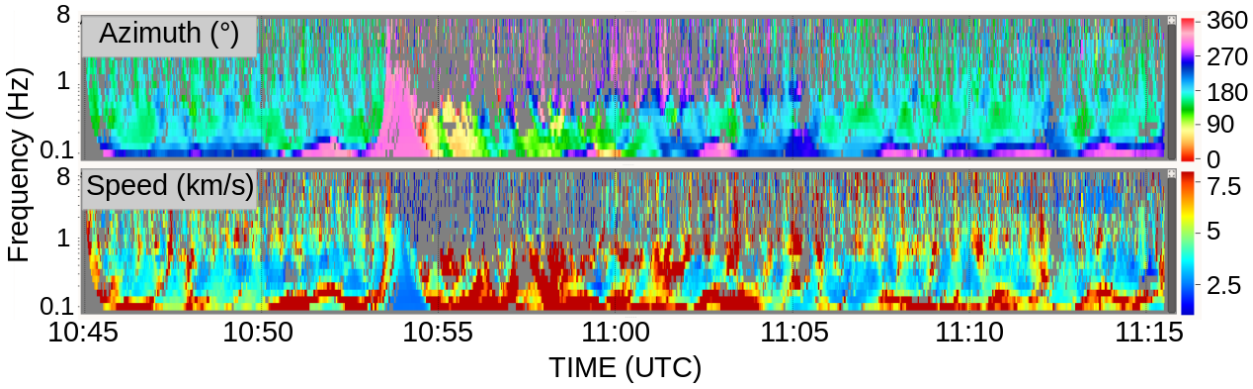

Figure II.2.18: Detections of the Le Teil event recorded by the LSBB and processed by PMCC between 10h45 UTC and 11h15 UTC. The upper plot represents the back azimuth estimates while the lower plot represents the apparent velocity estimates as a function of the time and the frequency.

km/s, while a large variance and a systematic bias towards higher velocities (>4 km/s) are calculated by the PMCC algorithm. Thus, even if the detections of PMCC and MCML are in accordance about the azimuth parameter, the velocity estimation is closer to the expected wave propagation model with the novel MCML method.

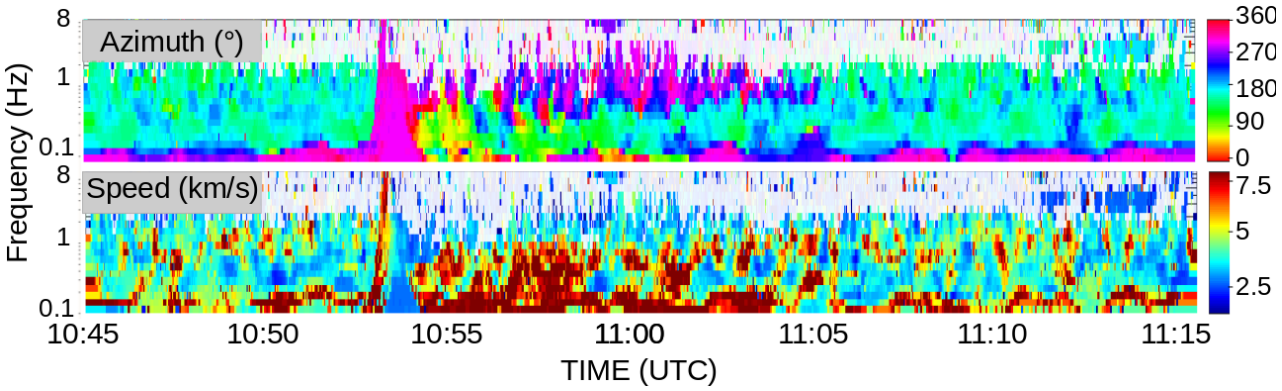

Figure II.2.19: Detections of the Le Teil event recorded by the LSBB and processed by MCML between 10h45 UTC and 11h15 UTC. The upper plot represents the back azimuth estimates while the lower plot represents the apparent velocity estimates as a function of the time and the frequency.

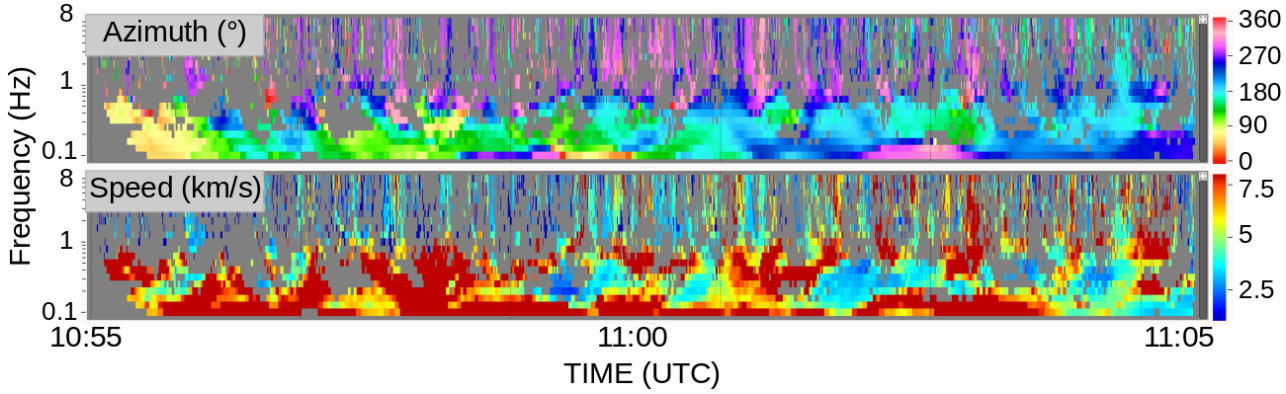

Figure II.2.20: Detections of the coda of the Le Teil event recorded by the LSBB and processed by MCML between 10h55 UTC and 11h05 UTC. The upper plot represents the back azimuth estimates while the lower plot represents the apparent velocity estimates as a function of the time and the frequency.

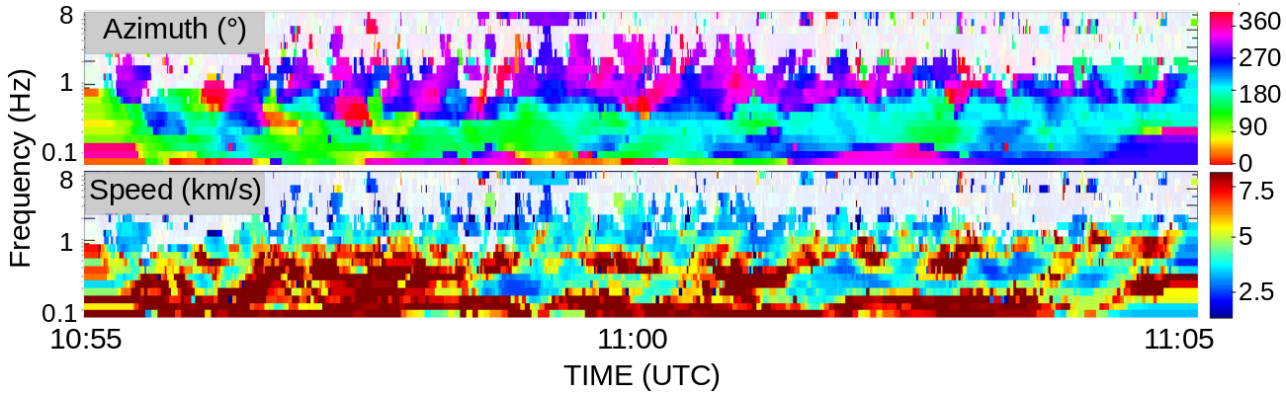

Figure II.2.21: Detections of the coda of the Le Teil event recorded by the LSBB and processed by MCML between 10h55 UTC and 11h05 UTC. The upper plot represents the back azimuth estimates while the lower plot represents the apparent velocity estimates as a function of the time and the frequency.

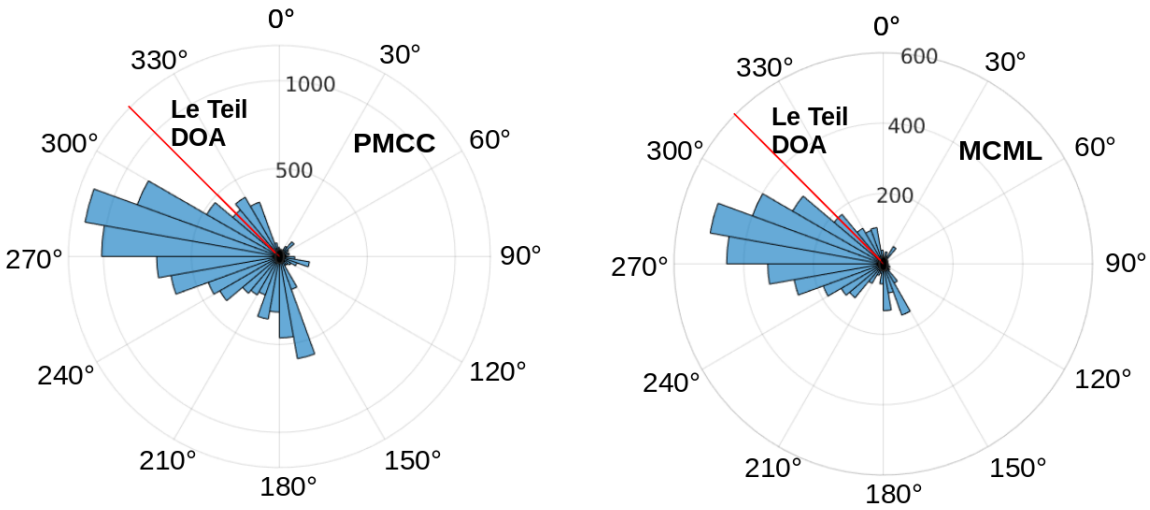

Figure II.2.22: Polar histogram of the azimuth detections by PMCC on the left and MCML on the right. The real DOA of Le Teil is plotted at 315° (red line).

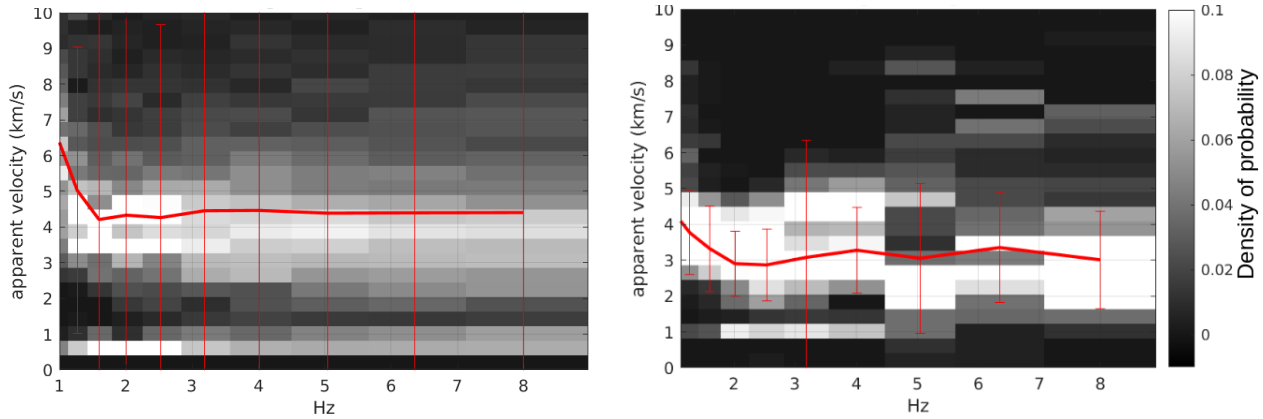

Figure II.2.23: Average dispersion curve with error bars (in red) of the estimated velocities as a function of the frequency by PMCC on the left and MCML on the right. The background colour displays the detection probability density as a function of the frequency and apparent velocity.

II.2.5 Discussion and conclusion

The Multi-Channel Maximum Likelihood (MCML) algorithm was developed to detect and estimate wave parameters of infrasound planar wavefronts crossing an array of infrasound sensors. It is based on the maximum likelihood approach and calculates the SNR and asymptotic errors of the wave parameters using the likelihood expression of MLE. The $p-$value, under the noise-only hypothesis, is derived from the closed form expression of the asymptotic distribution of the GLR. In contrast to consistency, the p-value enables an objective decision to be made based on the probability of a false alarm, depending on the monitoring objectives. The Multi-Channel Maximum Likelihood (MCML) algorithm is implemented in the PMCC time-frequency domain framework, enabling the detection of overlapping signals from natural or anthropogenic sources in the frequency band of interest.

This study compares MLE estimations to TDOA results using controlled synthetic SOI and noise sequences. The corresponding detectors are compared in terms of ROC curves and EAUC. The comparisons show that MCML outperforms the state-of-the-art multi-channel algorithm in terms of detection probability and false alarm rate, especially at low SNR values. The performance of the grid-search approach contributes to its robustness, which minimises the risk of outliers (biased or false detections) resulting from non-optimal situations such as anisotropic array geometry, low SNR, loss of coherency. Additionally, the sensor location is an integral part of the likelihood function.

The detection and estimation capabilities of MCML and PMCC were compared through real case analyses using different array geometries with ground truth informations. Raw pressure data in the $[0.1 - 4]\ Hz$ band was processed, and the MCML algorithm yielded improved detection results in low SNR conditions, particularly when multiple signals interfere. This situation is evident in the lower part of the frequency domain where the SNR decreases. According to [Pilger et al., 2021a], MCML detections could offer further constraints for estimating the yield of the Beirut explosion. Additionally, they are of particular interest in using remote observations to characterise weaker energy, low SNR explosive sources. An example of use on seismic data showed how the novel method can improve velocity estimation needed to validate layer models.

The multi-channels (sensors and frequency bands) and grid search approach already allow the MCML code to be efficiently parallelised, taking advantage of multiprocessor environments. Currently, one day of signals recorded at a 10-element array, sampled at 20 Hz, can be processed in around 10 minutes using a DELL Precision 7920 Tower workstation with 40 cores allowing for real time processing. Additional studies are, however, needed to optimise the algorithm in order to further reduce its computational cost because PMCC is still five to ten times faster than MCML. Other studies are needed to evaluate MCML on various array configurations and a multi-year dataset [Ceranna et al., 2019]. Finally, it would be interesting to test this new method on more seismic data or hydroacoustic data.

Conclusion (in english)

This section presents two methods developed by the CEA, one based on cross-correlation of sensors pairs and the other on the likelihood method. The first one, developed in the 1990s, called PMCC, demonstrated its robustness within the framework of the CTBTO mission. Indeed, PMCC is capable of identifying infrasound arrivals generated by events of interest such as the Amatrice earthquake or the chemical explosion in Beirut thousands of kilometres away from the source. On the other hand, by highlighting errors in detections, particularly when recording conditions are degraded (low SNR or interference of the sources), a new algorithm turns out to be necessary. Thus, in collaboration with the IMT, the CEA has developed MCML, which shows more numerous detections and build more continuous events in time and frequency, both with infrasonic and seismic technology. Furthermore, MCML has been optimised for real-time computation necessary for operational use. Its use has shown that the sources interfered with each other simultaneously in the same frequency. An extension of MCML is developed for multisource use and compared to the state-of-the-art described in the following section.

Conclusion (en français)

Cette partie présente deux méthodes développées par le CEA, l'une basée sur la corrélation croisée des paires de capteurs et l'autre sur la méthode de vraisemblance. La première, développée dans les années 1995, appelée PMCC a montré sa robustesse dans le cadre de la mission de l'OTICE. En effet, PMCC est capable d'identifier des arrivées infrasons générées par des évènements d'intérêt comme le séisme d'Amatrice ou encore l'explosion chimique à Beyrouth à des milliers de kilomètres de la source. En revanche, des erreurs de détections, particulièrement lorsque les conditions d'enregistrement sont dégradées (SNR bas ou interférences de sources), montre qu'un nouvel algorithme s'avère nécessaire. Ainsi en collaboration avec l'IMT, le CEA a développé MCML, qui montre des détections plus nombreuses et construisant des évènements plus continus en temps et en fréquence pour les technologies sismique et infrason. De plus, MCML a été optimisé pour un calcul en temps réel nécessaire à une utilisation opérationnelle. Son utilisation a démontré que des sources interféraient entre elles simultanément à une même fréquence. Une extension de MCML est développé pour une utilisation multisource et comparé à l'état de l'art décrit dans la partie suivante.

Part III

Multisource state-of-the-art methods

Abstract

The significant increase in the number of detections by MCML shows more than ever that the sources overlap both in time and frequency. Thus, the segmentation in the time-frequency domain is not sufficient to separate the signals of interest. That is why it is necessary to study state-of-the-art algorithms to calculate multiple wave vector simultaneously and to identify those that are best suited to address our problem.

Several approaches are considered as subspace decomposition methods that separate the characteristics of noise and signal from the covariance or spectral density matrix of the signals. Other approaches based on energy calculation according to the direction of arrival are described as the Frequency-Wavenumber (F-K) spectrum, the Capon spectrum relying on spatial filtering of energy, or even time-domain beamforming like FTBeam. Statistical methods are also studied, among which are Fisher statistics. This method is sometimes combined with other approaches, as it is the case with one of the implementations of CLEAN [den Ouden et al., 2020] in which the Capon method is more robust with Fisher statistics. Finally, the last type of approach studied is the robust regression. Indeed, PMCC uses TDOA as an estimator, but it is sensitive to outliers, whereas the techniques developed here are designed to reduce these biases.

Résumé

La hausse importante du nombre de detections par MCML montre plus qu'auparavant que les sources se recouvrent en temps et en fréquence, et ainsi, que le découpage dans le domaine temps-fréquence n'est pas suffisant pour séparer les signaux d'intérêt. C'est pourquoi il est nécessaire d'étudier les algorithmes de l'état de l'art pour calculer plusieurs vecteurs d'onde au même instant et identifier ceux qui sont le plus à même de répondre à notre problématique.

Plusieurs approches sont considérées comme les approches de décomposition en sous-espaces séparant les caractéristiques du bruit et du signal à partir de la matrice de covariance ou spectrale des signaux. D'autres approches basées sur le calcul de l'énergie selon la direction d'arrivée sont décrites comme le spectre Frequency-Wavenumber (F-K), le spectre de Capon reposant sur le filtrage spatial de l'énergie ou encore le *beamforming* en temps comme FTBeam. Des méthodes statistiques sont également étudiées, parmi lesquelles figurent les statistiques de Fisher. Cette méthode est parfois couplée à d'autres approches, comme c'est le cas d'une des implémentations de CLEAN [den Ouden et al., 2020] dans laquelle le spectre de Capon est rendu plus robuste par les statistiques de Fisher. Enfin, le dernier type d'approche étudié est la régression robuste. En effet, PMCC utilise la TDOA comme estimateur, mais celle-ci est sensible aux valeurs aberrantes, alors que les techniques développées ici sont construites pour réduire ces biais.

Chapter III.1

Subspace decomposition approaches

Subspace decomposition methods are used in order to separate the characteristic of the noise from the characteristic of the SOI. This approach carries out characteristic decomposition of the covariance matrix resulting in a signal subspace orthogonal to the noise subspace. The algorithm MUltiple SIgnal Classification (MUSIC) only uses the noise subspace in order to estimate the wavefront parameters while Test of Orthogonality of Projected Subspaces (TOPS) uses the both subspace.

III.1.1 Multiple signal classification (MUSIC)

The algorithm MUltiple SIgnal Classification (MUSIC) developed by Schmidt [Schmidt, 1986] is a narrowband method based on subspace decomposition widely used as frequency or direction of arrival estimation (Lin et al. [2006]; Peruzzetto et al. [2018]; Heck et al. [2019]). This approach relies on several hypotheses:

- In the observed signal $z(t)$, the number of sources N is lower than the number of sensors M.
- All the different sources are considered stationary in the time window.
- The noise is not correlated to the sources.

The next subsection will explain the method using a narrowband assumption and then the subsection III.1.1.2 will deal with the focusing technique used to adapt this algorithm to the broadband signal model.

III.1.1.1 A narrowband method

The MUltiple SIgnal Classification (MUSIC) algorithm is based on the signal model of the equation I.3.5 and the associated matrix expression I.3.6. As a reminder, the covariance matrix model of such signals is

$$\mathbf{R_{zz}} = \mathbf{A}\mathbf{R_{ss}}\mathbf{A}^H + \mathbf{R_{nn}} \tag{III.1.1}$$

When the noise is Gaussian and white $\mathbf{R_{nn}} = \sigma^2\mathbf{I}$. The rank of $\mathbf{A}\mathbf{R_{ss}}\mathbf{A}^H$ is N as the number of independent sources if $\mathbf{R_{ss}}$ is non-singular. The latter is also positive definite and $\mathbf{A}\mathbf{R_{ss}}\mathbf{A}^H$ semi positive definite. This means that the number of sources can be estimated by the real eigenvalues of the hermitian matrix $\mathbf{R_{zz}}$ [Schmidt, 1986].

It is well known that the number of sources N can be obtained from the covariance matrix eigenvalues. Ideally, we should have N principal eigenvalues strictly larger than σ^2 (the noise power) and $M - N$ eigenvalues equal to σ^2. However, in practice, it can be difficult to find at which point the N eigenvalues of the eigenvalues curve end. This point is called the knee of the curved and can be defined mathematically as the maximum curvature of the function [Satopaa et al., 2011]. Different methods are used to find the knee of the curve:

- Finding the first point with the maximum second derivative [Scott Harris et al., 2000] or the second derivative above a threshold [Foss and Zaïane, 2002].

– The L-method, which finds the intersection between two lines that fit the curve (Salvador and Chan [2004]; Antunes et al. [2018]).

– The point of the curve which is the furthest from the line which connects the extremities of the curve [Satopaa et al., 2011].

For a nine-sensor array with a synthetic signal composed of three sources at the same SNR crossing the array, the real eigenvalues are represented in the figure III.1.1. It is worth noting that the eigenvalues differ from one to another. Then we need to find the knee of the curve to estimate the number of sources. Here the knee of the curve is located at the third eigenvalue. It is the point that is the furthest from the line connecting the extremities of the curve. It means that the number of sources is probably three as synthesised.

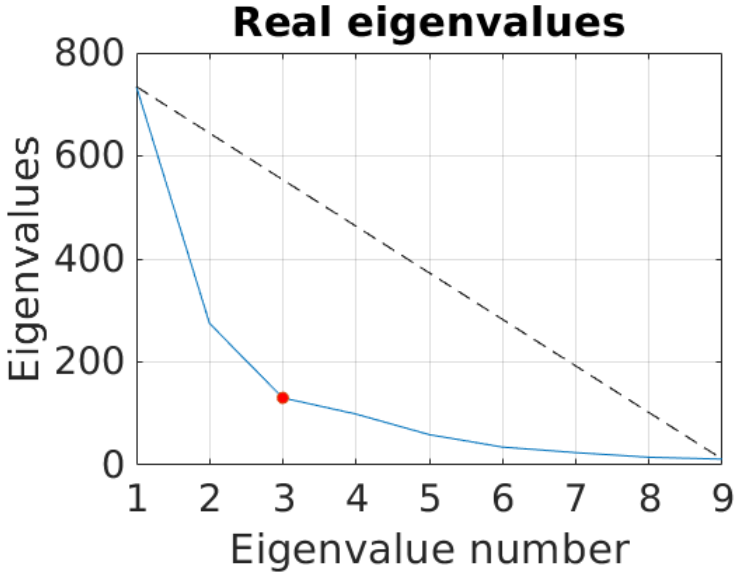

Figure III.1.1: Real eigenvalues of the matrix $\mathbf{R_{zz}}$ where there are three sources at 5 dB for $\sigma^2 = 1$. The red dot denotes the furthest point from the line connecting the extremities of the dotted curve in black.

Due to the definition of $\mathbf{R_{zz}}$ (equation I.3.7), the matrix is hermitian, then each of the M eigenvalues is linked to one eigenvector among the orthogonal base $\{v_{p1}, v_{p2}, \ldots, v_{pM}\}$. This statement can be written as

$$\mathbf{R_{zz}} v_{pi} = \lambda_i v_{pi} \tag{III.1.2}$$

Now let $i = N+1, ..., M$, thus $\lambda_i = \sigma^2$ as provided by the theory, then

$$(\mathbf{A}\mathbf{R_{ss}}\mathbf{A}^H + \sigma^2\mathbf{I})v_{pi} = \sigma^2 v_{pi} \tag{III.1.3}$$

Due to the noise assumption, it comes that

$$\mathbf{A}\mathbf{R_{ss}}\mathbf{A}^H v_{pi} = 0 \tag{III.1.4}$$

and the $\mathbf{A}^H v_{pi} = 0$ for $i = N+1, \ldots, M$ [Tang, 2014].

Subsequently the noise subspace can be defined as the space spanned by the v_{pi} perpendicular to the steering matrix $\mathbf{A}$.

Thanks to the previous wise choices of clusters of noise and signal eigenvalues we define a matrix $\mathbf{W}$ composed of the $M - N$ noise eigenvectors: $\mathbf{W} = [v_{pN+1}, \ldots, v_{pM}]$. This matrix characterises the noise subspace. Finally for each steering vector $a(\theta, v)$ the spectrum function of MUSIC is

$$F_{MUSIC}(f_i, \theta, v) = \frac{1}{a^H(\theta, v)\mathbf{W}\mathbf{W}^H a(\theta, v)} \tag{III.1.5}$$

The MUSIC function is a distance measure of $a(\theta, v)$ to the noise subspace. When $a(\theta, v)$ is orthogonal to the noise subspace, the value of the denominator is zero. However, the presence of noise causes a non-perfect estimate of $\mathbf{W}$ preventing this issue and the function increases for the true arrivals. It means that the N higher peaks of the function are also the furthest arrival from the noise subspace, so the most likely to be part of the signal subspace. Here, the noise subspace is used for the MUSIC function instead of the signal subspace because the peaks are narrower with the noise subspace, thus the resolution is better.

III.1.1.2 From narrowband to broadband : the focusing approach

As stated previously, the MUSIC algorithm is a narrowband method. Then, it can not be applied in this condition to a broadband signal model. The most commonly used method to solve this issue is to decompose the received broadband signal into narrowband components and to perform the narrowband analysis on these narrowband components to get accurate estimates

One approach is the Incoherent Signal Subspace Method (ISSM) [Wax et al., 1984] where an estimate of the wave parameters is provided for each narrowband frequency. Then, a final result is obtained by averaging all estimates of the frequency bins. This approach is accurate for high SNR signals, however, it is seriously impacted when the SNR decreases due to a high sensitivity to outliers. In addition, a simple mean of the estimates is not appropriate for coherent sources due to the non-flat shape of their spectrum.

The second approach is the Coherent Signal Subspace Method (CSSM) where focusing is used [Hung and Kaveh, 1988]. Focusing is a method that transforms each narrowband components into a correct representation at the central frequency, f_0. In the frequency domain, the spectral density matrix of the frequency bin f_i for N sources is given by the equation I.3.14 and can be written as

$$\mathbf{C}(f_i) = \mathbf{A}(f_i)\mathbf{C_{ss}}(f_i)\mathbf{A}^H(f_i) + \sigma^2\mathbf{I} \tag{III.1.6}$$

where $\mathbf{C_{ss}}$ is the spectral density matrix of the sources. Assuming a constant SNR in the bandwidth B, the coherently averaged spectral matrix $\mathbf{C_{focusing}}$ at the frequency f_0 is

$$\mathbf{C_{focusing}} = \sum_{k=1}^{K} \mathbf{T}(f_k)\mathbf{C}(f_k)\mathbf{T}^H(f_k) \tag{III.1.7}$$

where $\mathbf{T}$ is the focusing matrix.
Then the MUSIC method can be applied on the new spectral density matrix. However, a focusing loss defined as the SNR before and after the focusing operation will impact the estimation. This loss can be minimised by the choice of the focusing matrix. Several classes of focusing matrices exist including the unitary and nonunitary matrices. A unitary matrix is defined as $\mathbf{U}^H \times \mathbf{U} = \mathbf{U} \times \mathbf{U}^H = \mathbf{I}$.

The nonunitary focusing matrices (Yang and Kaveh [1983]; Wang and Kaveh [1985]) cause, in general, lower performance than unitary matrices. This is because the nonunitary focusing matrices have a higher loss during the pre-processing rank reduction and a higher deterioration of the coherent signal during the spatial whitening stage included in this class.

The unitary matrix searched must satisfy this constraint [Hung and Kaveh, 1988] :

$$\min_{\mathbf{T}(f_i)} ||\mathbf{A}(f_0, \hat{\theta}, \hat{v}) - \mathbf{T}(f_i)\mathbf{A}(f_i, \hat{\theta}, \hat{v})||_F \tag{III.1.8}$$

where $||.||_F$ is the Frobenius norm and $(\hat{\theta}, \hat{v})$ the preliminary estimates of the angles obtained by a beam-sum estimator or a higher resolution algorithm such as the Minimum Variance Distortionless Response (explained in chapter III.2). The chosen focusing matrix is part of the Rotational Signal Subspace (RSS) class. A unitary solution of equation III.1.8 is

$$\mathbf{T}(f_i) = \mathbf{V}(f_i)\mathbf{U}^H(f_i) \tag{III.1.9}$$

where $\mathbf{U}$ and $\mathbf{V}$ are the matrix of the left and right singular vectors of $\mathbf{A}(f_i, \hat{\theta})\mathbf{A}^H(f_0, \hat{\theta})$, respectively. It is worth noting that, the closer the estimated angles are from the true source, the more accurate the final estimates will be. A second iteration is possible to increase the resolution. The RSS class is then shown to be the most efficient in resolution [Hung and Kaveh, 1988]. If the SNR is nonuniform, as previously stated, then a weighted spectral density matrix is the most suitable way of data reduction.

III.1.2 Test of orthogonality of projected subspaces (TOPS)

The use of MUSIC in a broadband case requires its adaptation to the model by the application of the focusing method. This focusing method needs a prior estimation of the true angle by the use of another estimator. Thus, a wrong prior estimation leads to a wrong result. This constraint has been solved by a new algorithm called Test of Orthogonality of Projected Subspaces (TOPS) [Yoon et al., 2006]. Similarly to the previous estimator, this algorithm uses the spectral density matrix and the RSS class of focusing matrices. But contrary to the wideband MUSIC, TOPS does not need any prior estimate because the focusing is done on each hypothesised DOA on a grid and the orthogonality test is performed between this transform subspace and the noise subspace. Thus, in this case, both of the subspaces are used, contrary to MUSIC.

Let $\mathbf{C}(f_i)$ be the spectral density matrix of the signal at the frequency f_i. The first step is to compute the signal subspace $\mathbf{F}(f_i)$ and the noise subspace $\mathbf{W}(f_i)$ for each frequency bin. It can be done by a singular value decomposition of $\mathbf{C}(f_i)$ and the use of the vectors characterising the left singular matrix $\mathbf{U}(f_i)$. As for MUSIC, the number of sources has to be estimated to select the correct number of vectors in $\mathbf{U}(f_i)$ in order to construct the signal and noise subspaces. The same previously mentioned methods can be used.

The second step is the focusing of both of the subspaces into the central frequency. The transform matrix used is part of the RSS class and is diagonal. It is written as

$$[\mathbf{T}(f_i, \tau_i)]_{(k,k)} = e^{-2i\pi f_i \tau_i} \tag{III.1.10}$$

Starting from this expression of $\mathbf{T}(f_i, \tau_i)$, a link can be established between a potential (θ, v) couple and the true parameter $(\theta^\star, v^\star)$ between a frequency i and j. Indeed, the range space of $\mathbf{F}(f_i)$ and $\mathbf{A}(f_i, \theta, v)$ are identical:

$$\begin{aligned} \mathbf{T}(\Delta f, \theta, v)\mathbf{F}(f_i) &= \mathbf{T}(\Delta f, \theta, v)\mathbf{A}(f_i, \theta^\star, v^\star)\mathbf{G}(f_i) \\ &= \mathbf{A}(f_j, \hat{\theta}, \hat{v})\mathbf{G}(f_i) \end{aligned} \tag{III.1.11}$$

where $\Delta f = f_j - f_i$ and $\mathbf{G}(f_i)$ a full rank square matrix such as $\mathbf{F}(f_i) = \mathbf{A}(f_i, \theta^\star, v^\star)\mathbf{G}(f_i)$. This transformation preserves the array manifolds. It means that it is possible to focus the frequency i into the focused j without changing the parameters of the wavefront. By fixing $f_j = f_0$, it is possible to derive a test on the central frequency where the rank of the matrix decreases when the hypothetical (θ, v) couple is the true parameter.

Thus, for every possible (θ, v) couple with a $\Delta f = f_i - f_0$ a matrix $\mathbf{U}(f_i, \theta, v)$ can be defined thanks to the previous equations III.1.10 and III.1.11

$$\mathbf{U}(f_i, \theta, v) = \mathbf{T}(\Delta f, \theta, v)\mathbf{F}(f_0) \tag{III.1.12}$$

From this statement, another matrix $\mathbf{D}(\theta, v)$ can be formulated

$$\mathbf{D}(\theta, v) = [\mathbf{U}^H(f_1, \theta, v)\mathbf{W}(f_1) \dots \mathbf{U}^H(f_2, \theta, v)\mathbf{W}(f_2) \dots \mathbf{U}^H(f_{K-1}, \theta, v)\mathbf{W}(f_{K-1})] \tag{III.1.13}$$

where the matrix $\mathbf{D}(\theta, v)$ is $N \times (K-1)(M-N)$, K the number of frequency bins. The dimension of $(K-1)(M-N)$ is due to the fact that the central frequency is not taken into account because of the focusing towards this frequency bin. Then, if $\theta = \theta^\star$ and $v = v^\star$ the matrix $\mathbf{D}(\theta, v)$ becomes rank deficient. If it is not the case, the matrix is full rank. However this statement holds only if the SOI are

not completely correlated. Indeed, this correlation provokes a decrease of the signal subspace dimension.

If the spectral density matrix is poorly estimated, the error of the matrix $\mathbf{D}(\theta, v)$ can increase, it is thus possible to reduce this error by subspace projection. Let us define a projection matrix $\mathbf{P}(f_i, \theta, v)$ onto the null space of $a(f_i, \theta, v)$

$$\mathbf{P}(f_i, \theta, v) = \mathbf{I} - (a^H(f_i, \theta, v)a(f_i, \theta, v))^{-1}a(f_i, \theta, v)a^H(f_i, \theta, v) \tag{III.1.14}$$

The matrix $\mathbf{D}(\theta, v)$ can be re-estimated by the modified matrix $\mathbf{U}(f_i, \theta, v)$

$$\mathbf{U_{projected}}(f_i, \theta, v) = \mathbf{P}(f_i, \theta, v)\mathbf{U}(f_i, \theta, v) \tag{III.1.15}$$

This projection allows for a better performance by avoiding the signal subspace component leakage in the estimated noise subspace. However, this projection must not be used if the distance between sensors is higher than half the wavelength of the highest frequency of the bandwidth B. Aliasing can occur otherwise. Due to different sensor distances in the array we do not apply this estimation improvement. Indeed not all distances respect this property.

For a frequency bin, the TOPS function can finally be defined by:

$$F_{TOPS}(\theta, v) = arg\max_{\theta, v} \frac{1}{\sigma_{min}(\theta, v)} \tag{III.1.16}$$

where $\sigma_{min}(\theta, v)$ is the smallest singular value of $\mathbf{D}(\theta, v)$. Then the N higher peaks correspond to the N sources searched.

Chapter III.2

Beamforming approaches

III.2.1 Frequency-wavenumber spectrum (F-K)

The conventional F-K spectrum is the simplest method to estimate the DOA and the trace velocity of a signal [Capon, 1969]. This approach is widely used in different studies involving seismic or infrasound wavefronts (Asten and Henstridge [1984]; Bishop et al. [2020]). This method analyses the spatial and frequency characteristics of the wavefront. Stationary random processes can be characterised by a spectral density function that calculates the energy of the signal for a frequency. The same idea is applied to propagating waves where a power spectral density function is calculated to retrieve the DOA and the apparent velocity. Let $z(t, r)$ be the monochromatic plane wave recorded at the array sensor:

$$z_m(t) = e^{i(2\pi f_i t - k_i r_m)} \tag{III.2.1}$$

where f_i and k_i are the frequency and wavenumber of the plane wave, respectively, r_m is the sensor position. The method analyses this plane wave in the frequency domain, such that the Fourier transform of the signal can be written as

$$Z_m(f_i, k) = \int_{-\infty}^{+\infty} z_m(t) e^{-i2\pi f t} dt = \delta(f - f_i) e^{-ik_i r_m} \tag{III.2.2}$$

The F-K power spectral density function of the plane wave is then defined [Denholm-Price and Rees, 1999] as

$$P(f_i, k) = \int_R w(r) Z_m(f_i) e^{ikr_m} dr = \delta(f - f_i, k - k_i) \tag{III.2.3}$$

where $w(r) = 1$ denoting that the sensors are equally sensitive to the wavefront. The maximum of the spectrum is found at f_i and k_i, which are the frequency and wave number of the plane wave.
The discrete form of the F-K spectrum for every wavenumber k is given by [Smart and Flinn, 1971]

$$P(f_i, k) = \sum_{j=1}^{M} \sum_{l=1}^{M} \mathbf{C}_{jm}(f_i) e^{ik(r_j - r_l)} \tag{III.2.4}$$

where $\mathbf{C}_{jm}(f_i)$ is the spectral density matrix for the sensors j and m.
The latter expression is linked explicitly to the wavefront parameters when rewritten as

$$\begin{aligned} P(f_i, k) &= \left(\sum_{j=1}^{M} \alpha_j e^{-2i\pi f_i \tau_j(\theta, v) - ikr_j} \right)^H \left(\sum_{l=1}^{M} \alpha_l e^{-2i\pi f_i \tau_l(\theta, v) - ikr_l} \right) \\ &= \left| \sum_{m=1}^{M} \alpha_m e^{-2i\pi f_i \tau_m(\theta, v)} e^{-ikr_m} \right|^2 = \left| \sum_{m=1}^{M} Z_m(f_i) e^{-ikr_m} \right|^2 \end{aligned} \tag{III.2.5}$$

where α_m containing the amplitude information of the wavefront. $Z_m(f_i)$ refers to the Fourier transform of the signal and e^{-ikr_m} to the array response.

III.2.2 Minimum Variance Distortionless Response (MVDR)

The Minimum Variance Distortionless Response (MVDR) [Capon, 1969], also called the Capon spectrum for its developer's name, is a method based on spatial filtering. The aim is to mitigate the signal coming from every direction except from the actual DOA. This spatial filtering involves the application of a filter for each sensor. It can be expressed as

$$\mathbf{Z_w}(f_i) = w^H(f_i)\mathbf{Z}(f_i) \tag{III.2.6}$$

where w is the finite impulse response of length M. The power of the filter output is

$$\mathbb{E}\{|\mathbf{Z_w}(f_i)|^2\} = w^H(f_i)\mathbf{C}(f_i)w(f_i) \tag{III.2.7}$$

The filter has to fulfil different properties. For a signal containing N different sources, the first property states that it is essential to avoid signal attenuation or distortion in the considered DOA and is written as

$$w^H(f_i)a(f_i, \theta = \theta_n^\star, v = v_n^\star) = 1 \tag{III.2.8}$$

The second property refers to the filtering of the undesirable signal coming from other directions. Perfectly following both properties is impossible due to the infinity of constraint. However, it is possible to mitigate the undesirable signal energy coming from other DOA. Thus, applying this new constraint plus the first property, the problem can be written as

$$\min_w = w^H(f_i)\mathbf{C}(f_i)w(f_i) \text{ subject to } w^H(f_i)a(f_i, \theta_n^\star, v_n^\star) = 1 \tag{III.2.9}$$

There is a unique solution for this minimisation problem

$$w(f_i) = \frac{\mathbf{C}(f_i)^{-1}a(f_i, \theta, v)}{a^H(f_i, \theta, v)\mathbf{C}(f_i)^{-1}a(f_i, \theta, v)} \tag{III.2.10}$$

Where $\mathbf{C}(f_i) > 0$. The power spectrum can now be expressed as a maximisation of the output filter in the desired direction. By replacing the expression III.2.10 in the equation III.2.7 we have

$$F_{Capon}(f_i, \theta, v) = \mathbb{E}\{|\mathbf{Z_w}(f_i)|^2\} = \frac{1}{a^H(f_i, \theta, v)\mathbf{C}(f_i)^{-1}a(f_i, \theta, v)} \tag{III.2.11}$$

For the purposes of a multisource signal, several maxima have to be selected. The MVDR has better resolution and interference rejection performance than the other classical beamformers. However the performances of the estimator are worse either when the assumed wavefront differs from the real one (i.e the DOA tested are quite different from the true DOA) or when the amplitude of the signal measured at each sensor differs by more than a critical amount [Seligson, 1970]. Many methods have been implemented to avoid these effects. Indeed, an algorithm that adapts weights to minimise noise power in the array output in the direction of interest by linear or derivative constraint can be developed (Frost [1972]; Zhang and Thng [2002]). However, these kind of constraints are not truly related to the uncertainty of the steering vector. Moreover, each linear constraint causes the loss of one degree of freedom for interference suppression. Other methods based on subspace estimation are also provided to calculate the weight of the estimator (Feldman and Griffiths [1994]; Lee and Lee [1997]). However these methods are still sensitive to the steering vector error and to the knowledge of the noise covariance matrix [Li et al., 2003]. Another method named diagonal loading ends up with equal weights on all sensor outputs [Cox et al., 1987]. Let the equation I.3.14 be rewritten as

$$\mathbf{C}(f_i) = \mathbf{C}_{ss}(f_i) + \sigma^2\mathbf{I} \tag{III.2.12}$$

We can apply the diagonal loading as follow

$$\mathbf{C}(f_i) = \mathbf{C}_{ss}(f_i) + \sigma^2\mathbf{I} + \epsilon\mathbf{I} \tag{III.2.13}$$

This is equivalent to adding spatially uncorrelated white noise to all sensors outputs, when ϵ is very large, then we get $\mathbf{C}(f_i) = \sigma_{new}^2\mathbf{I}$. Thus the weights can be rewritten as

$$w = \frac{\mathbf{C}(f_i)^{-1}a(f_i, \theta, v)}{a^H(f_i, \theta, v)\mathbf{C}(f_i)^{-1}a(f_i, \theta, v)} = \frac{(\sigma_{new}^2\mathbf{I})^{-1}a(f_i, \theta, v)}{a^H(f_i, \theta, v)(\sigma_{new}^2\mathbf{I})^{-1}a(f_i, \theta, v)} = \frac{a(f_i, \theta, v)}{a^H(f_i, \theta, v)a(f_i, \theta, v)} = \frac{a(f_i, \theta, v)}{M} \tag{III.2.14}$$

It comes that the weight is equal for all sensor outputs. However the choice of the diagonal loading is empirically fixed. For example, it can be proportional to the variance in the data: $\epsilon = \alpha\ trace(\mathbf{C}(f_i))$ where α is empirically chosen. Other methods of diagonal loading exists with different constraints, such as the flat ellipsoidal constraint [Li et al., 2003] or following the peak sidelobe level desired [Wu et al., 1996].

III.2.3 FTBeam

Various beamforming methods have been developed to estimate the DOA and trace velocity from array sensors [DeMuth, 1977]. The goal of beamforming is to find shift the signal timeseries based on a DOA and trace velocity (i.e. beam) and to find the maximum of the sum of the shifted signals. The beamforming in time domain is

$$F_{FTBEAM}(\theta, v) = \sum_{j=1}^{L} \left(\sum_{m=1}^{M} z_m(t_j + \tau_m(\theta, v)) \right)^2 \tag{III.2.15}$$

For all possible time shift of a grid (θ, v) one can calculate the amplitude of the beam by summing the shifted waveforms of the array of M sensors with a record of length L. In [Walker, 2012] the authors proposed applying the sum of the beamformed signals in the time frequency space proposed by the CEA, taking advantage of the space designed for PMCC. Then the individual frequencies are averaged across multiple frequency bins. This method has been successfully applied to monitor permanent sources such as microbaroms but also transient events such as earthquakes [Walker et al., 2013] and yields similar results compared to PMCC.

Chapter III.3

Statistical approaches

III.3.1 The Fisher statistic

The Fisher statistic is a test based on the work of R.A Fisher [Fisher, 2018] widely used in the literature and by numerous NDCs (Melton and Bailey [1957]; Denholm-Price and Rees [1999]; Arrowsmith et al. [2009]; Bishop et al. [2020]). The Fisher statistic has been derived by [Smart and Flinn, 1971] in order to build a detector for each maximum of the F-K spectrum. Let's recall the equation III.2.5 which is the F-K power spectral density function

$$P(f_i,k) = \left| \sum_{m=1}^{M} Z_m(f_i) e^{-ikr_m} \right|^2 \tag{III.3.1}$$

When a SOI is present then the signal power expresses as

$$P_S(f_i,k) = \left| \sum_{m=1}^{M} \frac{1}{M} Z_m(f_i) e^{-ikr_m} \right|^2 = \frac{1}{M^2} \left| \sum_{m=1}^{M} Z_m(f_i) e^{-ikr_m} \right|^2 = \frac{1}{M^2} P(f_i,k) \tag{III.3.2}$$

This expression is simply the F-K power spectral density function weighted by the number of sensors at a given frequency. The total power found in the record for a frequency bin is

$$P_T(f_i) = \frac{1}{M} \left| \sum_{m=1}^{M} Z_m(f_i) \right|^2 \tag{III.3.3}$$

This equation includes both noise and signal power. The Fisher statistics can be derived for the F-K power spectral density function to define a kind of SNR measure [Shumway, 1971]. The ratio is written as

$$F_{ratio}(f_i,k) = \frac{P_S(f_i,k)}{P_T(f_i) - P_S(f_i,k)}(M-1) \tag{III.3.4}$$

As previously stated, the numerator is the power of the signal and the denominator is the total amount of energy minus the signal power leading to the noise power. It worth noting that $P_T(f_i,k) \geq P_S(f_i,k)$, the $F_{ratio}(f_i,k)$ ranges between zero and infinity. This method allows for a reduction of the side lobe prominence and then to better distinguish between main lobes and side lobes of the sources.

III.3.2 The CLEAN algorithm

The CLEAN algorithm was initially designed for radio astronomy in order to avoid side lobe effects for star cluster observations [Högbom, 1974]. Since many CLEAN algorithms have been developed to enhance DOA and velocity estimation (Wang et al. [2004]; Sijtsma [2007]; Gal et al. [2016]; den Ouden et al. [2020]). CLEAN assumes that every point acts like a point source. The goal is to deconvolve the array response of each maximum to obtain a "clean" map of the real lobes corresponding to true wavefront

parameters and a "dirty" map of side lobes removed by the process.

A wideband approach of CLEAN has been proposed in [Wang et al., 2004]. This method is applied directly to the signal. This signal is decomposed into L frequency bins by the Fourier Transform approaching thus the multisource narrowband model as

$$Z(f_i) = \mathbf{A}(f_i, \theta, v)S(f_i) + N(f_i) \tag{III.3.5}$$

A first estimation of the (θ, v) couple can be found by minimising the least-squares cost function

$$f = \sum_{i=1}^{L}(Z(f_i) - \mathbf{A}(f_i, \theta, v)S^H(f_i))(Z(f_i) - \mathbf{A}(f_i, \theta, v)S(f_i)) \tag{III.3.6}$$

The first estimation of the (θ, v) couple is expressed as

$$(\hat{\theta}, \hat{v}) = arg\ max \sum_{i=1}^{L} \frac{|\mathbf{A}^H(f_i, \theta, v)Z(f_i)|^2}{||\mathbf{A}^H(f_i, \theta, v)||^2} \tag{III.3.7}$$

Then the power of the signal is calculated by

$$\hat{S}(f_i) = \frac{\mathbf{A}^H(f_i, \hat{\theta}, \hat{v})Z(f_i)}{\mathbf{A}^H(f_i, \hat{\theta}, \hat{v})\mathbf{A}(f_i, \hat{\theta}, \hat{v})} \tag{III.3.8}$$

Once the slowness vector and the power of the signal estimated, the source can be deconvolved from the signal

$$Z_{CLEAN}(f_i) = Z(f_i) - \phi\mathbf{A}(f_i, \hat{\theta}, \hat{v})\hat{S}(f_i) \tag{III.3.9}$$

This procedure is done iteratively until no significant signal is left in $Z(f_i)$. The factor, ϕ, is the percentage of the source to remove from the total signal which value usually varies between 0.1 and 0.25. The stopping criterion is based on the entropy of the distribution of $\hat{S}(f_i)$ over all the L frequencies. However, the threshold of this function is set empirically at 4.35 by the authors [Wang et al., 2004].

Due to many estimations, N groups of distributed sources $\{g_n\}_{n=1}^{N}$ are established for a K iteration procedure such that

$$(\hat{\theta}, \hat{v})_n = \sum_{i=1}^{L}\sum_{k\in N} |\phi\hat{S}(f_i)|^2 \tag{III.3.10}$$

To avoid any empirical threshold for the detection criterion another version of CLEAN has been developed in den Ouden et al. [2020]. This version uses the MVDR spectrum previously introduced in the section III.2.2 as an estimator. Let's recall the equation III.2.10 about the spatial filtering coefficient and the equation III.2.11 about the Capon spectrum. The main idea is to remove the phase and amplitude information of the main contribution, from the spectral density matrix $\mathbf{C}(f)$ (Sijtsma [2007]; Gal et al. [2016]). Thus, the new matrix is

$$\mathbf{C_{CLEAN}}(f_i) = \mathbf{C}(f_i) - \phi\ \max(F_{CAPON}(f_i, \theta, v))w_{MAX}(f_i)w_{MAX}^H(f_i) \tag{III.3.11}$$

Then, the weight can be calculated to estimate the power spectrum $F_{CAPON}(f_i, \theta, v)$ deconvolved from the previous source. At the same time the CLEAN spectrum is iteratively incremented for the K iterations

$$F_{CLEAN}(f_i, \theta, v) = \sum_{i=1}^{K} \phi \max(F_{CAPON}(f_i, \theta, v)) \tag{III.3.12}$$

In this case, the detection criterion is based on the Fisher statistic developed in the previous section III.3.1. For the Capon method the F_{ratio} can be related to the equation III.3.4 with

$$\begin{cases} P_S(f_i, \theta, v) = \max(F_{CAPON}(f_i, \theta, v)) \\ P_T(f_i) = \frac{1}{M}\sum_{m=1}^{M}\mathbf{C}_{mm}(f_i) \end{cases} \tag{III.3.13}$$

Using the Fisher law, the method stops when $F_{ratio} \leq F(P, \nu_1, \nu_2)$, with $P = 0.95$ to avoid false alarm and $\nu_1 = 2L$ and $\nu_2 = 2L(M-1)$, is satisfied [Shumway, 1971]. Moreover, a relation do exists between the F-ratio and the SNR allowing the calculation of the latter [Melton and Bailey, 1957]:

$$F_{ratio} = M\mathrm{SNR}^2 + 1 \tag{III.3.14}$$

Chapter III.4

Robust regression techniques

The characterisation of the wavefront parameters can be also approached as a regression problem [Szuberla and Olson, 2004]. The TDOA, explained in the subsection II.1.1.2, is one such method. Regression techniques are usually sensitive to outliers even if the results are inconsistent with the plane wave model [Rousseeuw and Leroy, 2005]. However robust regression techniques have been developed to overcome this problem [Ryan, 2008]. The presented methods are all derived from the maxima of the cross correlation functions. Though, they are designed to have a high breakdown value, in other words, a high outlier number is necessary to bias the estimation.

In the regression problem, the model is

$$\tau = \mathbf{X}p + \epsilon \tag{III.4.1}$$

where τ is all the $M(M-1)/2$ inter-element delays, $\mathbf{X}$ is the 2D matrix of the relative positions of all the sensor pairs

$$\mathbf{X} = \begin{bmatrix} r_{1,1} - r_{2,1} & r_{1,2} - r_{2,2} \\ \vdots & \vdots \\ r_{M-1,1} - r_{M,1} & r_{M-1,2} - r_{M,2} \end{bmatrix} \tag{III.4.2}$$

ϵ is the error on the estimation of the true delays and p the slowness vector.

The goal of the regression is to minimise the residual vector $q = \tau - \mathbf{X}p$ with some constraints that differ from one method to another.

III.4.1 M-estimator

M-estimators can be defined as a generalisation of the maximum likelihood estimator [Peter, 2004]. Instead of the ordinary least square method, where the outliers give a strong effect on the minimisation problem, M-estimators try to reduce their impact by replacing the squared residuals by another function of the residuals

$$\hat{p} = \min_p \sum_{i=1}^{M(M-1)/2} \rho\left(q_i(p)\right) = \min_p \sum_{i=1}^{M(M-1)/2} \rho\left(\tau_i - \mathbf{X}_i p\right) \tag{III.4.3}$$

where ρ is a symmetric, positive-definite function of the residuals with a unique minimum at zero. The function is chosen to be less sensitive to outliers than the squared one. If $\rho = \frac{1}{2}x^2$ or $\rho = |x|$ the minimisation problem comes back to the L_2-norm or the L_1-norm estimation respectively. It is possible to take into account the data units by dividing the residuals by a scaling factor, S_1, for example the median absolute deviation that is proportional to the cumulative distribution function for standard normal distribution [Rousseeuw and Leroy, 2005]. The minimisation of the equation III.4.3 is now written as

$$\sum_{i=1}^{M(M-1)/2} q_i' \psi\left(\frac{q_i}{S_1}\right) = \sum_{i=1}^{M(M-1)/2} \mathbf{X}_{ij} \psi\left(\frac{q_i}{S_1}\right) = 0 \tag{III.4.4}$$

where ψ is the derivative called the influence function [Montgomery et al., 2021]. The latter quantifies the influence of a value on the parameter to estimate. As an example, if $\rho = \frac{1}{2}x^2$ then $\psi = x$, indicating that the influence of a value on the estimate increases linearly with the error, it confirms the non-robusteness of the least-squares estimate. The main property of a robust function is that any single observation is insufficient to cause a significant offset of the model [Rey, 2012]. That is why the function $\rho(x)$ must follow robust constraints such as the bounded influence, unique minimum, and a non null ψ function. A weighted function of ψ can be constructed as

$$w(x) = \frac{\psi(x)}{x} \tag{III.4.5}$$

The expression III.4.4 is then written as

$$\sum_{i=1}^{M(M-1)/2} q_i w(q_i) \mathbf{X}_{ij} = 0 \tag{III.4.6}$$

This equation is relative to iterative reweighted least-squares [Beaton and Tukey, 1974]. In the study of [Bishop et al., 2020], the chosen weighting function is the bi-weighted function [Phillips and Eyring, 1983]:

$$\begin{cases} w_i = & (1 - (\frac{q_i}{kS_2})^2)^2 & |q_i| < kS_2 \\ w_i = & 0 & |q_i| > kS_2 \end{cases} \tag{III.4.7}$$

where k is a constant that determines how harshly residuals are treated, and S_2 is a scale factor, often the median of the absolute values of the residuals [Mosteller and Tukey, 1977]. Bishop et al. [2020] applied first a L_1-norm fit and then, after the standardised calculation of $\frac{q_i}{S_1}$, the bi-weight function is used in order to downgrade the influence of data points with large residuals. The M-estimators are known to be more accurate than the least squares when the data errors are non normal or when outliers are presents [Tiede and Pagano, 1979].

III.4.2 Least trimmed squares

The Least Trimmed Squares (LTS) is another high breakdown value estimator based on subset fit of residuals defined as

$$\hat{p} = \min_p \sum_{i=1}^{h} |q_i(p)|^2 \tag{III.4.8}$$

where h is the subset size of the ascending order residuals $q_1^2 \leq q_2^2 \leq \ldots \leq q_{M(M-1)/2}^2$ [Rousseeuw, 1984]. Usually $M(M-1)/4 \leq h \leq M(M-1)/2$ is taken. This constant sets the breakdown value because $[M(M-1)/2] - h$ values will affect the estimation. Indeed a high h leads to a low breakdown value but also to a higher statistical efficiency. When $h = M(M-1)/2$ we recover the least mean squares method with a breakdown point equal to zero but a high statistical efficiency. A high breakdown point can be reached with high statistical efficiency by the LTS with $h = [M(M-1)/4] + [(\alpha+1)/2]$ where α is the number of coefficients of the linear fit model, including the intercept term [Rousseeuw and Van Driessen, 2006]. The algorithm makes use of hundreds of iterations on subset of size h. Each iteration reaches a smaller residual than the current one. The ten best fits are saved after this initial fit. The algorithm makes further convergence steps on these models to find the optimal solution. To increase statistical efficiency a weighted least-squares can be done. The weight is binary between outliers and non-outlier data points and is described as

$$\begin{cases} w_i = 0 & \text{if } \left|\frac{q_i}{S_2}\right| > 2.5, \\ w_i = 1 & \text{otherwise} \end{cases} \tag{III.4.9}$$

where $S_2 = 1.483\sqrt{median(q_i^2)}$, it allows us to get rid of outliers (Rousseeuw [1991]; Rousseeuw and Hubert [1997]). This method was applied by Bishop et al. [2020] and has been shown improved results compared to other least-squares methods.

Conclusion (in english)

The state-of-the-art in multi-source signal processing methods shows that it is possible to use different quantities to estimate these sources. Some methods have been particularly influential, such as MUSIC, and have enabled the analysis of events of interest (Peruzzetto et al. [2018]; Heck et al. [2019]). The TOPS algorithm brings innovation, as it considers both the noise subspace and the signal subspace. Methods such as the MVDR spectrum and Fisher statistics have also been evaluated in several studies (Bishop et al. [2022]; Bishop et al. [2020]; Meng et al. [2015]). However, no comparison between these methods has been made to date for operational use.

Moreover, the interest in capitalising on the recent developments in MCML is leading to further methodological research. The following section presents multisource algorithms based on likelihood. In particular, we will first focus on the use of monosource MLE to estimate multiple sources, which will then be mathematically generalised to multisource. In a second phase, alternative methods for blind source separation and dictionary coding will be examined before comparing them on synthetic and real signals.

Conclusion (en français)

L'état de l'art des méthodes de traitement de signaux à sources multiples montre qu'il est possible d'utiliser différentes quantités pour estimer ces sources. Certaines méthodes ont été particulièrement influentes comme MUSIC et ont permis d'effectuer des analyses d'évènements d'intérêt (Peruzzetto et al. [2018] ; Heck et al. [2019]). L'algorithme TOPS apporte une innovation, car il considère à la fois le sous espace bruit et le sous espace signal. Des méthodes telles que le spectre MVDR ou les statistiques de Fisher ont également été évaluées dans plusieurs études (Bishop et al. [2022] ; Bishop et al. [2020] ; Meng et al. [2015]). Cependant, aucune comparaison entre ces méthodes n'a été réalisée à ce jour pour une exploitation à des fins opérationnelles.

De plus, l'intérêt de capitaliser sur les récents développements de MCML motive la poursuite de recherches méthodologiques. La partie suivante propose des algorithmes multisources basés sur la vraisemblance. En particulier, nous nous concentrerons d'abord sur l'utilisation du MLE monosource pour estimer plusieurs sources, il sera ensuite généralisé mathématiquement au multisource. Dans un second temps, des méthodes alternatives de séparation aveugle des sources et de *dictionnary coding* seront examinées avant de les comparer sur signaux synthétiques et réels.

Part IV

Towards new multisource processing

Abstract

The results of MCML have demonstrated the contribution of this method compared to the state-of-the-art, particularly in relation to PMCC. On the other hand, the algorithm is currently unable to estimate multiple wave vectors simultaneously at the same frequency and therefore cannot be compared in its current state to algorithms such as MUSIC. This section first discusses the relevance of using monosource MLE for multisource estimation. Indeed, the use of single-source MLE reduces computational costs compared to a multi-source MLE algorithm [Lin and Barkat, 1991]. To achieve this, various methods are developed, such as the iterative deflation of source signals to maintain a single-source assumption, the selection of multiple maxima on the likelihood function, or iterative image processing methods. In a second step, the MLE is generalised to a treatment with N sources, taking into account each of the previously located sources.

Subsequently, alternative methods of blind separation (Independent Component Analysis (ICA)) are studied with the aim of separating the source signals before individually estimating the wavefront parameters using MCML. Another method is also presented: dictionary coding with the Least Absolute Shrinkage and Selection Operator (LASSO) and Orthogonal Matching Pursuit (OMP) approaches, aiming to use their sparse properties. Sparsity implies that there is a limited number of recorded arrivals. Thus, these algorithms return a limited number of wave vectors leading to the reconstruction of the observation with multiple sources. By using the inter-sensor delays as a dictionary variable or the likelihood functions of classical MLE, we assess the relevance of implementing such methods.
Then, the relevant developed methods are evaluated on synthetic and real signals to identify the most accurate and least computationally expensive method for operational use.

Finally, the considerable increase in the number of detections due to MCML and the multisource processing requires a rethinking of the family clustering of detections. That is why a new approach using Gaussian mixture is proposed.

Résumé

Les résultats de MCML ont montré l'apport de cette méthode par rapport à l'état de l'art et en particulier face à PMCC. En revanche, l'algorithme n'est actuellement pas en mesure d'estimer plusieurs vecteurs d'onde simultanément à une même fréquence et donc ne peut pas être comparé dans l'état à des algorithmes tels que MUSIC. Cette partie discute tout d'abord de la pertinence de l'utilisation du MLE monosource pour l'estimation multisource. En effet, l'utilisation du MLE monosource permet de réduire les coûts en calcul par rapport à un algorithme MLE multisource [Lin and Barkat, 1991]. Pour cela, différentes méthodes sont élaborées, comme la soustraction itérative de signaux sources afin de rester dans une hypothèse de source unique, la sélection de plusieurs maxima sur la fonction de vraisemblance ou encore les méthodes de traitement d'images itératives. Dans un second temps, le MLE est généralisé à un traitement à N sources en prenant en compte chacune des sources précédemment localisées.

Par la suite, des méthodes alternatives de type séparation aveugle (Analyse en Composantes Indépendantes (ACI)) sont étudiées dans le but de séparer les signaux sources avant d'estimer individuellement les paramètres de front d'onde avec MCML. Une autre méthode est également présentée : le *dictionary coding* avec les approches LASSO et OMP dans le but d'utiliser leur propriété parcimonieuse. La parcimonie implique qu'il existe un nombre limité d'arrivées enregistrées. Ainsi, ces algorithmes renvoient donc un nombre limité de vecteurs d'onde conduisant à la reconstruction de l'observable à sources multiples. En utilisant comme variable du dictionnaire les retards inter-capteurs ainsi que les fonctions de vraisemblance du MLE classique, nous évaluons la pertinence de l'implémentation de telles méthodes.
Ensuite, les méthodes élaborées pertinentes sont évaluées sur signaux synthétiques et réels afin d'identifier la méthode la plus précise et la moins coûteuse en temps de calcul dans la perspective d'une utilisation opérationnelle.

Enfin, l'augmentation considérable du nombre de détections apporté par MCML et le traitement multisource nécessite une refonte du regroupement en famille des détections. C'est pourquoi une nouvelle approche par mélange de gaussiennes est proposée.

Chapter IV.1

The multisource estimation by Maximum Likelihood Estimation

IV.1.1 The use of the monosource estimator

A first naive approach, to capitalise on the recent developments, is to determine whether the single-source estimator is able to detect multiple sources or not. Indeed a real multisource MLE would be far to costly because of the maximisation of likelihood function with around 10 variables for 3 sources (i.e the three sources have to be estimated simultaneously). For this purpose, a simple test on synthetic signals of 500 s long at a frequency band of [0.8 - 1] Hz and a frequency sampling of 20 Hz at a station with nine sensors to achieve asymptotic results was proceeded. The signal consists of three sources of azimuths and trace velocities equal to [100, 200, 300]° and [340, 400, 450] m/s respectively. The sources have equal SNR. The results are shown on figures IV.1.1 where the likelihood function is plotted for SNR of 5 dB, 0 dB and -5 dB respectively. It is worth noting that three maxima corresponding to the true sources can be determined. Thus the monosource algorithm is able to determine multiple sources whatever the SNR is. However, in operational process we are not in asymptotic conditions anymore. That is why the test is done once again but this time with used time windows during operational processing from the third octave decomposition explained in section I.3.4 (i.e 30 s, which is around 10 periods in a time window). This is illustrated by the figures IV.1.2. It can be observed that whatever the SNR is, the first source is correctly estimated, which is consistent with MCML results [Poste et al., 2023b]. However, at 0 dB only two sources can be estimated correctly and then at -5 dB there is only one source properly estimated.

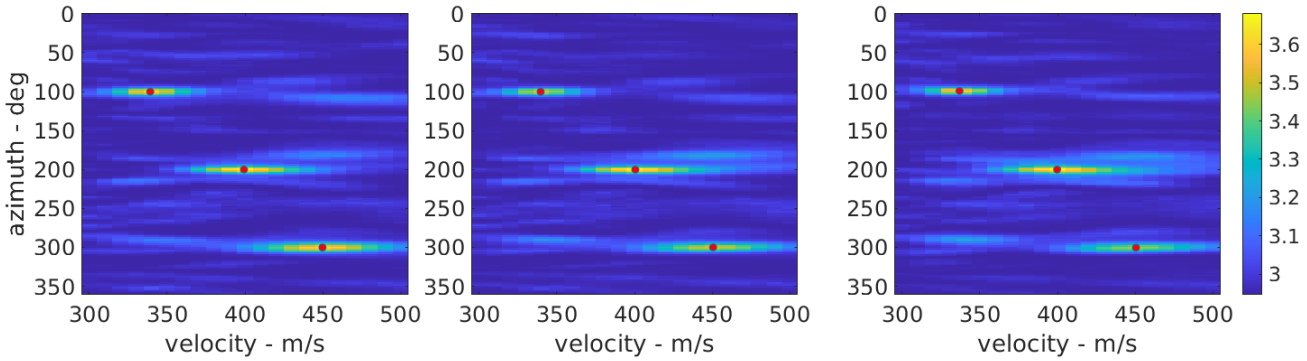

Figure IV.1.1: Estimation of wavefront parameters under asymptotic performance conditions on the likelihood function at 5, 0 and -5 dB respectively from the left to the right. The red dots represents the three maxima values of azimuths and trace velocities on the likelihood function.

These results are showing that the third octave decomposition as implemented for the monosource algorithm is not appropriate for multisource purpose due to the loss of information with decreasing SNR between sources. A first requirement is to study how to improve the time-frequency decomposition, then

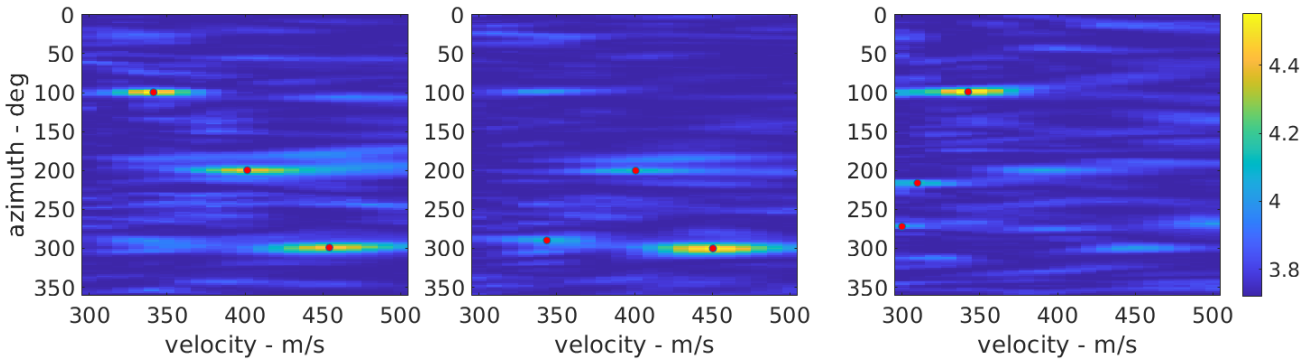

Figure IV.1.2: Estimation of wavefront parameters under operational conditions on the likelihood function at 5, 0 and -5 dB respectively from the left to the right. The red dots represents the three maxima values of azimuths and trace velocities on the likelihood function.

several methods are set up in order to take advantage of the monosource algorithm. These methods includes iterative source signal deflation; 2D peak finder on likelihood function or image processing methods like Gaussian likelihood subtraction; active contour subtraction and subtraction of array response by image generation of the source.

IV.1.1.1 Multisource time-frequency decomposition

To optimise the estimator for a multisource purpose, it is necessary to conduct a study of the sources of error in the estimator with a view to reducing them. The equation for the covariance matrix $\mathbf{R}_{MLE}^{\theta,v}$ is written as in the equation II.2.36 and following ones. For a reminder

$$\sqrt{T}\left((\hat{\theta},\hat{v})_{\text{MLE}} - (\theta^\star, v^\star)\right) \xrightarrow{T\to+\infty} \mathcal{N}(0, \mathbf{R}_{MLE}^{\theta,v}) \tag{IV.1.1}$$

where $\mathbf{R}_{MLE}^{\theta,v}$ is the inverse of the Fisher Information matrix with respect to the parameter (θ, v)

$$\mathbf{R}_{MLE}^{\theta,v} = \mathbf{J}\boldsymbol{\Gamma}_0\mathbf{J}^T, \tag{IV.1.2}$$

$\mathbf{J}$ is the Jacobian matrix of the transformation for the true parameters,

$$\mathbf{J} = \begin{bmatrix} -v^\star\cos(\theta^\star) & v^\star\sin(\theta_\star) \\ v^{2\star}\sin(\theta^\star) & v^{2\star}\cos(\theta^\star) \end{bmatrix} \tag{IV.1.3}$$

with

$$\boldsymbol{\Gamma}_0 = \frac{\int 4\pi^2 f^2 |H(f)|^4 \ (M \times SNR^\star + 1)\, df}{\left(\int 4\pi^2 f^2 M \times SNR^\star \times |H(f)|^2 df\right)^2} \times \left(\mathbf{X}_{MLE}^T \boldsymbol{\Pi}_M^\perp \mathbf{X}_{MLE}\right)^{-1} \tag{IV.1.4}$$

However when $T \to +\infty$ is not respected as seen previously, the equation IV.1.2 becomes

$$\mathbf{R}_{MLE}^{\theta,v} = \mathbf{J}\boldsymbol{\Gamma}\mathbf{J}^T, \tag{IV.1.5}$$

with

$$\boldsymbol{\Gamma} = \frac{\boldsymbol{\Gamma_0}}{T_{obs}} \tag{IV.1.6}$$

where T_{obs} is the observation time.
The equation for the estimator's covariance matrix shows that it is only possible to influence the signal's bandwidth and observation time. The wider the bandwidth and the longer the observation time, the smaller the error in theory. However, this is counterbalanced by a decrease in frequency and time accuracy, particularly for non-stationary sources. In order to quantify the impact of these two parameters, we

calculate the velocity errors averaged for all possible azimuths of the grid and a velocity fixed at 340 m/s thanks to the covariance matrix equation for a SNR of 0 dB. The frequency divisions studied are the third (figure IV.1.3), half (figure IV.1.4), two-thirds (figure IV.1.5) and octave (figure IV.1.6) decomposition as a function of the unit, doubled, tripled and quadrupled observation time used currently for operational processing. In the following figures, this variable is called $Tfactor$ refereeing to n times the current observation time. This one is currently based on ten times the central period of the bandwidth.

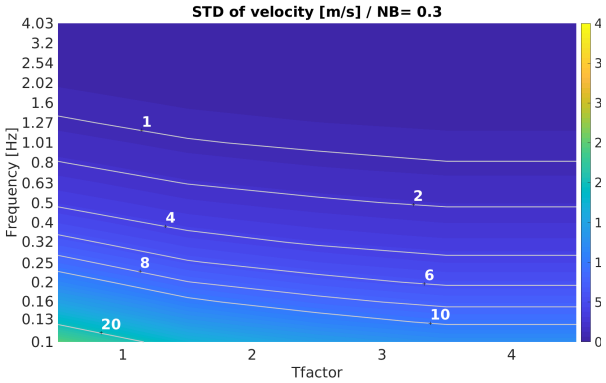

Figure IV.1.3: Velocity errors by third octave frequency decomposition as a function of multiples of the operational observation time.

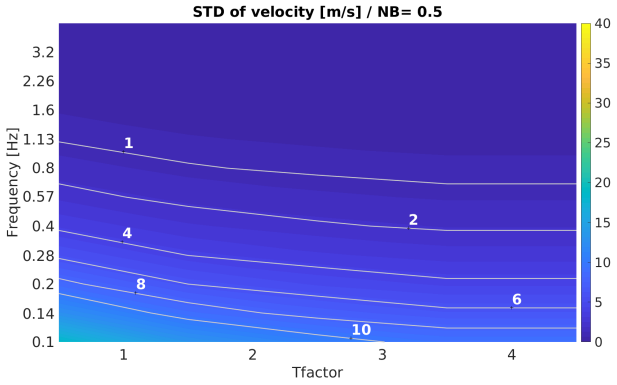

Figure IV.1.4: Velocity errors by half octave frequency decomposition as a function of multiples of the operational observation time

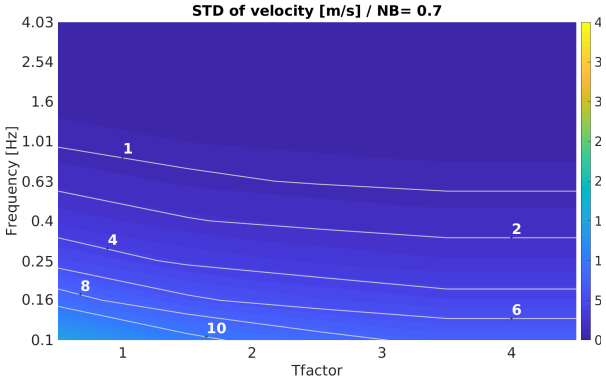

Figure IV.1.5: Velocity errors by two third octave frequency decomposition as a function of multiples of the operational observation time.

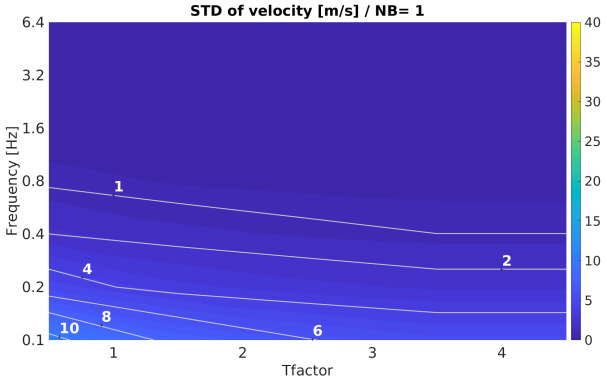

Figure IV.1.6: Velocity errors by octave frequency decomposition as a function of multiples of the operational observation time.

In each case, we observe that the error decreases with increasing observation time, as theoretically expected, but with a progressively decreasing gain. For example, the velocity error for the third octave is almost halved between the current observation time and the quadrupled observation time at 0.2 Hz, ranging from 10 m/s to 6 m/s. Similarly, widening the band significantly reduces the error. The velocity error from the third to an octave decomposition decreases from 10 m/s to 4 m/s at 0.2 Hz for a unit operational observation time. In theory, the most appropriate division is into octaves, with observation time quadrupled compared with the current observation time. However, such a division degrades the characterisation of events circumscribed in time and frequency, such as explosions. Increasing the time window and the frequency band too much leads to the risk of averaging several transient sources, especially at high frequencies. This reduces the accuracy of the detection.

200 synthetic signals containing three sources were simulated at -5 dB and [0.8 - 1] Hz in different configurations in order to validate the theoretical improvement of the estimator. Figures IV.1.7, IV.1.8, IV.1.9 and IV.1.10 show the dispersion of the azimuth/velocity pairs for the third and half octaves for the

operational observation time currently used ($Tfactor = 1$) and twice the operational observation time currently used ($Tfactor = 2$) retained in the theoretical study in order to minimise the loss of frequency and time accuracy. Here the three main maxima are picked on the likelihood function.

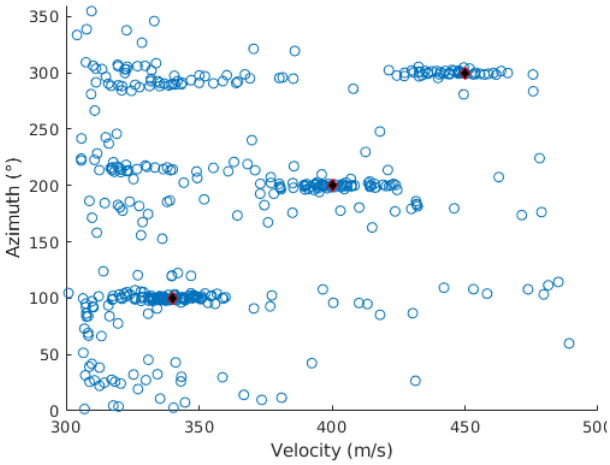

Figure IV.1.7: Estimation for the three sources for a third octave decomposition with an operational observation window.

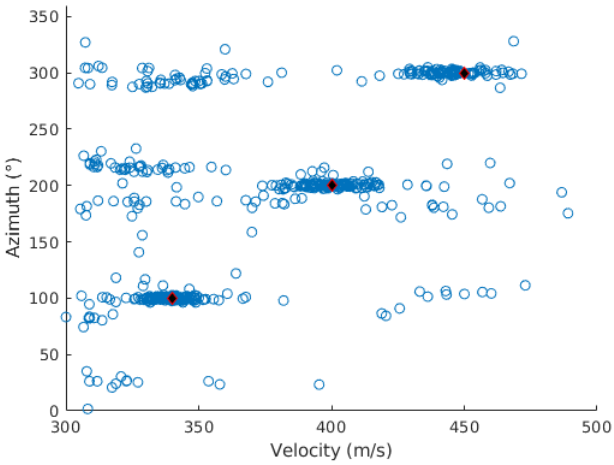

Figure IV.1.8: Estimation for the three sources for a third octave decomposition with a doubled operational observation window.

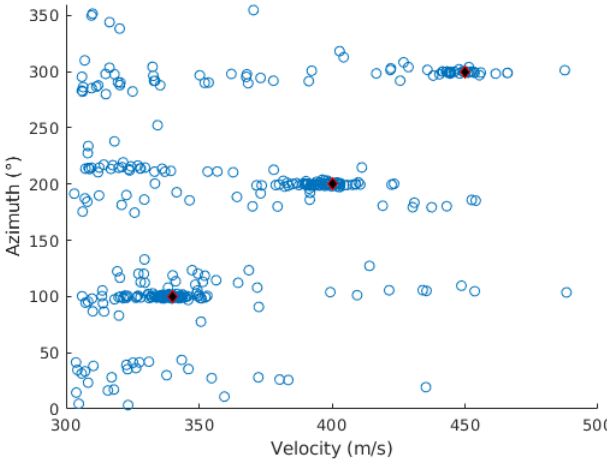

Figure IV.1.9: Estimation for the three sources for a half-octave decomposition with an operational observation window.

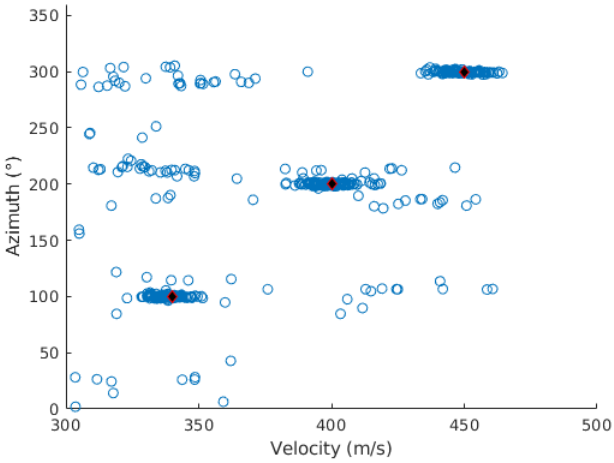

Figure IV.1.10: Estimation for the three sources for a half-octave split with a doubled operational observation window.

Confirming the theory, widening the frequency band and the observation time improves the localisation of the three sources by focusing the estimates on the true wave parameters. Changing the frequency division is more effective than changing the time division as indicated above, but it is the time division that most degrades the characterisation of impulsive events in the time-frequency domain. This is why we increase the observation time window by a factor of two compared with the current division. This method is better suited to the situation of multiple sources without degrading the accuracy of the MCML algorithm (i.e windows constructed from ten times the central period of the bandwidth to twenty). Finally, it is possible to counterbalance the degradation in accuracy due to the enlargement of the time window, producing fewer detections by increasing the window overlap rate. This is effective as the computation time is reduced by increasing the observation time window, thus saving this computation time to increase the overlap rate.

IV.1.1.2 The iterative source signal deflation

One way to use the single source algorithm in a multisource context is to attempt to maintain a single source problem. It is possible then to iteratively subtract the SOI from the records and then perform the estimation by MLE again. This method is analogous in concept to one version of CLEAN described in section III.3.2 but integrating the robustness in statistics of MLE. Let the recordings be written as in the equation I.3.9

$$z_m(t) = \sum_{n=1}^{N} s_n(t - \tau_m(\theta_n, v_n)) + n_m(t) \tag{IV.1.7}$$

The first iteration calculates the M different delays $\tau_m(\theta_1, v_1)$, the $N-1$ other sources can be considered as noise for the first source. Indeed, while adding $+\tau_m(\hat{\theta}_1, \hat{v}_1)$ to all the different records for a couple $(\hat{\theta}_1, \hat{v}_1)$ different from the true value $(\theta_1^\star, v_1^\star)$ we have

$$z_m(t + \tau_m(\hat{\theta}_1, \hat{v}_1)) = \underbrace{s_n(t - \tau_m(\theta_n^\star, v_n^\star) + \tau_m(\hat{\theta}_1, \hat{v}_1))}_{u_m^n(t)} + n'_m(t) \tag{IV.1.8}$$

where the noise $n'_m(t)$ and $u_m^n(t)$ are supposed Gaussian, temporally and spatially white. But now, adding the appropriate $+\tau_m(\theta_1^\star, v_1^\star)$ we can state that the equation IV.1.7 becomes

$$z_m(t + \tau_m(\theta_1^\star, v_1^\star)) = s_1(t) + n'_m(t) \tag{IV.1.9}$$

When all the M sensor records are averaged, the white Gaussian noise is considered as greatly reduced (i.e the higher M, the better the noise is reduced). Thus once $s_1(t)$ is approximated, it is possible to subtract it from each record adding back $-\tau_m(\theta_1^\star, v_1^\star)$

$$z'_m(t) = \sum_{n=1}^{N} s_n(t - \tau_m(\theta_n^\star, v_n^\star)) + n_m(t) - s_1(t - \tau_m(\theta_1^\star, v_1^\star)) = \sum_{n=2}^{N} s_n(t - \tau_m(\theta_n^\star, v_n^\star)) + n_m(t) \tag{IV.1.10}$$

Note that it is possible to remove only a percentage α of $s_1(t - \tau_m(\theta_1^\star, v_1^\star))$ to avoid any sharp subtraction. When the the SOI is removed from the records it is possible to run once again MCML to estimate other sources. An example is provided by the figure IV.1.11 where three SOI are synthesised with a SNR of 5 dB at [100, 200, 300]°. The figure on the left shows the first estimation of MCML with the red dot as the first SOI to be estimated. Subtracting iteratively 25% of the source signal, as mention in CLEAN, allows us to estimate the other sources at 100° and then 300°.
A more statistical test has been done by generating 200 synthetic signals at [0.8 - 1] Hz with the characteristics that there are three sources with wavefront parameters corresponding to [100, 200, 300]° and [340, 400, 450] m/s. Two cases are simulated, at 5 dB and -5 dB. The results can be observed on figures IV.1.12 and IV.1.13. At 5 dB the estimations are all correct, however the dispersion is higher when the SNR is lower but it can be seen at the first order that the proposed deflation-based method is valid.

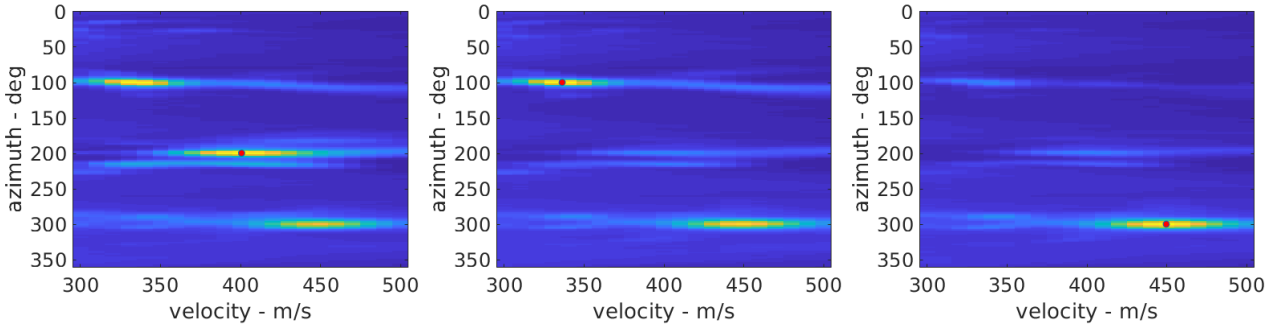

Figure IV.1.11: Results of iterative deflation of SOI on the records. Each figure represents the estimation of the likelihood function and the red dot is the maximum on the 2D likelihood function. The three sources are at 5 dB, [100, 200, 300]° and [340, 400, 450] m/s.

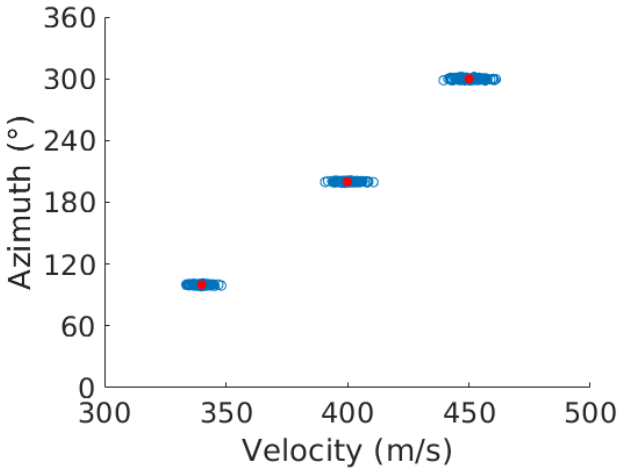

Figure IV.1.12: Estimation for the three sources at 5 dB located by the red dots at [100, 200, 300]° and [340, 400, 450] m/s.

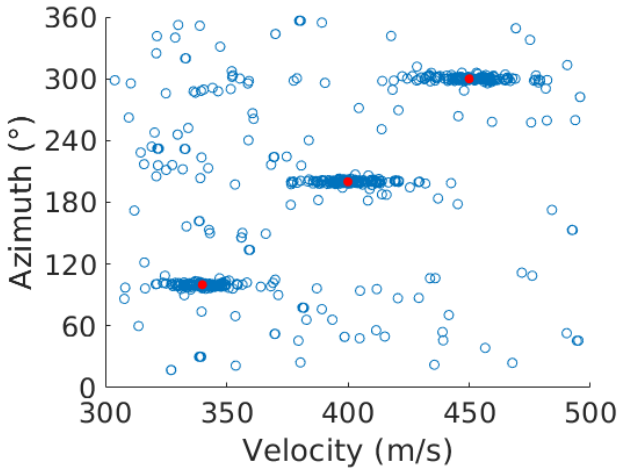

Figure IV.1.13: Estimation for the three sources at -5 dB located by the red dots at [100, 200, 300]° and [340, 400, 450] m/s.

IV.1.1.3 2D peak finder on likelihood function

Instead of iteratively removing the SOI and calculate N times the likelihood function it is possible to pick directly the main lobes on the likelihood function. This is done by an algorithm that find multiple maxima on a 2D function called *extrema2* [Aguilera, 2016] already used in some studies (Freire et al. [2021]; Ørregaard Nielsen and Ksawery Popiel [2018]). The maxima are searched in rows, columns and diagonals of the 2D likelihood function. However, we need to sort the maxima at the output of this algorithm by likelihood amplitude in order to get consistent results. Therefore, the *filter peaks* function was implemented to keep only the most relevant maxima. The function takes as input the maxima $(\hat{\theta}, \hat{v})$ found by *extrema2*, along with the associated p-values and SNR for each peak. These values are sorted in descending order of likelihood, so that the maxima with the highest likelihood is located at the beginning of the vector. Additionally, the array's geometry, time window, sampling frequency, and filter bank are required variables for accurately calculating the covariance of the estimation errors. The algorithm begins by filtering the p-values at 1 %. Next, we calculate the errors associated with the remaining estimates. A value of $\delta\hat{\theta}$ and $\delta\hat{v}$ is then available for each estimation. Let the maxima i associated to $\hat{\theta}_i$ and $\hat{v}_i$. If the maxima $i-1$ is included in the interval $[\hat{\theta}_i - \delta\hat{\theta}_i; \hat{\theta}_i + \delta\hat{\theta}_i]$ and $[\hat{v}_i - \delta\hat{v}_i; \hat{v}_i + \delta\hat{v}_i]$ then the maxima i is removed. If not, the maxima is now compared with the maxima no longer $i-1$ but $i-2$ until we reach $i=1$. In summary, the confidence interval of all the preceding maxima in index is compared with the considered maxima. The aim is to identify and prioritise the secondary sources with the highest likelihood. Finally, if we consider M sensors, we delete the maxima whose index is greater than M-1

in order to comply with an over determined system. More generally we fix $N < M - 1$ and it is also possible to add a supplementary condition such as the fact that any two peaks have to be more than a certain number of degrees apart from each other (i.e arbitrary $\delta\hat{\theta}$ or based on the grid step). Conducting a similar test, the results are shown by figures IV.1.14 and IV.1.15; the algorithm works effectively even though the accuracy is decreasing at lower SNR.

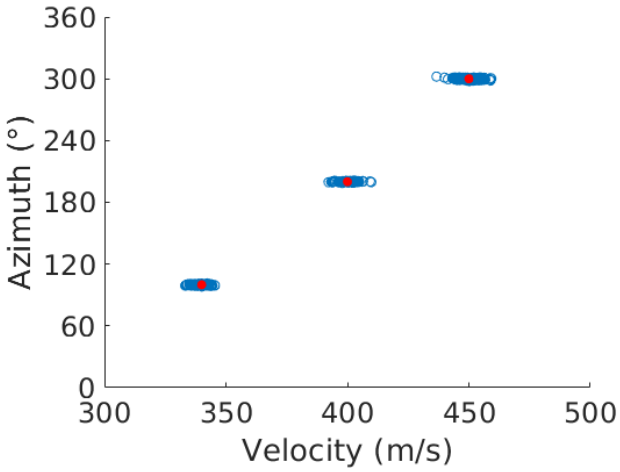

Figure IV.1.14: Estimation for the three sources at 5 dB located by the red dots at [100, 200, 300]° and [340, 400, 450] m/s.

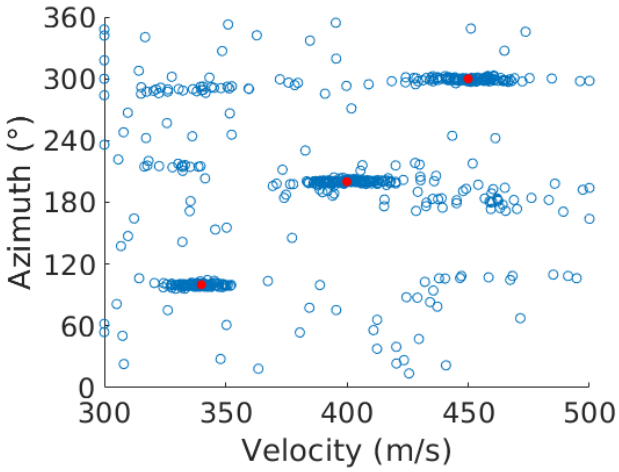

Figure IV.1.15: Estimation for the three sources at -5 dB located by the red dots at [100, 200, 300]° and [340, 400, 450] m/s.

However some tests on real signals have shown that an accumulation of maxima on the grid edges can occur. To overcome this issue the maxima modulo 360 are selected by replicating the likelihood at ±180° on the lower and upper edges. The search for maxima is then performed between -100° and 460° to avoid edge effects. To avoid detections of the same maxima due to the replication of the likelihood, it is specified that a source may not be repeated in the list of maxima. The same thing was done for velocities by extending the grid from [300 - 400] m/s to [250 - 550] m/s and restricting the search space to between [300 - 500] m/s. More generally we search on $[v_{min} + 50; v_{max} - 50]$. The counterpart is a higher computation time.

IV.1.1.4 Image processing methods

Another ways of processing was studied, those of image processing.

The first try was to subtract a Gaussian to the likelihood function in order to subtract the array response of a source and then do it iteratively. The generated Gaussian writes

$$f(x) = A \exp\left(-\frac{1}{2}(x - \overline{m})^T \mathbf{R}_{MLE}^{\theta,v\,-1}(x - \overline{m})\right) \tag{IV.1.11}$$

where x is the vectorised grid in azimuth and velocity, $\overline{m}$ the centre of the Gaussian (i.e the source localisation on the azimuth/velocity plan), $\mathbf{R}_{MLE}^{\theta,v}$ the covariance matrix of the estimator controlling the dimension of the Gaussian and A is the amplitude of the Gaussian. This amplitude is controlled by the maximum amplitude of the likelihood function (i.e the searched maximum) and the mean amplitude of the likelihood function (i.e calculated arbitrary as the 30th quantile, q). Thus the amplitude is expressed as

$$f(x)_{Amp} = (f(x)/\max_{\theta,v} f(x)) \times (\max_{\theta,v} \mathcal{L}(\mu) - q) \tag{IV.1.12}$$

The multiple iterations are illustrated by the following figure IV.1.16 where the Gaussian peak of the sources are iteratively and correctly subtracted. However it is essential to report that the Gaussian fits the true peak when the covariance matrix $\mathbf{R}_{MLE}^{\theta,v}$ is multiplied by two coefficients, the first is depending

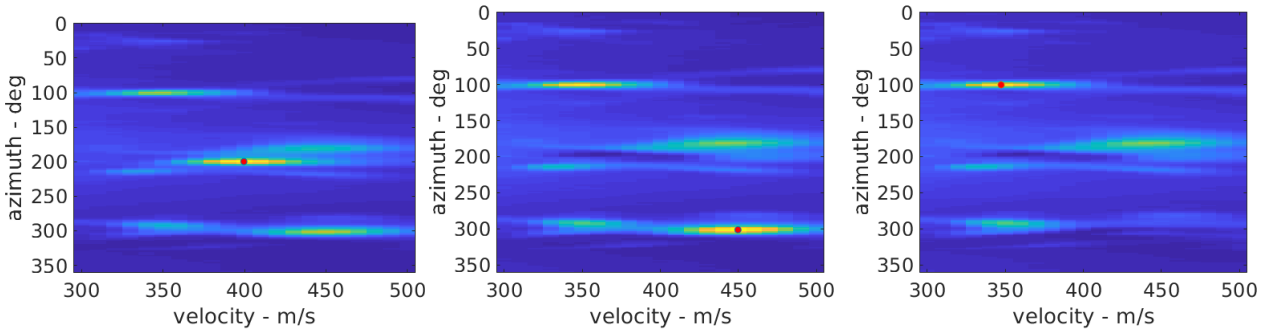

Figure IV.1.16: Results of iterative deflation of a Gaussian on the likelihood function centred at the estimation point. Each figure represents the estimation of the likelihood function and the red dot is the maximum on the 2D likelihood function. The three sources are at 5 dB, [100, 200, 300]° azimuth and [340, 400, 450] m/s.

on T_{obs} and the second one is $-2log(1-\alpha)$ (i.e the log-likelihood ratio test statistic threshold equation) with $\alpha = 0.4$. There is so an important and arbitrary setting.
The test is done once again to verify the quality of the method and the results are presented in the figures IV.1.17 and IV.1.17. The two tests show valid results comparing to the other methods. However further tests have shown that the settings used are not valid anymore in terms of amplitude depending on the frequency and width depending on the station used. Indeed the array response depends on the frequency band and on the array geometry. Thus this method is not universal and has not been adopted.

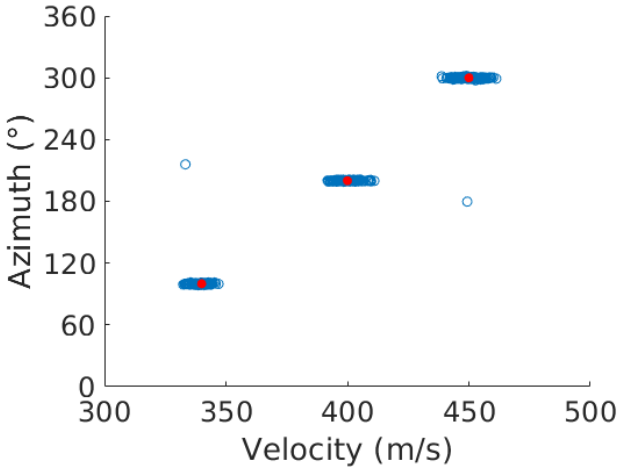

Figure IV.1.17: Estimation for the three sources at 5 dB located by the red dots at [100, 200, 300]° and [340, 400, 450] m/s.

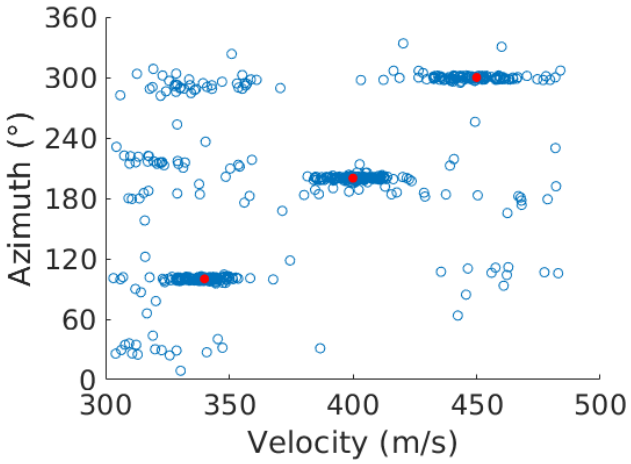

Figure IV.1.18: Estimation for the three sources at -5 dB located by the red dots at [100, 200, 300]° and [340, 400, 450] m/s.

Another kind of subtraction is studied, it is the subtraction of the likelihood function normalised by another likelihood function built by synthetic signal. For this purpose, the MLE is performed and then the first source is estimated with its associated azimuth, trace velocity and signal power. Then a synthetic signal is generated with this setting in order to estimate the likelihood function of this single source by MLE. Once the estimation of the likelihood function is done we subtract the likelihood with the monosource condition to the multisource condition. The expected suppression of the array response on the likelihood is in reality imperfect.

The final way of subtraction studied is the one based on active contour on the likelihood image in order to subtract the entire array response of the image iteratively. Active contours are tools used in image processing to detect and track the contours of objects on an image. They are widely used in areas such as computer vision, pattern recognition and image segmentation [Kass et al., 1988]. The used method is the Van-Chese method developed in the early 2000 in order to detect objects in a given image, based on techniques of curve evolution without any gradient prior (Chan et al. [2000]; Chan and Vese [2001]). The Chan-Vese method focuses on region-based segmentation, it seeks to divide the image into homogeneous regions rather than detecting precise contours. Several steps characterise the image segmentation. The first set is the initialisation where an initial outline is defined around the region of interest in the image. This contour can be a simple geometric shape, such as a circle or rectangle, or it can be more complex depending on the needs of the application (i.e in our case it is a rectangle). The second step is about energy modelling. The Chan-Vese method is based on the minimisation of an energy function that measures the coherence of pixels inside and outside the contour. This energy function consists of two main terms: the data attachment term, which measures the similarity of the intensities of the pixels inside and outside the contour, and the regularisation term, which promotes the spatial regularity of the contour. This energy function of the contour C writes

$$F(C) = \psi L(C) + \nu A(R_1) + \lambda_1 D(R_1) + \lambda_2 D(R_2) \tag{IV.1.13}$$

where ψ and ν are weighting terms, $L(C)$ is the contour length, $A(R_1)$ the area of the inner region R_1 bounded by the contour C, $D(R_1)$, $D(R_2)$ are data attachment terms that measure the dissimilarity between pixels inside and outside the contour with homogeneous region models respectively, λ_1 and λ_2 are weighting coefficients for the data attachment terms. In the Chan-Vese active contour, the data attachment terms $D(R_1)$ and $D(R_2)$ are generally function of the averages of the image inside and outside the contour. In [Chan and Vese, 2001] the authors set ν equal to zero and $\lambda_1 = \lambda_2 = \lambda$ in order to best fit the contour to the image characterisation. Once the energy function has been defined, the aim is to find the contour that minimises this energy. This can be achieved using numerical optimisation methods such as the level set method [Osher and Sethian, 1988]. Afterwards, the image is segmented into regions based on this contour. Pixels inside the contour are assigned to one class, while pixels outside the contour are assigned to another class, usually using a threshold value based on pixel intensities. In many cases, several iterations are required to refine the contour and obtain accurate segmentation (i.e we have done up to 100 iterations). During each iteration, the contour is updated according to the energy function, and the segmentation process is repeated until convergence is achieved. The goal is thus to delimit an area on the likelihood function calculated from a synthetic signal and then to avoid picking maxima in this range of azimuth/velocity around the selected maximum in order to reduce error induced by the array response. In order to test this method, the Chan-Vese active contour was applied on the likelihood function on four cases: two stations IS31, IS46 at two frequency bands [0.5 - 0.6] Hz and [3.2 - 4] Hz. The incident source is centred in the grid at 200° and 400 m/s. The figure IV.1.19 represents the likelihood function response to the incident signal at IS31 and the applied Chan-Vese active contour. It is worth to notice that the main lobe is well constrained. The secondary lobes are however not taken into account. The secondary lobes are taken into account in the example at IS46 (IV.1.20) but it leads to a large area where a second source can not be seen. Thus, at the first order, the used method exhibits different results depending on the array geometry.

We now evaluate if the frequency band and the associated response impact the active contour results. Figures IV.1.21 and IV.1.22 represent the likelihood function to the incident signal and the applied Chan-Vese active contour at IS31 and IS46 respectively. The frequency band is [3.2 - 4] Hz leading to a narrower array response but with some likelihood disturbances. It is worth noting than the array response of IS31 is well defined by the active contour. However it is definitely not the case for IS46 where a large area is defined whereas the real maximum is thin. The disturbances seem to make the active contour to fail recognising the real shape of the lobe. This issue has been solved by rising the number of iterations of the active contour arbitrary from 100 to 190. However this rise changes the previous frequency band result. It means than the parameters of active contour has to be tuned for each station and each frequency band in order to be precise. Too many iterations should not be used because leading to failures at high frequency (i.e an number of iterations at 200 leads to a too constrain lobe shape). This method can not applied in definitive for operational use. Indeed an analyst must tune and verify for each station and each frequency band if the array response pattern is well defined by the active contour. Moreover the quality of an array response well defined is subjective leading to result variability. Should the secondary lobes be

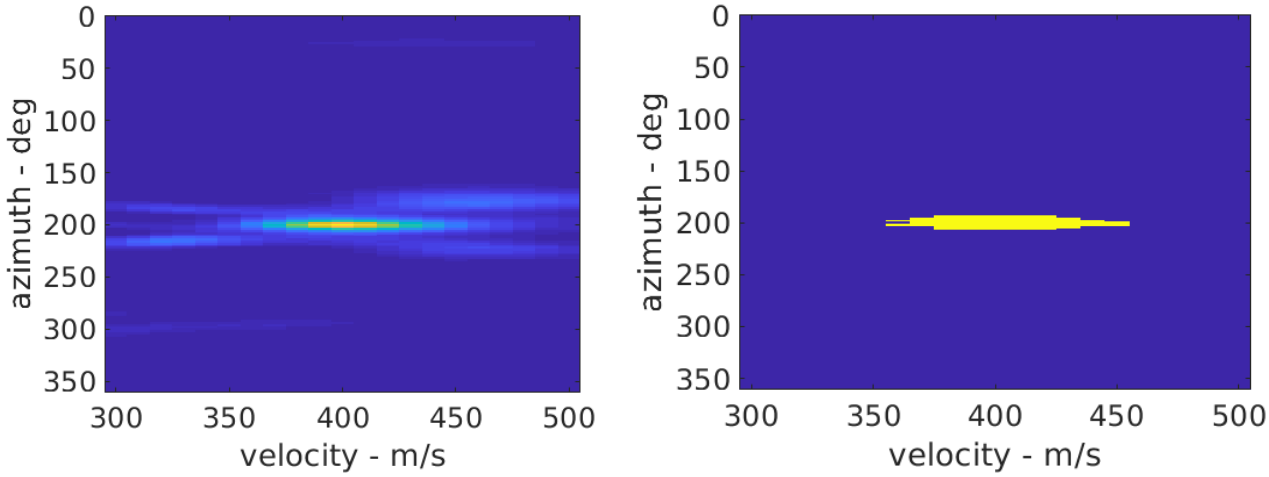

Figure IV.1.19: Likelihood function for a single source at 200° and 400 m/s, 5 dB for IS31 (left). Chan-Vese active contour applied. The yellow shape represents the contour of the likelihood maximum (right).

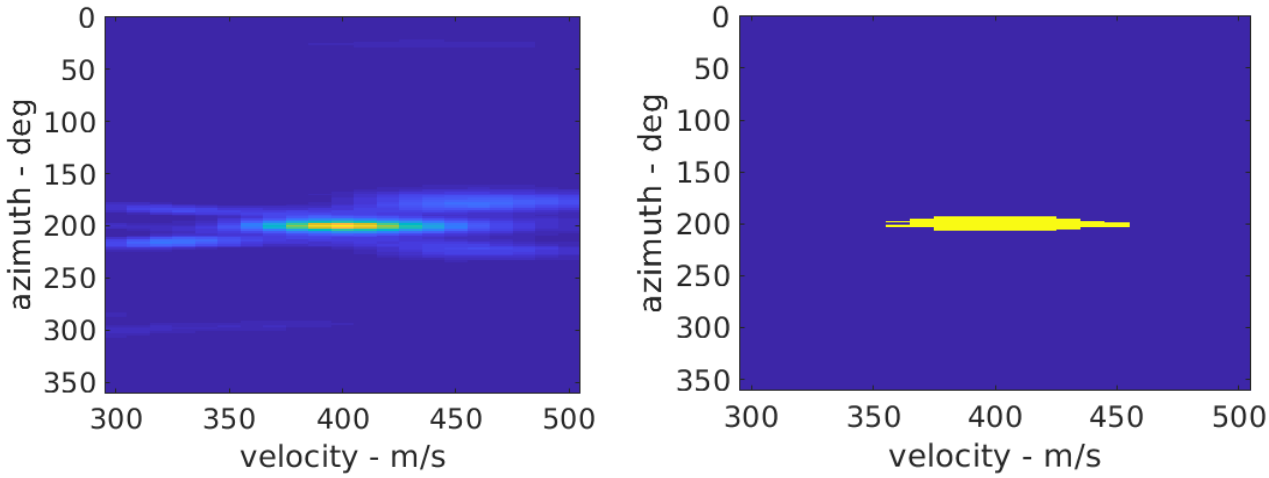

Figure IV.1.20: Likelihood function for a single source at 200° and 400 m/s, 5 dB for IS46 (left). Chan-Vese active contour applied. The yellow shape represents the contour of the likelihood maximum (right).

in the contour even if the area is larger (i.e leading to a poorer capability to detect close sources)? If not, the secondary lobes of a high SNR source can be greater in amplitude than a source of weaker energy. That is why the following method takes into account mathematically the array response to efficiently subtract it.

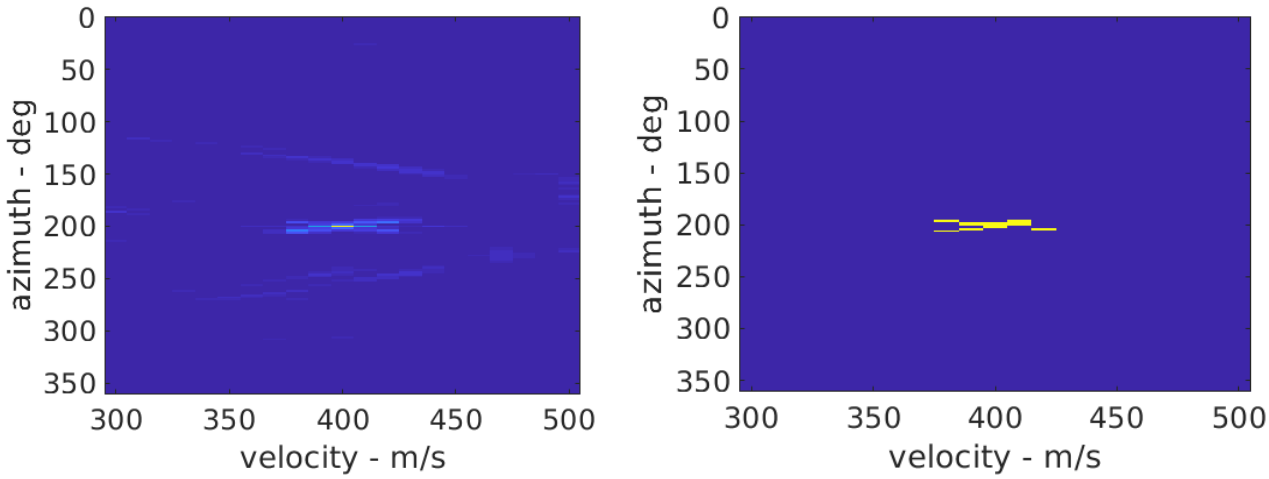

Figure IV.1.21: Likelihood function for a single source at 200° and 400 m/s, 5 dB for IS31 (left). Chan-Vese active contour applied. The yellow shape represents the contour of the likelihood maximum (right).

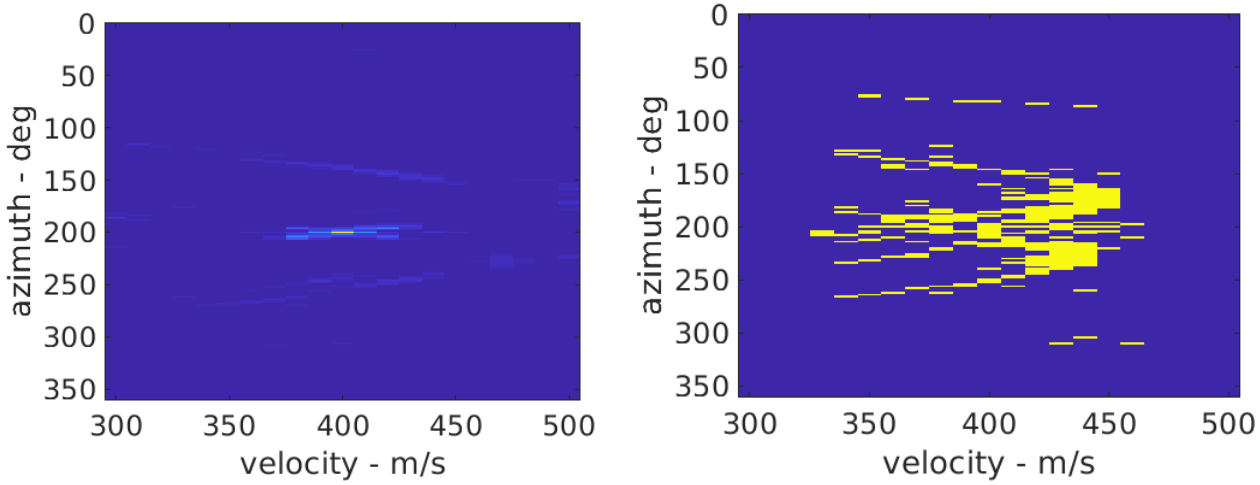

Figure IV.1.22: Likelihood function for a single source at 200° and 400 m/s, 5 dB for IS46 (left). Chan-Vese active contour applied. The yellow shape represents the contour of the likelihood maximum (right).

IV.1.2 Spectral approximation of multisource Maximum Likelihood Estimator

As previously stated, the multisource estimation was made by the monosource estimator in order to capitalise on the current development and reduce calculation time. An approximation of the extension to the multisource has been implemented in order to quantify the difference in terms of computation cost and estimation of the Parameter Of Stochastic Model (POSM), μ. This approximated multisource estimator is implemented in the frequency domain thanks to the Whittle likelihood that writes [Whittle, 1951]

$$\mathcal{L}(\mu) = \sum_{f=f_{min}}^{f_{max}} \log(\det(\mathbf{C}(f)^{-1}) - Z^H(f)\mathbf{C}(f)^{-1}Z(f) \tag{IV.1.14}$$

where $Z(f)$ is the vector of the Fourier transform of the matrix of the records at frequency f and $\mathbf{C}(f)$ is the spectral density matrix. The appendix A.3 shows the agreement between the MLE implemented in the time domain and in the frequency domain. The appendix A.4 illustrates the development of an approximated bisource MLE. Here, we show how it is possible to generalise this approximated bisource MLE for multisource purpose (i.e more than two sources as in the previous hypothesis) and to estimate a n-th source, assuming that the $n-1$ sources are identified (parameters θ, v) and characterised (signal powers).We talk here about approximated bisource or approximated multisource because we calculate the different source not simultaneously but one by one thanks to different iterations. Let the spectral density matrix containing N sources be

$$\mathbf{C}^n(f_i) = \mathbf{C}^{n-1}(f_i) + a_n(f_i,\theta,v)\sigma^2_{s_n}a_n^H(f_i,\theta,v) \tag{IV.1.15}$$

where $\mathbf{C}^{n-1}(f_i)$ is the theoretical spectral density matrix containing the $n-1$ sources information. It is possible to maximise the equation IV.1.14 with $\mathbf{C}^{-1}(f_i)$ which is written by generalising A.24

$$\mathbf{C}^n(f_i)^{-1} = \mathbf{C}^{n-1}(f_i)^{-1} - \frac{\sigma^2_{s_n}(\mathbf{C}^{n-1}(f_i)^{-1}a_n(f_i,\theta,v))(\mathbf{C}^{n-1}(f_i)^{-1}a_n^H(f_i,\theta,v))}{1+\sigma^2_{s_n}a_n^H(f_i,\theta,v)\mathbf{C}^{n-1}(f_i)^{-1}a_n(f_i,\theta,v)} \tag{IV.1.16}$$

By replacing this new expression in the equation IV.1.14 we obtain the following likelihood to be maximised

$$\mathcal{L}(\mu) = \sum_{f_{min}}^{f_{max}} \log(\det(\mathbf{C}^n(f_i)^{-1}) + \frac{\sigma^2_{s_n}|Z^H(f_i)\mathbf{C}^{n-1}(f_i)^{-1}a_n(f_i,\theta,v)|^2}{1+\sigma^2_{s_n}a_n^H(f_i,\theta,v)\mathbf{C}^{n-1}(f_i)^{-1}a_n(f_i,\theta,v)} \tag{IV.1.17}$$

Once the likelihood has been maximised, the parameter μ gives the DOA and the power of the source, the spectral density matrix in equation IV.1.15 can be updated to find other sources.

Two different ways of implementation have been studied, the first one was to simplify calculation of the multisource likelihood function to reduce the computational cost introducing approximations in the calculation of $\log(\det(\mathbf{C}^n(f_i)^{-1})$ which can be heavy due to multiple matrix inversion. To overcome this issue we calculate theoretically the determinant of $\mathbf{C}(f_B)$ once for all, defined as the mean of all the $\mathbf{C}(f_i)$ calculated in the band. The second approach was to calculate the likelihood function without approximations.

In addition to the extension of the estimator to the multisource, the detector also needs to be adapted to handle multiple SOI crossing the sensor array. To achieve this, we establish a projection of the likelihood function on the orthogonal plan of the source (n-1)-th [Mayyala et al., 2022].

Let $z(t)$ be a multisource signal with the first source estimated $a_1(f_i,\hat{\theta},\hat{v})$, it is possible to express the projector of rank $M-1$ into the orthogonal plan of $a_1(f_i,\hat{\theta},\hat{v})$ as

$$\mathbf{\Pi}^{\perp}_{a_1}(f_i) = \mathbf{I}_M - M^{-1}a_1(f_i,\hat{\theta},\hat{v})a_1^H(f_i,\hat{\theta},\hat{v}) \tag{IV.1.18}$$

which can be expressed by the singular value decomposition, leading to the full rank matrix

$$\mathbf{\Pi}^{\perp}_{a_1}(f_i) = \sum_{k=1}^{M-1} U_k U_k^H \tag{IV.1.19}$$

we note

$$\widetilde{\mathbf{U}}_{a_1}(f_i,\hat{\theta},\hat{v}) = [U_1 \dots U_{M-1}] \tag{IV.1.20}$$

the matrix of dimension $M \times (M-1)$ whose columns are the U_k components. The filter of the first source $a_1(f_i,\hat{\theta},\hat{v})$ is then defined as

$$H(f_i) = \widetilde{\mathbf{U}}^H_{a_1}(f_i,\hat{\theta},\hat{v})Z(f_i) \tag{IV.1.21}$$

We can then measure the orthogonality of this vector to the orthogonal projection of $\widetilde{\mathbf{U}}^H_{a_1}(f_i,\hat{\theta},\hat{v})a_2(f_i,\theta,v)$ by

$$F_{ms} = \sum_{f_{min}}^{f_{max}} Z^H(f_i)\widetilde{\mathbf{U}}_{a_1}(f_i,\hat{\theta},\hat{v})\widetilde{\mathbf{U}}^H_{a_1}(f_i,\hat{\theta},\hat{v})a_2(f_i,\theta,v) \tag{IV.1.22}$$

It supposed that if $a_2(f_i,\theta,v)$ is orthogonal to the first source, then the function F_{ms} is maximised. Several iterations can be done for the next possible SOI sources but with continuous decreasing size of the projector (i.e M - number of detected sources) and increasing incertitude.

Now that a multisource TS is implemented, it remains to calculate the iterative H_0 distribution in order to generate the associated p-value threshold. Lets remind the equation II.2.29 that writes

$$\boldsymbol{\xi}((\theta,v),(\theta',v')) = 2 \times \frac{\int |H(f)|^4 \sum_{k=1}^{M}\sum_{k'=1}^{M} e^{2i\pi f(\tau_k(\theta,v)-\tau_{k'}(\theta',v'))}df}{\left(\int |H(f)|^2 df\right)^2} \tag{IV.1.23}$$

In a multisource point of view,the following covariance must be calculated for each source

$$\boldsymbol{\xi}((\theta,v),(\theta',v')) = 2 \times \frac{\int |H(f)|^4 \sum_{k'=1}^{M-1} \widetilde{\mathbf{A}}(f_i,\theta,v)\widetilde{\mathbf{A}}^H(f_i,\theta',v')df}{\left(\int |H(f)|^2 df\right)^2} \tag{IV.1.24}$$

where $\widetilde{\mathbf{A}}(f_i,\theta,v)$ expresses as

$$\widetilde{\mathbf{A}}(f_i,\theta,v) = \boldsymbol{\Pi}^{\perp}_{a_1}(f_i)\mathbf{A}(f_i,\theta,v) \tag{IV.1.25}$$

However due to time computation cost which would be very huge, this detection method has not be implemented. Indeed, for the monosource the computation of $\boldsymbol{\xi}((\theta,v),(\theta',v'))$ is done once at the beginning of the process. But here, the calculation has to be done for each iteration of each detection due to the different projections in the time frequency domain with respect to the found POSM. The algorithm would not be operational in this case. Thus the monosource p-value is kept knowing that it is not sufficient until a better detector or threshold are designed.

Chapter IV.2

Blind source separation approach

IV.2.1 Independent Component Analysis (ICA)

IV.2.1.1 Methods

The objective is to estimate the wavefront parameters of multiple SOI embedded in the same recorded signals $z(t)$. An alternative approach studied here is to separate the different signals $s(t)$ in $z(t)$ to reduce the multi-source problem to a single-source one. If the separation is perfectly done, a monosource algorithm like MCML can be used on the separate source signal to estimate the POSM. To separate the different SOI, the Independent Component Analysis (ICA) method is applied [Ans et al., 1985]. This is a method of blind source separation [Stone, 2004]. This method estimates the different unknown sources from a set of observations. ICA assumes that the records $z(t)$ is a weighted sum of pure source $s(t)$. This situation is also called the "Cocktail Party Problem". Each of the M recorded signals from the array writes

$$\begin{aligned} z_1(t) &= w_{11}s_1(t) + w_{12}s_2(t) + \ldots + w_{1N}s_N(t) \\ &\vdots \\ z_M(t) &= w_{M1}s_1(t) + w_{M2}s_2(t) + \ldots + w_{MN}s_N(t) \end{aligned} \tag{IV.2.1}$$

with w_{mn} the weight of the n-th source for the m-th sensor and $s_n(t)$ the pure signal from the n-th source. The matrix notation is

$$\mathbf{Z} = \mathbf{WS} \tag{IV.2.2}$$

where $\mathbf{W}$ is the mixing matrix, fulfilled of pure signal proportions. Thus the objective of ICA is to find the demixing matrix $\mathbf{W}^{-1}$ to calculate the pure signal matrix

$$\mathbf{S} = \mathbf{W}^{-1}\mathbf{Z} \tag{IV.2.3}$$

For the over determined problem, $M > N$. Several assumptions are required for ICA. The first one is that the source signals are independent one from each other. One pure signal is not correlated to any other pure signals. However the signal mixture is not independent because the signal mixture $\mathbf{Z}$ shares the same source signals $\mathbf{S}$. The second one is that the distribution of the samples of each pure signal is not Gaussian even if the distribution of the sum of pure signals tends to a Gaussian distribution according to the central limit theorem.

The number of sources can be estimated by two methods. The first one developed in [Bouveresse et al., 2012] is the ICA block by block. The aim is to apply the ICA on at least two blocks of data (i.e we assume that the permanent sources in the different blocks are the same) with one to N supposed sources. Then we compare each block by calculating the correlations between all pairs of estimated signals from the different blocks for a given model. Then the optimal number of ICA to apply is relative to the highest dimensional ICA with an appropriate correlation. The second method is based on the building of N ICA on all data, a deflation of the pure signal on the original record is made for each model. The criterion of Durbin-Watson is calculated to estimate if it still contains structured information or if only noise is

remaining [Durbin and Watson, 1950].

Here two ICA algorithms are studied to separate the pure signals: Joint Approximate Diagonalization of Eigenmatrices (JADE) and Second-Order Blind Identification (SOBI).

JADE

Joint Approximate Diagonalization of Eigenmatrices (JADE) is an algorithm that extracts independent non-Gaussian sources from mixture including Gaussian noise [Rutledge and Bouveresse, 2013]. This algorithm relies on four different steps leading to the fourth-order cumulants array estimation.

The first step is the whitening of the centred signal mixtures $\mathbf{Z}_c$ $(M \times N_e)$ by a Principal Component Analysis (PCA) method, reducing thus the N_e number of samples. Assuming that we have N sources, a N PCAs procedure is done by the reduced singular value decomposition in order to obtain a whitening matrix that writes

$$\mathbf{B} = \sqrt{N_e} \times \mathbf{S}_{SVD}^{-1} \times \mathbf{U}^H \tag{IV.2.4}$$

where $\mathbf{S}_{SVD}$ is the singular value matrix and must not be confused with $\mathbf{S}$. The matrix $\mathbf{U}$ is the left singular vector matrix. The matrix $\mathbf{B}$ is of size $(N \times M)$. The whitened matrix of the data can now be calculated

$$\mathbf{P}_w^H = \mathbf{B} \times \mathbf{Z}_c \tag{IV.2.5}$$

where $\mathbf{P}_w^H$ is of size $(N \times N_e)$ with orthogonal and equal variance columns. The main property of this matrix is that whatever the rotation, the columns of $\mathbf{P}_w$ are still uncorrelated. The algorithm assumes that the pure signal matrix $\mathbf{S}$ can be obtained by a rotation of $\mathbf{P}_w$ resulting on not only uncorrelated but also independent columns. To find the optimum rotation we use, in a second step, the cumulants from higher-order statistics. In this problem, the algorithm calculates for each observed signals the diagonal auto-cumulants and the non diagonal cross-cumulants depending on whether the cumulants are calculated with the signals themselves or with all combinations of signals. The cumulants are defined as follow:

- The first order auto-cumulant is the expectation $\overline{m} = \mathbb{E}\{X\}$.
- The second order auto-cumulant is the variance $v = \mathbb{E}\{(X - \mathbb{E}\{X\})^2\} = \mathbb{E}\{(X - \overline{m})^2\}$.
- The third order auto-cumulant is the skewness $s_3 = \frac{\mathbb{E}\{(X-\mathbb{E}\{X\})^3\}}{\mathbb{E}\{(X-\mathbb{E}\{X\})^2\}^{3/2}} = \mathbb{E}\{(\frac{X-\overline{m}}{\sqrt{v}})^3\}$ that is a measure of the asymmetry of the probability distribution of X compared to its mean.
- The fourth order auto-cumulant is defined as the kurtosis κ and is an indirect measure of distribution flatness. When signal vectors are independent then the auto-cumulant is maximum and the cross-cumulant is zero.

The latter one is defined by the auto-cumulant as

$$\kappa(X, X, X, X) = \mathbb{E}\{(X - \mathbb{E}\{X\})^4\} - 3(\mathbb{E}\{(X - \mathbb{E}\{X\})^2\})^2 \tag{IV.2.6}$$

and the cross-cumulant for four different combinations of vectors with zero mean of $\mathbf{P}_w$ write as

$$\kappa(X_1, X_2, X_3, X_4) = \mathbb{E}\{X_1X_2 \cdot X_3X_4\} - \mathbb{E}\{X_1X_2\} \cdot \mathbb{E}\{X_3X_4\} - \mathbb{E}\{X_1X_3\} \cdot \mathbb{E}\{X_2X_4\} - \mathbb{E}\{X_1X_4\} \cdot \mathbb{E}\{X_2X_3\} \tag{IV.2.7}$$

The third step is the decomposition of the cumulant tensor into a set of $N(N+1)/2$ orthogonal eigenmatrices of dimension $N \times N$.

The final step is based on the diagonalisation of the eigenmatrices whose aim is to minimise the sum-of-squares of the non-diagonal elements corresponding to the fourth order cross cumulants. The rotation matrix allowing the diagonalisation is $\mathbf{V}$. The latter produces independent vectors by diagonalising the matrices derived from the fourth-order tensor. These vectors define the orthonormal basis of independent vectors of the original data matrix $\mathbf{Z}$. Thus the approximate of the demixing matrix $\mathbf{W}^{-1}$ writes

$$\mathbf{W}^{-1} = \mathbf{V}^H \mathbf{B} \tag{IV.2.8}$$

The expression IV.2.3 can thus be applied to calculate the pure signal matrix $\mathbf{S}$. It is also possible to calculate the signal proportion $\mathbf{W}$, not by inverting the obtained matrix $\mathbf{W}^{-1}$ which is an approximation, but using the original matrix $\mathbf{Z}$ and $\mathbf{S}$

$$\mathbf{W} = \mathbf{Z} \times \mathbf{S}^H(\mathbf{S}\mathbf{S}^H)^{-1} \tag{IV.2.9}$$

SOBI

Second-Order Blind Identification (SOBI) is a blind source separation method based on the exploitation of the source signal time coherence. In contrary to JADE, SOBI can deal with Gaussian sources [Belouchrani et al., 1997]. This method account for a temporally and spatially white Gaussian noise while the sources are either a deterministic sequence or a stationary multivariate process and the signal source are short range dependent (i.e auto regressive signal model).

The covariance matrix of the signal in function of the time lag τ writes thus

$$\begin{aligned} \mathbf{R}(\tau) &= \mathbf{A}\mathbf{R}_{ss}(\tau)\mathbf{A}^H \\ \mathbf{R}(0) &= \mathbf{A}\mathbf{R}_{ss}(0)\mathbf{A}^H + \sigma^2\mathbf{I} \end{aligned} \tag{IV.2.10}$$

The sources are assumed uncorrelated. The ICA separates the different sources by a single scale factor, we assume that they are of equal power, then $\mathbf{R}_{ss}(0) = \mathbf{I}$.
As the JADE algorithm, the first step is the whitening of the data. For this purpose, the whitening is based on the estimation of eigenstructure of $\mathbf{R}_{ss}(0)$ and σ^2. Indeed let note that $\lambda_1, \ldots, \lambda_M$ and $v_1, \ldots, v_M$ the decreasing order eigenvalues and eigenvectors respectively. The σ^2 can be estimated as the average of the smallest $M - N$ eigenvalues, N the number of estimated sources and M the number of sensors. The whitening matrix can thus be defined as

$$\mathbf{B} = [(\lambda_1 - \sigma^2)^{-(1/2)}v_1, \ldots, (\lambda_N - \sigma^2)^{-(1/2)}v_N]^H \tag{IV.2.11}$$

This whitening matrix must verify the following property

$$\mathbf{B}\mathbf{R}_{ss}(0)\mathbf{B}^H = \mathbf{B}\mathbf{A}\mathbf{A}^H\mathbf{B}^H = \mathbf{I} \tag{IV.2.12}$$

It means that $\mathbf{BA}$ is a unitary matrix. Thus the whitening process $\mathbf{P} = \mathbf{BZ}$ still obeys to a linear model.

$$y(t) = \mathbf{B}z(t) = \mathbf{B}[\mathbf{A}s(t) + n(t)] = \mathbf{V}s(t) + \mathbf{B}n(t) \tag{IV.2.13}$$

the signal part is a unitary mixture of the source signal.

Let consider the whitening of the covariance matrix

$$\overline{\mathbf{R}}(\tau) = \mathbf{B}\mathbf{R}_{ss}(\tau)\mathbf{B}^H = \mathbf{V}\mathbf{R}_{ss}(\tau)\mathbf{V}^H \tag{IV.2.14}$$

It is worth to notice that $\mathbf{V}$ is unitary and $\mathbf{R}_{ss}$ diagonal, so $\overline{\mathbf{R}}(\tau)$ is a unitary diagonalisable matrix [Horn and Johnson, 2012]. The diagonalisation of this matrix yields the relevant parameter for source separation if $\overline{\mathbf{R}}(\tau)$ has distinct eigenvalues, especially when source signals have different spectral shapes [Tong et al., 1990]. To avoid an unfortunate choice of τ leading to a close eigenvalue degeneracy and thus a wrong estimation of $\mathbf{V}$, the SOBI algorithm uses the joint diagonalisation of a set of $\overline{\mathbf{R}}(\tau_k)$, this is called the second order identifiability condition [Tong et al., 1991]. Said differently there is always a set of time lag that can satisfy the non degeneracy property if the sources have a different spectra.

$$\begin{aligned} &\forall 1 \leq k \leq K \quad \mathbf{V}^H\overline{\mathbf{R}}(\tau_k)\mathbf{V} = \mathrm{diag}[d_1(k), \ldots, d_m(k)] \\ &\forall 1 \leq i \neq j \leq m \quad \exists k, \forall 1 \leq k \leq K \quad d_i(k) \neq d_j(k) \end{aligned} \tag{IV.2.15}$$

This technique also allows a more statistical efficiency. The joint diagonalisation is defined with the joint diagonality criterion that writes

$$\mathcal{C}(\overline{\mathbf{R}}(\tau_k), \mathbf{V}) = \sum_k \mathbf{off}(\mathbf{V}^H\overline{\mathbf{R}}_k\mathbf{V}) \tag{IV.2.16}$$

where

$$\mathbf{off}(\mathbf{V}) = \sum_{1 \leq i \neq j \leq m} |\mathbf{V}_{ij}|^2 \tag{IV.2.17}$$

Then, a unitary matrix $\mathbf{V}$ is a joint diagonaliser of the matrix set when it minimises the criterion overall the set of matrices. Once the unitary matrix obtained as joint diagonaliser, the source signals are calculated by

$$\hat{s}(t) = \hat{\mathbf{V}}^H \hat{\mathbf{B}} z(t) \tag{IV.2.18}$$

the mixing matrix can also be calculated by

$$\hat{\mathbf{A}} = \hat{\mathbf{B}}^{\#} \hat{\mathbf{V}} \tag{IV.2.19}$$

where the matrix $\hat{\mathbf{B}}^{\#}$ is the Moore-Penrose pseudo inverse of $\hat{\mathbf{B}}$.

IV.2.1.2 Adaptation to broadband

It is worth noticing that both algorithms have a narrowband model, whereas the signal model considered in our work is broadband. Indeed, while in the narrowband model, the mixture is described as instantaneous (expression IV.2.2), the broadband model has convolutive mixture that writes

$$\mathbf{Z} = \mathbf{W} * \mathbf{S} \tag{IV.2.20}$$

One disadvantage of this model is that a broadband ICA algorithm can effectively retrieve the pure signals but loses the delays that interest us in the following procedure of DOA and trace velocity estimation. One idea would be to process the ICA in the frequency domain for each frequency bin similarly to the focusing technique used for MUSIC. However this is not appropriate here due to the possible permutation of the signal for each frequency bin. Some robust algorithms seem to be implemented to deal with this problem [Sawada et al., 2004] however the computational cost is really heavy, inconsistent with operational processing [Lv et al., 2005].

The method studied here is the blind equalisation of Finite Impulse Response (FIR) with the aim of transform the convolutive mixture to the instantaneous desired mixture. The term blind is relative here to the non prior assumption on the nature of the sources or how they were mixed. One of the techniques studied is the Mutually Referenced Equalizers (MRE) [Gesbert et al., 1997]. Let note the channel diversity of the array for a n-th sample and the m-th sensor :

$$z^m(t) = \sum_{k=-\infty}^{+\infty} s(k) h^m(t-k) + n^m(t) \tag{IV.2.21}$$

with h^m the impulse response of the m-th sensor. The same sequence $s(k)$ is observed through different sensors and thus different filters. The equation is linear and can be rewritten as

$$\mathbf{Z} = \mathbf{H}\mathbf{S} + \mathbf{N} \tag{IV.2.22}$$

where the matrix $\mathbf{Z}$ is obtained using a window of length L and $\mathbf{H}$ is the channel convolution matrix with more rows than columns. The blind equalizability of the previous equation is under the condition of the left invertibility of $\mathbf{H}$, it means that the matrix is full rank K (i.e the number of column of the matrix). In the absence of noise the signal recovery can be perfect at a time t

$$\Phi^H z(t) = \rho s(t - \tau_d) \tag{IV.2.23}$$

with Φ^H the vector of filter coefficients, ρ the gain and τ_d an arbitrary constant time delay. It is possible to show how a delay diversity can be used to allow a blind determination of the channel inverses. The main idea of MRE is that if Φ_i^H and Φ_{i+1}^H satisfy the equation IV.2.23 with $\tau_d = i$ and $\tau_d = i+1$ then

$$\Phi^H(i) z(t) = \Phi^H(i+1) z(t+1) \tag{IV.2.24}$$

The equalizers i and $i+1$ are said referenced to each other up to a time delay. The generalisation of the previous expression is

$$\Phi^H(k) z(t) = \Phi^H(i) z(t+i-k) \tag{IV.2.25}$$

Here, the redundant set of all the pairs of simple relationship may serve as necessary conditions for the filter to be ideal in the noise free case. These properties correspond to

$$\mathbf{\Phi}^H \mathbf{H} = \rho \mathbf{I}_K \tag{IV.2.26}$$

When noise is present it is impossible to retrieve the perfect solution but it can be constrained by a mean square error like equalisation criterion based on the following minimisation

$$J(\mathbf{\Phi}) = \mathbb{E}[E(t)]^2 \tag{IV.2.27}$$

with the error vector

$$E(t) = (\mathbf{I}_{K-1}, \mathbf{0})\mathbf{\Phi}^H z(t) - (\mathbf{0}, \mathbf{I}_{K-1})\mathbf{\Phi}^H z(t+1) \tag{IV.2.28}$$

where the found $\mathbf{\Phi}^H$ must follow the constraint of the nontriviality. It is worth to notice that each filter output serves as a training signal to update the following one.

Unfortunately, after few tests the method was a failure because the matrix $\mathbf{H}$ must be irreducible and well conditionned, but this is not the case due to the sparsity of the channel. This is due to the large delays involved in our context as compared to the sampling frequency.

Another technique named Blind Identification via Decorrelating Subchannels (BIDS) was studied [Hua et al., 2003]. This method estimates the filter term $\mathbf{H}$ by multiple decorrelation of subarray in order to estimate the instantaneous mixture. But the method is not valid in our context due to the sparsity of the number of sources.

Despite of SOBI's functionality on narrowband signal, the idea of the ICA has been abandoned but gives another idea of exploiting the sparsity of the solution: the dictionary coding.

Chapter IV.3

Dictionary coding

IV.3.1 Methods

The dictionary coding, is a signal processing method that aims to efficiently represent complex data by breaking it down into a combination of few terms taken from a predefined dictionary [Olshausen and Field, 1997]. The resulting model is called a sparse model because of the simpler way to describe a phenomenon [Chardon, 2012]. The sparsity of a model is a useful constraint because when modelling complex phenomena, it is common to work with a large number of potential variables, which not all necessarily contribute to the prediction or understanding of the phenomenon being studied. Furthermore, these models can be prone to over-fitting, where the model adapts too precisely to the training data, thus capturing noise and losing its ability to generalise to new data.
The dictionary, in another side, consists of a set of elementary explanatory variables also called atoms. The dictionary is predefined and remains fixed throughout the process but the dictionary can be learned from the input data itself. This means that the dictionary can be adapted to best represent the specific characteristics of the observed data which are used to represent the input data. When the dictionary is learned, we refer to dictionary learning. The explanatory variables used here are the delays between sensors pairs for each back-azimuth and trace velocity considered or the 2D likelihood function for one considered synthetic incident wavefront. Two widely used methods in this field are Least Absolute Shrinkage and Selection Operator (LASSO) and the Orthogonal Matching Pursuit (OMP). They combine two objectives: regularisation to control the complexity of the model and variable selection to identify the most important variables. These techniques are invaluable in particular for data compression, image reconstruction and detecting patterns in complex signals.

IV.3.1.1 The use of Least Absolute Shrinkage and Selection Operator (LASSO)

The Least Absolute Shrinkage and Selection Operator (LASSO) algorithm is a regression algorithm introduced in Tibshirani [1996]. The aim is to solve an optimisation problem where the cost function is written as

$$\min_{\beta \in \mathbb{R}^p} \frac{1}{2} \|X - \mathbf{D}\beta\|_2^2 + \lambda \|\beta\|_1 \tag{IV.3.1}$$

where D is the dictionary of all elementary explanatory variables, X the observation and β the p coefficients to estimate in order to fit the dictionary with the observation. The variable λ is a regularisation parameter, when $\lambda \geq 0$. In the case of $\lambda = 0$ we have an Ordinary Least Squares (OLS) problem. It is worth to notice that the LASSO regularisation is a combination of two terms. The first one which measures the difference between the values predicted by the model and the actual values observed (i.e the OLS) and the second one, the L1-norm which is proportional to the sum of the absolute values of the model coefficients. It induces sparse regularisation by favouring solutions with a minimal number of significant variables. In fact, by minimising this penalty, some of the model's coefficients are forced to be zero, which is equivalent to a selection of variables. Figure IV.3.1 represents the difference between the L2-norm (i.e also called ridge regression) and the L1-norm. It illustrates on a 2-D case how coefficients can be forced to be zero.

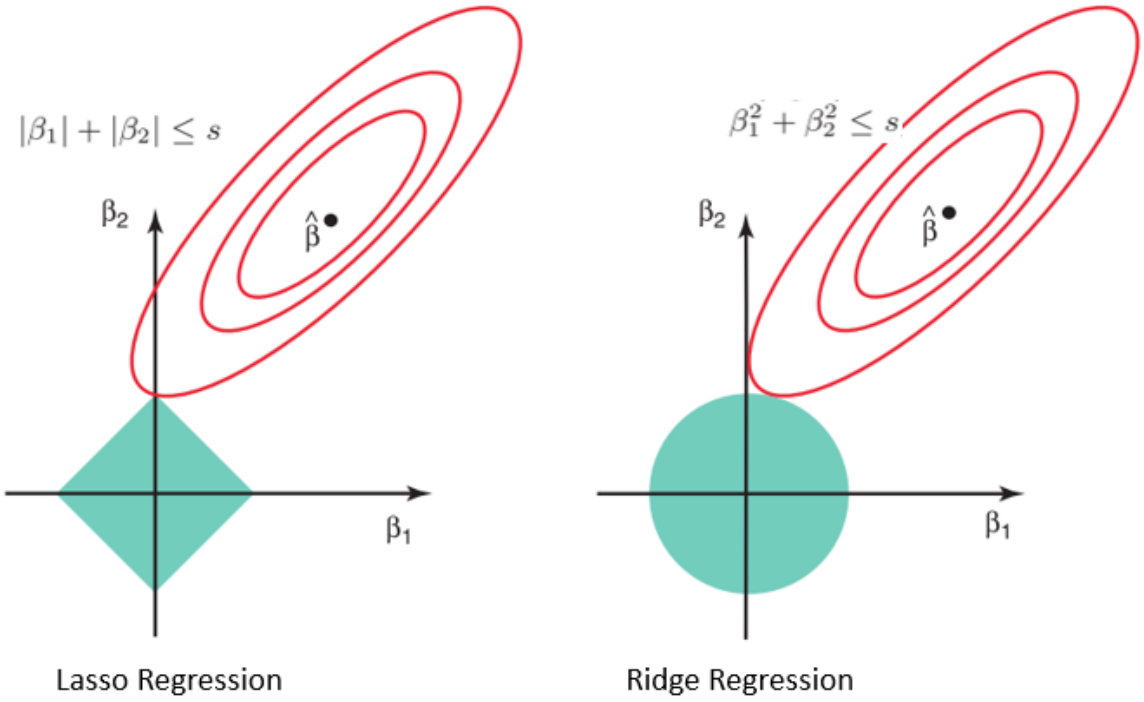

Figure IV.3.1: Illustration of the difference between the solution of a L1-norm and a L2-norm respectively. The green square and circle represent the constrained regions and the red ellipses are the least square errors. When the red ellipse touches the constrained region of LASSO, one coefficient is set to zero (extracted from [DataCamp-Team]).

IV.3.1.2 The Orthogonal Matching Pursuit (OMP)

The Orthogonal Matching Pursuit (OMP) is another sparse signal reconstruction method first used for wavelet decomposition [Pati et al., 1993]. The main goal is to iteratively choose the atom from the dictionary that maximises the correlation with the input by dot products method. This can be written as

$$j = \arg\max_j \mathbf{D}(:, j)q \tag{IV.3.2}$$

where D is the dictionary, j represents the index of the selected atom and q the residuals, between the atom of the dictionary and the atom models, that are initially equals to the input data. When the atom is correctly chosen, coefficients for each atoms have to be updated in order to reconstruct properly the input data. This is done by a L2-norm

$$\hat{\alpha} = \arg\min_{\alpha \in \mathbb{R}^p} \|X - \mathbf{D}\alpha\|_2^2 \tag{IV.3.3}$$

where α is atom coefficients. The cost function is then similar to the previous one but without the L1-norm regularisation. Then the residuals are updated by

$$q = X - \mathbf{D}\hat{\alpha} \tag{IV.3.4}$$

The stopping criterion can be either the number of atoms or the remaining errors between the input data and the selected atoms. Thus, when this stopping criterion is reached, the whole model is expressed as a summation of the K chosen atoms with their adapted coefficients

$$\hat{X} = \sum_{k=1}^{K} \mathbf{D}(:, j_k)\hat{\alpha}_{j_k} \tag{IV.3.5}$$

where $\hat{X}$ is the sparse representation of X resulting from the OMP. Figure IV.3.2 illustrates this method of signal reconstruction by the OMP when only the black dots are available as input. The regression at the end perfectly match the initial signal thanks to an adequate dictionary and an accurate selection of atom coefficients.

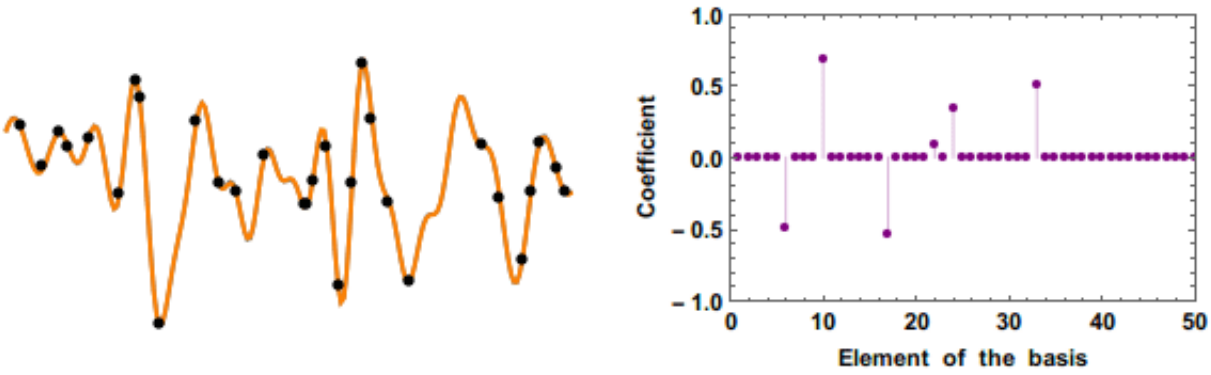

Figure IV.3.2: Retrieving an unknown signal from a small number of measurements (black dots) by OMP method (extracted from [Bertolotti]). It is worth noticing that the summation only of a few atoms can retrieve a complex signal. The majority of the coefficients are equal to zero, this is why it is called a sparse method.

IV.3.2 Delays as atoms

The DOA estimation by the dictionary coding is already mentioned in papers, in particular with the LASSO algorithm [Chardon et al., 2019].
One of the possibilities to estimate the wavefront parameters from the signal is to calculate the accurate delays via the spectral density matrix of the records. The cross terms of the spectral matrix for one source signal, $\mathbf{C}$, are theoretically equal to

$$\mathbf{C}_{i,j}(f) = \alpha e^{2i\pi f(\tau_j - \tau_i)} \tag{IV.3.6}$$

where α is the amplitude, i and j are two sensors index from the array with $i \neq j$. The coefficients of the spectral density matrix are related to the intersensors delays. The dictionary is then fulfilled by intersensors delays for each possible DOA and trace velocity without adding a prior value of amplitude α to the SOI. The dictionary includes both the real part and the imaginary part of the spectral density matrix components. It can be written as

$$\mathbf{D}(n,k) = \begin{bmatrix} \mathbb{R}\{e^{2i\pi f(\tau_2(1,1)-\tau_1(1,1)}\} & \dots & \mathbb{R}\{e^{2i\pi f(\tau_2(Laz,Lve)-\tau_1(Laz,Lve)}\} \\ \vdots & \vdots & \vdots \\ \mathbb{R}\{e^{2i\pi f(\tau_M(1,1)-\tau_{M-1}(1,1)}\} & \dots & \mathbb{R}\{e^{2i\pi f(\tau_M(Laz,Lve)-\tau_{M-1}(Laz,Lve)}\} \\ \mathbb{I}m\{e^{2i\pi f(\tau_2(1,1)-\tau_1(1,1)}\} & \dots & \mathbb{I}m\{e^{2i\pi f(\tau_2(Laz,Lve)-\tau_1(Laz,Lve)}\} \\ \vdots & \vdots & \vdots \\ \mathbb{I}m\{e^{2i\pi f(\tau_M(1,1)-\tau_{M-1}(1,1)}\} & \dots & \mathbb{I}m\{e^{2i\pi f(\tau_M(Laz,Lve)-\tau_{M-1}(Laz,Lve)}\} \end{bmatrix} \tag{IV.3.7}$$

The indices of $\mathbf{D}(n,k)$ represents respectively the number of a considered sensors combination, n, and the indices of a case in (θ, v), k. The dictionary is then of dimension $(N_{combinations} \times 2) \times (Laz \times Lve)$ where $N_{combinations}$ is the total number of sensor pair combinations for the array. The dimension is multiplied by two in order to reflect the real and the imaginary part of the exponential. Then Laz and Lve represent the number of azimuth and apparent velocity bins respectively. The dictionary can be quickly huge, for example, for a nine-sensor station and a grid step of 2° and 10 m/s between 300 m/s and 500 m/s the dictionary has a size of 72×3801. This dictionary is then compared to the non diagonal

term of the estimated spectral density matrix $\mathbf{C}$ at the central frequency of the bandwidth. No significant improvement is observed with several frequencies, however, it results in an increase of computation time.

The LASSO and the OMP algorithms are used, the parameters λ can be tough to adjust. That is why the LASSO is configured by default with a large λ range (i.e 100 by default). Then the λ with the higher amplitude coefficient α is used in order to select the N main maxima of the function related to the N sources detected. The possibility to constrain the number of non zero atoms leads to worst results. For the OMP the number of atoms to be non zero is equal to the number of sources. The similarity between two close atoms can be high, to avoid the selection of N maxima around the main peak we constrain the maxima to be ± 5 degrees apart to each other.

The following figures IV.3.3 show the result of LASSO for three sources at 100°, 200° and 300° with 340 m/s at 5 dB. The left-hand figure represents the result of LASSO for an exact spectral density matrix while the right-hand figure represents the result for the estimated spectral density matrix. The red dots represent the accurate atoms of the sources.

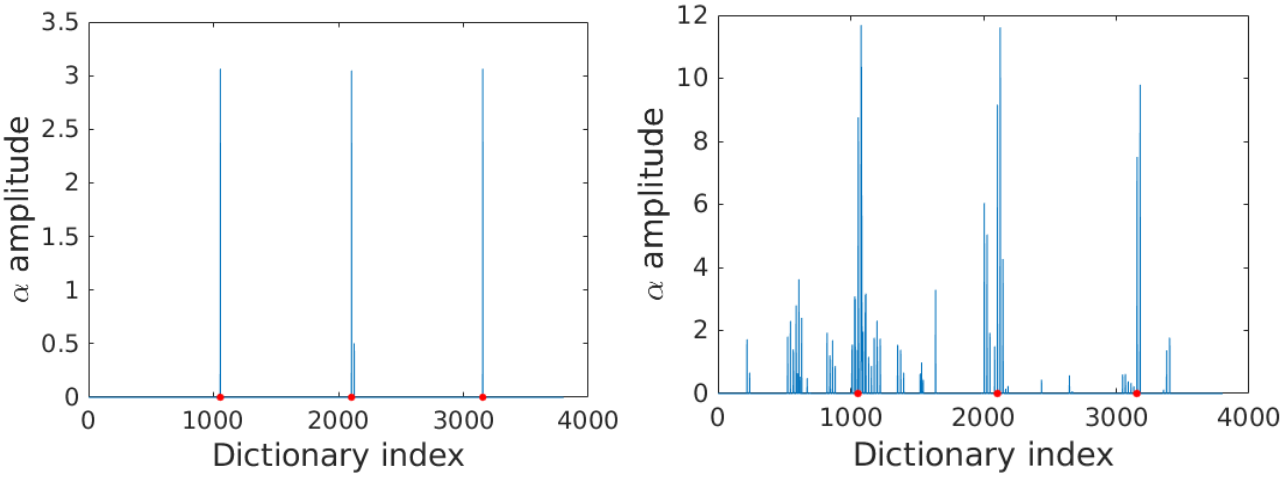

Figure IV.3.3: Dictionary coding with LASSO on theoretical (left) and real (right) intersensors delays for the three sources at 5 dB located by the red dots at [100, 200, 300]° and 340 m/s. The frequency band is [0.8 - 1] Hz.

There is a true difference between the ideal and real cases when the spectral density matrix is estimated. On the real case many atoms are involved but the resulting three maxima are [102, 200, 300]° at [360, 340, 360] m/s thanks to the 5 degrees difference imposed between the selected atoms. The discrepancy between theoretically and real case is that the spectral density matrix is badly estimated as shown previously with the multisource MLE. Moreover the computational cost is high. While the dictionary took only 0.6 s to be computed, a study on 200 signals has shown that LASSO computes between one and ten minutes with a mean at around five minutes. This method with this kind of atoms is not operational at all. To be more competitive, a calculation of λ has to be done efficiently but the λ range changes between one case to another and depends on the SNR of the sources.

However a test on 200 synthetic signals at [0.8 - 1] Hz containing three sources at [100°, 200°, 300°] and [340, 400, 450] m/s with 5 dB shows the following results illustrated by the figure IV.3.4.

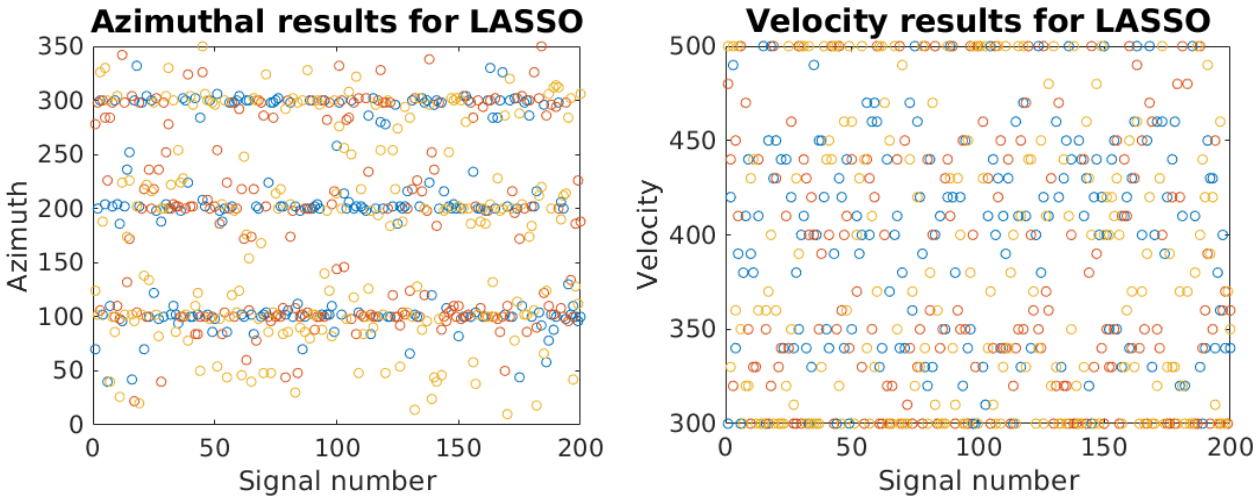

Figure IV.3.4: Dictionary coding with LASSO on 200 synthetic signals with three sources at [100°, 200°, 300°] and [340, 400, 450] m/s at [0.8 - 1] Hz with 5 dB. The figure illustrates the azimuth (left) and velocity (right) estimates of LASSO as a function of the number of signals.

It can be observed at the first order that the velocity can not be resolved by LASSO, indeed the estimation of the velocity is nearly random with an accumulation at the grid border and some estimations around the generated trace velocity. On the other hand the estimation of the azimuth are clustered along fixed azimuths. High amount of errors are seen while the SNR is high (5 dB). Taking into account the high computational time and the mediocre results, the LASSO algorithm is not efficient for this kind of atoms.

The next following figure IV.3.5 shows the results for the OMP for three sources at 100°, 200° and 300° with 340 m/s at 5 dB. Similarly to the previous figures, the left-hand figure represents the result of the OMP for an exact spectral density matrix while the right-hand figure represents the results for the estimated spectral density matrix. The red dots represent the accurate atoms of the sources.

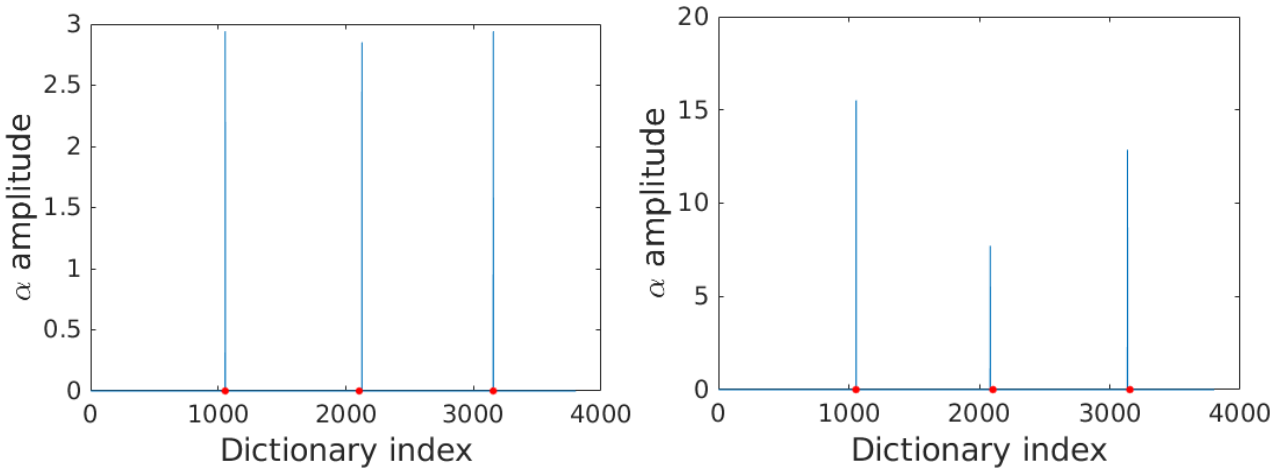

Figure IV.3.5: Dictionary coding with OMP on theoretical (left) and real (right) intersensors delays for the three sources at 5 dB located by the red dots at [100, 200, 300]° and 340 m/s. The frequency band is [0.8 - 1] Hz.

As opposed to LASSO, there is a similarity between the ideal and real cases when the spectral density matrix is estimated. On the real case just three atoms are involved and the resulting three maxima are [100, 198, 298]° at [350, 340, 360] m/s. Here the computational cost is much smaller than the one

of LASSO. A study on 200 signals shows that the OMP computes in less than 0.1 s with a mean computational cost of 0.0104 s. This method can be operational if the results are accurate for a wide range of signals that is why the same test has been done on the OMP with the same signals described previously for LASSO. The following figure IV.3.6 illustrates the results of this test for the OMP.

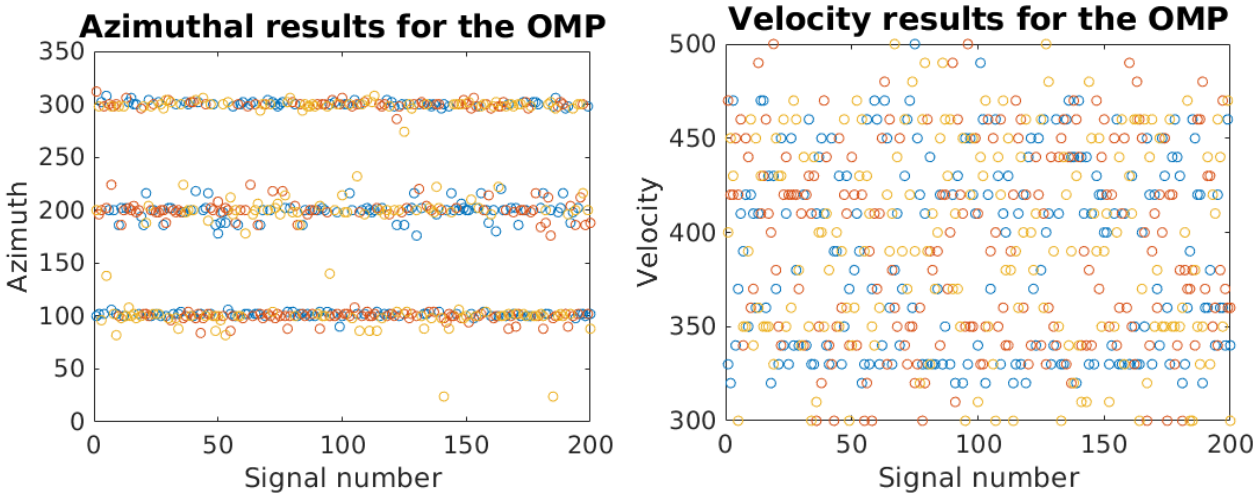

Figure IV.3.6: Dictionary coding with OMP on 200 synthetic signals with three sources at [100°, 200°, 300°] and [340, 400, 450] m/s at [0.8 - 1] Hz with 5 dB. The figure illustrates the azimuth (left) and velocity (right) estimates of LASSO as a function of the number of signals.

As for the previous example the estimation of the trace velocity is poor however the azimuth results are accurate even if some errors are clearly visible. Taking into account the low computational cost and the relative good result in azimuth we keep the OMP with this kind of atoms for the next large protocol of evaluation between the different algorithms.

IV.3.3 Likelihood function as atoms

Another kind of atom was studied with LASSO and the OMP, corresponding to the 2D likelihood function given by the monosource MLE. The 2D likelihood is vectorised rows by rows and normalised by the maximum of likelihood to avoid any bias by the amplitude of the likelihood. The SNR of the signals used to build the dictionary is 0 dB. Thus each atom is a long vector of the likelihood function for one source at one azimuth and one trace velocity. This can be expressed as

$$\mathbf{D}(\theta, v) = \begin{bmatrix} \mathcal{L}_{(1,1)}(1,1)/\max(\mathcal{L}_{(1,1)}(\theta, v)) & \dots & \mathcal{L}_{(Laz,Lve)}(1,1)/\max(\mathcal{L}_{(Laz,Lve)}(\theta, v)) \\ \vdots & \vdots & \vdots \\ \mathcal{L}_{(1,1)}(Laz, Lve)/\max(\mathcal{L}_{(1,1)}(\theta, v)) & \dots & \mathcal{L}_{(Laz,Lve)}(Laz, Lve)/\max(\mathcal{L}_{(Laz,Lve)}(\theta, v)) \end{bmatrix} \quad \text{(IV.3.8)}$$

where $\mathcal{L}_{(1,1)}(\theta, v)$ is the likelihood amplitude for the bin (θ, v) considered for a source generation located at the first bin of azimuth and trace velocity. The dictionary is then of size $(Laz \times Lve) \times (Laz \times Lve)$, it is bigger than the dictionary with delays because for the same example taken previously this dictionary would be of size 3801×3801. The goal is thus to recover the N sources by picking a number of atoms equal to the number of sources by stating that the likelihood function of the MLE in a multisource condition is a sum of different monosource likelihood in the dictionary. The settings of LASSO are the same as the previous case, in other words 100 λ are studied by the algorithm and the λ with the highest α coefficient in the results is taken in order to select the N sources. For the OMP, the parameter that selects three atoms is not taken because the stopping criterion with the minimum residual at 0.5 gives better results. Both algorithms are tested with the same input signals used as previously. The results of both algorithms are illustrated in the following figures IV.3.7 and IV.3.8.

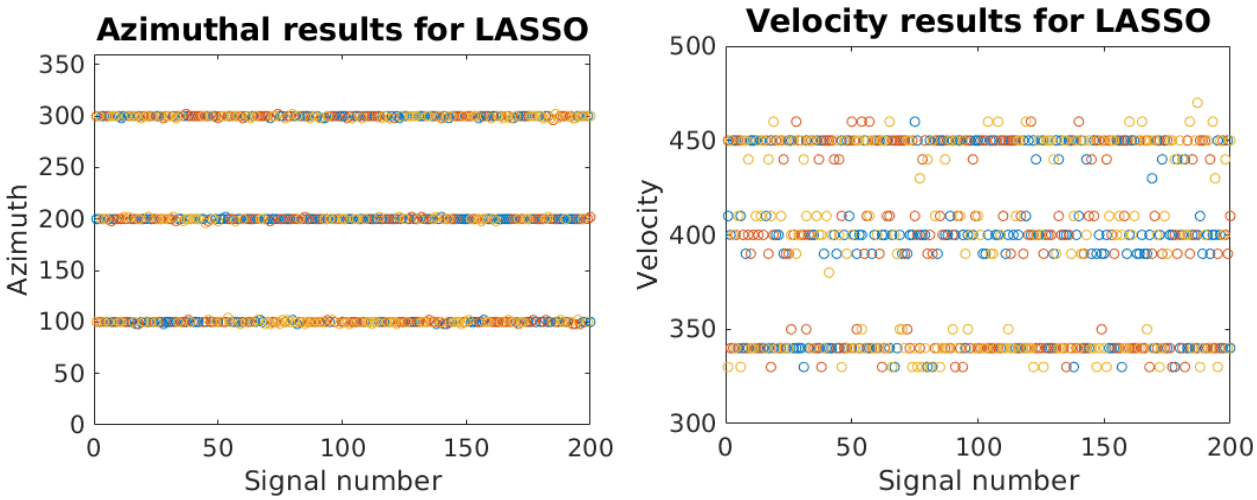

Figure IV.3.7: Dictionary coding with LASSO on 200 synthetic signals with three sources at [100°, 200°, 300°] and [340, 400, 450] m/s at [0.8 - 1] Hz with 5 dB. The figure illustrates the azimuth (left) and velocity (right) estimates of LASSO as a function of the number of signals.

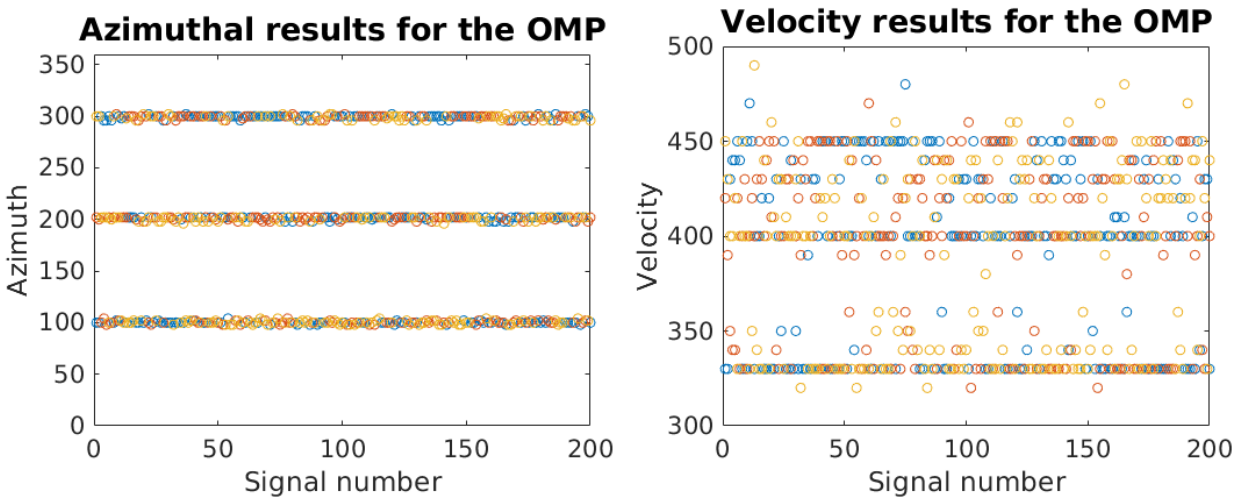

Figure IV.3.8: Dictionary coding with OMP on 200 synthetic signals with three sources at [100°, 200°, 300°] and [340, 400, 450] m/s at [0.8 - 1] Hz with 5 dB. The figure illustrates the azimuth (left) and velocity (right) estimates of OMP as a function of the number of signals.

The results are better than obtained previously both for azimuth and trace velocity estimation. The estimation of azimuths are almost all correct whereas the estimation of the apparent velocities seems to be accurate enough to be competitive with the other algorithms. It should be noted that when there is error on azimuth or apparent velocity the algorithm makes a mistake of one atom in the majority of the cases. LASSO is more robust to estimate the velocity than the OMP. Concerning the computation time, the building of the dictionary is more expensive due to the iterative MLE processing in order to cover all the grid nodes. The computation time of the dictionary is around 25 minutes on a DELL precision 3260 with 12 cores. It has to be done once for all for a frequency band. The computation time of LASSO is however faster than for the previous atoms as it takes around 12s to compute. The OMP is faster than LASSO with a mean computation time of one third of a second. This final algorithm is also adopted for the large comparison protocol.

Chapter IV.4

Comparison of the multisource approaches

IV.4.1 On ground truth controlled data

The previous parts concerned the state-of-the-art multisource estimation methods but also to the novel developed methods. Some of the latter have proved to have potential, while others were not selected. (i.e broadband ICA for example). The algorithms selected for the study are the following ones

- MUltiple SIgnal Classification (MUSIC) with focusing method to be adapted to broadband signals
- Test of Orthogonality of Projected Subspaces (TOPS)
- Fisher in the frequency domain
- Minimum Variance Distortionless Response (MVDR) with or without diagonal loading
- Monosource MLE with iterative SOI deflation
- Monosource MLE with the 2D peak finder
- Spectral MLE with or without simplification for computational cost
- OMP with delay atoms
- LASSO with monosource likelihood function atoms
- OMP with monosource likelihood function atoms

However there is a need to distinguish them in terms of accuracy and computation time cost. In order to do that, a test on ground truth controlled data was done. This test was performed using synthetic signals as used in the section II.2.2. By the same process, the SOI is generated randomly and delayed in accordance with the considered DOA, trace velocity and the M sensor locations of the chosen geometry. The SOI of the M sensors are then filtered in the selected frequency band with an order 2 Chebychev filter and windowed according to the bandwidth (twenty times the central period of the bandwidth refereeing to needed improvement developed in IV.1.1.1). The source of noise is a white Gaussian noise. A protocol of test has been set up with a 1000 generated signals with three sources per case that can be described as

- A grid step equal for all the algorithms with an azimuth grid step of 2° and an apparent velocity grid between 300 and 500 m/s with a step of 10 m/s.
- Random azimuth between 0 and 360 with a difference between the source angles of at least 10 degrees for the [0.1 - 0.12] Hz frequency band, 5° for the [0.50 - 0.64] Hz frequency band and the [3.20 - 4.03] Hz frequency band. The first, eighth and sixteenth band from the third octave decomposition are indeed selected. The random sources are taken with an angle difference in order to take into account the higher errors that we can make with the used station IS31. Indeed the

higher error is 5° for [0.1 - 0.12] Hz, then we decide to have a safety margin choosing 10° with IS31 due to large lobe effect at this frequency band. The 5° for the other bands is chosen because we do not expect to be accurate under this limit. The errors are calculated with the MLE expression of the error because it corresponds asymptotically to the CRB [Cramér, 1999].

- Random speed between 340 and 450 m/s.
- Use of equal SNR between sources and variable SNR between sources in the set [-5, 0, 5] dB.
- Use of IS31 and IS46 station geometries (figure II.2.3). The same angle difference is chosen for IS46 in order to have the same method of signal generation.

Two metrics are used to quantify the accuracy of the algorithms. The first is to calculate the error between the estimates and the ground truth. This is done by calculating the six possible azimuth error combinations and then minimising them. The second metric consists of measuring the amount of "accurate estimations" made. For any error greater than 10° or 50 m/s the estimate is considered erroneous and considered as a false estimation. Those values are chosen to be the acceptable value of errors in order to well characterise the events. The aim is to plot the false estimation rate as a function of the SNR or the global error made by the estimators.

The figure IV.4.1 represents the false estimation sources percentage in function of the SNR. In this case and for the following figures IV.4.2, IV.4.3 and IV.4.4 the SNR are equal between the sources. Each subplot shows the results of a category of algorithm, the first one is from the state-of-the-art algorithms, the second subplot refers to the developed algorithms based on MCML and the last one refers to dictionary coding methods. The frequency band used is the low frequency band [0.1 - 0.12] Hz and the station of study is IS31. The percentage of false estimation is really high whatever the SNR or the algorithm used. The MUSIC algorithm is the best state-of-the-art algorithm for this configuration. The percentage of false estimation starts from 49.6 % at 5 dB and rises to 83.4 % at -5 dB and followed immediately by the Capon algorithm with approximately the same order of percentage. For the MCML extension, the best version is the iterative signal deflation with 43.3 % of false estimations at 5 dB and rises to 68.9 % at -5 dB. The algorithm constructed with a multisource spectral density matrix for its part has 54.5 % of false estimation sources at 5 dB and 76.4 % at -5 dB. The latter ones are more accurate than the state-of-the-art algorithms especially at low SNR. Finally the orthogonal matching pursuit (OMP) with likelihood grid as atoms has 69.6 % of false estimations at 5 dB and 76.1 % at -5 dB being also more accurate than the state-of-the-art algorithms at low SNR but less than the MCML based algorithms. It should be noted than even if MCML with the iterative signal deflation is the best algorithm in this case, a high failure rate is observed mainly due to a large array response at this frequency.

The figure IV.4.2 represents the false estimation percentage in function of the SNR at IS31 for the [0.50 - 0.64] Hz band. As previously MUSIC is the best state-of-the-art algorithm with 4.5 % of false estimations at 5 dB and rise to 27 % at -5 dB. In contrast, the iterative signal deflation based on MCML has 0.5 % of false estimations at 5 dB and it is rising to 2.8 % at -5 dB. The worst result for this algorithm is better than the best score at 5 dB for MUSIC. The spectral MLE algorithm has a similar false estimation percentage starting from 1 % at 5 dB to 4.7 % at -5 dB. This algorithm is also far much better than MUSIC. In another side, the best dictionary coding are both methods (OMP and LASSO) using the likelihood grid as atoms. The OMP has 5.4 % of false estimations at 5 dB and 20 % at -5 dB. For LASSO in contrary the algorithm has 8.3 % of false estimations at 5 dB, it is indeed higher than for the OMP but when the SNR decreases the false estimations rise to only 13.9 %, it shows that this algorithm seems more robust to SNR decrease than the OMP. Thus, in brief, the OMP is equivalent to MUSIC, the best state-of-the-art algorithm but LASSO, the spectral MLE and above all the iterative signal deflation are better than the actual state-of-the-art algorithms in this case.

The figure IV.4.3 represents the false estimation percentage in function of the SNR at IS31 for the [3.2 - 4] Hz band. The best state-of-the-art algorithms are Capon and MUSIC with a false estimation percentage of 2.3 % at 5 dB rising to 18.3 % at -5 dB and 3.7 % at 5 dB rising to 21 % at -5 dB for Capon and MUSIC respectively. The results are similar between this frequency band and the previous one for MUSIC indicating a stable behaviour with medium and high frequency. In contrast for the MCML based algorithms, the iterative signal deflation has a stable false estimation percentage of around 0.4 % across

the SNR from 5 dB to -5 dB showing the robustness of this algorithm. The MCML based algorithm with the multisource spectral model has 1.1 % of false estimations at 5 dB and 2.1 % at -5 dB. The MCML based algorithms are better than the state-of-the-art algorithm especially at low SNR. The dictionary coding also shows some interesting results. The first one is that the likelihood based algorithm with LASSO has a stable range of false estimations between 1.2 % and 0.9 % whereas the false estimations are slightly higher with the OMP ranging from 0.5 % to 18.4 %. The SNR impacts the algorithm greatly at -5 dB because the errors at -2.5 dB is only 1.6 %. Once again the MCML based algorithms and particularly the iterative signal deflation are more accurate than all the other tested methods.

The last example shown by the figure IV.4.4 concerns signals with equal SNR at [0.50 - 0.64] Hz, at the 4 sensor station IS46 with a larger aperture (i.e around 2.7 km). Theses results must be put in perspectives with those of the figure IV.4.2. The first point is that the false estimation percentage are greater overall algorithms mainly due to the larger aperture and fewer sensors. The second point is that the state-of-the-art algorithms are not able to find multisource events in this configuration. Indeed the algorithm with the lower false estimation percentage is the Capon algorithm ranging from 66 % to 75.5 %. In contrast MUSIC which seemed to be the best state of algorithm has a 90 % of false estimations, showing how high is the geometry impact on this estimator, even restricting the monosource estimation. In another hand, the iterative signal deflation algorithm has better results with at first a false estimation percentage from 6.8 % at 5 dB, stable until -2.5 dB with 13.8 % but high false estimation with 41.5 % at -5 dB indicating how the SNR impacts more sharply this algorithm. The spectral MLE based algorithm for its part has a higher error ranging from 12 % at 5 dB to 43.7 % at -5 dB. However the increasing errors seems to be more smooth because the false estimations is 29 % at -2.5 dB. The dictionary coding methods have also better results than the state-of-the-art algorithm. Indeed, both the OMP and LASSO algorithms with the likelihood atoms have a false estimations range from 16.5-19.5 % at 5 dB to 50 % at -5 dB. Thus, the iterative signal deflation is once again the best estimator in this case followed by the spectral MLE algorithm.

As a conclusion for the equal SNR cases on synthetics, the multisource estimation is tough at low frequency with a lot of false estimations for every algorithms, the accurate estimations is increasing with frequency and number of sensors. For each studied frequency band the best state-of-the-art algorithms were MUSIC and Capon, already known for their robustness. However, they show their limits not only with low frequency and SNR decrease but also with array having fewer sensors and larger aperture. Indeed, not even the first source is correctly estimated, making the common monitoring impossible for station with few sensors. And in general they have poorer correct estimation than the developed methods. Indeed overall developed ones, the iterative signal deflation and the spectral MLE methods have the greatest accuracy in percentage of estimated events. The multipeak selection algorithm is not as well accurate as the other algorithms and the fast spectral MLE algorithm with simplification shows a degraded accuracy compared to the formal algorithm without simplifications. In many cases, the OMP and especially the LASSO algorithm with likelihood atoms have accurate results compared to the state-of-the-art algorithms. However they do not exceed the accuracy of the two previous stated algorithms. To conclude on the tests with equal SNR sources, both the iterative signal deflation and the spectral MLE algorithms provide the most accurate results. But what if the SNR is varying between the sources? This being closer to reality.

For [0.1 - 0.12] Hz, [0.50 - 0.64] Hz and [3.20 - 4.03] Hz at IS31 and [0.50 - 0.64] Hz at IS46 the tests are also done with different SNR comprised in the set [-5, 0, 5] dB in the same generated signals. The figures IV.4.5, IV.4.6, IV.4.7 and IV.4.8 represent the false estimation rate in function of the 95th quantile of the absolute errors on azimuth for each algorithm. Each figure is composed of three scatter illustrating the accuracy of the estimator with sources at 5, 0 and -5 dB. On the figure IV.4.5, it should be noted that the interference of several sources, even with a minimum difference of 10° in azimuth implemented, has a significant effect on the ability to correctly estimate the sources, even for the first one. Indeed, for 5 dB sources, while the MLE based algorithms have between 4.2 % and 7.2 % of false estimations, the iterative signal deflation algorithm in the lead followed by spectral MLE with 5.9 %, the other algorithms have a larger false estimation rate. The following one is the dictionary coding with LASSO and its likelihood atoms with 15 % of false estimations. The gap is growing with the state-of-the-art algorithms with a false estimation rate of 23.7 % with the Capon regularised, 27 % with MUSIC, 30.7 % with the classical

Capon and 40.6 % with the Fisher statistic. Then, the other dictionary coding algorithms and TOPS are following. Note that the latter does not appear on the graph due to the 100 % of false estimation rate. The absolute error on azimuth is between seven and nine degrees for all the different algorithm except TOPS but it is in accordance to the high errors made at low frequency. For the source with SNR at 0 dB the iterative signal deflation has a false estimation rate of 43.6 % while the second best algorithm is the spectral MLE with 64.5 % of false estimations rate. The state-of-the-art algorithms like MUSIC or Capon have 65.5 % and 68.3 % of false estimations rate, respectively. The fast spectral MLE has 78.5 % of false estimations showing a discrepancy with the classical spectral MLE. Thus, only the iterative signal deflation contrasts with the group even if the error are still large (around 9°). However, the sources at -5 dB are globally not well estimated by the different algorithm, the iterative signal deflation showing 87 % of false estimations rate while all the other algorithm miss are superior to 90 %. Therefore, even if the global absolute error on azimuth is high the best algorithm in terms of accurate estimation is the iterative signal deflation.

The figure IV.4.6 illustrates the false estimations rate and the errors for the [0.50 - 0.64] Hz band at IS31. The first scatter is about the sources at 5 dB estimated by the different algorithms. The iterative signal deflation and the LASSO dictionary coding have 0 % of false estimations rate and with 1° and 2° of absolute azimuth errors respectively. Fisher and MUSIC have the same absolute azimuth errors and false estimation rate of 0.1 % and 2°. TOPS is not illustrated due to 100 % of false estimation rate. Then, it is worth to notice that all the different algorithms, except TOPS and the OMP with delay atoms (90.6 % of false estimation rate), are suitable for this case, the iterative signal deflation in the lead with absolute error around 0.1° while the other algorithms have an absolute error lower than 3°. Then, trying to estimate the sources at 0 dB and -5 dB leads to greater false estimation rate and error on azimuth estimation. Indeed the estimation for the sources at 0 dB are missed at 0.6 % with an absolute error of around 2.1° by the iterative signal deflation. Both the formal spectral and fast MLE algorithms are following with 1.9 % and 4.5 % of false estimation rate and an absolute error of around 3° while MUSIC is close to the fast spectral MLE with 5.5 % of false estimation rate for 3° of absolute azimuth errors. The Capon spectrum also has a low false estimation rate of 16.3 % with an absolute error of 4°, far behind the best algorithm nevertheless. It is worth to notice that the multipeak MLE algorithm is not adequate for this estimation with 71 % of false estimations and almost 5° of absolute error. Finally, the estimation of the source at -5 dB leads to a failure for most of the algorithms except the iterative signal deflation with 24.4 % of false estimated event and around 4° of absolute error. The second algorithm with the lowest false estimation rate and absolute error is MUSIC with 68.7 % of false estimations and an absolute error of 7°. Thus, the best algorithm in terms of accurate estimate and absolute error is the iterative signal deflation which is even able to detect the third source at -5 dB.

The figure IV.4.7 shows the results for [3.2 - 4] Hz. The global false estimation rate is really low for all the different algorithms. At 5 dB, the worst one is the OMP with delay atoms at 14.8 %. The false estimation rate even achieves 0 % for MUSIC, Fisher and the dictionary coding using LASSO with the likelihood atoms. The different MLE based algorithms, Capon spectrum with or without regularisation and the OMP with likelihood atoms are close to the best algorithm with between 0.1 and 0.2 % of false estimations. The error on azimuths are the lowest with the MLE based algorithm with a value lower to one degree. All the others have an error equal to 1°. The algorithm with the lowest false estimation rate at 0 dB is MUSIC with 3 % followed by the Capon spectrum at 5 %, the spectral MLE and the iterative signal deflation around 6 % but with a lower absolute error of 0.6/0.7° compare to MUSIC which has an absolute error higher than one degree. However, the errors being lower to the grid step for azimuth (i.e 2 degrees) the errors are then comparable, no conclusion can be drawn from this last observation. It should be noted that TOPS is able to estimate different sources with a relative low false estimated events rate of 27 % showing that the algorithm is in operating condition but maybe at high frequency. Finally the last sources at -5 dB is not well estimated by the different algorithms, all the false estimation percentage being superior to 90 %. Thus, the best algorithm in terms of accurate estimation and absolute error are MUSIC, Capon, the spectral MLE and the iterative signal deflation.

The last figure IV.4.8 represents the same experiments as in the figure IV.4.6 but done with the station IS46 composed of four sensors and a large array aperture. The first source at 5 dB is well estimated by every algorithms except TOPS, MUSIC and the dictionary with OMP and delay as atoms which have

between 75 and 85 % of false estimated events. Algorithms like the spectral MLE, the fast spectral MLE, both dictionary coding (i.e LASSO and OMP) with the likelihood function as atoms even have 0 % of false estimated events with absolute error on azimuth equal or lower to one degree. The iterative signal deflation algorithm has similar results both in errors and in false estimations as the multipeak selection algorithm with 0.2 % of false estimation rate and around 0.6° of errors. Algorithms like Fisher and both Capon spectrum seem to be accurate with a range of false estimations from 0.7 to 3.6 % and an error of 2° maximum. Once again MUSIC is unsuccessful when the geometry is not adequate, the false estimation rate is 85.5 % for 7° of errors. Indeed, MUSIC is strongly dependant to the geometry and then is unable to estimate correctly even the first source at this kind of station. The source at 0 dB is well estimated only by the iterative signal deflation with 4 % of false estimation rate and absolute errors of 1.3°. The following algorithms are both dictionary coding with likelihood atoms and the spectral MLE with around 60 % of false estimations and almost 4° of errors. Finally no algorithm is accurate for the source at -5 dB, the lower false estimation rate being the iterative signal deflation with 84 % and around 8° of errors while the other algorithms have a false estimation rate higher than 90 %. Thus, the best algorithm in terms of accurate estimation and absolute error is the iterative signal deflation which is the only algorithm to have correct estimation for the second source at 0 dB.

A conclusion can be drawn from all the observations of the evaluation. The first one is that the state-of-the-art algorithms like MUSIC and Capon are robust as expected whether the SNR are equal between the sources or not. However, MUSIC is strongly dependant of the array geometry, if the array geometry is composed of few sensors and has a aperture inducing a spatial aliasing then the estimation is inaccurate even for the first source at high SNR. The second conclusion is the robustness of most of the developed algorithms compared to the global state-of-the-art. Indeed, MLE based algorithms are often more accurate than the state-of-the-art algorithms. The dictionary coding except the one based on the delay with the OMP solver are also robust for the estimation in particular the LASSO approach. One strong observation is that the monosource hypothesis of the MLE with the multipeak finder must be verified. Indeed, when it is not the case and when the SNR are different between the sources then the estimations are inaccurate compared to the spectral methods or the method with iterative signal deflation. The two latter approaches have revealed to be the best approaches compared to all the developed methods and the state-of-the-art methods. Indeed they have the lower false estimated events rate in most of the frequency band, SNR of the sources or array geometry cases. However, the implementation of a fast spectral MLE algorithm has shown degradation of the estimation quality compared to the raw method. The raw spectral MLE algorithm and especially the iterative signal deflation algorithms have demonstrated their robustness to different studied cases.

With regard to calculation time, they indeed depend on frequency band (i.e number of samples, level of difficulty to find pertinent sources), SNR of the sources (i.e more iterations) and array geometry (i.e number of sensors, aperture). But the trend is the same overall the case between the algorithms. From the faster to the slower is the OMP with the delay atoms with 0.01 s, the time to compute the dictionary is fast with 0.59 s and done once for all for a frequency band and a station, computed at 5 dB. The Fisher algorithm comes in second place with 0.02 s for one iteration, followed by the iterative signal deflation with 0.09 s. The multiple peak selection MLE comes next with 0.28 s, however a larger grid (to avoid grid edges selection) can be critical at the end, especially at high frequency. One iteration of the OMP with likelihood atoms makes only 0.35 s in computation time. However the construction of the dictionary is quite consuming due to the MLE processing for each grid point with 1.25×10^3 s (around 21 minutes). The Capon spectrum with or without regularisation have a time computation cost around 0.6 s. The last algorithm under one second of computation is MUSIC with 0.82 s. The algorithm TOPS is around one second of computation time for one iteration. The fast spectral MLE algorithm is around 2.67 s whereas the formal spectral MLE is almost three times longer in calculation time with 6.57 s. Note that the computation time can vary a lot if the SNR is different between the sources because of the multiple deflation of the stronger sources to succeed in estimating all the three sources. Finally, the algorithm LASSO with likelihood atoms is the most time-consuming with 14 s without taking into account the construction of the dictionary which is the same as the one of the OMP (i.e 1.25×10^3 s). Thus, while the spectral MLE algorithm without simplification and the iterative signal deflation algorithm have been shown to be globally the best algorithms in terms of accuracy the latter has a strong advantage to be

compatible with operational processing.

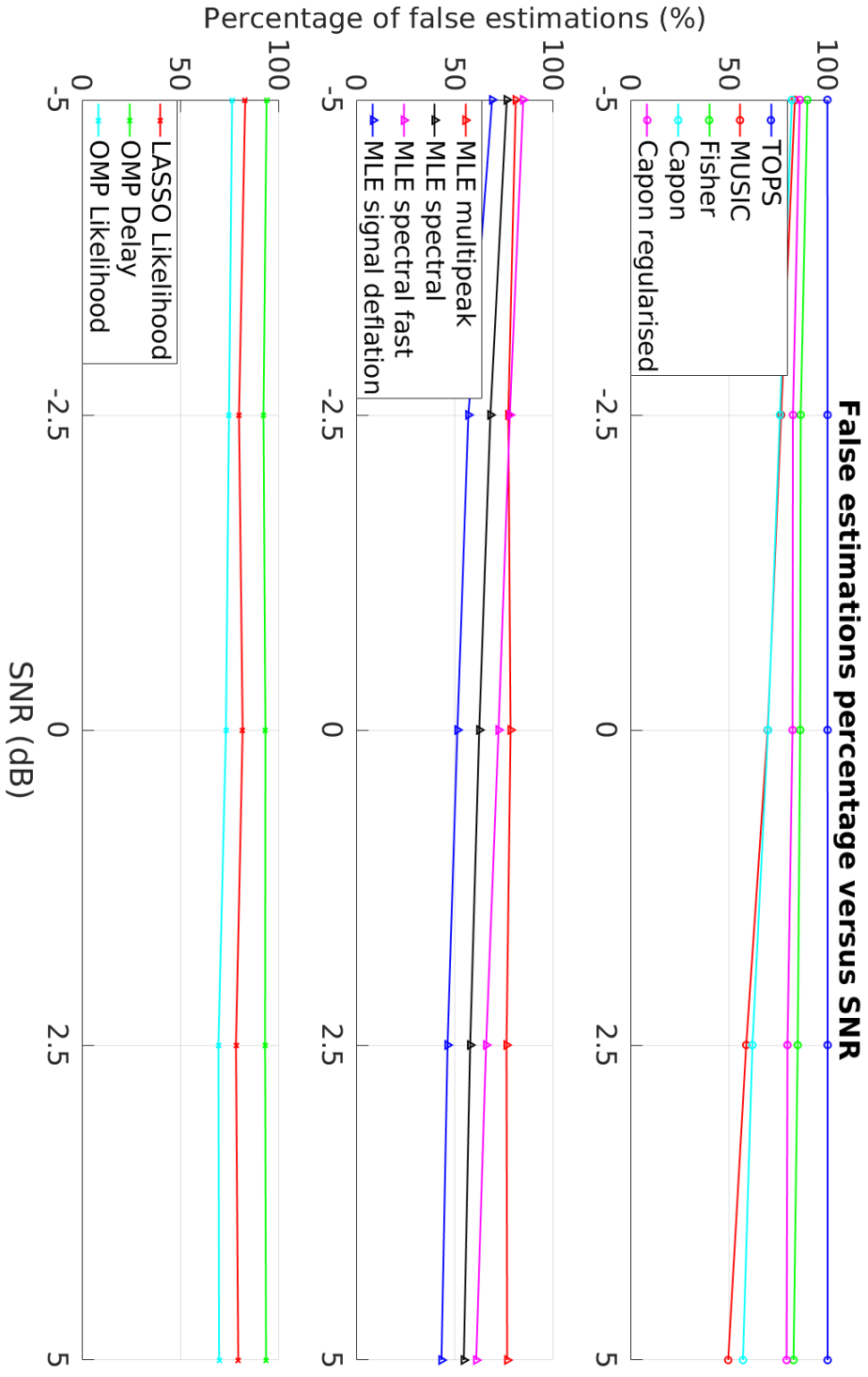

Figure IV.4.1: False estimation percentage of the sources in function of the SNR for the different algorithms at IS31 (i.e the SNR of the sources are equal). For a better readability the state-of-the-art algorithms are separated in subplot from the MLE-based algorithms and from the dictionary coding. The frequency band studied is [0.1 - 0.12] Hz.

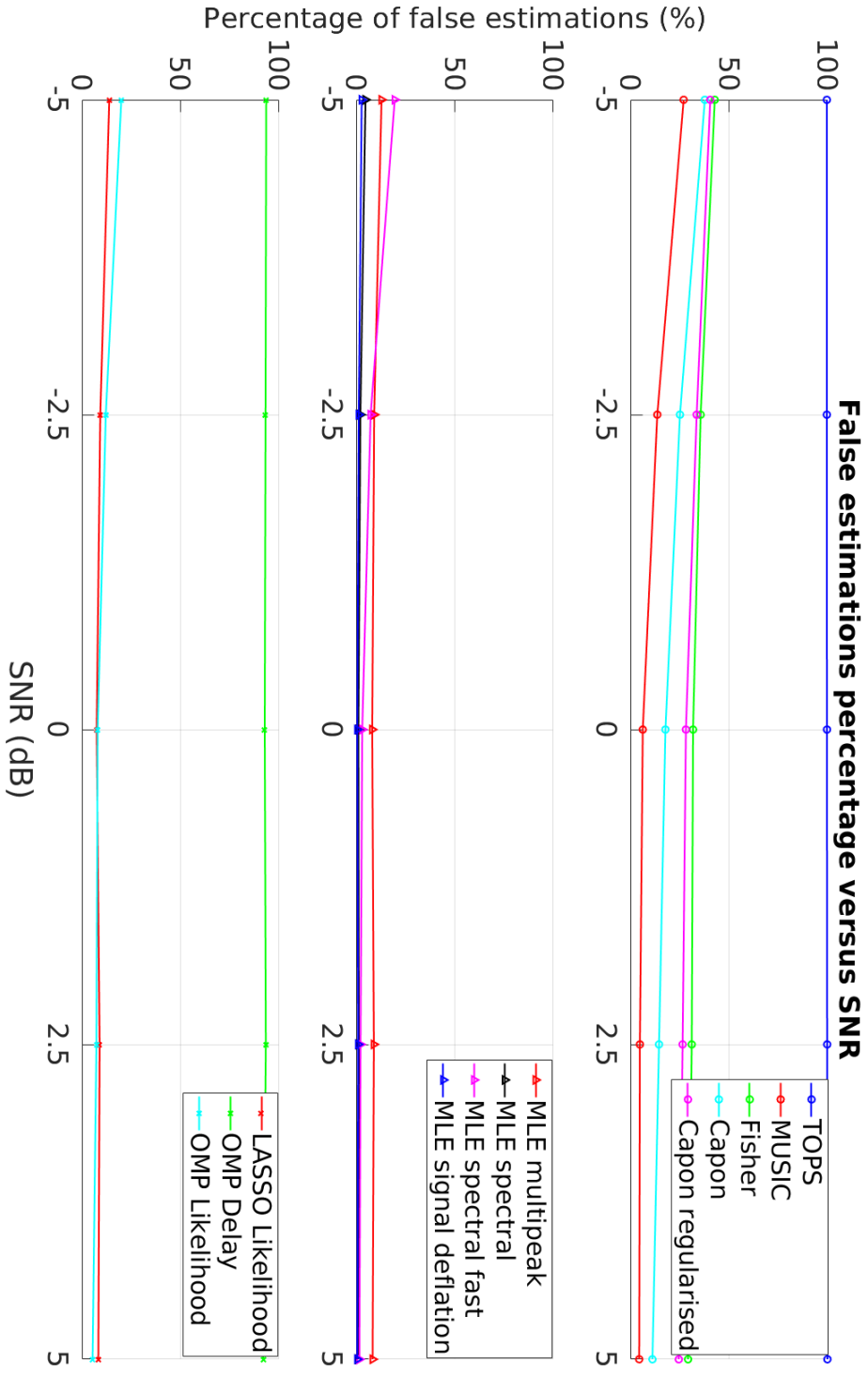

Figure IV.4.2: False estimation percentage of the sources in function of the SNR for the different algorithms at IS31 (i.e the SNR of the sources are equal). For a better readability the state-of-the-art algorithms are separated in subplot from the MLE-based algorithms and from the dictionary coding. The frequency band studied is [0.50 - 0.64] Hz.

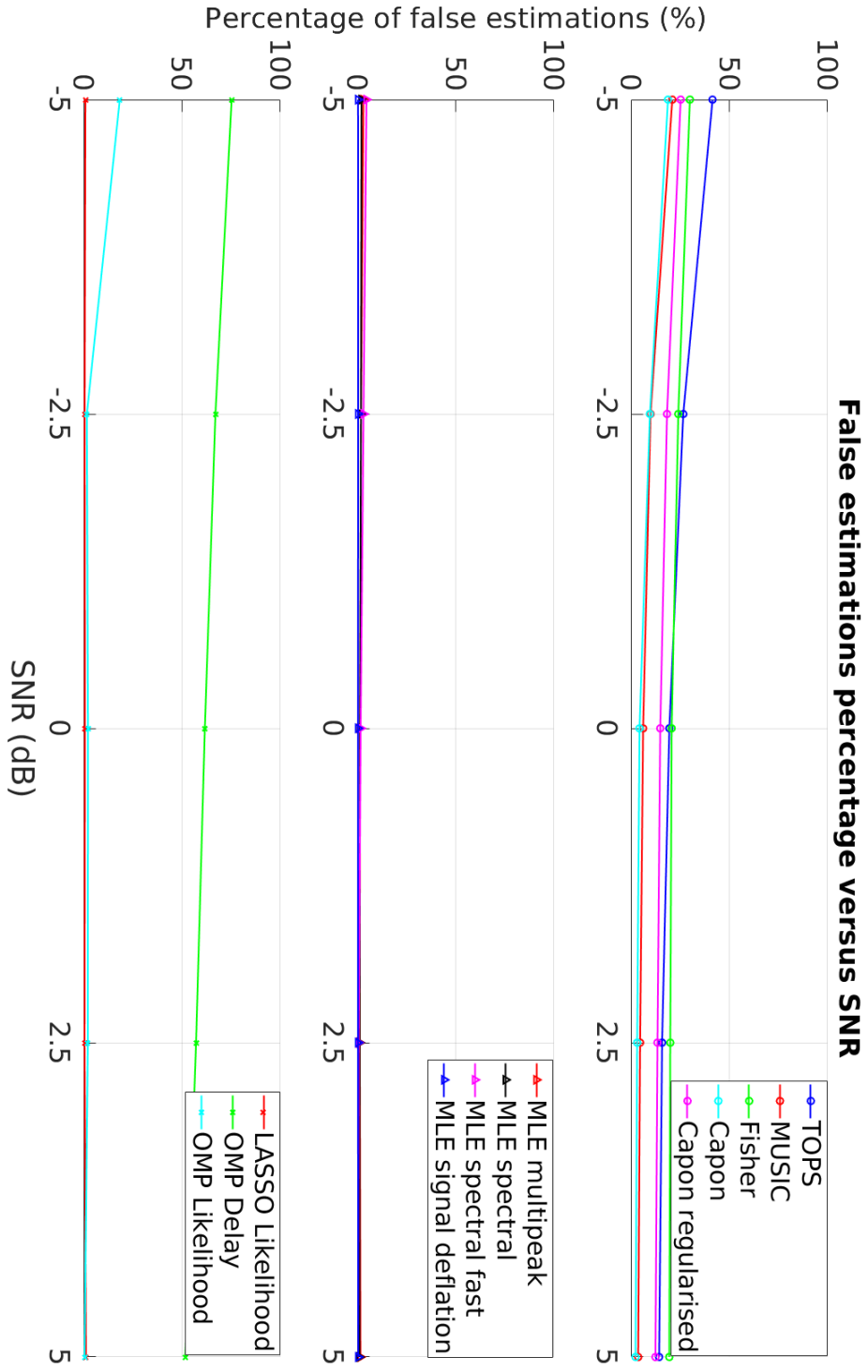

Figure IV.4.3: False estimation percentage of the sources in function of the SNR for the different algorithms at IS31 (i.e the SNR of the sources are equal). For a better readability the state-of-the-art algorithms are separated in subplot from the MLE-based algorithms and from the dictionary coding. The frequency band studied is [3.2 - 4] Hz.

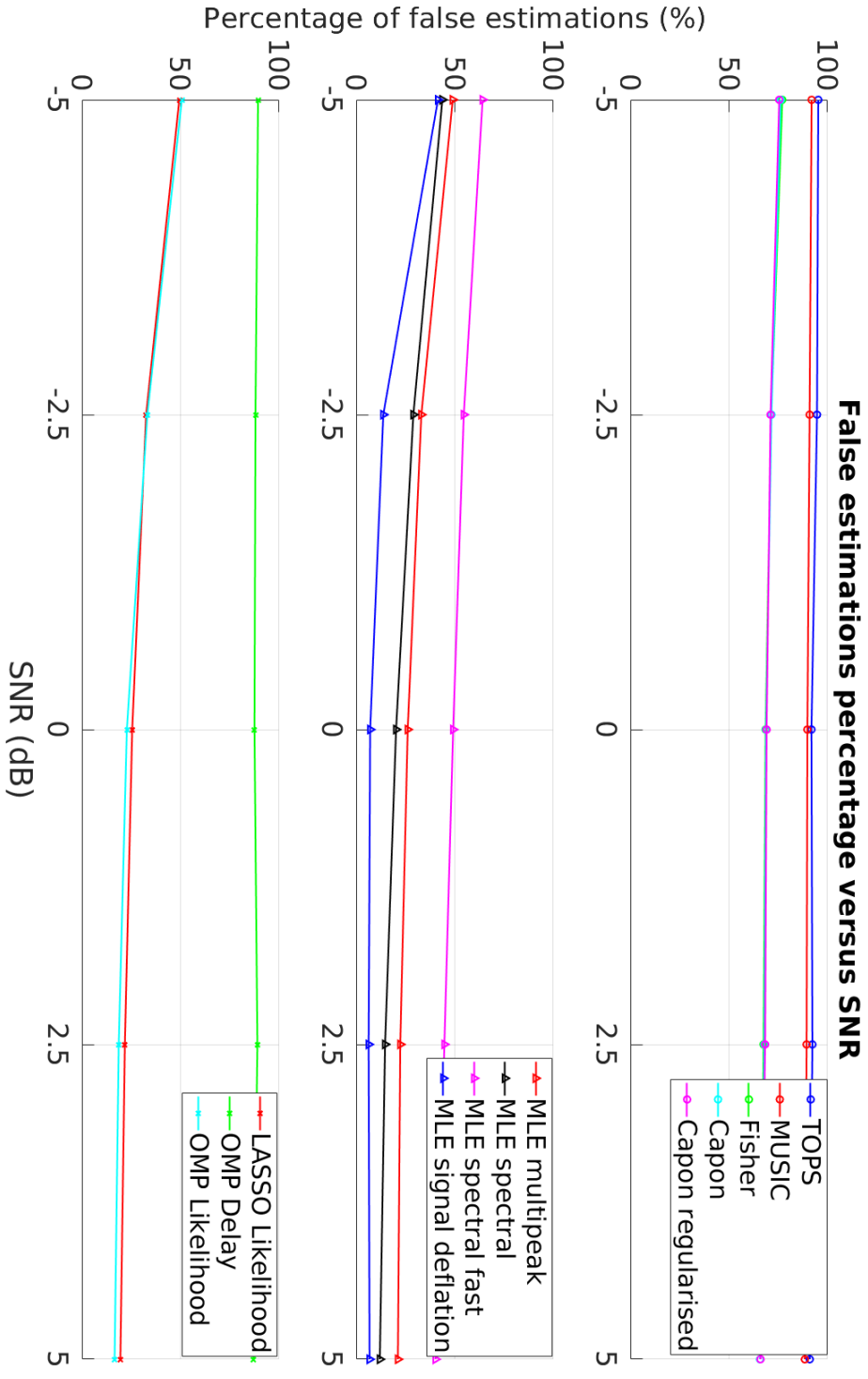

Figure IV.4.4: False estimation percentage of the sources in function of the SNR for the different algorithms at IS46 (i.e the SNR of the sources are equal). For a better readability the state-of-the-art algorithms are separated in subplot from the MLE-based algorithms and from the dictionary coding. The frequency band studied is [0.50 - 0.64] Hz.

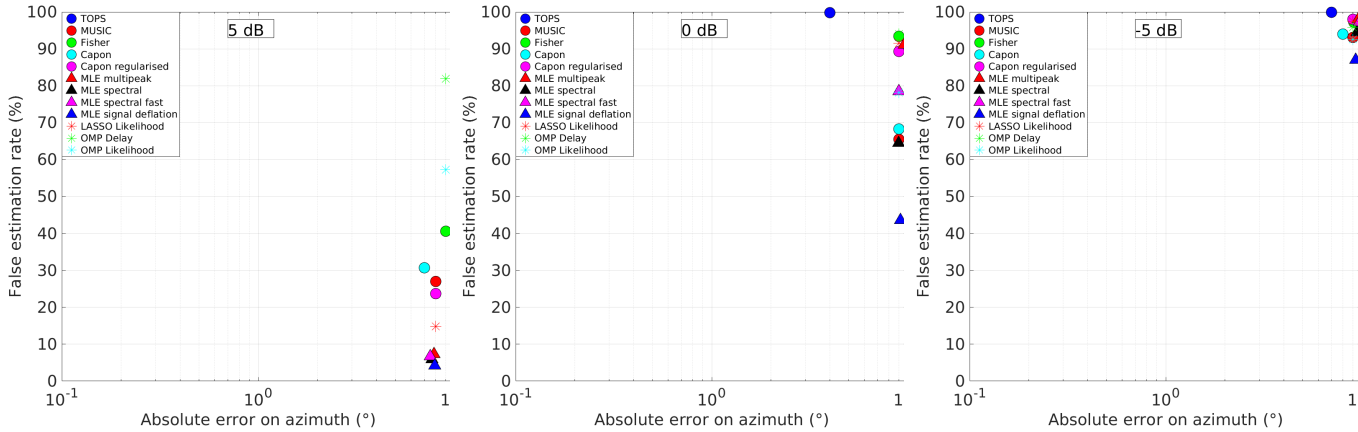

Figure IV.4.5: Scatters of the false estimation rate in function of the absolute error in azimuth of the different algorithms for the [0.1 - 0.12] Hz band at IS31. Three scatters are illustrating theses metrics for the sources with different SNR in the same signal (5 dB, 0 dB, -5 dB).

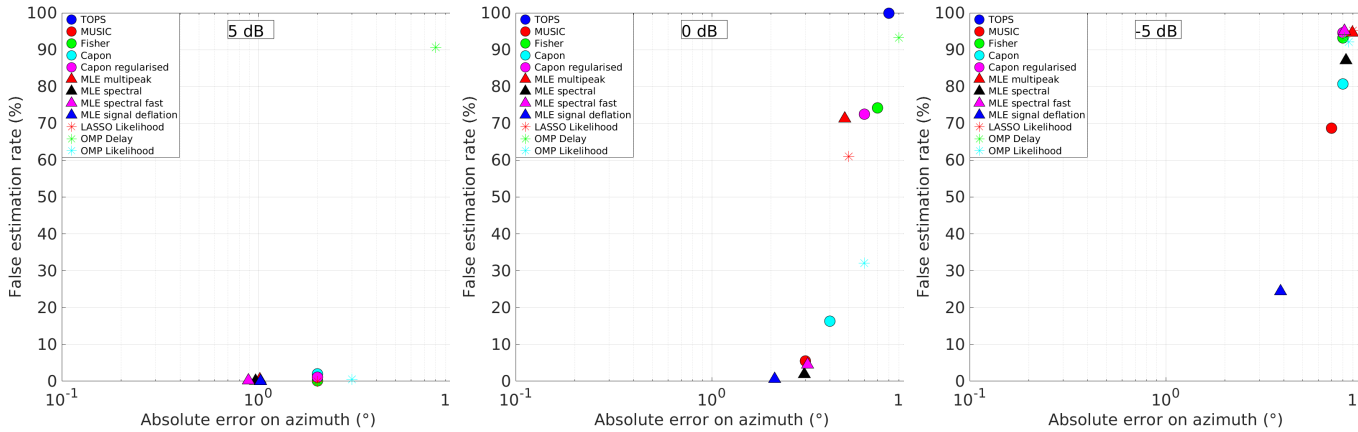

Figure IV.4.6: Scatters of the false estimation rate in function of the absolute error in azimuth of the different algorithms for the [0.5 - 0.64] Hz band at IS31. Three scatters are illustrating theses metrics for the sources with different SNR in the same signal (5 dB, 0 dB, -5 dB).

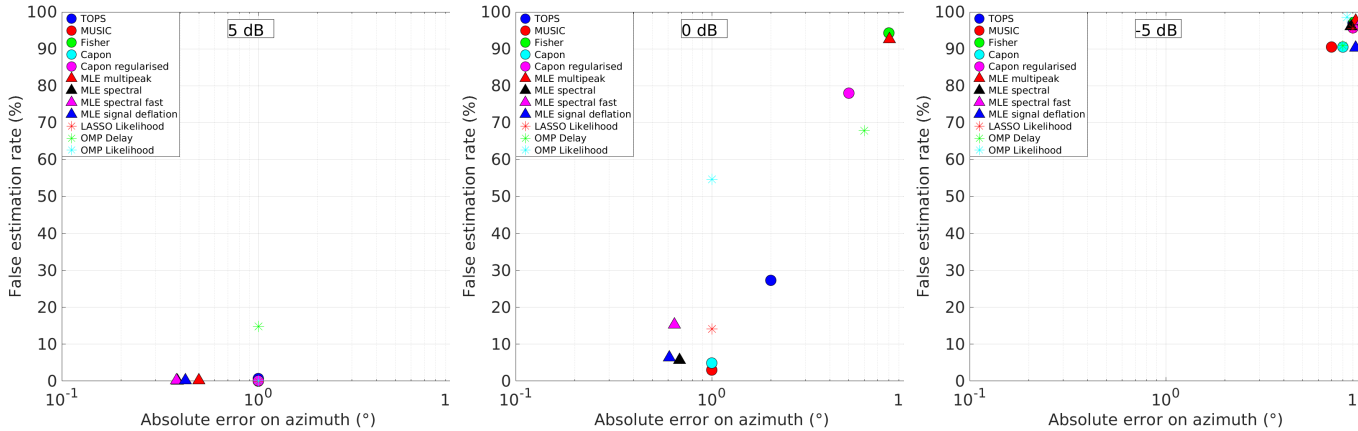

Figure IV.4.7: Scatters of the false estimation rate in function of the absolute error in azimuth of the different algorithms for the [3.2 - 4] Hz band at IS31. Three scatters are illustrating theses metrics for the sources with different SNR in the same signal (5 dB, 0 dB, -5 dB).

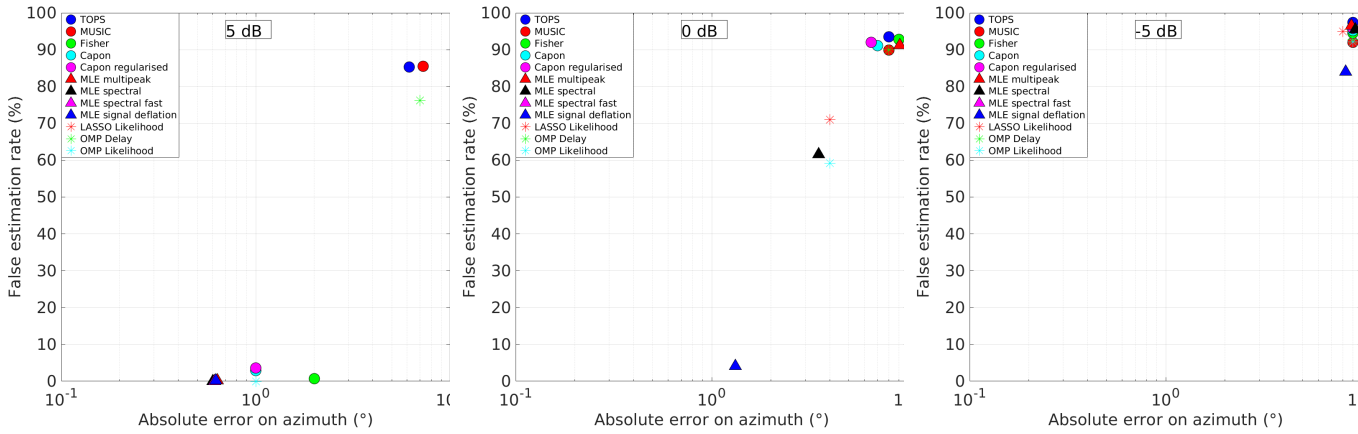

Figure IV.4.8: Scatters of the false estimation rate in function of the absolute error in azimuth of the different algorithms for the [0.5 - 0.64] Hz band at IS46. Three scatters are illustrating theses metrics for the sources with different SNR in the same signal (5 dB, 0 dB, -5 dB).

IV.4.2 On real data

Tests on synthetic data are of major importance to quantify the accuracy of estimators thanks to ground truth knowledge. However, synthetics data are built on a signal model with ideal conditions. It is thus necessary to make tests on real data in order to further confirm the previous results. That is why three algorithms have been selected among the entire list to be confronted to real source of infrasound. Indeed, MUSIC is the best state-of-the-art algorithm in term of accuracy despite its low estimation capability with low number of sensors. Its computation time is in accordance with an operational processing use. In the other hand, two algorithms based on MCML are selected. The first one is the iterative signal deflation MLE and the other one is the spectral MLE. Those two algorithms gave better results than MUSIC in most cases on synthetics data, however only the iterative signal deflation MLE is applicable to real-time processing due to the high computation cost of the spectral MLE. This test is imperative especially for the iterative signal deflation MLE because the signal model is directly implicated in the deflation iteration. Note that the two MLE estimators are assisted by a detector derived from the likelihood function (i.e the GLR with the associated p-value) in order to suppress noise estimation while MUSIC has no detector. This is also one of the advantage to be based on the recent developments. The used detector for MCML is a single source detector, in the iterative signal deflation algorithm we place ourselves in a monosource assumption at each iteration while it is not the case for the spectral MLE algorithm which takes into account several sources in its likelihood function. Thus, the detector may be of greater confidence with the iterative signal deflation algorithm than with the spectral MLE algorithm. In the following processing the number of sources is assumed to be three all the time.

Two examples have been studied here. The first one is the rocket launch from the Baikonur cosmodrome in Kazakhstan. This event is away from more than 600 km to IS31, the infrasound station of the IMS which recorded the event on August, 21th 2021 at around 22h40 UTC. The array processing has been done from 22h00 to 24h00 UTC between 0.1 Hz and 4 Hz. The figure IV.4.9 represents the azimuth detection of the rocket launch by the algorithms PMCC and MCML respectively in function of time and frequency. At the bottom of the plot, the signal recorded at the station shows a maximum overpressure of around 0.2 Pa at 22h40 UTC. Different sources can be observed thanks to PMCC and MCML. At low frequency, between 0.1 and 0.4 Hz, a source (in blue on the graph) coming with a DOA of 210° is detected during all the time duration and represents the microbaroms probably coming from south Atlantic. However, this source is not detected between 22h40 and 23h00 UTC due to the impulsive wideband rocket launch arrivals (in green on the graph) which are coming from a little deviated DOA of 135° compared to the Baikonur azimuth of 140°. This deviation is caused by wind in the travel path. Two wideband permanent sources with close azimuth of 40° and 60° are also detected by both algorithms at higher frequency between 0.5 Hz and 4 Hz. They represent two wind farms located close to the village of Badamsha at tens of kilometres from the station. A third permanent wideband source can be noticed around 100° (in green on the graph) which competes with the wind farms sources but can not be linked precisely to a source. Finally high frequencies sources around 3 - 4 Hz coming from 110° (in green on the graph) and 265° (in purple on the MCML graph) are detected along the time duration by PMCC for one of the two sources and by MCML for both of them. Those two sources correspond to close industrial or mining activities. It is worth noticing that PMCC has a lack of detection compared to MCML, not only for the industrial activity from 265° but also for mid and high frequency sources. The noise level is low, indeed, the wind speed has a mean of 1 m/s and a maximum of 2 m/s on this time duration. Thus, PMCC misses detection due to the overlap of different sources and not due to noise power. This assumption is verified by the detection of multiple interfering sources of the microbaroms, green wideband source, the two windfarms, the industrial activities and of course the rocket launch. MCML shows thus a lot of different sources interfering in the same time and in the same frequency band. All of them are interfering with at least one other source in its frequency band.

That is why this example has been selected in order to confirm the ability of the three selected algorithms to estimate the different sources. Thus we can expect that the results will lead to an increase of detection of the overlapping permanent sources. We can also hypothesising thanks to synthetics test that multisource detection under the Baikonur event will be difficult due to the high SNR difference between the main event (almost 20 dB) and the permanent sources (around 0 dB or less). All the multisource detections should have velocities in accordance with the monosource one or be explicable by another

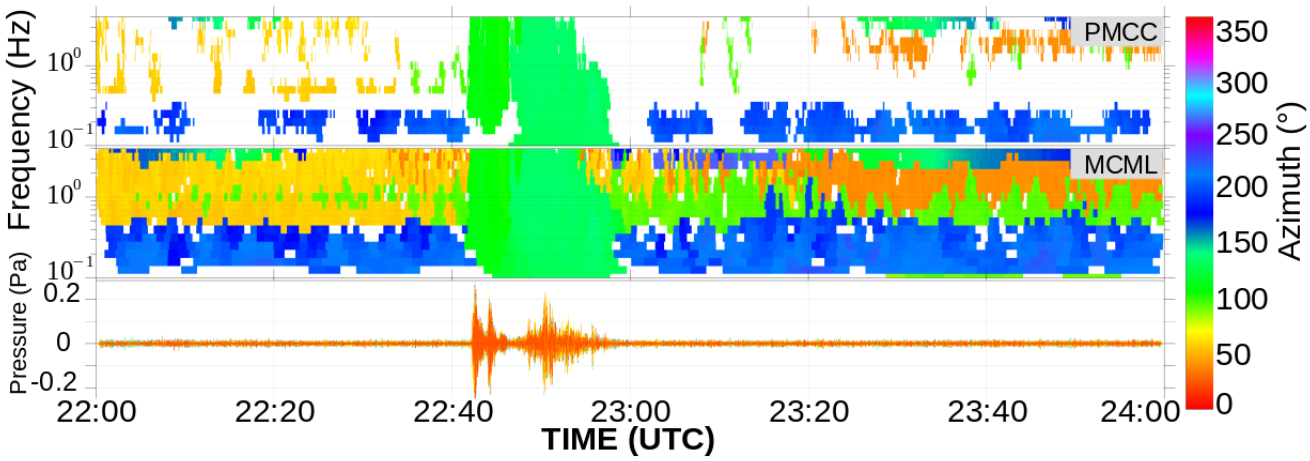

Figure IV.4.9: Plot of the azimuth detection of the Baikonur event by PMCC and MCML from top to bottom in function of time and frequency. The last plot is the signal recorded at the station. The rocket launch has provoked a maximum overpressure of around 0.2 Pa at 22h40 UTC.

path (due to stratospheric, thermospheric waveguide...). All the algorithms have been ran with the grid construction of MCML based on its error at 0 dB in order to compare similar calculation conditions.

The figures IV.4.10 and IV.4.11 represent the monosource (i.e the first detected source) polar plot of the azimuth detections and the monosource apparent velocity histograms for the iterative signal deflation, the spectral MLE and MUSIC. The monosource results on the polar plot and apparent velocity histogram of both MLE are really similar due to the same code used for the monosource. Indeed, the polar plot are showing the same sources with the same DOA while the velocities are almost identical. A really small variability can be seen and may be caused by the stochastic model, it is however marginal. The results of MUSIC are also similar for the azimuths. Only the estimations of the microbaroms and the unknown wideband source at 100° seem wider in azimuth extent than for both MLE but no ground truth information can relate on the appropriate wide source or not. The only clue about a possible bad estimation is the wider azimuth detection around the Baikonur event compared to both MLE which must be precisely pointed in theory. In general, the azimuth detections are in accordance between both MLE with a similar maximum of around 300 detections for each events. The MUSIC algorithm, having no detector has however some false detections between 270° to 360°. In another hand, while both MLE have an apparent velocity estimation centred around 340-350 m/s and have a non negligible higher estimation between 360 and 390 m/s due to the stratospheric or thermospheric arrivals of the microbaroms (around 1000 counts), it is worth noticing than MUSIC fails to estimate this kind of arrivals but have in contrast a lot of arrivals with apparent velocities inferior to 340 m/s which are not physical. Moreover, it seems that there is an accumulation of apparent velocity estimations on the edge of the grid. This observation is of significant importance, as the apparent velocity is a fundamental aspect in the comprehension of the waveguide for infrasound propagation.

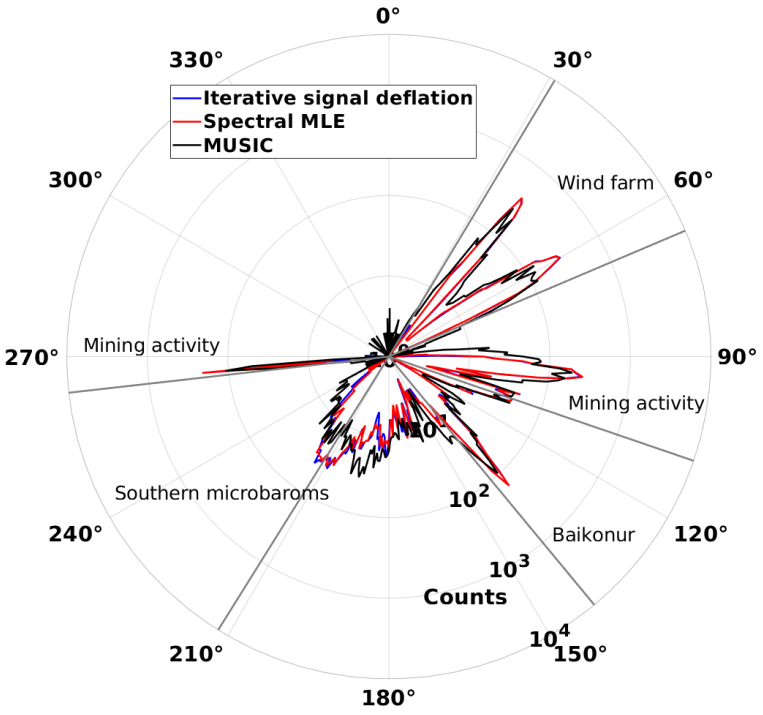

Figure IV.4.10: Monosource polar histogram of the detected azimuths and the knowledge of the major sources detected by the iterative signal deflation MLE, the spectral MLE and MUSIC.

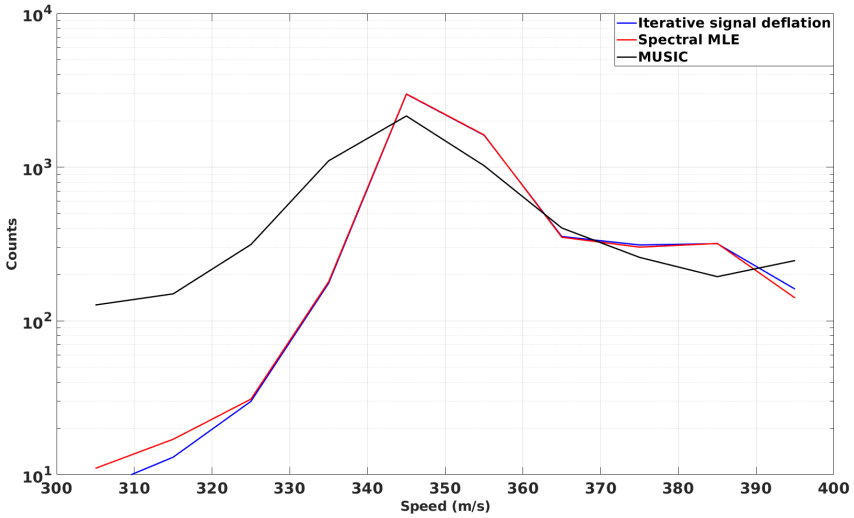

Figure IV.4.11: Monosource apparent velocity histogram for the iterative signal deflation MLE, the spectral MLE and MUSIC.

Now the same comparison can be made on the multisource plots on the figures IV.4.10 and IV.4.11 (i.e all the three detected sources). Lets compare first both MLE with the polarplot of the azimuth detections.

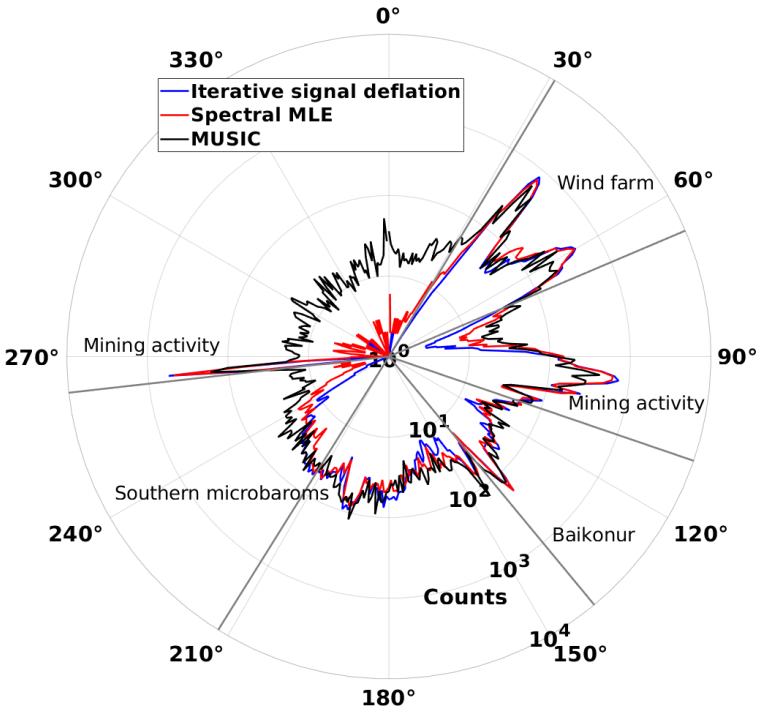

Figure IV.4.12: Multisource polar histogram of the detected azimuths and the knowledge of the major sources detected by the iterative signal deflation MLE, the spectral MLE and MUSIC.

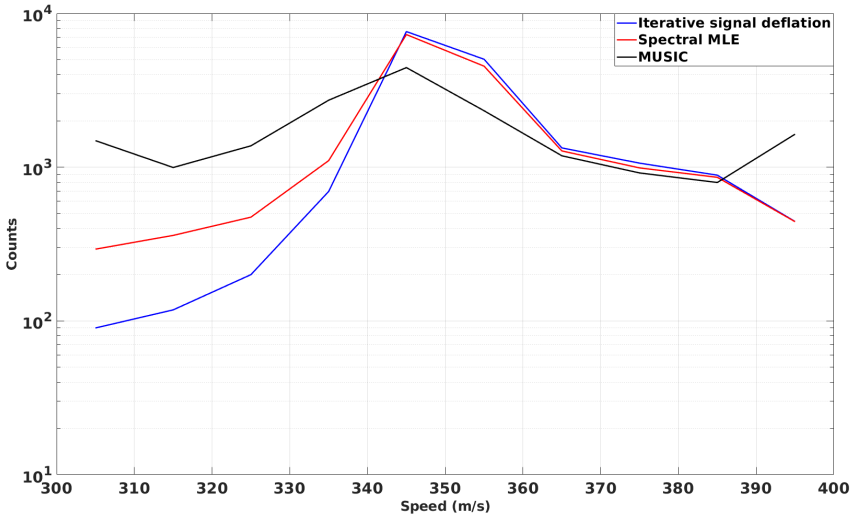

Figure IV.4.13: Multisource apparent velocity histogram for the iterative signal deflation MLE, the spectral MLE and MUSIC.

For both MLE, a larger number of detections for the microbaroms resulting from different wave train from this source and from the detection beside the Baikonur event are observed. While the number of pixels from the Baikonur event is quite similar from the monosource to the multisource, the two wind farms, the permanent wideband source at 100° and the mining activities are more detected by both MLE algorithms and with the same order of magnitude (i.e around 700 detections each). However, the spectral MLE detections are noisier as it can be seen with more non physical detections between 270° and 360° than with the iterative signal deflation MLE. It is also more difficult to separate the microbaroms from the Baikonur event with the spectral MLE on the polar plot, probably due to undesirable detections. This can be explained by the monosource assumption of the p-value which is not respected by the latter algorithm but respected by the iterative signal deflation. About the velocity estimation illustrated by the histogram IV.4.13 it is worth noting that the trend of the monosource description written above is more visible with the iterative signal deflation MLE than with the spectral MLE which has more non physical velocities than the first one (apparent velocities inferior to 340 m/s). This velocity range is in fact related to noisy estimation in most of the case.

The MUSIC algorithm can thus be compared to two MLE. The number of noisy detections is really high for MUSIC, this can be observed by the levelling of all the azimuths, almost making the microbaroms equal in number of detections to the non physical 270°-360° detections. The Baikonur event and the mining activity at 110° are almost indistinguishable while wind farms which were clearly marked by two peaks in the monosource estimation are now just above the noise levelling. The non existence of a detector can not be invoked as a part of the problem since the number of p-value inferior to the threshold is around 2 % for the iterative signal deflation algorithm, the quality of the estimator is clearly involved. The histogram shows, of course, a centred apparent velocity estimation at 340 m/s but also a levelling of all the different apparent velocity and an edge effect as previously seen.

This example shows how the developed MLE are better than the state-of-the-art algorithm MUSIC in particular when the multisource estimation is involved. Indeed the monosource estimation is quite similar from an algorithm to another (except for the velocity estimation by MUSIC). However, when multisource estimations are analysed, a clear noisy estimation in azimuth and velocity is observed with MUSIC while both MLE are highlighting the different overlapping sources. The iterative signal deflation algorithm has however less wrong detections than the spectral MLE due to the monosource assumption of the detector each time respected for the first one. Finally, the computational time for operational processing is in favour of the iterative signal deflation with 2 minutes for 2h of signal computed with 24 cores while it takes 15 minutes for MUSIC and around 3 hours for the spectral MLE algorithm.

In order to create a visual illustration of the estimation gain, the estimation of some event from the iterative signal deflation has been clustered by azimuth. In order to achieve this, the family post processing characterised by an euclidean distance in azimuth, velocity, time and frequency between pixels has been used to group small pockets of similar pixels (maximum 50 pixels). This method has been explained in details in the subsection II.1.1.4. Then in order to group pockets into large events, an algorithm called Density-Based Spatial Clustering of Applications with Noise (DBSCAN) is used. The principle is to group similar pockets in terms of azimuth and frequency content by estimating the density of pockets in the space azimuth/frequency. If two pockets are close then they form the same event. We are finally able to illustrate the multisource estimations by these multisource sheets in the figure IV.4.14. Indeed in order to avoid illustration complexity, only five major events have been plotted, from the left to the right: the two wind farms, the permanent wideband signal at 100°, the Baikonur launch and finally the microbaroms. However, the clustering is not perfect, due to close azimuths of a mining activity, permanent wideband signal and Baikonur. Indeed DBSCAN forms event in the near field of each cluster, if they are too close from one to another they will be part of the same event. A perspective would be to include the apparent velocity or another parameters like the SNR or the RMS in order to discriminate the events. However this is sufficient here to illustrate the ability of the algorithm to estimate the interfering sources, in particular the two wind farms and the permanent wideband signal at 100° with close SNR. Because the SNR with the Baikonur rocket launch is too different these three events are not estimated anymore behind the main event. In contrast, the microbaroms can be observed under the Baikonur launch even if there is no detection across all the Baikonur launch. This limit has been already pointed out by synthetics data.

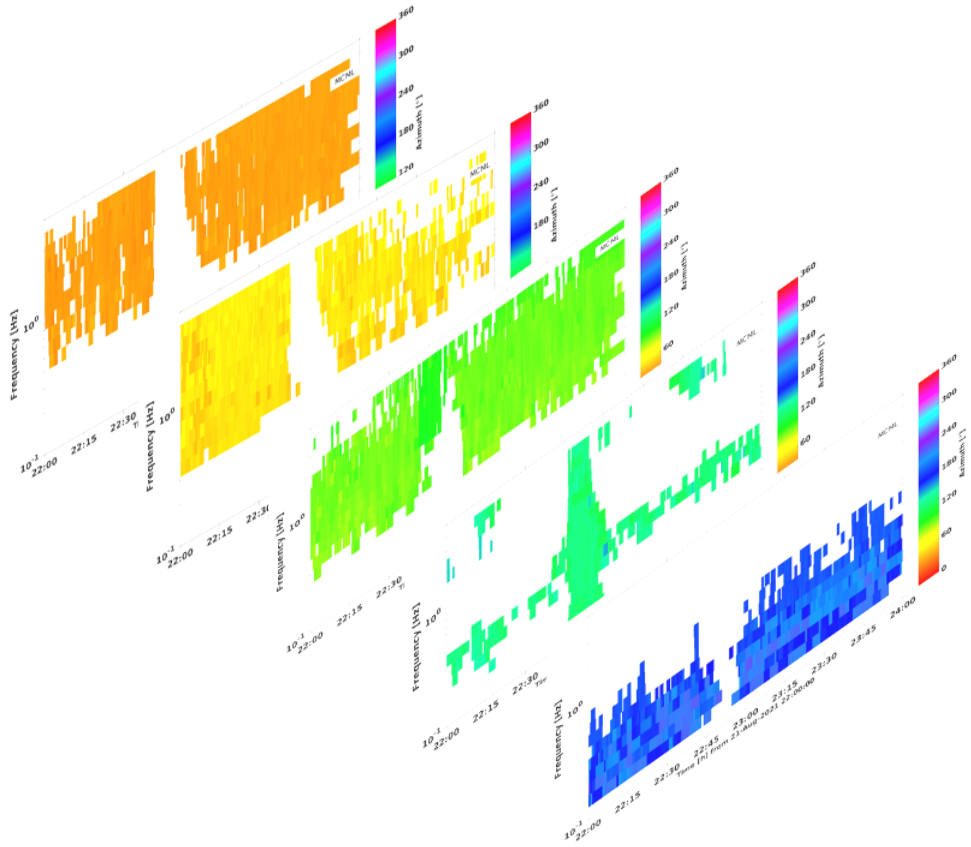

Figure IV.4.14: Multisource sheets of the detected azimuths in function of the time and the frequency. Five major events have been plotted, from the left to the right: the two wind farms, the permanent wideband signal at 100°, the Baikonur launch and finally the microbaroms.

The second example is the detection of the disintegration of a meteor 500 km off the Namibia coast on February, 7th 2022 and has been recorded at the IMS station IS19 located in Djibouti at around 01h40 UTC February, 8th (figure IV.4.15). The total distance from the main event and the IMS station IS19

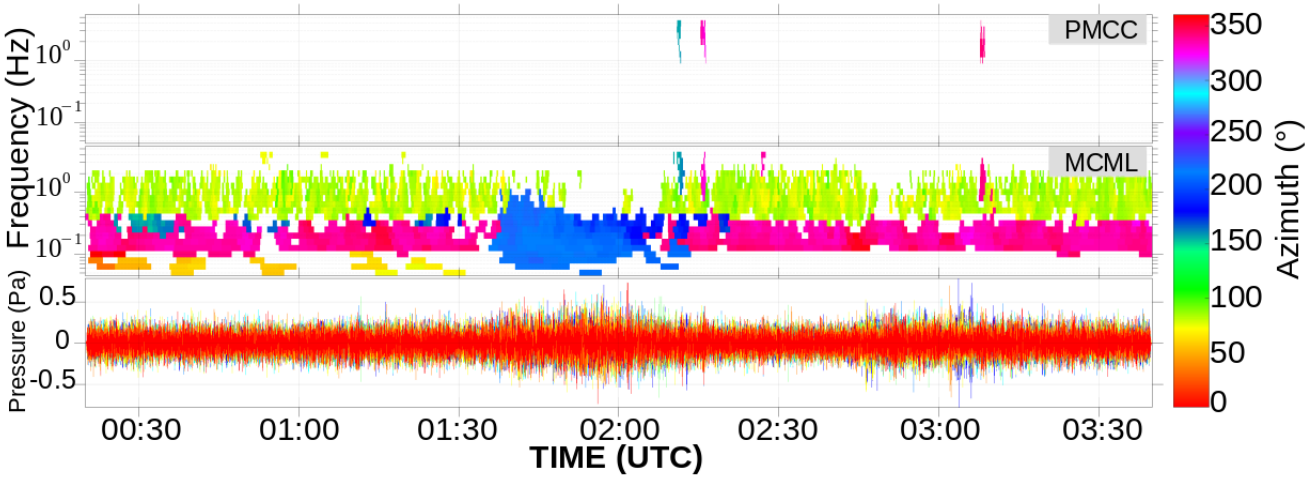

Figure IV.4.15: Plot of the azimuth detections of the meteor event by PMCC and MCML from top to bottom in function of time and frequency. The last plot is the signal recorded at the station. The meteor has provoked a maximum overpressure of around 0.5 Pa at 01h40 UTC.

is more than 5000 km and the power of the source was around 7 kT equivalent TNT, half of the power of the Hiroshima bomb. The array processing has been done from 00h30 to 03h30 UTC between 0.05 Hz and 4 Hz. This event has not been detected by PMCC at this station because one sensor was noisy. However, the maximum recorded pressure is 0.5 Pa at 01h40 until 02h15 UTC, more than twice the maximum amplitude of the Baikonur launch recorded at IS31. In contrast, MCML is able to estimate different sources despite of this noisy sensor, showing how this algorithm can be resilient to this issue. At low frequency, between 0.1 Hz and 0.4 Hz, two microbaroms are identifiable across the selected time window at around 340° from north Atlantic and at around 170° from the south Indian ocean (in pink and light blue on the graph). At 01h40 UTC, the meteor is detected at 220° (in dark blue on the graph) between 0.05 Hz and 0.7 Hz. Finally, a wideband signal above 0.8 Hz is detected during all the time duration with a mean DOA of the 80°. This source is assumed to be surf noise which is the noise made by the breaking of ocean waves on the coast. This example is interesting to see if the removing of a noisy channel can impact multisource estimation by changing the geometry lowering the number of sensors and if the interfering microbaroms with the meteor can be identified better especially the hidden one from the Indian ocean. Thus, we can expect that the results will lead to an increase of detection of the overlapping microbaroms in particular. The SNR of the meteor is around 0 dB and sometime positive, thus the detection of the microbaroms behind the meteor should be possible given that the microbaroms have a SNR around 0 dB. All the multisource detections should have apparent velocities in accordance with the monosource one or be explicable by another path (like stratospheric, thermospheric waveguide...). All the algorithms have been ran with the grid construction of MCML based on its error at 0 dB in order to compare similar calculation conditions.

The figures IV.4.16 and IV.4.17 represent the monosource polar plot of the azimuth detections and the monosource apparent velocity histogram for the iterative signal deflation, the spectral MLE and MUSIC. The monosource polar plot and velocity histograms of both MLE are really similar due to the same code used for the monosource.

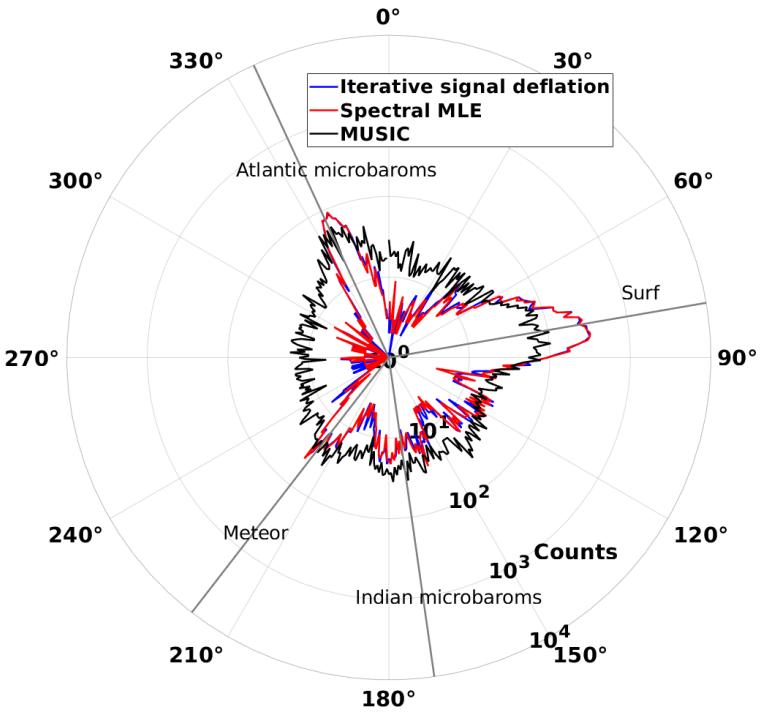

Figure IV.4.16: Monosource polar histogram of the detected azimuths and the knowledge of the major sources detected by the iterative signal deflation MLE, the spectral MLE and MUSIC.

Indeed, the polar plot are showing the same sources with the same DOA while the apparent velocities

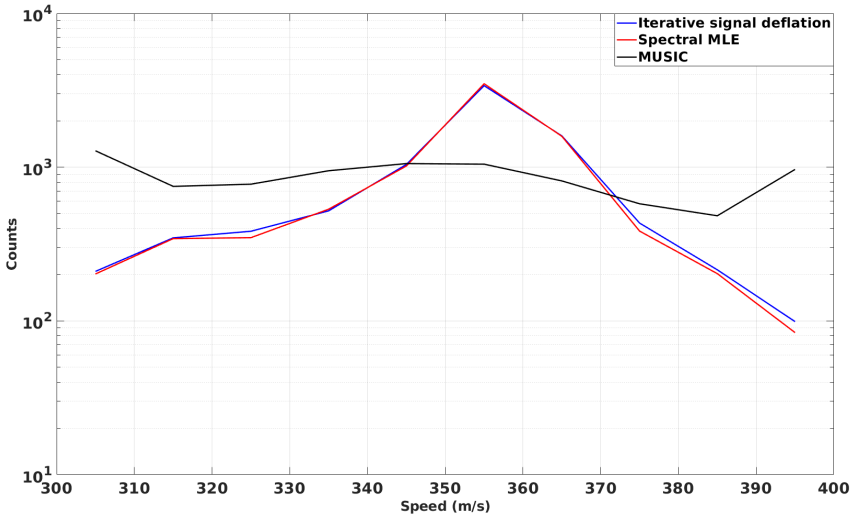

Figure IV.4.17: Monosource apparent velocity histogram for the iterative signal deflation MLE, the spectral MLE and MUSIC.

are almost identical. A really small variability can be seen and may be caused by the stochastic model again, it is however marginal. The plots of MUSIC are quite different. Indeed, a lot of different azimuths are also seen, provoking a difficulty to clearly identify the sources in the polar plot by the levelling of the azimuth. The absence of a detector in MUSIC can not be involved due to only 2 % of p-value inferior to the threshold for both MLE in multisource. However the azimuth detections relative to the sources are in accordance with both MLE even if both MLE have more Atlantic microbaroms and surf detection than MUSIC (i.e around 100 and 300 detections for both sources for the two MLE while MUSIC has around 50 and 100 detections for both sources). In another hand, while both MLE have an apparent velocity estimation centred around 350-360 m/s due to the stratospheric or thermospheric arrivals of the microbaroms (around 3500), it is worth noticing than MUSIC fails to estimate this kind of arrivals but have a flat response of the apparent velocity. Moreover, it seems that there is again an accumulation of velocity estimations on the edge of the grid. This observation is of significant importance, as the apparent velocity is a fundamental aspect in the comprehension of the waveguide for infrasound propagation.

Now the same comparison can be made on the multisource plots. Lets compare first both MLE with the polarplot of the azimuth detections with the figures IV.4.18.
For both algorithms a larger number of detections for both microbaroms especially the ones from the south Indian ocean due to their interactions is observed (i.e maximum around 70 compared with 20 for monosource). While the number of pixels from the meteor event is quite similar from the monosource to the multisource, the surf is detected in a wider range of azimuth. The spectral MLE detections are not noisier than the iterative signal deflation MLE as it was previously seen with the Baikonur example. About the apparent velocity estimations illustrated by the histogram IV.4.19 it is worth noting that the trend of the monosource description written above is still visible with the two MLE. Thus both algorithms are quite similar in results.

The MUSIC algorithm can thus be compared to the two MLE. The level of noisy detections is really high for MUSIC, this can be observed by the levelling of all azimuths, almost making the surf equal in number of detections to the noisy detections. The meteor event and the other events are indistinguishable from the noisy detections. The non existence of a detector is a part of the problem but the quality of the estimator is also involved since the number of p-value inferior to the threshold is around 27 % for the iterative signal deflation algorithm and 24 % for the spectral MLE in multisource. The histogram of the trace velocities shows again a levelling of all the different apparent velocities and an edge effect as previously.

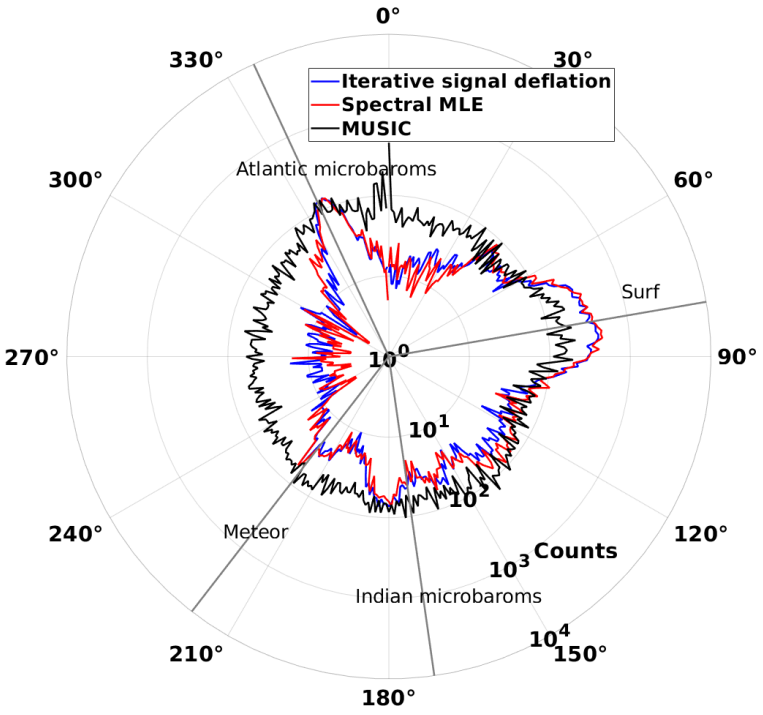

Figure IV.4.18: Multisource polar histogram of the detected azimuths and the knowledge of the major sources detected by the iterative signal deflation MLE, the spectral MLE and MUSIC.

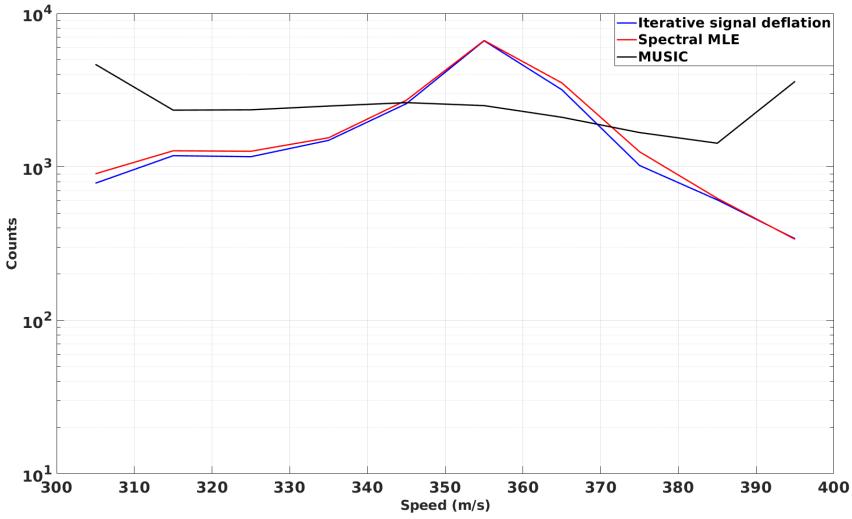

Figure IV.4.19: Multisource apparent velocity histogram for the iterative signal deflation MLE, the spectral MLE and MUSIC.

This second example shows again how the developed MLE are better than the state-of-the-art algorithm MUSIC. Here from the monosource estimation the MUSIC algorithm has shown discrepancy in the results, it can be related to the aspect shown with the synthetics when the geometry is composed of less numerous sensors. When multisource estimations are analysed a clear noisy estimation in azimuth and velocity is observed with MUSIC while both MLE are highlighting the different overlapping sources.

The iterative signal deflation and the spectral MLE have similar results both in azimuth and apparent velocity. Finally the computational time for operational processing is in favour of the iterative signal deflation with 170s for 3h of signal computed with 24 cores while it takes 15 minutes for MUSIC (i.e same time as previously but we remind that there is not the same number of sensors and frequency band) and around eight hours for the multisource algorithm making the latter one clearly a non operational method in terms of calculation time.

We finally illustrate the multisource sheets in the figure IV.4.20 of the iterative signal deflation MLE. The four major events have been plotted, from the left to the right: the surf noise, the Atlantic microbaroms, the Indian microbaroms and finally the meteor. Once again the clustering is not perfect, due to close azimuths of the meteor and Indian microbaroms, for the same reason previously stated. Indeed, the large Indian microbaroms detections can be linked by DBSCAN to the meteor, it is the case with one frequency band here. However this illustrate once again the ability of the algorithm to estimate the interfering sources, in particular both interfering microbaroms. Because the SNR of the meteor is not too different from the Atlantic/Indian microbaroms and the surf, they are detected behind the it.

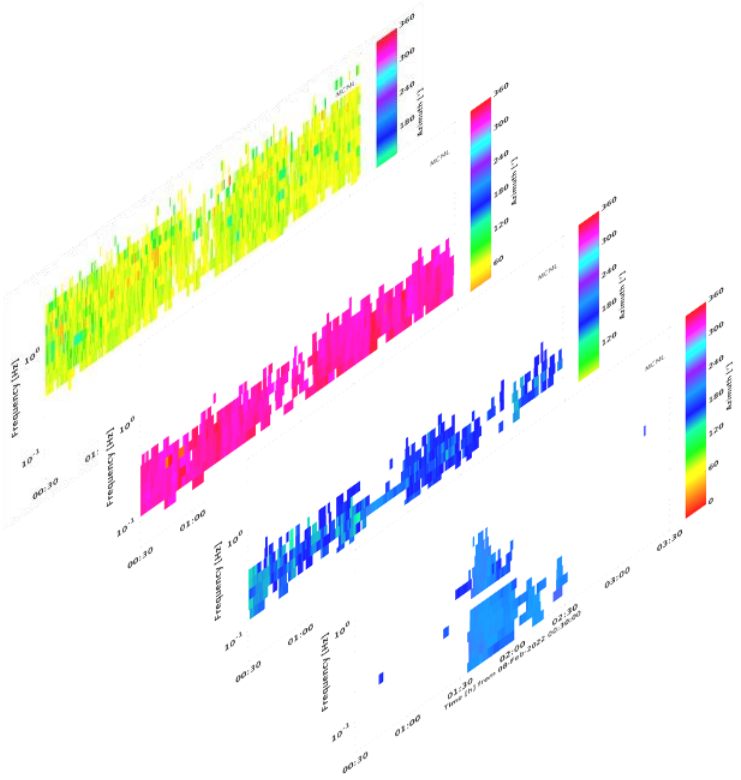

Figure IV.4.20: Multisource sheets of the detected azimuths in function of the time and the frequency. Four major events have been plotted, from the left to the right: the surf noise, the Atlantic microbaroms, the Indian microbaroms and finally the meteor.

IV.4.3 Discussion and conclusion

As a conclusion, different multisource algorithms from the state-of-the-art have been implemented in order to compare them to the developed methods based on either MLE or on the dictionary coding. This comparison was a two-stage process.

The first one was the elaboration of a protocol with synthetic signals because of the ground truth knowledge on such conditions, with many different cases in order to study different scenarios which could happen in reality (different azimuth/trace velocity, SNR between sources, frequency band, array geometry). This first test was applied to four state-of-the-art algorithms and six developed algorithms. The conclusion from this multiple tests was that the state-of-the-art algorithms Capon and especially MUSIC were robust in many complex cases but were really sensitive to the array geometry. In contrast, two developed algorithms were able to compete MUSIC and Capon. Those ones are the iterative signal deflation MLE and the spectral MLE algorithms. Indeed, they are more accurate in most of the studied cases whether the frequency band, the SNR between the sources or the array geometry. However only MUSIC and the iterative signal deflation MLE are not too much time consuming for operational processing. Indeed, while one estimation for the spectral MLE takes 5 to 15s depending on the context (frequency band, array geometry, SNR of the sources involving a possible high number of iterations to estimate the three sources), the MUSIC and the iterative signal deflation takes less than 1s with around 0.8 s for MUSIC and 0.1 s for the iterative signal deflation making them more adequate for operational processing.

This evaluation leads to the first conclusion that especially the state-of-the-art MUSIC was enough accurate to be confronted to both developed algorithms on real case. This is the second stage of the comparison. Indeed the three algorithms has been compared on two real cases. The first one was the Baikonur rocket event recorded at the IS31, an array consisting of nine sensors. It was shown that the three algorithms had similar results on the first source in particular for the azimuth parameter. Indeed they are all able to estimate the dominating source of infrasound. MUSIC is however unable to precisely estimate the apparent velocity and have a clear artefact at the grid border. The secondary and the third source are detected by both MLE with similar amount of detections. It seems nevertheless that the detector produces better results with the suppression of more undesirable pixels with the iterative signal deflation due to respect of the monosource assumption of the p-value. The apparent velocity histograms are close from one to the another but the more noisy detections with the spectral MLE lead to a greater amount of estimation below 340 m/s. MUSIC is in contrast much more noisy with a kind of levelling of all azimuths and apparent velocities, the sources trends are however still visible. It means that MUSIC works effectively but has a high amount of noisy estimations too. The second example is following the same trend with similar estimations between both MLE whether for monosource and multisource results and highlight the difficulty of MUSIC to estimate with a lower number of sensors, even impacting the single source estimation. Thus taking into account the synthetics and real test on one hand, the computational cost in the other, the iterative signal deflation MLE is the better algorithm both for accuracy and time computation allowing an operational processing.

Finally, illustrations of the final product has been generated in the continuity of the single source illustration. After a classical post processing of clustering, the different small clusters has been gathered by the algorithm DBSCAN in order to produce the different event sheets showing how the interfering sources has been estimated and separated. However, this method has a clear limit when some clusters are close from one to another (i.e Baikonur launch close the permanent event and microbaroms close to the meteor). That is why, in order to improve this post processing task, essential to take advantage of the results of the multisource, it is necessary to develop a more accurate way of clustering pixels into events and that is the point of the next chapter IV.5.

Chapter IV.5

The clustering of detections into families of events

IV.5.1 Methods

Following the signal processing aiming at estimate the azimuth/trace velocity parameters of the sources, the characterisation of events is made by the family post processing studied in the subsection II.1.1.4. A novel clustering method based on a Gaussian Mixture Model (GMM) that uses the new uncertainty calculation obtained by MCML is investigated here by the Mines Telecom Institute and the CEA. This method avoids empirical rules and metrics provided by experts as it is for the current family clustering. It also provides a statistical interpretation of the resulting clustering. This new method is studied in the monosource case but with a desire to generalise it to the multisource algorithm in the future.

For the need of the method we define a cluster (event) of interest as a group of pixel characterised by a minimum and maximum frequency, a start time and an end time with similar values of azimuth/trace velocity. This definition of events leads to classical clustering methods because packets are formed on the basis of similarities between pixels. These clustering methods can be supervised or unsupervised, the fact that in the case of infrasound signals a small number of labelled data are accessible, especially at low SNR, leads us to consider an unsupervised approach. The used approach must suit *a priori* this situation and that is the goal of hidden variable method. It consists to suppose that each observation is generated by a distribution of hidden probability. The hidden variable method used here is the Gaussian Mixture Model (GMM). In this case, the assumption is that the data are generated by several Gaussian distributions, each one associated to a probability. Then the posterior law gives the probability of an observation to be generated by one of the cluster. The main goal is to estimate the parameters of the different Gaussian of the mixture in order to proper cluster the different pixels, forming an event.

Let $Y = (Y_1, ..., Y_N)$ be an independent and identically distributed list of observations in which each Y_i is a vector of dimension d, with d the dimension depending on the number of observations for each pixel, typically in our case the observations are the time, log frequency, SNR, azimuth and trace velocity of each pixel. The observation's law equation of the GMM for N pixels and K family clusters is expressed as

$$p_{\zeta,\alpha}^{Y_n}(y) = \sum_{k=0}^{K} \alpha_k f_k(Y_n; \zeta) \tag{IV.5.1}$$

with α_k the mixture proportions comprised between 0 and 1 such as $\sum_k \alpha_k = 1$ and f_k the probability density configured by the parameter set ζ to fit to a cluster of pixels. This settings need to be calculated in order to fit the observations at best. We define a variable $\eta = (\alpha, \zeta)$ grouping the parameters of interest of the clusters. Each of the observation Y_i is linked to a hidden variable X_i that can take K+1 discrete values $I_0, I_1, ..., I_K$. The complete distribution law for a cluster is thus expressed as

$$p_{\eta}^{X_n,Y_n}(k, y) = \alpha_k f_k(y; \zeta) \tag{IV.5.2}$$

The parameter set η which control the Gaussian dimension to fit the data can be estimated by a Maximum Likelihood Estimation (MLE) that expresses as

$$\hat{\eta}_K = \arg\max \mathcal{L}(Y, \eta; K) \tag{IV.5.3}$$

with $\mathcal{L}(\zeta; k)$ writing as

$$\mathcal{L}(Y, \eta; k) = \sum_{n=1}^{N} \log \left(\sum_{k=0}^{K} \alpha_k f_k(Y_n; \zeta) \right) \tag{IV.5.4}$$

The estimation of the parameter set η is made difficult by the sum in $\sum_{k=0}^{K} \alpha_k f_k(Y; \zeta)$ leading to the non-convexity of $\mathcal{L}(\eta; k)$. This mean that a clear analytical expression does not exist because of many maxima existence. That is why an iterative algorithm called Expectation Maximisation (EM) [Dempster et al., 1977] is used. The main property of this algorithm is that it constantly improves the likelihood at each iteration as express in the following statement

$$\mathcal{L}(Y, \hat{\eta}^j; k) \geq \mathcal{L}(Y, \hat{\eta}^{j-1}; k) \tag{IV.5.5}$$

However it does not avoid the possibility to fall into a local maximum. This algorithm at the iteration j writes in two steps, the first one is

$$Q(\eta, \eta^{j-1}, Y) = \sum_{n=1}^{N} \mathbb{E}_{\hat{\eta}^{j-1}} \{ \log p_{\eta}^{X_n, Y_n}(X_n, Y_n | Y_n) \} \tag{IV.5.6}$$

This is called the E step for expectation of the complete law described in the expression IV.5.2, depending on the observation Y_n. The second step, called the M step for maximisation has the goal to maximise $Q(\eta, \eta^{j-1}, Y)$ in order to optimise the parameter η

$$\hat{\eta}^j = \arg\max Q(\eta, \eta^{j-1}, Y) \tag{IV.5.7}$$

The iteration of the algorithm stops when the increase of the likelihood is inferior to an imposed threshold. In addition, because of the sensitivity of the algorithm to the initial η^0 chosen, it is necessary to run several times the EM algorithm to get rid of this limitation. Finally, the run with the maximum of likelihood is retained. In our case the initial value η^0 is deduce from the observations.

Different kinds of conditional laws for the model are established. The first one is the conditional law of the cluster located in time. The conditional law is written as a product of three Gaussian law especially in time, frequency f and slowness p, it can be express as for the k-th cluster

$$p(Y_n, k \neq 0) = \mathcal{N}(p_n; \zeta_k^p, \mathbf{\Gamma}_n) \times \mathcal{N}(f_n; \zeta_k^F, \sigma_k^F) \times \mathcal{N}(t_n; \zeta_k^T, \sigma_k^T) \tag{IV.5.8}$$

It is worth to notice that the conditional law is function of the MCML covariance matrix of the estimation $\mathbf{\Gamma}_n$. If the SNR is low, then the Gaussian $\mathcal{N}(p_n; \zeta_k^p, \mathbf{\Gamma}_n)$ will be narrower. Another conditional law is implemented in order to get rid of the isolated pixels considered as noise. The law expresses as

$$p(Y_n, k = 0) = \alpha_0 \left(\frac{1}{\pi(V_{min}^{-2} - V_{max}^{-2})} \times \frac{1}{(T_{max} - T_{min})} \times \frac{1}{(F_{max} - F_{min})} \right) \tag{IV.5.9}$$

This law is uniform on time, frequency and slowness to represent the random noisy detection. The parameter α_0 is arbitrary fixed to $1e-24$ because the MCML has in general only few noisy pixels. This constant can be calibrated for different array and frequency band before an operational in continuous time processing. In the following this cluster is called I_0. It is possible to add a last law about permanent sources like microbaroms that is a combination of the two previous law

$$p(Y_n, k \neq 0) = \mathcal{N}(p_n; \zeta_k^p, \mathbf{\Gamma}_n) \times \mathcal{N}(f_n; \zeta_k^F, \sigma_k^F) \times \frac{\alpha_k}{(T_{max} - T_{min})} \tag{IV.5.10}$$

The law is Gaussian for the slowness vector and frequency but uniform in time. However in the following only the two first laws are applied because the last one have shown some errors of clustering.

An estimate of the number of clusters has yet to be made in order to calculate the different conditional law and their parameters. In this context, different criterion are studied in particular the Akaike Information Criterion (AIC) (Akaike [1974]; Akaike [1998]) and the Bayesian Information Criterion (BIC) [Wit et al., 2012] that can be defined for a total number of clusters K as

$$\mathrm{AIC}(K) = -2\mathcal{L}(\hat{\eta}; P) + 2P \tag{IV.5.11}$$
$$\mathrm{BIC}(K) = -2\mathcal{L}(\hat{\eta}; P) + P\log(N) \tag{IV.5.12}$$

where P is the number of model parameters and N the number of observations. In our case there are three parameters per cluster (the two dimensional spaced parameters ζ_k^p, ζ_k^F and ζ_k^T), thus $P = 6K$. Studies have shown that the first criterion has a greater tendency to overestimated the number of clusters (Wax and Kailath [1985]; Celeux and Soromenho [1996]; Yang [2005]; Drton and Plummer [2017]; Celeux et al. [2019]). The BIC estimates a lower number of clusters if the number of observations is above a threshold that is $N < 7$ [Lebarbier and Mary-Huard, 2004]. The Bayesian criterion has a better penalty term than the one of Akaike, preventing an overestimation of the number of clusters. That is why the BIC is used in the following development. Once the criterion is calculated for each K possible number of clusters, the minimum of the function is the number of clusters chosen to estimate the different conditional laws as it can be seen on the figure IV.5.1 where the optimal number of clusters to estimate is eight. The K

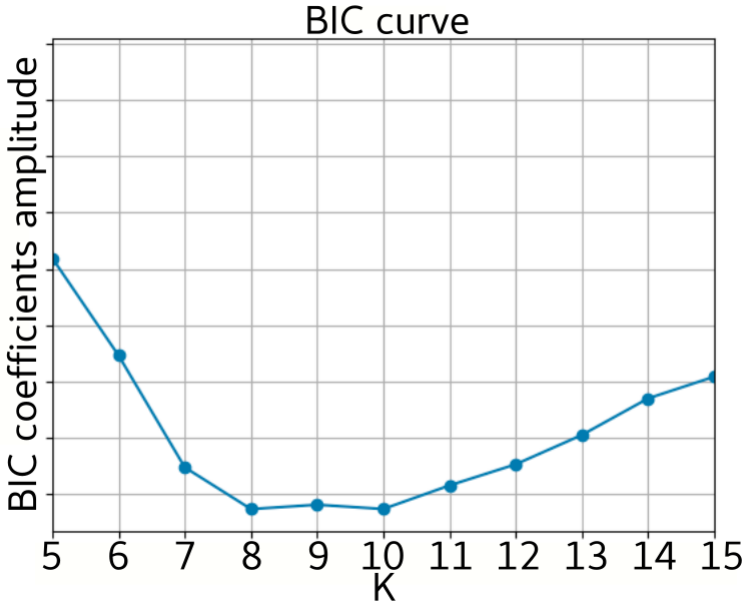

Figure IV.5.1: BIC coefficients in function of the total number of clusters K. The optimal number is found at the minimum of the function.

different conditional laws can now thus be calculated by the EM algorithm. Finally each pixels needs to be associated to an estimated cluster in order to complete the family clustering. Two probabilities exist in order to assign a pixel to a cluster. The first one is the prior probability that writes for all observations

$$p_\alpha^{X_n}(k) = \alpha_k \tag{IV.5.13}$$

Indeed this prior distribution shows that the probability of a pixel to be assigns to a cluster is only a function of the size of the cluster. This is clearly not satisfactory that is why a posterior distribution is calculated and expresses as

$$k \to p_{\alpha,\zeta}^{X_n|Y_n}(k|Y_n) = \frac{f_k(Y_n;\zeta_k)\alpha_k}{\sum_{j=1}^K f_j(Y_n;\zeta_j)\alpha_j} \tag{IV.5.14}$$

The maximum of this a posterior distribution indicates which cluster is prevailing at each time frequency cell. The process is illustrated by the figure IV.5.2, thus the probability of a pixel to be associated to a

cluster is at first function of the cluster size (i.e a priori $p_{\alpha}^{X_n}(k)$) . Here it can be seen that the first and the second clusters are the largest because of the higher probabilities (around 25%). However when the observation is taken into account (i.e $p_{\alpha,\zeta}^{X_n|Y_n}(k|Y_n)$) then the probabilities change and the first cluster has a very low probability of around 5% whereas the second one rises to around 60%.

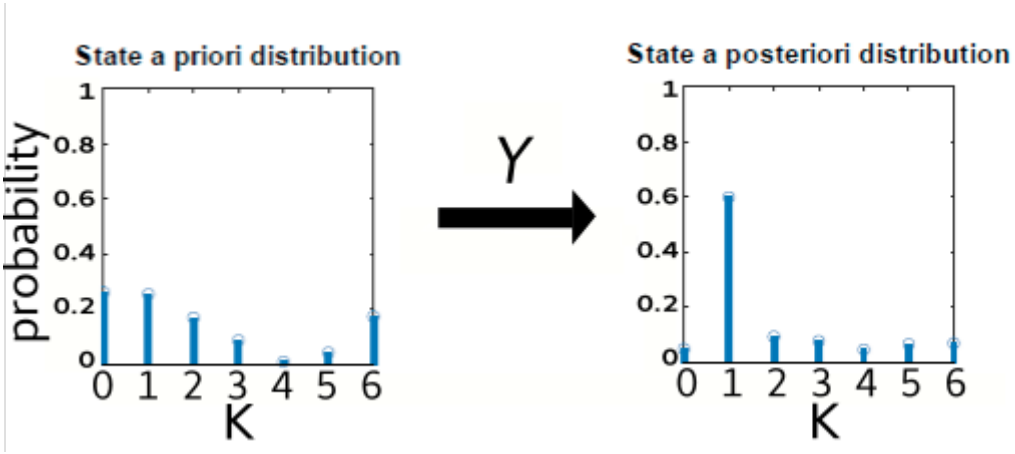

Figure IV.5.2: Illustration of the probabilities of a pixel to be assigned to a cluster without and then with the knowledge of the observation.

IV.5.2 Results

Two different examples are studied to illustrate how the new method of clustering works, its advantages and disadvantages compared to the current approach. The parameters for the EM is set to 20 runs in order to avoid local maximum as far as possible.

The first example is a meteor event, which happened on June, 21th in 2018 and was located around Voroneh in Russia. It was detected at around 03:00 UTC by the station IS37 in Norway. The following figures IV.5.3 and IV.5.4 show the pixels detected by MCML on a one hour lasting time window of the azimuth and the SNR. It is worth noticing that the high SNR event (more than 10 dB at low frequency) is the meteor event located with DOA of 140° from the station. This event is buried into microbaroms (i.e from Barents in orange and from Northern Atlantic in violet) and steam background noise of lower SNR (from moderate SNR of 5 dB to low SNR of -10 dB).
The classical procedure for family clustering gives the following figure IV.5.5 for the MCML and the PMCC algorithms. A total of 25 families are created for MCML and 15 for PMCC due to a lack of detection compared to the new algorithm. The number of families is too numerous regarding the number of sources that are present in the observed time window. In this case it would be better to gather the isolated families of similar characteristics that are probably separated due to switch of detected source.

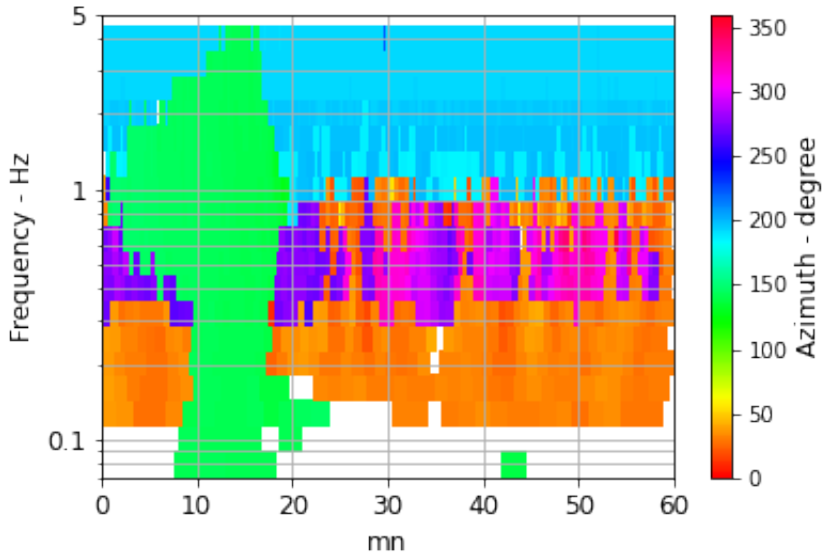

Figure IV.5.3: Detected azimuths by MCML on June, 21th in 2018 in function of the time and the frequency. The meteor event in green is detected with DOA of 140°, the event is buried in microbaroms and river noises.

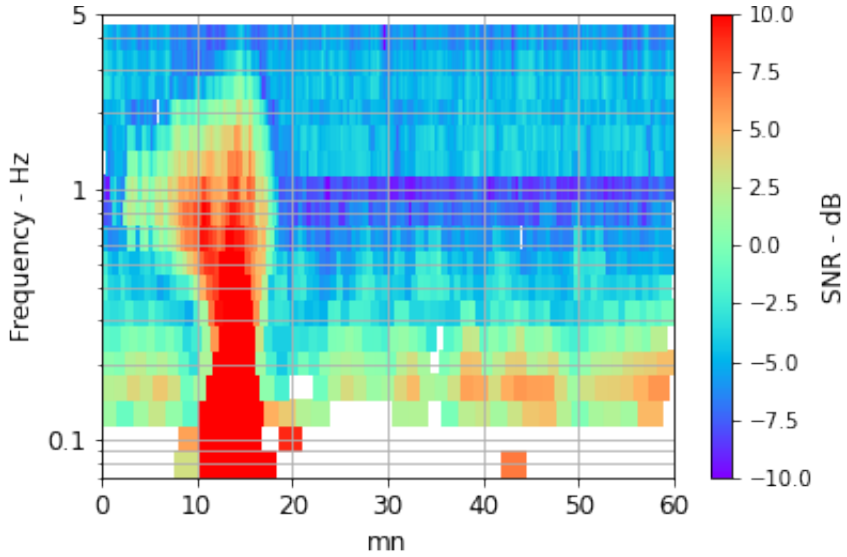

Figure IV.5.4: SNR of detected pixels by MCML on June, 21th in 2018 in function of the time and the frequency. The meteor event has a high SNR value compared to the surrounding background noise.

The BIC algorithm is used with a hypothesis of a number of clusters between $K = 5$ and $K = 15$. The results are shown in the figure IV.5.6 where we can see an asymptotic convergence of the function starting at nine clusters. We thus impose this number of clusters in the settings of the GMM. The results of the clustering are shown by the posterior maximum on the figure IV.5.7 and are to compared with the figures IV.5.3 and IV.5.4.
It is worth to notice that the pixels of microbaroms coming from a direction of around 20°-30° (in orange in the figure IV.5.3) are almost clustered in one and unique family along all the time window despite the interruption of microbaroms detections due to the meteor event. Indeed another small family centred around 20° is constructed with around 70 pixels whereas the major one has around 280 pixels. The fact that two clusters are dedicated to one microbaroms can be explained by the extended source in azimuth that characterise microbaroms. For the microbaroms we divide by two the number of family compared to the precedent processing. One source of microbaroms coming from around 290° (in violet in the figure

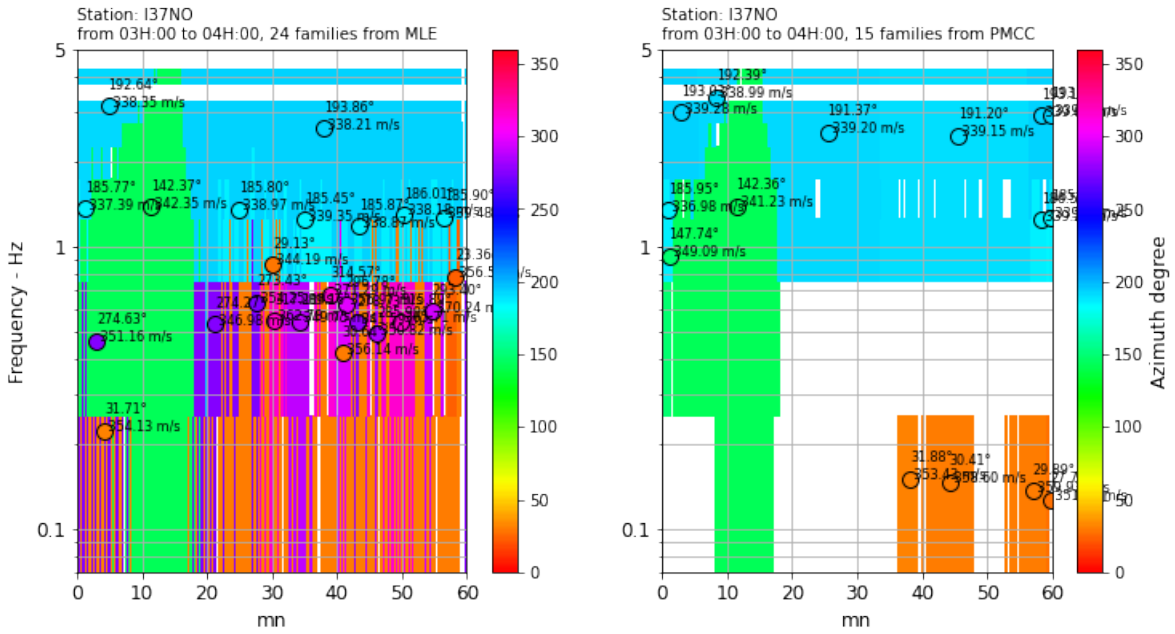

Figure IV.5.5: Current family clustering procedure. The superimposed scatter indicates the mean azimuth and trace velocity of the families. It can be seen a total of 25 families are created for MCML and 15 for PMCC due to less detections. However it is evident that there is less than 25 events in the time window.

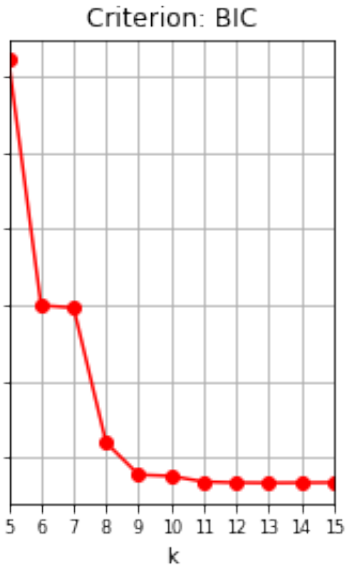

Figure IV.5.6: BIC coefficients in function of the total number of clusters K. The optimal number is found at the minimum of the function.

IV.5.3) is gathered in one cluster instead of nine families by the current algorithm. Another source is the high frequency noise coming from steam around the station (in blue in the figure IV.5.3). This source is gathered into four clusters due to azimuth dispersion instead of nine families with the current family algorithm. Finally the meteor event located at around 140° is gathered into two clusters. A clear separation in time can be observed between the two clusters. The cause is the SNR change, indeed the cluster associated with the pixel of 141° has a high SNR of around 10 dB. This leads to a low incertitude on the

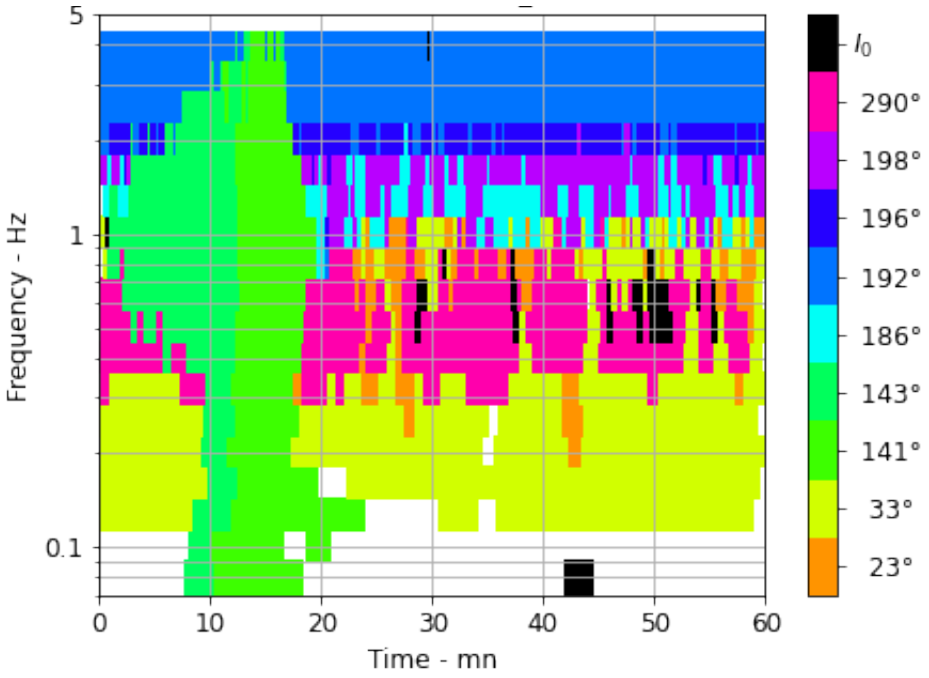

Figure IV.5.7: Detected azimuths by MCML on June, 21th in 2018 in function of the time and the frequency. Each color represents the mean azimuth of the cluster. The cluster I0 represents the pixels remaining that do not belong to any cluster.

wavefront parameters, thus the cluster is constructed with a narrow azimuth dispersion. When different arrivals cross the station with an azimuth a little bit different from the characteristic of the Gaussian then these pixels form another cluster with a mean azimuth close to the first cluster. This separation allows us to work on different arrivals of the event especially when stratospheric/thermospheric arrivals cross the antenna. We thus, thanks to the new approach, better gather pixels into a smaller number of families from 25 to 10.

The posterior maximum defines the results of clustering but it is also possible to look at the probability of pixels belonging to different cluster. The three figures IV.5.8, IV.5.9 and IV.5.10 represent the posterior probability of each pixels for the cluster of the microbaroms coming from the north and the both meteor clusters respectively. It is worth to notice that some pixels belonging to the other microbaroms cluster whose mean back-azimuth is 23° have a non zero probability to be included in the 33° mean azimuth cluster. That means that the wide source of microbaroms can be gathered in a second step of metafamily. The two others figures about the meteor event show that there is a clear belongings of pixels to their own cluster and that the probability of a pixel to belong to the other meteor cluster is near zero. It means that a clear feature distinguishes the two cluster from one to another. This feature is as said previously a slight difference in back-azimuth that becomes too much taking into account the incertitude of the estimation as a cluster parameter. Indeed they are really low for the cluster of the figure IV.5.9 due to a high SNR.

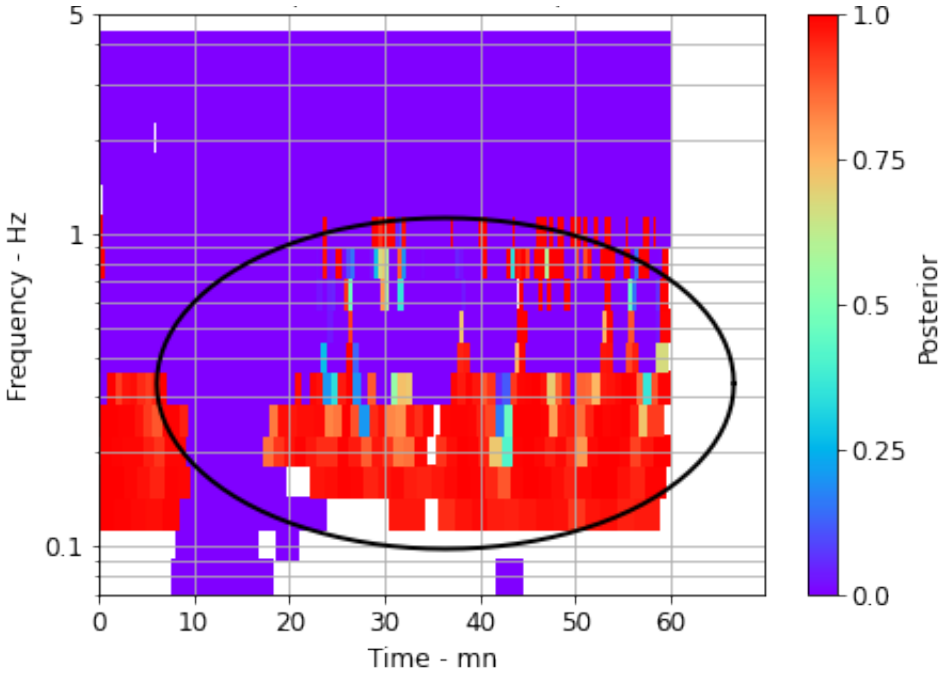

Figure IV.5.8: Posterior probability of each pixel for the microbaroms cluster with a mean DOA of 33°. The color represents the probability between zero and one to belong to the presented cluster. The black ellipse represents the confidence region at 80% of the conditional law $p(Y_n, k)$.

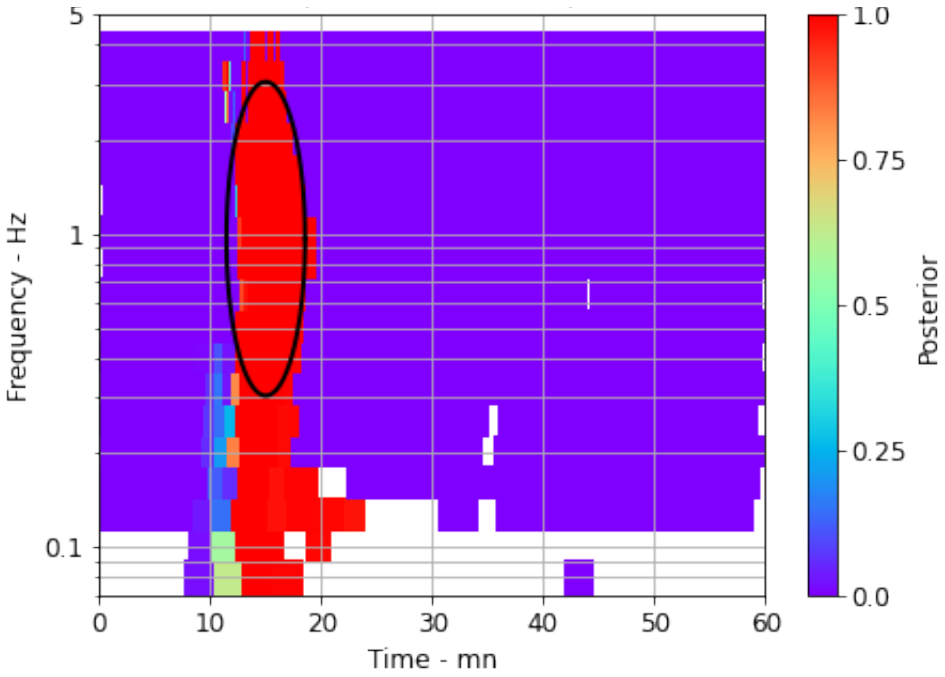

Figure IV.5.9: Posterior probability of each pixel for the meteor cluster with a mean DOA of 140°. The color represents the probability between zero and one to belong to the presented cluster. The black ellipse represents the confidence region at 80% of the conditional law $p(Y_n, k)$.

The previous example was performed in order to show how the new method was able to deal with discontinuous source detections leading to many family creations. The following example is about the detection of a Soyouz rocket launch from Plesetzk cosmodrome in the same direction as the Atlantic

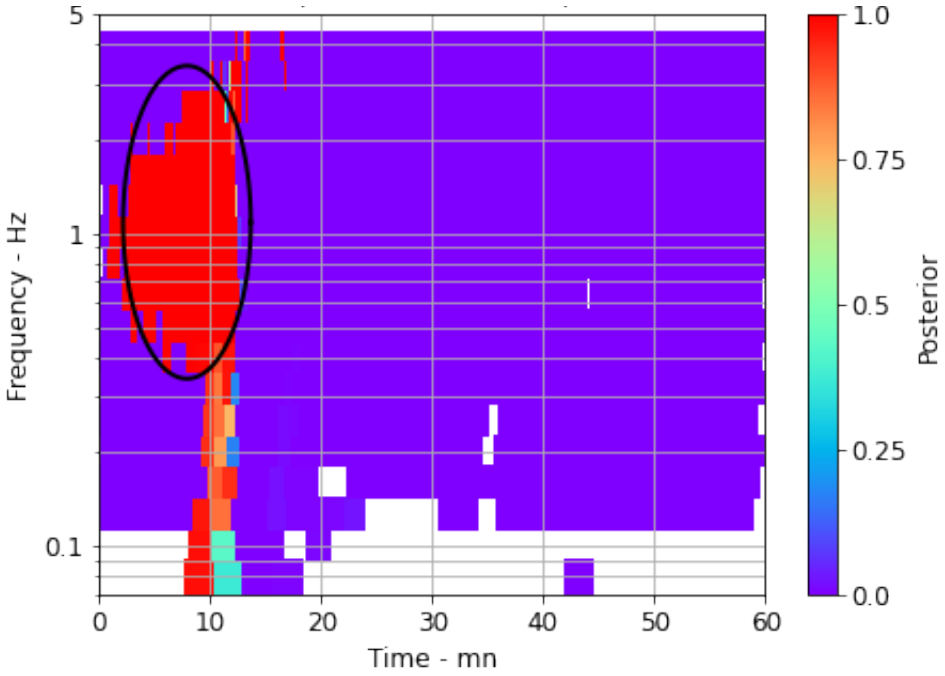

Figure IV.5.10: Posterior probability of each pixel for the meteor cluster with a mean DOA of 143°. The color represents the probability between zero and one to belong to the presented cluster. The black ellipse represents the confidence region at 80% of the conditional law $p(Y_n, k)$.

microbaroms. This event is detected by the station IS46 in April, 7th in 2022 at around 07:40 UTC, the detection by MCML are shown in the figure IV.5.11 for the back azimuth and IV.5.12 for the SNR values.

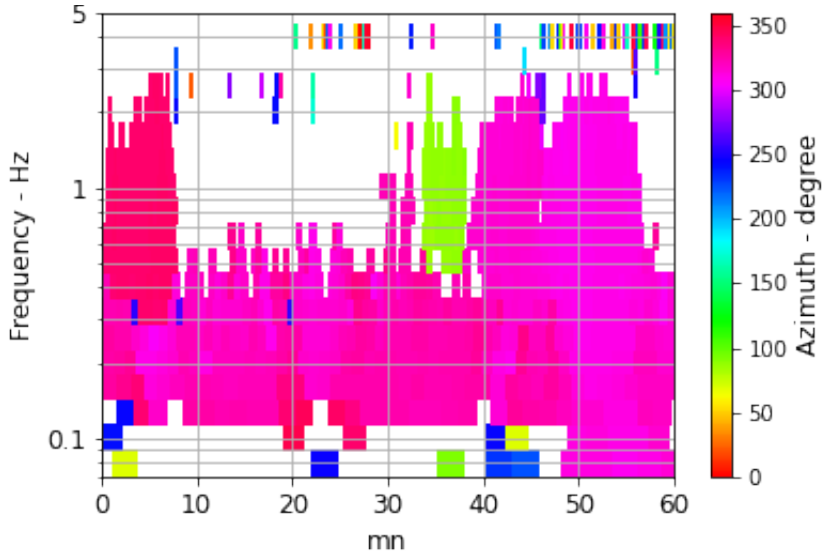

Figure IV.5.11: Detected azimuths by MCML on April, 7th in 2022 in function of the time and the frequency. The rocket event in pink is detected at around 340°, the event is buried in microbaroms of similar azimuths.

The current procedure for family clustering gives the following results IV.5.13 for the MCML and the PMCC algorithms. A total of seven families are created for MCML and six for PMCC. It is worth to notice that the actual procedure gathers both the microbaroms and the rocket launch due to similar back-azimuth and velocity values. It is a main problem since it gathers two different events (i.e in term

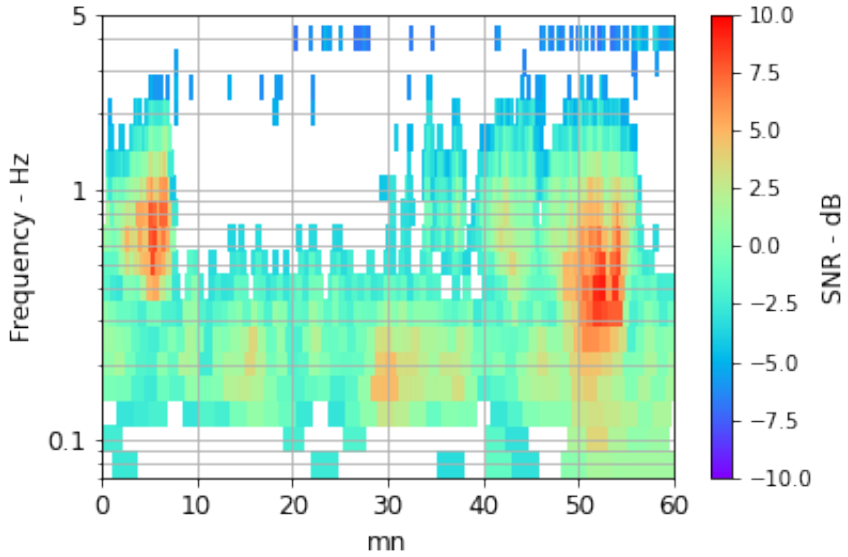

Figure IV.5.12: SNR of detected pixels by MCML on April, 7th in 2022 in function of the time and the frequency. The rocket launch event has a high SNR value compared to the surrounding background noise.

of source, frequency content, time etc...) and because the rocket launch is an event of interest compared to the background microbaroms noise for the CTBTO mission. Thus, the goal is to separate the different arrivals of the rocket from the microbaroms.

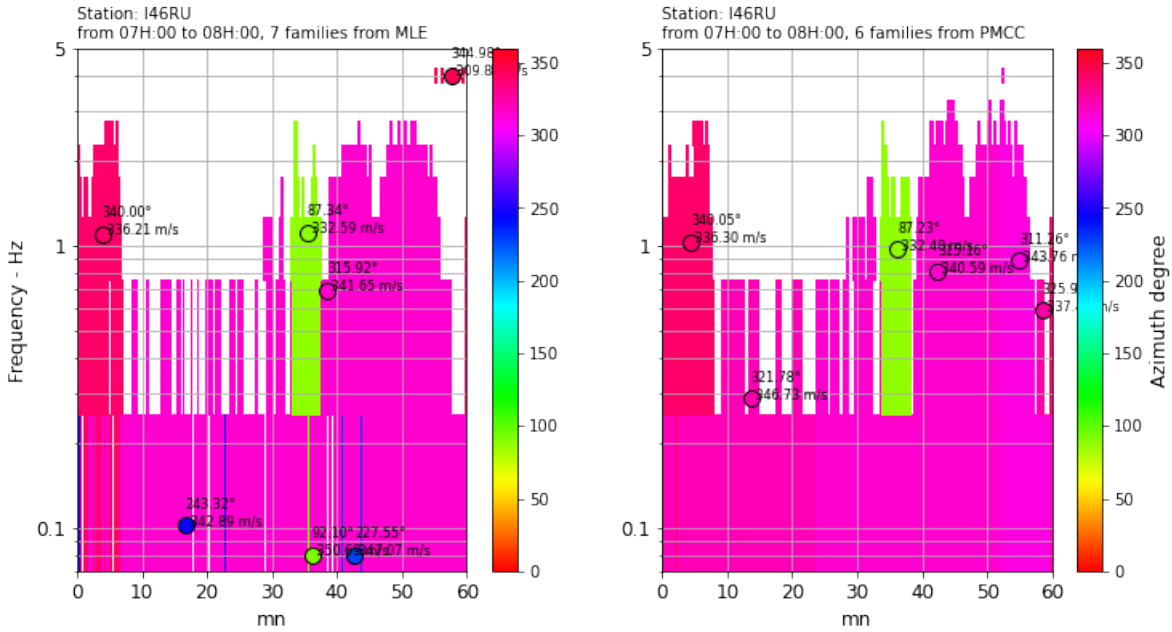

Figure IV.5.13: Current family clustering procedure. The superimposed scatter indicates the mean azimuth and trace velocity of the family. It can be seen a total of seven families are created for MCML and six for PMCC.The main issue is the gathering of the microbaroms and the rocket launch.

The BIC algorithm was used once again with the same range as previously studied that was between $K = 5$ and $K = 15$. The results are shown in the figure IV.5.14 where we can see an asymptotic convergence of the function starting at twelve clusters. We thus impose this number of clusters in the settings of the GMM.

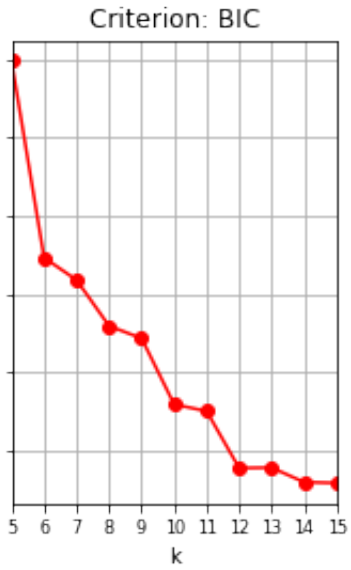

Figure IV.5.14: BIC coefficients in function of the total number of cluster K. The optimal number is found at the minimum of the function.

The results of the clustering are shown by the posterior maximum on the figure IV.5.15 and are to compared with the figures IV.5.11 and IV.5.12.
The first observation that we can be made is that the microbaroms and the different arrivals of the rocket launch are effectively separated into different clusters mainly thanks to SNR bursts of the different arrivals. It is worth to notice that the GMM allows to separate different sources with only a few back-azimuth angle of difference. The source at 340° is also separated into two clusters due to the difference of SNR showing how the inclusion of this parameter can be very important to form the new families. A similar case is shown with the cluster with a mean of 308° and 310° in green where the main difference is the SNR level of the event section. A total of four families are created only for the microbaroms, this can be explained by SNR variation in the background noise. Indeed, the cluster in blue at 321° is characterised by a high SNR compared to the other microbaroms clusters (i.e 326° in dark blue, 332° in purple). The mean of back-azimuth is of course different from one cluster to another but the extended source model of the microbaroms includes a variation in the cluster itself. A metafamily processing should gathers the four clusters. This example shows how the class I0 allows a cleaning of undesirable detection at high frequency.

The three figures IV.5.16, IV.5.17 and IV.5.18 represent the posterior probability of each pixel for the arrival clusters of a rocket launch and one of the microbaroms, respectively, both events coming from the same direction. It is worth to notice that the arrivals of the rocket launch are subdivided due to the SNR variation represented in the previous figure IV.5.12. It is also easy to see that the border of the two clusters are ambiguous, particularly when the frequency band decreases. It means that the both clusters are close from one to the other. This is confirmed by the proximity of the two clusters in time, frequency but also by their similar back-azimuth of 308° and 310°. The figure IV.5.18 is the posterior distribution of the most important cluster of microbaroms. It can be observed that there is no ambiguity between this cluster of the clusters of the different arrivals. This means that contrary to the current way of gathering pixels into families, the new method is able to discriminate two events coming from the same direction thanks to the SNR contrast associated to the time-frequency content. In another hand there

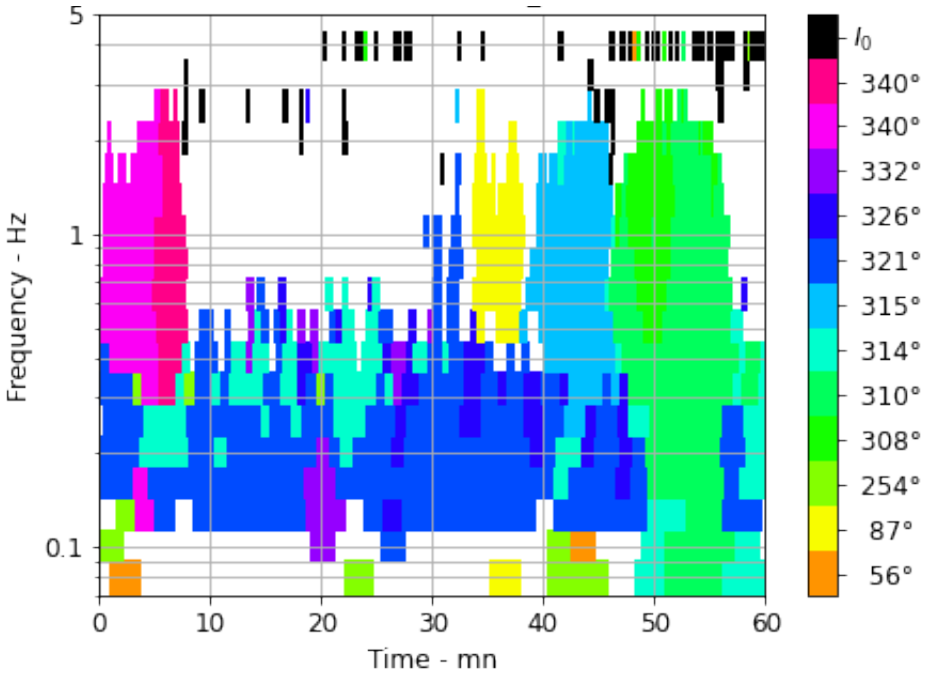

Figure IV.5.15: Detected azimuths by MCML on April, 7th in 2018 in function of the time and the frequency. Each color represents the mean azimuth of the cluster. The cluster I0 represents the pixels remaining that do not belong to any cluster.

is non negligible probability of pixels belonging to other microbaroms clusters to be associated to this cluster. It clearly shows that the different cluster of microbaroms have close features and can be gathered by the metafamily processing.

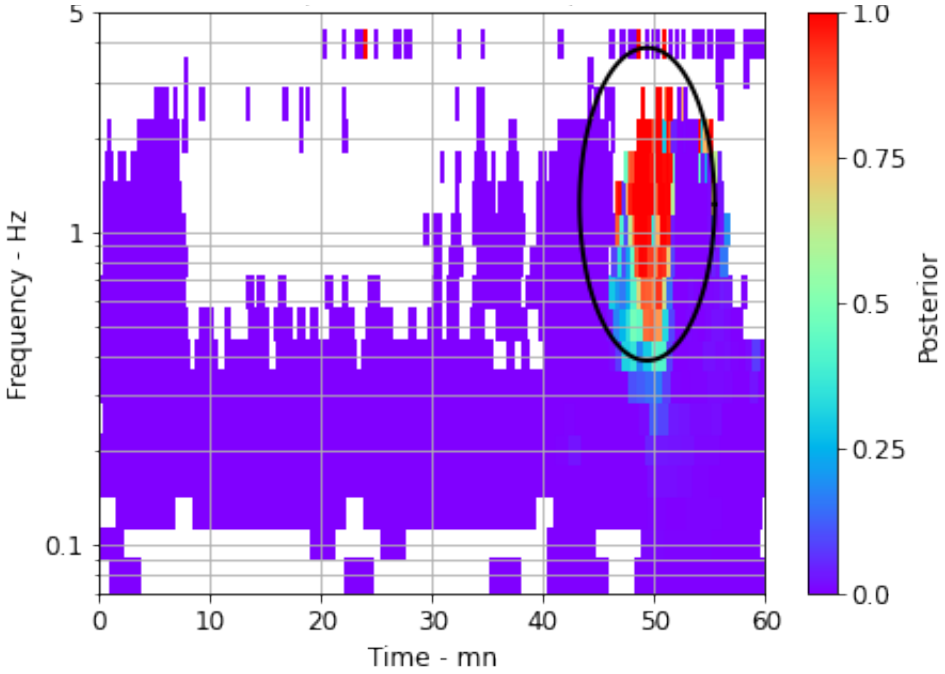

Figure IV.5.16: Posterior probability of each pixel for the rocket launch arrival cluster with a mean DOA of 310°. The color represents the probability between zero and one to belong to the presented cluster. The black ellipse represents the confidence region at 80% of the conditional law $p(Y_n, k)$.

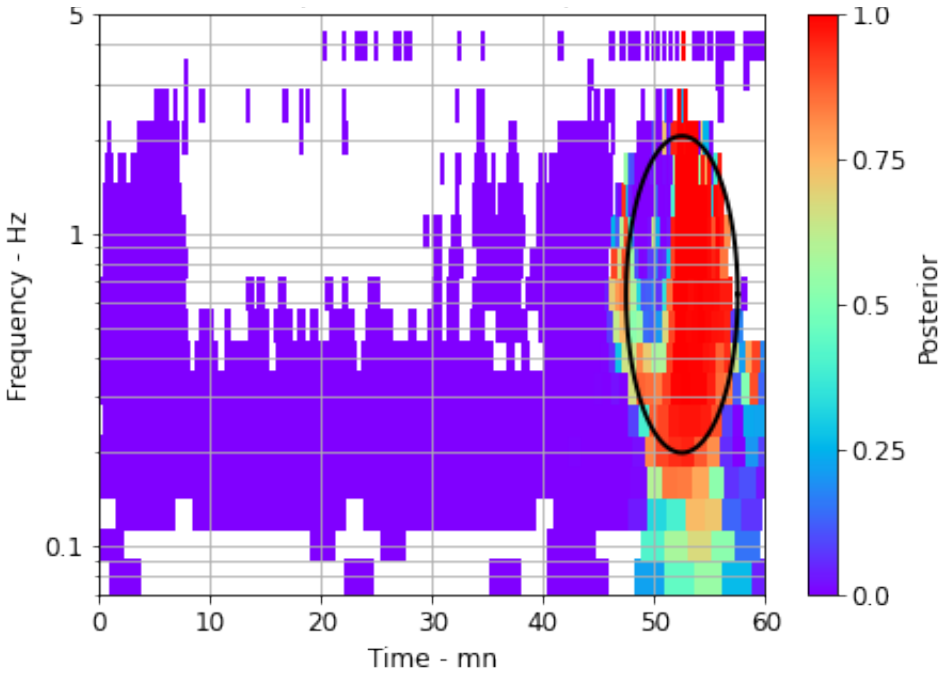

Figure IV.5.17: Posterior probability of each pixel for the rocket launch arrival cluster with a mean DOA of 308°. The black ellipse represents the confidence region at 80% of the conditional law $p(Y_n, k)$.

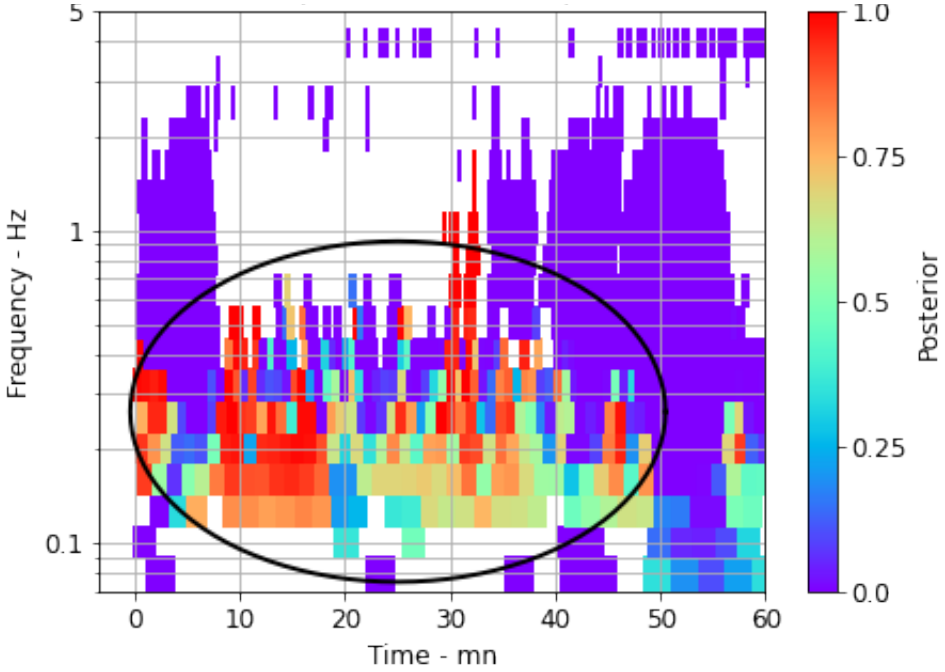

Figure IV.5.18: Posterior probability of each pixel for the Hukkakero cluster with a mean DOA of 143°. The black ellipse represents the confidence region at 80% of the conditional law $p(Y_n, k)$.

IV.5.3 Discussion and conclusion

The different examples have shown how the GMM was able to gather pixels into families for a better analysis and understanding than the current method. Indeed in the first example we have shown that the GMM was able to better perform agglomeration of pixels in condition of multiple sources interference in the time frequency domain. It allows a more continuous cluster in this domain and a fewer number of families, avoiding a too numerous number of families for an event as the microbaroms. This example and the following have shown how the contrast of SNR, reflecting the characteristic of the arrival, can shape the clustering for a more detailed analysis. The number of clusters has to be indicated as a parameter of the GMM and this need is fulfilled by a BIC evaluation of the number of sources presented in time window studied. In both examples, the BIC algorithm provided a correct number of sources and a quick try of a different number of clusters (i.e for example $K = 6$ for the IS46 based on visual estimation number of family, figure IV.5.19) leads to a wrong gathering of pixels (i.e sometime it gathers a part of microbaroms with an arrival of the rocket launch).

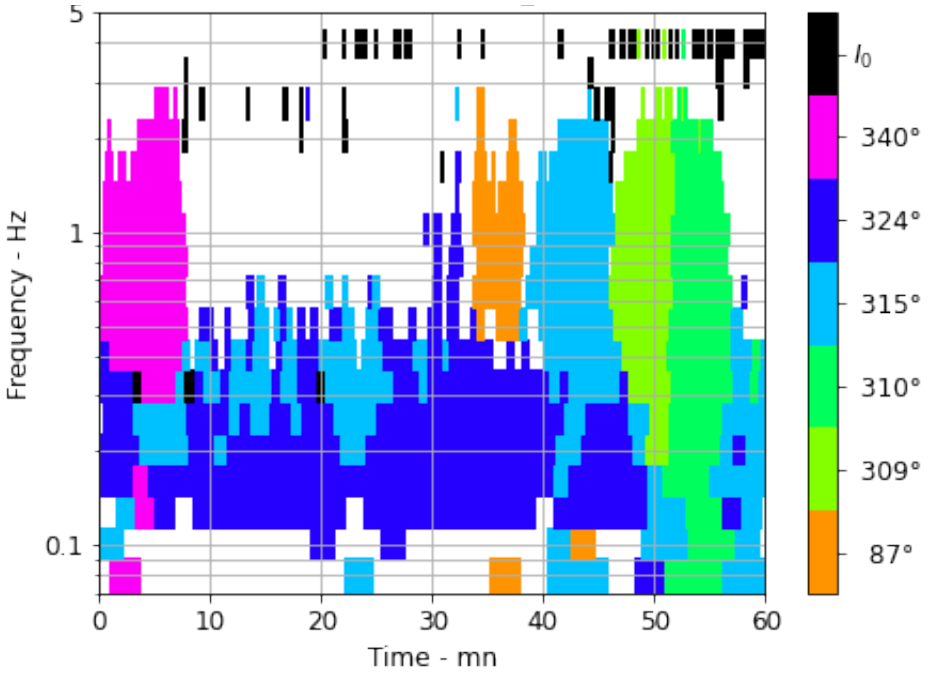

Figure IV.5.19: Detected azimuths by MCML on April, 7th in 2018 in function of the time and the frequency. Each color represents the mean azimuth of the cluster. The cluster I0 represents the pixels remaining that do not belong to any cluster. The number of clusters has been set arbitrary to six according to a visual appreciation of the number of sources in the figure IV.5.11.

However this process has to be done for each hour of signal record. The BIC evaluation has to be made within a range of possible K clusters. Indeed as previously seen a wrong number of clusters is leading to an incorrect gathering that is why a wide range of possible cluster has to be evaluated (i.e here we establish an interval of 5 to 15, we assume that more than 15 different sources in an hour is highly improbable). This process is at that moment costly in term of computation time (i.e around thirty minutes for the BIC algorithm between K=5 and K=15 with 20 runs for each hypothesis number of clusters). Indeed the higher the number of clusters is the more costly the calculation time is either. Thus the total time computation including the GMM is approximately between half of an hour. To optimise it, a paralleling computation of the Expectation Maximisation algorithm has to be done in order to hope a real time implementation. Finally a further work has to be done about the pixel gathering at high and low frequency originating from different sources whereas there is no any connection between this pixels that has a physical sense. A first approach was to change the observation from frequency to log frequency and this correction clearly avoids this kind of gathering, however some undesirable gathering still persist in some case as in the following example. The figures IV.5.20 IV.5.21 and IV.5.22 represent the azimuth,

apparent velocity and SNR of the detected arrivals at the IS37 on August, 22th between 13:00 and 14:00 UTC. It is worth to notice that there is several source at low frequency from microbaroms and at high frequency from steam background noise. The Hukkakero impulsive event is detected at around 13:50 with a back-azimuth at around 110°.

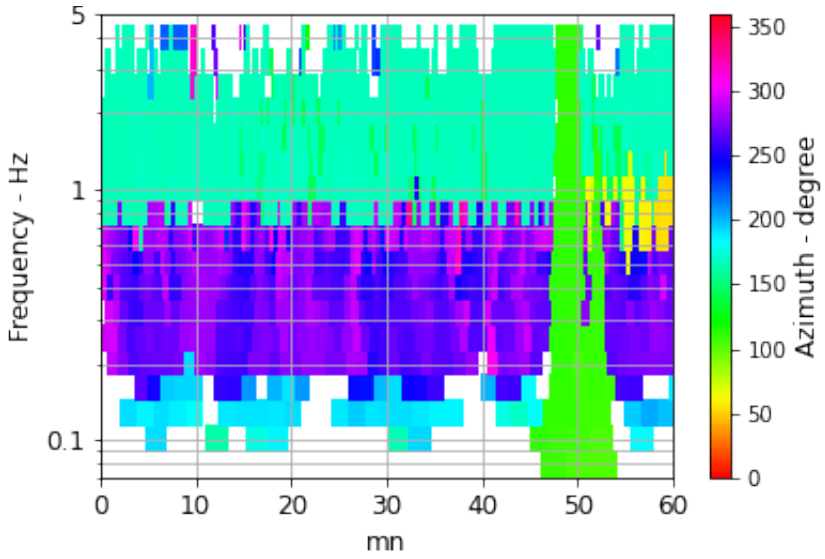

Figure IV.5.20: Detected azimuths by MCML on August, 22th in 2021 in function of the time and the frequency. The impulsive event at 13:50 UTC is the Hukkakero event. The background noise is composed of microbaroms and steam noise.

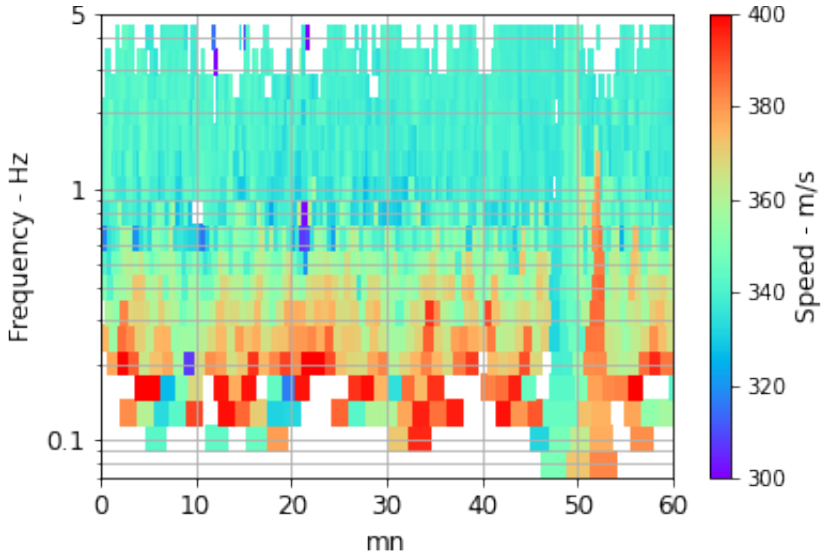

Figure IV.5.21: Speed of detected pixels by MCML on August, 22th in 2021 in function of the time and the frequency. The impulsive event at 13:50 UTC is the Hukkakero event.

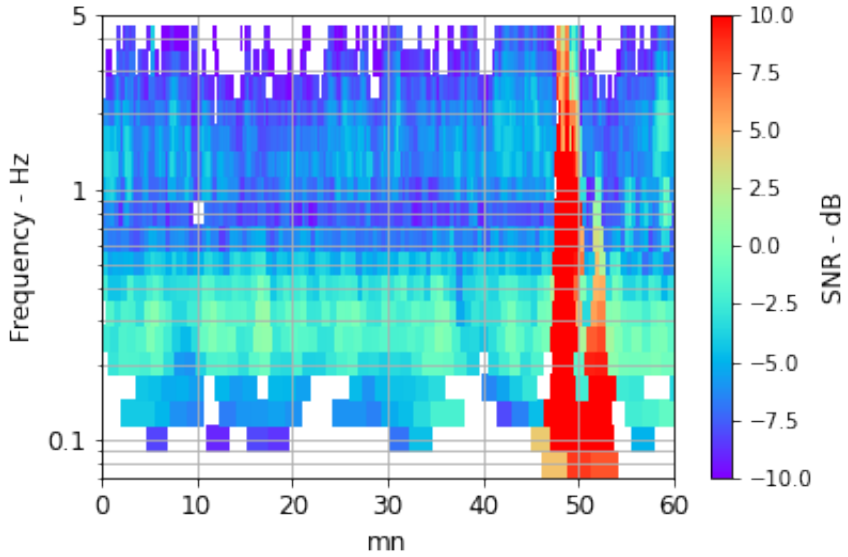

Figure IV.5.22: SNR of detected pixels by MCML on August, 22th in 2021 in function of the time and the frequency. The impulsive event at 13:50 UTC is the Hukkakero event.

The BIC algorithm gave a results of 11 distinct events, thus the GMM results are given by the clustering represented in the figure IV.5.23. It can be seen that the Hukkakero cluster is correctly modelled and that there is three clusters formed for the steam noise and three other events for the microbaroms. However the main point is that there is still some pixels at low frequency associated with pixels at high frequency as for example the ones at 167° around 13:40 UTC or at 222°, 262° or even at 283° around 13:10 UTC at high frequency linked to low frequency clustering. The aforementioned associations are primarily driven by the back-azimuth proximity of the pixels. Moreover some pixels at very low frequency with back-azimuth lower than 200° (i.e light blue) are linked to the clustering with mean back-azimuth of 262° as it can be seen at around 13:10, 13:20 and 13:40 UTC. The back azimuth is distinct between the two kind of pixels, no serious link can be done with speed nor SNR (i.e some pixels have a high SNR level as the ones at 13:40 UTC or a lower one as the ones at 13:10 UTC). Thus the only explanation is the proximity of frequency band with maybe some back-azimuth and SNR impact.

The both kind of absurd associations can be illustrated by the posterior probabilities of clusters. Indeed the figure IV.5.24 shows that the probability for pixels with low frequency to be associated to the pixels of the steam event at higher frequency is non zero even if they are no associated. It shows that there are similarities between the two groups. The figures IV.5.25 and IV.5.26 represent the posterior of two the involved microbaroms cluster at low frequency. It is worth noticing that the cluster at 262° tends to gather pixels of the other cluster indicating an ambiguity between the two clusters. This kind of erroneous association can distort the cluster information, as the mean back-azimuth, etc... This is particularly evident in the case of the cluster with a mean back-azimuth of 222°, which appears to deviate from the expected value of 180° (figure IV.5.20).

Finally as it has been shown, the GMM better cluster pixels to form families of events but some improvements have to be done in order to lower the computational cost and to avoid some absurd associations.

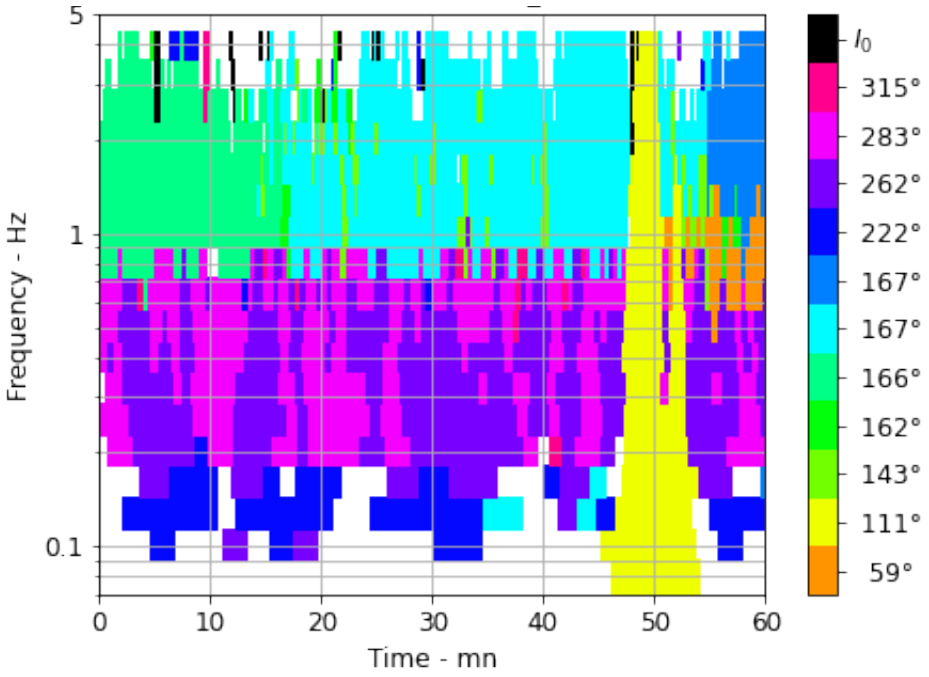

Figure IV.5.23: Detected azimuths by MCML on August, 22th in 2021 in function of the time and the frequency. Each color represents the mean azimuth of the cluster. The cluster I0 represents the pixels remaining that do not belong to any cluster. A few pixels of the clustering at 167°, 222°, 262° can be found associated together whereas they have different frequency contents.

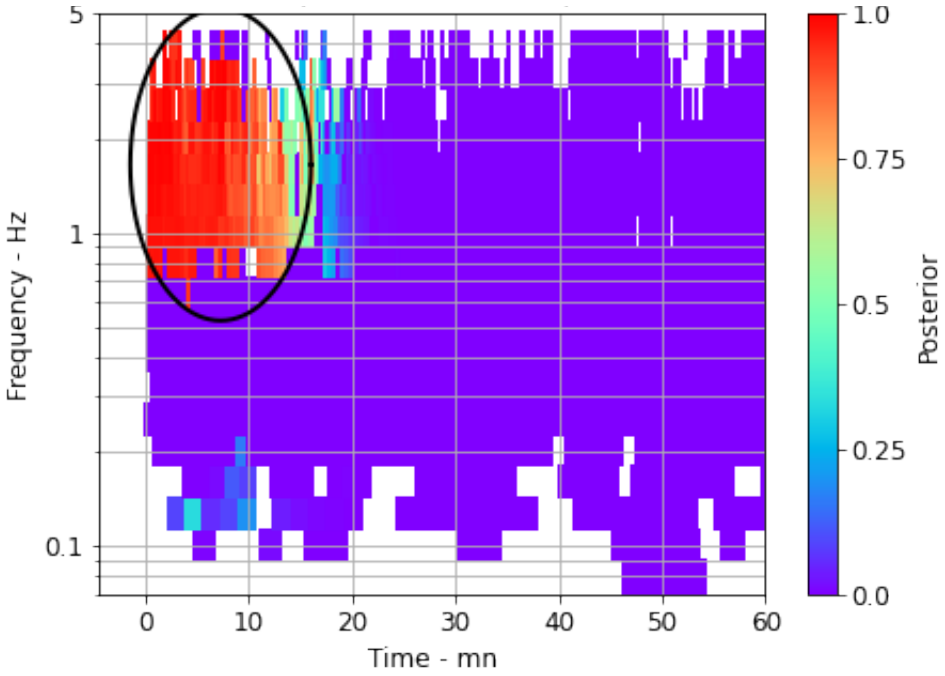

Figure IV.5.24: Posterior probability of each pixel for one steam cluster with a mean DOA of 166°. The black ellipse represents the confidence region at 80% of the conditional law $p(Y_n, k)$.

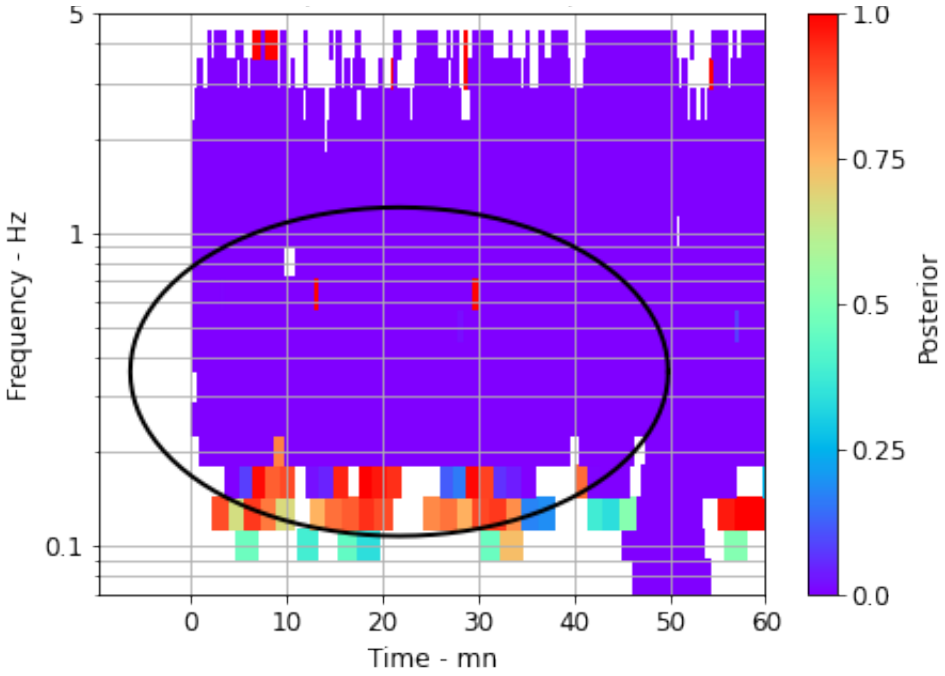

Figure IV.5.25: Posterior probability of each pixel for one microbaroms cluster with a mean DOA of 222°. The black ellipse represents the confidence region at 80% of the conditional law $p(Y_n, k)$.

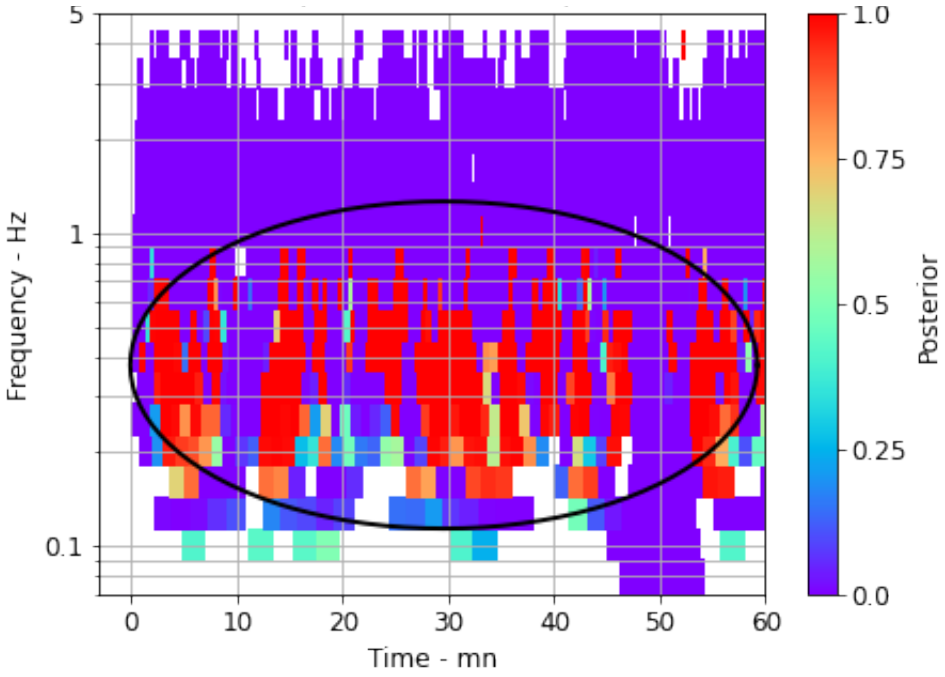

Figure IV.5.26: Posterior probability of each pixel for another microbaroms cluster with a mean DOA of 262°. The black ellipse represents the confidence region at 80% of the conditional law $p(Y_n, k)$.

Conclusion (in english)

Several methods have been developed and tested in this part. We first studied the ways to adjust the windows in time and frequency for the use of the monosource MLE. This study proved to be necessary in order to improve the accuracy of multisource estimates, multiplying by a factor two the length of the analysis window. It led to the establishment of methods leveraging the monosource MLE algorithm. Only the iterative source signal subtraction methods and the grid maximum selection method are selected. These two methods have shown good results in preliminary tests. This was not the case for methods involving image processing, such as the active contour method or iterative Gaussian subtraction, which proved to be too dependent on parameters that vary according to the frequency band. Subsequently, an approximation of a multisource MLE was developed in the frequency domain to quantify its contribution compared with the previously mentioned methods, as well as its computational cost. Other approaches were then studied, such as ICA, which appeared useless due to the broadband nature of the sources of interest and the sparsity of the number of sources. On the other hand, dictionary coding is an effective approach with both the OMP and LASSO.

In a second phase, tests on synthetic signals were conducted using selected approaches from the state-of-the-art as well as algorithms specifically developed to estimate the wavefront parameters. Table IV.5.1 and IV.5.2 are summarising the results of the different algorithms for the band [0.5 - 0.64] Hz at IS31 and IS46 respectively. The false estimation rate and the 95th quantile of the absolute errors are represented for each SNR of the different sources (5 dB, 0 dB and -5 dB) included in the same synthetic signal. The source at 5 dB is well estimated by the different algorithms except TOPS and the OMP with delay as atoms. Then, when sources with lower SNR are estimated, only the MUSIC algorithm, the spectral MLE and the MLE with iterative signal deflation are able to well constrain the wavefront parameters, the latter being the most accurate method. This observation can also be done with a worse geometry as the one of IS46, even if accuracy decreases, where only the MLE with iterative signal deflation estimates correctly multiple sources. Two events of interest have been analysed: a rocket launch at Baikonur, recorded by the Kazakh station IS31 of the IMS, and a meteor explosion off the coast of Namibia, recorded by the station IS19 in Djibouti. The results show that the iterative signal deflation MLE is the most accurate algorithm with a lower computational cost.

Finally, a new approach to pixel clustering for the creation of events of interest has been evaluated on signals of interest. This method proves to be more effective by creating fewer but more continuous families, facilitating the separation of different arrivals from different sources by exploiting the SNR of the arrivals. Developments are still needed to limit the clustering of pixels at frequencies that are too far apart and to address prohibitive computation times for operational conditions.

Table IV.5.1: False estimation rate and absolute errors on azimuth (95th quantile) for each algorithm for IS31 at [0.5 - 0.64] Hz. The MLE with iterative signal deflation is highlighted due to its high accuracy.

	False estimation rate			Absolute errors on azimuth		
Algorithms	5 dB	0 dB	-5 dB	5 dB	0 dB	-5 dB
State-of-the-art methods						
TOPS	100 %	99.9 %	100 %	∅	8.0°	∅
MUSIC	0.1 %	5.5 %	68.7 %	2.0°	3.0°	7.0°
Fisher	0.1 %	74.2 %	93.2 %	2.0°	7.0°	8.0°
MVDR	2.0 %	16.3 %	80.7 %	2.0°	4.0°	8.0°
MVDR regularised	1.1 %	72.5 %	94.6 %	2.0°	6.0°	8.0°
MLE-based methods						
MLE multipeak	0.5 %	71.3 %	94.6 %	1.0°	4.8°	8.9°
Spectral MLE	0.1 %	1.9 %	87.1 %	1.0°	3.0°	8.3°
Fast spectral MLE	0.2 %	4.5 %	95.1 %	0.9°	3.1°	8.1°
Iterative signal deflation	**0 %**	**0.6 %**	**24.4 %**	**1.0°**	**2.1°**	**3.8°**
Sparse methods						
LASSO Likelihood	0 %	61.0 %	95.2 %	2.0°	5.0°	9.0°
OMP Delay	90.6 %	93.3 %	99.3 %	8.0°	9.0°	8.2°
OMP Likelihood	0.5 %	32.1 %	92.1 %	3.0°	6.0°	8.6°

Table IV.5.2: False estimation rate and absolute errors on azimuth (95th quantile) for each algorithm for IS46 at [0.5 - 0.64] Hz. The MLE with iterative signal deflation is highlighted due to its high accuracy.

	False estimation rate			Absolute errors on azimuth		
Algorithms	5 dB	0 dB	-5 dB	5 dB	0 dB	-5 dB
State-of-the-art methods						
TOPS	85.3 %	93.5 %	97.4 %	6.2°	8.0°	9.0°
MUSIC	85.5 %	89.9 %	92.0 %	7.2°	8.0°	9.0°
Fisher	0.7 %	92.8 %	94.5 %	2.0°	9.0°	9.0°
MVDR	2.9%	91.1%	95.2%	1.0°	7.0°	9.0°
MVDR regularised	3.6 %	92.0 %	95.8 %	1.0°	6.5°	9.0°
MLE-based methods						
MLE multipeak	0.2 %	91.2 %	96.5 %	0.6°	9.1°	8.8°
Spectral MLE	0 %	61.6 %	95.5 %	0.6°	3.5°	9.3°
Fast spectral MLE	0 %	100 %	100 %	0.6°	∅	∅
Iterative signal deflation	**0.2 %**	**4.1 %**	**84.0 %**	**0.6°**	**1.3°**	**8.3°**
Sparse methods						
LASSO Likelihood	0 %	71.0 %	95.0 %	1.0°	4.0°	8.0°
OMP Delay	76.2 %	90.0 %	92.7 %	7.0°	8.0°	9.0°
OMP Likelihood	0 %	59.2 %	92.1 %	1.0°	4.0°	9.0°

Conclusion (en français)

Plusieurs méthodes ont été développées puis testées dans cette partie. Nous avons étudié tout d'abord les voies d'amélioration des fenêtres en temps et en fréquence pour l'utilisation du MLE monosource. Cette étude s'est avérée nécessaire afin d'améliorer la précision des estimations multisources en multipliant par deux la fenêtre d'analyse. Elle a conduit à la mise en place de méthodes tirant partie de l'algorithme MLE monosource. Seules les méthodes de soustraction itérative de signal source et la méthode de sélection de maxima sur la grille sont retenues. En effet, ces deux méthodes ont montré de bons résultats dans des tests préliminaires. Cela n'a pas été le cas des méthodes incluant du traitement d'image comme la méthode par contours actifs ou de soustraction itérative de gaussienne qui se révèlent trop dépendantes de paramètres variables selon la bande de fréquence. Par la suite, une approximation du MLE multisource a été développé dans le domaine fréquentielle pour quantifier son apport en précision par rapport aux méthodes précédemment citées ainsi que son coût en calcul. D'autres approches ont ensuite été étudiées, comme l'ACI qui s'est révélée infructueuse en raison de l'aspect large bande des sources d'intérêt et de la parcimonie du nombre de sources. En revanche, le *dictionary coding* s'est montré efficace tant avec l'OMP que LASSO.

Dans un second temps, des tests sur signaux synthétiques ont été effectués avec des algorithmes sélectionnés dans l'état de l'art ainsi que des algorithmes développés spécifiquement pour estimer les paramètres du vecteur d'onde. Les tableaux IV.5.1 et IV.5.2 résument les résultats des différents algorithmes pour la bande [0,5 - 0,64] Hz à IS31 et IS46 respectivement. Le taux de mauvaises estimations et le 95e quantile des erreurs absolues des azimuts sont représentés pour chaque SNR des différentes sources (5 dB, 0 dB et -5 dB) incluses dans le même signal synthétique. La source à 5 dB est bien estimée par tous les différents algorithmes, sauf par TOPS et l'OMP avec les retards en tant qu'atomes. Ensuite, lorsque des sources avec un SNR plus faible sont estimées, seuls les algorithmes MUSIC, le MLE spectral et le MLE avec déflation itérative du signal sont capables de bien contraindre les paramètres du front d'onde, ce dernier étant la méthode la plus précise. Cette observation peut également être réalisée avec une géométrie moins favorable comme IS46, même si la précision diminue, où seule le MLE avec déflation itérative de signaux est capable d'estimer correctement plusieurs sources. Les méthodes de soustraction itérative de signaux, les MLE basés sur la matrice spectrale ainsi que MUSIC ont donc été retenues pour des évaluations sur signaux réels au vu de leurs résultats prometteurs. Deux événements d'intérêt ont été analysés, un décollage de fusée à Baikonur, enregistré par la station kazakhe IS31 du SSI, et une explosion de météorite au large de la Namibie enregistrée par la station IS19 à Djibouti. Les résultats ont montré que l'algorithme MLE monosource de déflation itérative de signaux est plus performant avec un coût en calcul plus faible.

Enfin, une nouvelle approche de clustering de pixels pour la formation d'événements d'intérêt a été évaluée sur des signaux d'intérêt. Cette méthode s'est avérée plus efficace en créant moins de familles, mais plus continues, facilitant la séparation de différentes arrivées provenant de sources différentes en exploitant le SNR des arrivées. Des développements restent nécessaires pour limiter l'agglomération de pixels à des fréquences trop éloignées et un temps de calcul rédhibitoire pour des traitements opérationnels.

Part V

Conclusion and perspectives

English conclusion

The continuing development of infrasound monitoring systems, including the IMS, leads to more and more data to process. Currently, the principle data processing method used by the IDC of the CTBTO, and many NDCs (including the NDC in France), is PMCC due to its high efficiency. However, user feedback regarding the limitations of PMCC at low SNR or at distinguishing between multiple sources in the same frequency band, lead to the recent development of MCML, as described in chapter II.2. This new algorithm greatly improves the detection and characterisation of infrasound and seismic signals, especially at low SNR or when there are multiple interfering SOIs. Despite the increased computational costs of MCML, current computers are capable of running it at an operational level, which will allow for an increase in the number and accuracy of detections, especially at low SNR. This powerful capability of simultaneously detecting multiple overlapping wideband sources has been shown to allow MCML to detect two or three sources when PMCC can only detect one or, sometimes, no source. This can be especially useful in frequency bands where there are quasi-permanent nuisance sources, such as microbaroms or anthropogenic noise. This can be particularly of interest for the detection of nuclear explosions that are often low-frequency, overlapping with the microbaroms frequency band.

After an overview of the state-of-the-art methods presented in the part III, we decided to develop multisource algorithms, taking full advantage of MCML's increased detection capability. Several approaches were studied in the part IV, such as the iterative signal deflation and the multisource approximation of MLE. In order to capitalise on the monosource development of MLE, the ICA, which separates the different SOIs before estimating the wavefront parameters, was also studied. However, this method is not adapted to broadband signals, despite the Mutually Referenced Equalizers (MRE) applications, and has, therefore, been abandoned. The research on ICA led to the sparsity, a concept that is also present in dictionary coding. More specifically, the algorithms LASSO and OMP were studied in order to quantify the benefits of these methods with delays or likelihood functions as atoms in the dictionary.

From an operational perspective, it is necessary to find a method that is both accurate and cost-effective. To start, the state-of-the-art algorithms and the methods developed herein were compared using synthetic signals. This protocol has taken into account the variability of the wavefront parameters, the frequency band used, the SNR and the array geometry. Two metrics have been specially designed in order to evaluate the accuracy of the different algorithms: the number of false estimations, and the errors in the measured back azimuth and trace velocity. Across all the conditions, we have shown that several algorithms are of interest for multisource processing. LASSO, with likelihood function, has shown to have high accuracy for most cases but fails when the sources had different SNR values or when different array geometries were tested. Moreover, the computation cost is really high without taking into account the creation of the dictionary. The iterative signal deflation MLE and the spectral MLE have shown to have the best results in most of the conditions. While the first one is compatible with operational processing, the second is not, and the version with approximations to speed up the calculation time shows a discrepancy in the results. On the other side, MUSIC, even if the array geometry has a high impact on the estimation quality, is the best state-of-the-art algorithm with compatible computation cost for real time processing.

Thus, three algorithms; MUSIC, the iterative deflation of MLE, and spectral MLE; were selected and tested using real signals. Both the iterative deflation and spectral MLE methods were capable of accurately measuring multiple interfering sources, while MUSIC resulted in more lost detections and larger errors in the azimuth and trace velocity estimations, as well as, struggling when using data from IS19. Overall the synthetic and real data tests, it has been shown that the iterative signal deflation MLE, which is also less costly in calculation time, is the most accurate algorithm. Event data sheets, which gather all the detections of a single event, were used to present the multisource results. These event sheets clearly show how the overlapping sources were detected by the MLE-based algorithm. They also show, as predicted by analysis using synthetic signals, that when there is a too large difference in the SNR of two sources, the algorithm is not able to detect the weaker source. That is why microbaroms behind the meteor were detected but not behind the rocket launch from Baikonur, since its signal strength is too large relative to the microbaroms.

The improved detection capability of the MLE methods, in particular due to its multisource capability, has resulted in the need to improve the method of pixels grouping into so-called families. Therefore, a new clustering method, the GMM, was tested. This algorithm separates the data into Gaussian clusters taking into account the wavefront parameter errors calculated by MCML in order to best isolate the different events. The method relies on the prior estimation of the number of sources in the time window using the BIC (to generate the appropriate number of Gaussian clusters) and then on the estimation of the Gaussian parameters. This method provides improved results on real data, by providing mathematically rigorous cluster sizes rather than arbitrarily choosing a min/max cluster size, and by generating more accurate clusters even when different sources coming from similar azimuths are present. Moreover, the GMM gives access to the posterior distribution of each cluster, indicating the probability of each pixel being part of the cluster. Further work has to be done to reduce the computation time, required for the estimation of the number of events by BIC; this should be achieved by a parallel computation. In addition, further work must be done to reduce the number of incongruent pixel associations, such as linking high and low frequency pixels for different events. This can be done by inferring that the clusters must be contiguous in the frequency domain. This new method has demonstrated an improved pixel post-processing, both for monosource and multisource context.

In perspective, further work on the MLE-based algorithms needs to be done. The iterative signal deflation, at first, by optimising the choice of the deflation parameter, α, to improve the accuracy and lower the computational costs. Similarly, although the spectral MLE provides highly accurate results with relatively few lost detections, improved estimations of the relative signal and noise powers in the spectral domain would improve its accuracy. Further research about how to detect sources with highly different signal power should be investigated in order to detect weak SOI. ICA can also be investigated more deeply with, for example, the use of Finite Impulse Response (FIR) filters [Lv et al., 2005] in order to get rid of the wideband effect. Another method consisting of applying the narrowband ICA on narrowband filters of the frequency band of interest and thus selecting some of them would be relevant. However, it should be noted that a narrowband filter at frequencies in the band [0.1 - 4] Hz would probably produce an unstable output.

During this study, the problem of identifying the number of sources in the signal has not been addressed. Indeed, during the comparison on synthetic data, the number of sources is a prior knowledge. However, the number of sources for the real data tests is not known, and is set, arbitrarily, to three. This leads to the erroneous pixel identification, which complicates the post-processing pixel clustering. In this context, the entropy detector used by the CLEAN algorithm should be used to detect if information remains in the signal after the iterative signal deflation of MLE [Wang et al., 2004].

The benefits of artificial intelligence has been explored with Alice Janela Cameijo to identify the number of sources in the observed signals. The method developed relies on deep learning and is inspired by similar work carried out on radar signals (Rogers et al. [2021]; Poste et al. [2023a]). The chosen architecture was a Multi-Layer Perceptron (MLP) using the covariance matrices from signals and its eigenvalues as input. The objective is to train the MLP on a synthetic database before making predictions on real signals. Indeed, training on real data requires labels (number of sources in this case) to be known which is impossible in the absence of ground truth. Thus, the synthetic database has to be as close as possible to reality. That is why SNRs were randomly assigned to the sources present in each signal. Events produced by quasi-permanent sources (such as microbaroms) were assigned to a random SNR between -10 and 20 dB and those produced by impulsive sources (such as explosions) with a higher SNR of between 20 and 30 dB. In total, more than six million synthetic signals were generated, divided into sixteen frequency bands (from 0.1 to 4 Hz) according to the third octave decomposition used. The MLP is implemented in order to classify the input vectors depending on the number of sources. Performances were evaluated in terms of learning accuracy and range from 68% for the lowest frequencies ($<$ 0.3 Hz) to 60% for the highest (3.2 - 4 Hz). We explain these results by the phenomenon of spatial aliasing at high frequencies. Thus, despite all the effort to make a large and realistic database, the results using synthetic data have shown to be mitigated for the deep learning method. Some tests on real cases have been done; however, the deep learning network has almost systematically estimated the maximum number of sources. Moreover, there is a dichotomy in the confidence of the algorithm between frequencies below 2 Hz which is high and between frequencies above 2 Hz which is low. To improve results it would be relevant to build a database

of more realistic synthetic signals by adding real noise, better models of extended permanent sources, or introducing a signals coherence loss model. In addition, we believe that other architectures could be evaluated, such as recurrent neural networks capable of taking into account the sequential nature of the data and transformers. This preliminary work, which combines artificial intelligence and statistical signal processing methods, is an interesting perspective to pursue.

Conclusion française

Le développement continu des systèmes de surveillance infrason, y compris le SSI, entraîne une quantité de données de plus en plus importante à traiter. Actuellement, la méthode principale de traitement des données, utilisée par le CID de l'OTICE, et de nombreux CND (y compris le CND français), est PMCC en raison de son efficacité. Cependant, les retours des utilisateurs concernant les limitations de PMCC à faible SNR ou pour distinguer plusieurs sources dans la même bande de fréquence ont conduit au développement récent de MCML, comme décrit dans le chapitre II.2. Ce nouvel algorithme améliore considérablement la détection et la caractérisation des signaux infrasonores et sismiques, en particulier à faible SNR ou lorsqu'il y a plusieurs SOI interférents. Malgré l'augmentation des coûts de calcul de MCML, les moyens de calcul actuels autorisent des traitements en temps-réel, ce qui permettra d'augmenter le nombre et la précision des détections. MCML peut détecter et séparer simultanément plusieurs sources (jusqu'à trois sources) large bande qui superposent dans la même bande de fréquence alors que PMCC ne peut détecter qu'une seule source ou, parfois, aucune. Cela peut être particulièrement utile dans les bandes de fréquence où il existe des sources de bruit quasi permanentes, telle que la houle ou le bruit d'origine anthropique. Ces développements s'avèrent particulièrement intéressants pour la détection des explosions masquées dans la bande de fréquence de la houle.

Après une présentation des méthodes de l'état de l'art dans la partie III, nous avons développé des algorithmes multisources, tirant pleinement parti de la capacité de détection accrue de MCML. Plusieurs approches ont été étudiées dans la partie IV, telles que la déflation itérative du signal et l'approximation du MLE multisource. De la même manière, l'ACI, qui sépare les différents SOI avant d'estimer les paramètres du front d'onde, a également été étudiée. Cependant, cette méthode n'est pas adaptée aux signaux à large bande, malgré les applications de Mutually Referenced Equalizers (MRE), et a donc été abandonnée. La recherche sur l'ACI a conduit à la parcimonie, un concept qui est également présent dans le *dictionary coding*. Plus précisément, les algorithmes LASSO et OMP ont été étudiés afin de quantifier les avantages de ces méthodes avec des retards inter-capteurs ou des fonctions de vraisemblance comme atomes dans le dictionnaire.

D'un point de vue opérationnel, il est nécessaire de trouver une méthode qui soit à la fois précise et rapide. Pour commencer, les algorithmes de l'état de l'art et les méthodes développées ici ont été comparés en utilisant des signaux synthétiques. Ce protocole a pris en compte la variabilité des paramètres de front d'onde, la bande de fréquence utilisée, le SNR et la géométrie de l'antenne. Deux métriques ont été spécialement conçues pour évaluer la précision des différents algorithmes : le nombre de mauvaises estimations et les erreurs mesurées de l'azimut et de la vitesse horizontale. Dans toutes les situations, nous avons montré que plusieurs algorithmes sont d'intérêt pour le traitement multisource. LASSO, avec sa fonction de vraisemblance, a montré une grande précision dans la plupart des cas, mais échoue lorsque les sources ont des valeurs de SNR différentes ou lorsque différentes géométries d'antenne sont testées. De plus, le coût de calcul est très élevé sans prendre en compte la création du dictionnaire. La déflation itérative du signal par MLE et le MLE spectral ont montré de meilleurs résultats. Alors que la déflation itérative est compatible avec le traitement opérationnel, le MLE spectral ne l'est pas, et la version avec des approximations pour accélérer le temps de calcul montre une perte de précision. D'un autre côté, MUSIC, même si la géométrie de l'antenne a un impact considérable sur la qualité de l'estimation, est le meilleur algorithme de l'état de l'art avec un coût de calcul compatible pour le traitement en temps réel.

Ainsi, trois algorithmes : MUSIC, la déflation itérative du signal, et le MLE spectral ont été sélectionnés et testés en utilisant des signaux réels. Les méthodes de déflation itérative et le MLE spectral sont capables de mesurer avec précision plusieurs sources interférant simultanément, tandis que MUSIC a eu davantage de détections manquées et des erreurs plus importantes dans les estimations d'azimut et

de vitesse horizontale. Dans l'ensemble, les tests sur les données synthétiques et réelles ont montré que la déflation itérative du signal, qui est également moins coûteuse en temps de calcul, est l'algorithme le plus précis. Les feuillets d'événements, qui rassemblent toutes les détections d'un seul événement, ont été utilisées pour présenter les résultats multisources. Ces feuillets d'événements montrent clairement comment les sources interférentes ont été détectées par l'algorithme basé sur le MLE. Ils montrent également, comme prévu par l'analyse sur signaux synthétiques, que lorsqu'il y a une différence trop importante de SNR entre deux sources, l'algorithme n'est pas capable de détecter la source la plus faible. C'est pourquoi la houle et la météorite ont été détectées, à la différence de la houle lors du lancement de la fusée depuis Baïkonour en raison d'une différence trop importante de SNR.

La capacité de détection améliorée de MLE pour la détection de sources multiples a entraîné la nécessité d'améliorer la méthode de regroupement des pixels en familles. Par conséquent, une nouvelle méthode de regroupement, le GMM, a été testée. Cet algorithme sépare les données en clusters gaussiens en tenant compte des erreurs de paramètres du front d'onde calculées par MCML afin d'isoler au mieux les différents événements. La méthode repose sur l'estimation préalable du nombre de sources dans la fenêtre temporelle en utilisant le BIC pour générer le nombre approprié de clusters gaussiens, puis l'estimation les paramètres des gaussiennes. Cette méthode offre de meilleurs résultats sur des données réelles, en fournissant des dimensions de clusters mathématiquement rigoureuses plutôt qu'en choisissant arbitrairement une taille minimale/maximale de clusters et en fournissant des estimations plus précises des paramètres des vecteurs d'ondes. De plus, le GMM donne accès à la distribution a posteriori de chaque cluster, indiquant la probabilité que chaque pixel fasse partie du cluster. Un travail supplémentaire doit être effectué pour réduire le temps de calcul nécessaire à l'estimation du nombre de sources par BIC ; cela devrait être réalisé par un calcul parallèle. De plus, des travaux supplémentaires doivent être réalisés pour réduire le nombre d'associations fortuites de pixels, entre des pixels à haute et basse fréquence appartenant à différents événements. Cela peut être réalisé en déduisant que les clusters doivent être continus dans le domaine temps-fréquence. Cette nouvelle méthode a démontré une amélioration du post-traitement des pixels, tant dans un contexte monosource que multisource.

Dans les perspectives, des travaux supplémentaires sur les algorithmes basés sur MLE doivent être réalisés. La déflation itérative du signal, pour commencer, en optimisant le choix du paramètre de déflation, α, pour améliorer la précision et réduire les coûts de calcul. De même, bien que le MLE spectral fournisse des résultats très précis avec relativement peu de détections perdues, de meilleures estimations des puissances du signal et du bruit dans le domaine spectral amélioreraient sa précision. Des recherches supplémentaires sur la manière de détecter des sources ayant une puissance de signal très différente devront être menées afin de détecter des signaux d'intérêt de faible SNR. L'ACI peut également être étudiée plus en profondeur, par exemple, grâce à l'utilisation de filtres Finite Impulse Response (FIR) [Lv et al., 2005] afin d'éliminer l'effet large bande. Une autre méthode consistant à appliquer l'ACI à bande étroite sur des filtres à bande étroite de la bande de fréquence d'intérêt et à en sélectionner certains serait pertinente. Cependant, il convient de noter qu'un filtre à bande étroite aux fréquences dans la bande [0,1 - 4] Hz produirait probablement une sortie instable.

Au cours de cette étude, le problème de l'identification du nombre de sources dans le signal n'a pas été abordé. En effet, lors de la comparaison sur des données synthétiques, le nombre de sources était une connaissance a priori. Cependant, le nombre de sources pour les tests de données réelles n'est pas connu et est fixé, de manière arbitraire, à trois. Cela conduit à une identification erronée des pixels, ce qui complique le regroupement des pixels lors du post-traitement. Dans ce contexte, le détecteur d'entropie utilisé par l'algorithme CLEAN pourrait être employé pour détecter si de l'information subsistent dans le signal après la déflation itérative du signal par la méthode du maximum de vraisemblance [Wang et al., 2004].

Les avantages de l'intelligence artificielle ont été explorés avec Alice Janela Cameijo pour identifier le nombre de sources dans les signaux observés. La méthode développée repose sur l'apprentissage profond et s'inspire de travaux similaires réalisés sur des signaux radar (Rogers et al. [2021] ; Poste et al. [2023a]). L'architecture choisie était un Multi-Layer Perceptron (MLP) utilisant les matrices de covariance des signaux et ses valeurs propres comme entrée. L'objectif est d'entraîner le MLP sur une base de données synthétiques avant de faire des prédictions sur des signaux réels. En effet, l'entraînement sur des données

réelles nécessite que les labels (le nombre de sources dans ce cas) soient connus, ce qui est impossible en l'absence de vérité terrain. Ainsi, la base de données synthétiques doit être aussi proche que possible de la réalité. C'est pourquoi les SNR ont été attribués de manière aléatoire aux sources présentes dans chaque signal. Les événements produits par des sources quasi-permanentes (comme la houle) ont été attribués à un SNR compris entre -10 et 20 dB, tandis que ceux produits par des sources impulsives (comme les explosions) ont été associés à un SNR plus élevé, compris entre 20 et 30 dB. Au total, plus de six millions de signaux synthétiques ont été générés, répartis en seize bandes de fréquence (de 0,1 à 4 Hz) selon la décomposition en tiers d'octave. Le MLP est mis en œuvre afin de classer les vecteurs d'entrée en fonction du nombre de sources. Les performances ont été évaluées en termes de précision d'apprentissage et varient de 68 % pour les basses fréquences ($<$ 0,3 Hz) à 60 % pour les plus hautes (3.2 - 4 Hz). Nous expliquons ces résultats par le phénomène d'aliasing spatial à haute fréquence. Cependant, malgré tous les efforts pour créer une base de données large et réaliste, les résultats obtenus avec des données synthétiques se sont montrés mitigés. Des tests sur des cas réels ont été réalisés ; cependant, le réseau de d'apprentissage a presque systématiquement estimé le nombre maximum de sources. De plus, il existe une dichotomie dans la confiance de l'algorithme entre les fréquences inférieures à 2 Hz, qui est élevée, et celles supérieures à 2 Hz, qui est faible. Pour améliorer les résultats, il serait pertinent de construire une base de données de signaux synthétiques plus réaliste en ajoutant du bruit réel, de meilleurs modèles de sources permanentes étendues, ou en introduisant un modèle de perte de cohérence des signaux. Nous pensons que d'autres architectures pourraient être évaluées, telles que les réseaux de neurones récurrents capables de prendre en compte la nature séquentielle des données et les transformeurs. Ce travail préliminaire, qui combine l'intelligence artificielle et les méthodes de traitement statistique du signal, constitue une perspective intéressante à explorer.

Appendix A

Appendices

A.1 Calculation of the likelihood

To express the $\det \mathbf{R}_0$ we need to find the eigenvalue of $\mathbf{R}_0$, at first multiplying the right and the left side of the equation II.2.4 by $\mathbb{1}_M$:

$$\begin{aligned} \mathbf{R}_0 \mathbb{1}_M &= \sigma_s^2 \mathbb{1}_M (\mathbb{1}_M^T \mathbb{1}_M) + \sigma^2 \mathbf{I}_M \mathbb{1}_M \\ \mathbf{R}_0 \mathbb{1}_M &= \sigma_s^2 \mathbb{1}_M M + \sigma^2 \mathbb{1}_M \\ \mathbf{R}_0 \mathbb{1}_M &= (\sigma_s^2 M + \sigma^2) \mathbb{1}_M \end{aligned} \tag{A.1}$$

One of the eigenvalues is $(M\sigma_s^2 + \sigma^2)$. Now, multiplying R_0 by one of the $(M-1)$ orthogonal vectors, w, to $\mathbb{1}_M$ we obtain

$$\begin{aligned} \mathbf{R}_0 w &= \sigma_s^2 \mathbb{1}_M \mathbb{1}_M^T w + \sigma^2 \mathbf{I}_M w \\ \mathbf{R}_0 w &= \sigma^2 w \end{aligned} \tag{A.2}$$

It comes that $M-1$ eigenvalues are equal to σ^2 and finally

$$\det(\mathbf{R}_0) = (M\sigma_s^2 + \sigma^2)\sigma^{2(M-1)} \tag{A.3}$$

Then the log of the determinant of the covariance matrix $\mathbf{R}_0$ is

$$\log\det(\mathbf{R}_0) = \log(M\sigma_s^2 + \sigma^2) + (M-1)\log(\sigma^2) \tag{A.4}$$

If wet set $\rho^2 = \frac{M\sigma_s^2}{\sigma^2}$:

$$\begin{aligned} \log\det(\mathbf{R}_0) &= \log(\sigma^2(1+\rho^2)) + (M-1)\log(\sigma^2) \\ \log\det(\mathbf{R}_0) &= \log(\sigma^2) + \log(1+\rho^2) + (M-1)\log(\sigma^2) \\ \log\det(\mathbf{R}_0) &= \log(1+\rho^2) + M\log(\sigma^2) \end{aligned} \tag{A.5}$$

The expression of $\mathbf{R}_0^{-1}$ can be calculated by the Woodbury identity

$$\mathbf{R}_0^{-1} = \sigma^{-2}\mathbf{I}_M - \frac{\sigma^{-2}\rho^2}{1+\rho^2}\frac{1}{M}\mathbb{1}_M\mathbb{1}_M^T \tag{A.6}$$

A.2 Asymptotic covariance of the TS under the null hypothesis

Indeed we model the distribution of the GLR under the H_0 hypothesis. As stated in the equation II.2.24 it is necessary to determine the asymptotic behaviour of F under H_0, which in turn follows from that of

the empirical covariance matrix R_N of the white Gaussian noise.

It can be demonstrated that F asymptotically tends to zero of covariance

$$\boldsymbol{\xi}((\theta,v),(\theta',v')) = \frac{4\pi \sum_{k=1}^{M}\sum_{k'=1}^{M} \boldsymbol{\gamma}_{k,k'}(\tau_k(\theta,v)-\tau_k(\theta',v')-\tau_{k'}(\theta,v)+\tau_{k'}(\theta',v'))}{F_s\left(\sum_{k=1}^{M}\boldsymbol{\gamma}_k(0)\right)^2} \tag{A.7}$$

with

$$\begin{cases} \sum_{k=1}^{M}\boldsymbol{\gamma}_k(0) &= \int_{-\pi}^{\pi} \mathbb{1}_M^T f^n \\ \boldsymbol{\gamma}_{k,k'}(s) &= \int_{-\pi}^{\pi} e^{is\lambda} f_k^n(\lambda) f_{k'}^n(\lambda) d\lambda \end{cases} \tag{A.8}$$

where f^n is the diagonal of the spectral density matrix of the noise $\boldsymbol{\gamma}_{k,k'}$. This is not equal to $\sigma^2\mathbf{I}_M$ due to both the signal delays for each (θ,v) and the filter that causes a more general Gaussian noise whose law will be estimated by

$$f_k^n = \frac{\sigma^2}{2\pi}\left|\frac{\Theta(e^{-i\lambda})}{\Phi(e^{-i\lambda})}\right|^2 \tag{A.9}$$

With Θ and Φ the polynomials defined by the Chebychev filter used by the CEA which are, assumed here to be common to all sensors. We assume $\sigma^2 = 1$, we then have

$$\boldsymbol{\gamma}_{k,k'}(\tau;\Phi,\Theta) = \int_{-\pi}^{\pi}\frac{1}{2\pi}\left|\frac{\Theta(e^{-i\lambda})}{\Phi(e^{-i\lambda})}\right|^2 e^{i\tau\lambda}d\lambda \tag{A.10}$$

We obtain thus

$$\sum_{k=1}^{M}\boldsymbol{\gamma}_k(0) = M\sigma^2\boldsymbol{\gamma}(0;\Phi,\Theta) \tag{A.11}$$

and for all $k,k' \in \{1,\dots,M\}$ and all $\tau \in \mathbb{Z}$,

$$\boldsymbol{\gamma}_{k,k'}(\tau) = \frac{\sigma^4}{2\pi}\boldsymbol{\gamma}(\tau;\Phi^2,\Theta^2) \tag{A.12}$$

Finally it can establish that the asymptotic behaviour of test statistics under the H_0 hypothesis writes

$$\left(\frac{S_N}{T_N}-1\right)_{(\theta,v)} \xrightarrow{T\to+\infty} (\mathcal{R}(\theta,v))_{\theta,v} \tag{A.13}$$

where the $\mathcal{R}$ is a centred Gaussian process of covariance

$$\boldsymbol{\xi}((\theta,v),(\theta',v')) = \frac{2\sum_{k=1}^{M}\sum_{k'=1}^{M}\boldsymbol{\gamma}(\tau_k(\theta,v)-\tau_k(\theta',v')-\tau_{k'}(\theta,v)+\tau_{k'}(\theta',v');\Phi^2,\Theta^2)}{F_s M(\boldsymbol{\gamma}(0;\Phi,\Theta))^2} \tag{A.14}$$

A simpler way to express this matrix is

$$\boldsymbol{\xi}((\theta,v),(\theta',v')) = 2\times\frac{\int|H(f)|^4\sum_{k=1}^{M}\sum_{k'=1}^{M}e^{2i\pi f(\tau_k(\theta,v)-\tau_{k'}(\theta',v'))}df}{\left(\int|H(f)|^2df\right)^2} \tag{A.15}$$

where $H(f)$ denotes the frequency response of the selected filter of the filter bank. In a coarse calculation, we assume that $H(f) = 1$ in the frequency bandwidth $(F_{\min}, F_{\max})$ and 0 outside. In a finer approach, an appropriate algorithm can be used to perform the expression (A.15) directly from the coefficients of the transfer function, for example, with a Chebyschev filter.

A.3 Monosource MLE in the frequency domain

Thus, at first lets demonstrate that the temporal and the frequency implementation leads to the equivalent solution. Let the Whittle likelihood writes [Whittle, 1951]

$$\mathcal{L}(\mu) = \sum_{f=f_{min}}^{f_{max}} \log(\det(\mathbf{C}(f)^{-1}) - Z^H(f)\mathbf{C}(f)^{-1}Z(f) \tag{A.16}$$

with $Z(f)$ is the vector of the Fourier transform of the matrix of the records at frequency f and $\mathbf{C}(f)$ the spectral density matrix. The latter writes as the equation I.3.14 with N=1

$$\mathbf{C}(f_i) = a(f_i,\theta,v)\sigma_s^2 a^H(f_i,\theta,v) + \sigma^2\mathbf{I} = \sigma^2(\mathbf{I} + \frac{\sigma_s^2}{\sigma^2}a(f_i,\theta,v)a^H(f_i,\theta,v)) \tag{A.17}$$

Thanks to the Woodbury identity the inverse of the spectral matrix writes

$$\mathbf{C}(f_i)^{-1} = \frac{1}{\sigma^2}\left(\mathbf{I} - ka(f_i,\theta,v)a^H(f_i,\theta,v)\right) \tag{A.18}$$

with

$$k = \frac{\frac{\sigma_s^2}{\sigma^2}}{1 + M\frac{\sigma_s^2}{\sigma^2}} \tag{A.19}$$

with k independent from f_i knowing that $a^H(f_i,\theta,v)a(f_i,\theta,v) = |a(f_i,\theta,v)|^2 = M$.

To maximise the likelihood $\mathcal{L}$, we show that the determinant of the spectral density matrix depends only on the known constants σ^2 and σ_s^2. For a reminder they expressed thanks to II.2.12 for σ^2 and II.2.17 and II.2.7 for σ_s^2. Maximisation then depends only on

$$\begin{aligned}
&\max \textstyle\sum_{f_{min}}^{f_{max}} \mathcal{L}(\mu) \iff \min \textstyle\sum_{f_{min}}^{f_{max}} Z^H(f_i)\mathbf{C}^{-1}(f_i)Z(f_i) \\
&\iff \min \textstyle\sum_{f_{min}}^{f_{max}} Z^H(f_i)\frac{1}{\sigma^2}\left(\mathbf{I} - ka(f_i,\theta,v)a^H(f_i,\theta,v)\right)Z(f_i) \\
&\iff \max \textstyle\sum_{f_{min}}^{f_{max}} |Z^H(f_i)a(f_i,\theta,v)|^2 = \max \textstyle\sum_{f_{min}}^{f_{max}} |a^H(f_i,\theta,v)Z(f_i)|^2
\end{aligned} \tag{A.20}$$

By applying Parseval's equality, which states that the total energy of a signal does not depend on the representation chosen. The inverse Fourier transform $y(t)$ can be performed

$$\begin{aligned}
&a^H(f_i,\theta,v)Z(f_i) = \textstyle\sum_l exp(-2i\pi f_i\tau_l)Z_l(f_i) \\
&\iff y(t) = \textstyle\sum_l z(t+\tau_l) = 1_M^T z(t)
\end{aligned} \tag{A.21}$$

We can then check if σ_s^2 and σ^2 are known that the MLE in frequency and time are equivalent by

$$\max \sum_{f_{min}}^{f_{max}} |a^H(f_i,\theta,v)Z(f_i)|^2 = \max \sum_t |y(t)|^2 = \max(S_N(\theta,v)) \tag{A.22}$$

$S_N(\theta,v)$ being the only (θ,v) parameter dependent of F as state in the equation II.2.22.

A.4 Development of an approximated bisource MLE

We will show now how an approximated MLE bisource expressed (i.e estimated iteratively not simultaneously) before generalising it to a multisource case. Assuming the first source is known thanks to the single source MLE, we propose to iteratively search for a second source.

The spectral matrix model becomes

$$\mathbf{C}(f_i)_{bs} = a_1(f_i,\theta,v)\sigma_{s_1}^2 a_1^H(f_i,\theta,v) + a_2(f_i,\theta,v)\sigma_{s_2}^2 a_2^H(f_i,\theta,v) + \sigma^2\mathbf{I} \tag{A.23}$$

The monosource was used to identify $\sigma_{s_1}^2$ and σ^2 as well as the first source (θ_1, v_1), so we assume that these constants are known. $\sigma_{s_2}^2$ can be approximated by the same expression than $\sigma_{s_1}^2$ but for different back azimuth and horizontal trace velocity. It is assumed that $\sigma_{s_2}^2$ is also a known constant.

In the same way, we try to solve the equation A.16 with $C_{bs}^{-1}(f)$ which becomes

$$\mathbf{C}(f_i)_{bs}^{-1} = \mathbf{C}(f_i)^{-1} - \frac{\sigma_{s_2}^2(\mathbf{C}(f_i)^{-1}a_2(f_i,\theta,v))(\mathbf{C}(f_i)^{-1}a_2(f_i,\theta,v))^H}{1+\sigma_{s_2}^2 a_2^H(f_i,\theta,v)\mathbf{C}(f_i)^{-1}a_2(f_i,\theta,v)} \tag{A.24}$$

where $\mathbf{C}(f_i)^{-1}$ is given by the parameters of the first source and the equation A.18. The term $\mathbf{C}^{-1}(f_i)a_2(f_i,\theta,v)$ can be rewritten according to the equation A.18 as

$$\begin{aligned}\mathbf{C}(f_i)^{-1}a_2(f_i,\theta,v) &= \tfrac{1}{\sigma^2}\left(\mathbf{I} - k a_1(f_i,\theta,v)a_1^H(f_i,\theta,v)\right)a_2(f_i,\theta,v)\\ \mathbf{C}(f_i)^{-1}a_2(f_i,\theta,v) &= \tfrac{1}{\sigma^2}a_2(f_i,\theta,v) - k_2 a_1(f_i,\theta,v)\end{aligned} \tag{A.25}$$

with $k_2 = \frac{k}{\sigma^2}a_1^H(f_i,\theta,v)a_2(f_i,\theta,v)$. Replacing the expression A.25 in the equation A.24 gives

$$\mathbf{C}(f_i)_{bs}^{-1} = \frac{1}{\sigma^2}(\mathbf{I} - k a_1(f_i,\theta,v)a_1^H(f_i,\theta,v)) - \frac{\sigma_{s_2}^2(\frac{1}{\sigma^2}a_2(f_i,\theta,v) - k_2 a_1(f_i,\theta,v))(\frac{1}{\sigma^2}a_2(f_i,\theta,v) - k_2 a_1(f_i,\theta,v))^H}{1+\sigma_{s_2}^2(\frac{M}{\sigma^2} - \frac{k}{\sigma^2}|a_1^H(f_i,\theta,v)a_2(f_i,\theta,v)|^2)} \tag{A.26}$$

By injecting the expression of $\mathbf{C}_{bs}(f_i)^{-1}$ equation A.26 into $Z^H(f_i)\mathbf{C}(f_i)_{bs}^{-1}Z(f_i)$ it becomes

$$\begin{aligned}Z^H(f_i)\mathbf{C}(f_i)_{bs}^{-1}Z(f_i) = \frac{1}{\sigma^2}|Z(f_i)|^2 - \frac{k}{\sigma^2}|Z^H(f_i)a_1(f_i,\theta,v)|^2 -\\ \frac{\sigma_{s_2}^2}{1+\sigma_{s_2}^2(\frac{M}{\sigma^2} - \frac{k}{\sigma^2}|a_1^H(f_i,\theta,v)a_2(f_i,\theta,v)|^2)}|\frac{1}{\sigma^2}Z^H(f_i)a_2(f_i,\theta,v) - k_2 Z^H(f_i)a_1(f_i,\theta,v)|^2\end{aligned} \tag{A.27}$$

we can now optimise the equation A.16 according to the second source because θ_1 is assumed to be known.

$$\begin{aligned}\mathcal{L}(\mu) = \sum_{f_{min}}^{f_{max}} \log(\det(\mathbf{C}_{bs}(f_i)^{-1}) +\\ \frac{\sigma_{s_2}^2}{1+\sigma_{s_2}^2(\frac{M}{\sigma^2} - \frac{k}{\sigma^2}|a_1^H(f_i,\theta,v)a_2(f_i,\theta,v)|^2)}|\frac{1}{\sigma^2}Z^H(f_i)a_2(f_i,\theta,v) - k_2 Z^H(f_i)a_1(f_i,\theta,v)|^2\end{aligned} \tag{A.28}$$

It is possible to switch back to the time domain if we make the following approximation

$$a_1^H(f,\theta,v)a_2^H(f,\theta,v) \approx a_1^H(f_c,\theta,v)a_2^H(f_c,\theta,v) \tag{A.29}$$

f_c being the central frequency. With this approximation k_2 becomes frequency independent and a constant k_3 can be defined as

$$k_3 \approx \frac{\sigma_{s_2}^2}{1+\sigma_{s_2}^2(\frac{M}{\sigma^2} - \frac{k}{\sigma^2}|a_1^H(f_c,\theta,v)a_2(f_c,\theta,v)|^2)} \tag{A.30}$$

Thus the expression A.28 writes

$$\mathcal{L}(\mu) = \sum_{f_{min}}^{f_{max}} \log(\det(\mathbf{C}_{bs}(f_i)^{-1}) + k_3|\frac{1}{\sigma^2}Z^H(f_i)a_2(f_i,\theta,v) - k_2 Z^H(f_i)a_1(f_i,\theta,v)|^2 \tag{A.31}$$

Using the inverse Fourier transform, we obtain

$$\mathcal{L}(\mu) = \sum_{t_{min}}^{t_{max}} \log(\theta_{2,t}) + k_3|\frac{1}{\sigma^2}1_M^T z(t,\theta_2) - k_2 1_M^T z(t,\theta_1)|^2 \tag{A.32}$$

With $\log(\theta_{2,t})$ the inverse Fourier transform of $\log(\det(\mathbf{C}_{bs}(f_i)^{-1})$. However in the following steps we keep the expression in the frequency domain because the approximation made in the equation A.29 can be applied in the narrowband model but becomes tricky in the broadband model.

Until now the power of the second SOI, $\sigma^2_{s_2}$, was calculated by the expression of the monosource version of MCML. However by not taking into account the presence of several σ^2_s into the model, the estimation of such a constant can be rough. It is possible then to estimate $\sigma^2_{s_2}$ in order to construct the spectral matrix correctly for the second iteration before a possible generalisation to n-th source.
The estimation of the spectral matrix can be rewritten in the bisource context as

$$\begin{aligned}\widetilde{\mathbf{C}(f_i)} &= (\mathbf{I} - \tfrac{a_1(f_i,\theta,v)a_1^H(f_i,\theta,v)}{M})\mathbf{C}(f_i)(\mathbf{I} - \tfrac{a_1(f_i,\theta,v)a_1^H(f_i,\theta,v)}{M}) \\ \widetilde{\mathbf{C}(f_i)} &= \sigma^2_{s_2} a_2(\widetilde{f_i,\theta},v)a_2^H(\widetilde{f_i,\theta},v) + \sigma^2(\mathbf{I} - \tfrac{a_1(f_i,\theta,v)a_1^H(f_i,\theta,v)}{M})\end{aligned} \tag{A.33}$$

Where $\mathbf{C}(f_i)$ is the spectral density matrix model and $a_2(\widetilde{f_i,\theta},v)$ writes

$$a_2(\widetilde{f_i,\theta},v) = a_2(f_i,\theta,v) - \frac{a_1^H(f_i,\theta,v)a_2(f_i,\theta,v)}{M}a_1(f_i,\theta,v) \tag{A.34}$$

Then the trace of the estimated spectral density matrix $\widetilde{\mathbf{C}(f_i)}$ is

$$trace(\widetilde{\mathbf{C}(f_i)}) = (M-1)\sigma^2 + \sigma^2_{s_2}||a_2(\widetilde{f_i,\theta},v)||^2 \tag{A.35}$$

It is then possible to estimate the wanted constant $\sigma^2_{s_2}$ by

$$\sigma^2_{s_2} = \frac{(trace(\widetilde{\mathbf{C}(f_i)}) - (M-1)\sigma^2)}{||a_2(\widetilde{f_i,\theta},v)||^2} \tag{A.36}$$

However the estimation of the spectral density matrix can be often very noisy. Different kind of window (i.e Hanning, Bartlett, Kaiser) and different smoothing coefficient were used. Comparison with the real spectral density matrix and the estimated one have shown large differences leading to bad estimation of the power of the SOI. That is why by moving in the time domain

$$\begin{aligned}\int \widetilde{\mathbf{C}(f_i)} &= \int Trace(\mathbf{C}(f_i)) - \tfrac{1}{M}a_1^H(f_i,\theta,v)\mathbf{C}(f_i)a_1(f_i,\theta,v) \\ \int \widetilde{\mathbf{C}(f_i)} &= \int Trace(\mathbb{E}[Z(f_i)Z^H(f_i)]) - \tfrac{1}{M}\mathbb{E}[a_1^H(f_i,\theta,v)Z(f_i)Z^H(f_i)a_1(f_i,\theta,v)]\end{aligned} \tag{A.37}$$

Knowing that $\mathbb{E}[Z(f_i)Z(f_i)^H] = ||Z(f_i)||^2$ and using the Parseval theorem

$$\begin{aligned}\int ||Z(f_i)||^2 df &= \int ||z(t)||^2 dt \\ \int ||Z(f_i)||^2 df &= \tfrac{1}{T}(\textstyle\sum ||z(t)||^2 - \tfrac{1}{M}\sum ||y_1(t)||^2)\end{aligned} \tag{A.38}$$

With $y_1(t)$ being the delayed signals according to the first source estimated

$$y_1(t) = \begin{bmatrix} z(t+\tau_1) \\ \cdots \\ \cdots \\ z(t+\tau_M) \end{bmatrix} \tag{A.39}$$

Simulations on synthetics with sources with similar SNR values between them have have shown that the estimations of the monosource algorithm are no so far from the real implemented power. Due to higher errors on the described method we decided to keep the power estimation from the monosource algorithm. Improvement of the new methods are in perspectives.

Bibliography

C. A. V. Aguilera. Search all extrema points of a time series or a surface with/without NaN's, 2016. https://fr.mathworks.com/matlabcentral/fileexchange/12275-extrema-m-extrema2-m, (accessed: 11.04.2024).

H. Akaike. A new look at the statistical model identification. *IEEE transactions on automatic control*, 19(6):716–723, 1974.

H. Akaike. Information theory and an extension of the maximum likelihood principle. In *Selected papers of hirotugu akaike*, pages 199–213. Springer, 1998.

B. Alcoverro, P. Martysevich, and Y. Starovoit. Mechanical sensitivity of microbarometers MB2000 (DASE, France) and Chaparral 5 (USA) to vertical and horizontal ground motion. *Inframatics*, 9:1–10, 2005.

B. Ans, J. Hérault, and C. Jutten. Architectures neuromimétiques adaptatives: Détection de primitives. *Proceedings of Cognitiva*, 85:593–597, 1985.

M. Antunes, D. Gomes, and R. L. Aguiar. Knee/elbow estimation based on first derivative threshold. In *2018 IEEE Fourth International Conference on Big Data Computing Service and Applications (BigDataService)*, pages 237–240. IEEE, 2018.

S. Arrowsmith. False alarms and the IMS infrasound network: understanding the factors influencing the creation of false events. *Geophysical Journal International*, 215(2):1322–1337, 08 2018. ISSN 0956-540X. doi: 10.1093/gji/ggy350. URL https://doi.org/10.1093/gji/ggy350. doi : https://doi.org/10.1093/gji/ggy350.

S. Arrowsmith, R. Whitaker, C. Katz, and C. Hayward. The F-Detector revisited: an improved strategy for signal detection at seismic and infrasound arrays. *Bulletin of the Seismological Society of America*, 99(1):449–453, 2009. doi: https://doi.org/10.1785/0120080180. doi : https://doi.org/10.1785/0120080180.

J. Artru, P. Lognonné, and E. Blanc. Normal modes modelling of post-seismic ionospheric oscillations. *Geophysical Research Letters*, 28(4):697–700, 2001.

M. W. Asten and J. D. Henstridge. Array estimators and the use of microseisms for reconnaissance of sedimentary basins. *GEOPHYSICS*, 49(11):1828–1837, 1984. doi: 10.1190/1.1441596. URL https://doi.org/10.1190/1.1441596.

S. Atapattu, C. Tellambura, and H. Jiang. Analysis of area under the ROC curve of energy detection. *IEEE Transactions on wireless communications*, 9(3):1216–1225, 2010. doi: https://doi.org/10.1109/TWC.2010.03.091085. doi : https://doi.org/10.1109/TWC.2010.03.091085.

N. K. Balachandran, W. L. Donn, and D. H. Rind. Concorde sonic booms as an atmospheric probe. *Science*, 197(4298):47–49, 1977.

A. E. Beaton and J. W. Tukey. The fitting of power series, meaning polynomials, illustrated on band-spectroscopic data. *Technometrics*, 16(2):147–185, 1974.

A. Bedard, T. Georges, et al. Atmospheric infrasound. *Acoustics Australia*, 28(2):47–52, 2000.

A. J. Bedard. Low-frequency sound waves associated with avalanches, atmospheric turbulence, severe weather, and earthquakes. *The Journal of the Acoustical Society of America*, 94(3_Supplement):1872–1872, 1993.

A. J. Bedard Jr, B. Bartram, A. Keane, D. Welsh, and R. Nishiyama. The infrasound network (is-net): Background, design details, and display capability as an 88d adjunct tornado detection tool. In *Preprints, 22nd Conf. on Severe Local Storms, Hyannis, MA, Amer. Meteor. Soc*, volume 1, 2004.

G. Belli, F. Walter, B. McArdell, D. Gheri, and E. Marchetti. Infrasonic and seismic analysis of debris-flow events at illgraben (Switzerland): Relating signal features to flow parameters and to the seismo-acoustic source mechanism. *Journal of Geophysical Research: Earth Surface*, 127(6):e2021JF006576, 2022.

G. Belli, D. Gheri, E. Bovet, N. Durand, P. Dellavedova, and E. Marchetti. Decennial infrasonic array analysis of snow-avalanche activity and its weather forcing in Pennine Alps: implications for forecasting. *Available at SSRN 4814184*, 2024.

A. Belouchrani, K. Abed-Meraim, J.-F. Cardoso, and E. Moulines. A blind source separation technique using second-order statistics. *IEEE Transactions on signal processing*, 45(2):434–444, 1997.

J. Bertolotti. Retrieving an unknown signal from a small number of measurements. https://twitter.com/j_bertolotti/status/1214918749838594048, (accessed: 14.05.2024).

J. W. Bishop, D. Fee, and C. A. Szuberla. Improved infrasound array processing with robust estimators. *Geophysical Journal International*, 221(3):2058–2074, 2020.

J. W. Bishop, P. S. Blom, J. Webster, W. Reichard-Flynn, and Y. Lin. Deep learning categorization of infrasound array data. *The Journal of the Acoustical Society of America*, 152(4):2434–2445, 2022.

M. Bittner, K. Höppner, C. Pilger, and C. Schmidt. Mesopause temperature perturbations caused by infrasonic waves as a potential indicator for the detection of tsunamis and other geo-hazards. *Natural Hazards and Earth System Sciences*, 10(7):1431–1442, 2010.

E. M. Blixt, S. P. Näsholm, S. J. Gibbons, L. G. Evers, A. J. Charlton-Perez, Y. J. Orsolini, and T. Kværna. Estimating tropospheric and stratospheric winds using infrasound from explosions. *The Journal of the Acoustical Society of America*, 146(2):973–982, 2019.

P. Blom. Modeling infrasonic propagation through a spherical atmospheric layer—analysis of the stratospheric pair. *The Journal of the Acoustical Society of America*, 145(4):2198–2208, 2019.

I. Bondár, T. Šindelářová, D. Ghica, U. Mitterbauer, A. Liashchuk, J. Baše, J. Chum, C. Czanik, C. Ionescu, C. Neagoe, et al. Central and Eastern European Infrasound Network: contribution to infrasound monitoring. *Geophysical Journal International*, 230(1):565–579, 2022.

D. J.-R. Bouveresse, A. Moya-González, F. Ammari, and D. N. Rutledge. Two novel methods for the determination of the number of components in independent components analysis models. *Chemometrics and intelligent laboratory systems*, 112:24–32, 2012.

J. R. Bowman, G. E. Baker, and M. Bahavar. Ambient infrasound noise. *Geophysical research letters*, 32 (9), 2005.

N. Brachet, D. Brown, R. Le Bras, Y. Cansi, P. Mialle, and J. Coyne. Monitoring the Earth's atmosphere with the global IMS infrasound network. In *Infrasound monitoring for atmospheric studies*, pages 77–118. Springer, 2010. doi : https://doi.org/10.1007/978-1-4020-9508-5_3.

D. R. Brillinger et al. Asymptotic normality of finite fourier transforms of stationary generalized processes. *J. MULTIVARIATE ANALY.*, 12(1):64–71, 1982.

P. J. Brockwell and R. A. Davis. *Time Series: Theory and Methods*. Springer-Verlag Inc, 1991.

P. Campus and D. Christie. Worldwide observations of infrasonic waves. *Infrasound monitoring for atmospheric studies*, pages 185–234, 2009.

Y. Cansi. An automatic seismic event processing for detection and location: The P.M.C.C. Method. *Geophysical Research Letters*, 22(9):1021–1024, 1995. doi: https://doi.org/10.1029/95GL00468. doi : https://doi.org/10.1029/95GL00468.

Y. Cansi and Y. Klinger. An automated data processing method for mini-arrays. *Newsletter of the European-Mediterranean Seismological Center*, 11:2–4, 1997.

Y. Cansi and A. L. Pichon. Infrasound event detection using the progressive multi-channel correlation algorithm. In *Handbook of signal processing in acoustics*, pages 1425–1435. Springer, 2008.

J. Capon. High-resolution frequency-wavenumber spectrum analysis. *Proceedings of the IEEE*, 57(8): 1408–1418, 1969. doi: 10.1109/PROC.1969.7278.

G. Carter. Coherence and time delay estimation. *Proceedings of the IEEE*, 75(2):236–255, 1987. doi: 10.1109/PROC.1987.13723. doi : https://doi.org/10.1109/PROC.1987.13723.

M. Causse, C. Cornou, E. Maufroy, J.-R. Grasso, L. Baillet, and E. El Haber. Exceptional ground motion during the shallow Mw 4.9 2019 Le Teil earthquake, France. *Communications Earth & Environment*, 2(1):14, 2021.

G. Celeux and G. Soromenho. An entropy criterion for assessing the number of clusters in a mixture model. *Journal of classification*, 13:195–212, 1996.

G. Celeux, S. Frühwirth-Schnatter, and C. P. Robert. Model selection for mixture models–perspectives and strategies. In *Handbook of mixture analysis*, pages 117–154. Chapman and Hall/CRC, 2019.

L. Ceranna, R. Matoza, P. Hupe, A. Le Pichon, and M. Landès. Systematic array processing of a decade of global IMS infrasound data. In *Infrasound monitoring for atmospheric studies*, pages 471–482. Springer, 2019. doi : https://doi.org/10.1007/978-3-319-75140-5_13.

T. F. Chan and L. A. Vese. Active contours without edges. *IEEE Transactions on image processing*, 10 (2):266–277, 2001.

T. F. Chan, B. Y. Sandberg, and L. A. Vese. Active contours without edges for vector-valued images. *Journal of Visual Communication and Image Representation*, 11(2):130–141, 2000.

M. Charbit. *Digital Signal Processing (DSP) with python programming*. John Wiley & Sons, 2017.

M. Charbit, K. Abed-Meraim, G. Blanchet, A. Le Pichon, and Y. Cansi. OLS vs WLS for DOA estimation based on TDOA estimates: application to infrasonic signals. In *EGU General Assembly Conference Abstracts*, page 7410, 2012.

G. Chardon. *Approximations parcimonieuses et problèmes inverses en acoustique*. PhD thesis, Université Pierre et Marie Curie-Paris VI, 2012.

G. Chardon, F. Ollivier, J. Picheral, and S. Marcos. Approches parcimonieuses pour l'estimation de la matrice de covariance spatiale et la localisation de sources acoustiques. In *XXVIIème Colloque francophonede traitement du signal et des images (GRETSI 2019)*, 2019.

A. J. Charlton and L. M. Polvani. A new look at stratospheric sudden warmings. Part I: Climatology and modeling benchmarks. *Journal of climate*, 20(3):449–469, 2007.

I.-Y. Che, T. S. Kim, J.-S. Jeon, and H.-I. Lee. Infrasound observation of the apparent North Korean nuclear test of 25 May 2009. *Geophysical Research Letters*, 36(22), 2009.

I.-Y. Che, K. Kim, A. Le Pichon, J. Park, S. Arrowsmith, and B. Stump. Illuminating the North Korean nuclear explosion test in 2017 using remote infrasound observations. *Geophysical Journal International*, 228(1):308–315, 2022.

H. Cheung, Y. Chan, and F. Chan. Closed form formulae for Time-Difference-of-Arrival Estimation. *IEEE Trans. on Signal Processing*, June 2008. doi: 10.1109/TSP.2007.914342. doi : https://doi.org/10.1109/TSP.2007.914342.

L. Chiaraluce, R. Di Stefano, E. Tinti, L. Scognamiglio, M. Michele, E. Casarotti, M. Cattaneo, P. De Gori, C. Chiarabba, G. Monachesi, et al. The 2016 central Italy seismic sequence: A first look at the mainshocks, aftershocks, and source models. *Seismological Research Letters*, 88(3):757–771, 2017.

D. R. Christie and P. Campus. The IMS infrasound network: Design and establishment of infrasound stations. *Infrasound monitoring for atmospheric studies*, pages 29–75, 2009.

D. R. Christie, B. L. Kennett, and C. Tarlowski. Advances in infrasound technology with application to nuclear explosion monitoring. *Proceeding of the 29th monitoring research review. Los Alamos National Laboratory, Los Alamos, New Mexico*, pages 825–835, 2007.

I. Chunchuzov and S. Kulichkov. Internal gravity wave perturbations and their impacts on infrasound propagation in the atmosphere. *Infrasound monitoring for atmospheric studies: Challenges in middle atmosphere dynamics and Societal Benefits*, pages 551–590, 2019.

C. F. Chyba, P. J. Thomas, and K. J. Zahnle. The 1908 Tunguska explosion: atmospheric disruption of a stony asteroid. *Nature*, 361(6407):40–44, 1993.

H. Cox, R. Zeskind, and M. Owen. Robust adaptive beamforming. *IEEE Transactions on Acoustics, Speech, and Signal Processing*, 35(10):1365–1376, 1987. doi: 10.1109/TASSP.1987.1165054.

H. Cramér. *Mathematical methods of statistics*, volume 26. Princeton university press, 1999.

DataCamp-Team. Lasso and Ridge Regression in Python Tutorial. https://www.datacamp.com/tutorial/tutorial-lasso-ridge-regression, (accessed: 14.05.2024).

M. De Carlo. *Caractérisation du bruit ambiant atmosphérique d'origine océanique: modélisation des microbaroms à l'échelle globale et comparaison avec les observations infrasons du Système de Surveillance Internationale*. PhD thesis, Brest, 2020.

E. Defer, J.-P. Pinty, S. Coquillat, J.-M. Martin, S. Prieur, S. Soula, E. Richard, W. Rison, P. Krehbiel, R. Thomas, et al. An overview of the lightning and atmospheric electricity observations collected in southern France during the HYdrological cycle in Mediterranean EXperiment (HyMeX), Special Observation Period 1. *Atmospheric Measurement Techniques*, 8(2):649–669, 2015.

A. P. Dempster, N. M. Laird, and D. B. Rubin. Maximum likelihood from incomplete data via the EM algorithm. *Journal of the royal statistical society: series B (methodological)*, 39(1):1–22, 1977.

G. DeMuth. Frequency domain beamforming techniques. In *ICASSP '77. IEEE International Conference on Acoustics, Speech, and Signal Processing*, volume 2, pages 713–715, 1977. doi: 10.1109/ICASSP.1977.1170316.

O. F. den Ouden, J. D. Assink, P. S. Smets, S. Shani-Kadmiel, G. Averbuch, and L. G. Evers. CLEAN beamforming for the enhanced detection of multiple infrasonic sources. *Geophysical Journal International*, 221(1):305–317, 2020.

J. C. W. Denholm-Price and J. M. Rees. Detecting Waves Using an Array of Sensors. *Monthly Weather Review*, 127(1):57–69, 1999. doi: 10.1175/1520-0493(1999)127<0057:DWUAAO>2.0.CO;2. URL https://journals.ametsoc.org/view/journals/mwre/127/1/1520-0493_1999_127_0057_dwuaao_2.0.co_2.xml.

W. L. Donn and N. K. Balachandran. Mount St. Helens eruption of 18 May 1980: Air waves and explosive yield. *Science*, 213(4507):539–541, 1981.

W. L. Donn and D. Rind. Microbaroms and the temperature and wind of the upper atmosphere. *Journal of Atmospheric Sciences*, 29(1):156–172, 1972.

M. Drton and M. Plummer. A Bayesian information criterion for singular models. *Journal of the Royal Statistical Society Series B: Statistical Methodology*, 79(2):323–380, 2017.

J. Durbin and G. S. Watson. Testing for serial correlation in least squares regression: I. *Biometrika*, 37 (3/4):409–428, 1950.

W. N. Edwards. Meteor generated infrasound: Theory and observation. *Infrasound monitoring for atmospheric studies*, pages 361–414, 2009.

P. Embrechts, C. Klüppelberg, and T. Mikosch. Modelling extremal events, volume 33 of applications of mathematics, 1997.

V. A. Epanechnikov. Non-Parametric Estimation of a Multivariate Probability Density. *Theory of Probability & Its Applications*, 14(1):153–158, 1969. doi: 10.1137/1114019. URL https://doi.org/10.1137/1114019.

L. Evers and H. Haak. The detectability of infrasound in the Netherlands from the Italian volcano Mt. Etna. *Journal of Atmospheric and Solar-Terrestrial Physics*, 67(3):259–268, 2005.

L. G. Evers. The inaudible symphony: on the detection and source identification of atmospheric infrasound. 2008.

T. Farges and E. Blanc. Characteristics of infrasound from lightning and sprites near thunderstorm areas. *Journal of Geophysical Research: Space Physics*, 115(A6), 2010.

T. Farges, F. Coulouvrat, L.-J. Gallin, and R. Marchiano. Infrasound for detection, localization, and geometrical reconstruction of lightning flashes. *Infrasound Monitoring for Atmospheric Studies: Challenges in Middle Atmosphere Dynamics and Societal Benefits*, pages 911–938, 2019.

D. Fee, R. S. Matoza, K. L. Gee, T. B. Neilsen, and D. E. Ogden. Infrasonic crackle and supersonic jet noise from the eruption of Nabro Volcano, Eritrea. *Geophysical Research Letters*, 40(16):4199–4203, 2013.

D. Feldman and L. Griffiths. A projection approach for robust adaptive beamforming. *IEEE Transactions on Signal Processing*, 42(4):867–876, 1994. doi: 10.1109/78.285650.

A. Few. Power spectrum of thunder. *Journal of Geophysical Research*, 74(28):6926–6934, 1969.

A. Few. Lightning channel reconstruction from thunder measurements. *Journal of Geophysical Research*, 75(36):7517–7523, 1970.

R. A. Fisher. On the Interpretation of 2 from Contingency Tables, and the Calculation of P, Oct. 2018. URL https://doi.org/10.2307/2340521.

A. Foss and O. R. Zaïane. A parameterless method for efficiently discovering clusters of arbitrary shape in large datasets. In *2002 IEEE International Conference on Data Mining, 2002. Proceedings.*, pages 179–186. IEEE, 2002.

R. Freire, L. Fernandez, C. Mallafré-Muro, A. Martín-Gómez, F. Madrid-Gambin, L. Oliveira, A. Pardo, L. Arce, and S. Marco. Full workflows for the analysis of gas chromatography—ion mobility spectrometry in foodomics: application to the analysis of iberian ham aroma. *Sensors*, 21(18):6156, 2021.

O. Frost. An algorithm for linearly constrained adaptive array processing. *Proceedings of the IEEE*, 60 (8):926–935, 1972. doi: 10.1109/PROC.1972.8817.

M. Gal, A. Reading, S. Ellingsen, K. Koper, R. Burlacu, and S. Gibbons. Deconvolution enhanced direction of arrival estimation using one-and three-component seismic arrays applied to ocean induced microseisms. *Geophysical Journal International*, 206(1):345–359, 2016.

D. Gesbert, P. Duhamel, and S. Mayrargue. On-line blind multichannel equalization based on mutually referenced filters. *IEEE Transactions on Signal Processing*, 45(9):2307–2317, 1997.

D. Gheri, G. Belli, E. Marchetti, V. Boulenger, A. Le Pichon, P. Hupe, P. Näsholm, and P. Mialle. Long range monitoring of explosive volcanoes with ims infrasound arrays: testing the vis. Technical report, Copernicus Meetings, 2024.

J.-D. Gibbons and J.-W. Pratt. P-Values: interpretation and methodology. *The American Statistician*, 29(1):20–25, 1975. ISSN 00031305. URL http://www.jstor.org/stable/2683674. doi : https://doi.org/10.2307/2683674.

D. R. Glaser, D. K. Wilson, L. E. Waldrop, C. R. Hart, M. J. White, E. T. Nykaza, and M. E. Swearingen. Modeling of signal propagation and sensor performance for infrasound and blast noise. In *Ground/Air Multisensor Interoperability, Integration, and Networking for Persistent ISR VIII*, volume 10190, pages 254–264. SPIE, 2017.

E. E. Gossard and W. H. Hooke. Waves in the atmosphere. *Developments in Atmospheric Science, Elsevier*, 2, Jan. 1975.

D. N. Green. The spatial coherence structure of infrasonic waves: analysis of data from International Monitoring System arrays. *Geophysical Journal International*, 201(1):377–389, 02 2015. ISSN 0956-540X. doi: 10.1093/gji/ggu495. URL https://doi.org/10.1093/gji/ggu495.

D. N. Green, J. Guilbert, A. Le Pichon, O. Sebe, and D. Bowers. Modelling ground-to-air coupling for the shallow ML 4.3 Folkestone, United Kingdom, earthquake of 28 April 2007. *Bulletin of the Seismological Society of America*, 99(4):2541–2551, 2009.

M.-A. Guérard. *Estimation de la direction d'arrivée d'échos sonores à large bande noyés dans le signal direct*. PhD thesis, Université Laval, 2016.

J. Hanley and B. McNeil. The meaning and use of the area under a receiver operating characteristic (ROC) curve. *Radiology*, 143(1):29–36, 1982. doi: 10.1148/radiology.143.1.7063747. doi : https://doi.org/10.1148/radiology.143.1.7063747.

N. Hansen. The CMA evolution strategy: a comparing review. In *Towards a new evolutionary computation*, pages 75–102. Springer, 2006.

N. Hansen and A. Ostermeier. Convergence properties of evolution strategies with the derandomized covariance matrix adaptation. *Eufit*, 97:650–654, 1997.

D. Hart and R. Rembold. Evaluation of two chaparral physics model 50a infrasound sensors. *Sandia National Laboratories Tech. Rep*, 2010.

M. Heck, M. Hobiger, A. Van Herwijnen, J. Schweizer, and D. Fäh. Localization of seismic events produced by avalanches using multiple signal classification. *Geophysical Journal International*, 216(1): 201–217, 2019.

B. Hernandez, A. Le Pichon, J. Vergoz, P. Herry, L. Ceranna, C. Pilger, E. Marchetti, M. Ripepe, and R. Bossu. Estimating the ground-motion distribution of the 2016 Mw 6.2 Amatrice, Italy, earthquake using remote infrasound observations. *Seismological Research Letters*, 89(6):2227–2236, 2018.

C. O. Hines. Internal atmospheric gravity waves at ionospheric heights. *Canadian Journal of Physics*, 38 (11):1441–1481, 1960.

J. Högbom. Aperture synthesis with a non-regular distribution of interferometer baselines. *Astronomy and Astrophysics Supplement Series*, 15:417, 1974.

R. A. Horn and C. R. Johnson. *Matrix analysis*. Cambridge university press, 2012.

Y. Hua, S. An, and Y. Xiang. Blind identification of FIR MIMO channels by decorrelating subchannels. *IEEE Transactions on Signal Processing*, 51(5):1143–1155, 2003.

H. Hung and M. Kaveh. Focussing matrices for coherent signal-subspace processing. *IEEE Transactions on Acoustics, Speech, and Signal Processing*, 36(8):1272–1281, 1988. doi: 10.1109/29.1655. doi : https://doi.org/10.1109/29.1655.

P. Hupe, J. Vergoz, C. Pilger, and A. Le Pichon. Characterizing the 2022 South Atlantic fireball using infrasound recordings of the International Monitoring System. Technical report, Copernicus Meetings, 2024.

M. Kass, A. Witkin, and D. Terzopoulos. Snakes: Active contour models. *International journal of computer vision*, 1(4):321–331, 1988.

S. M. Kay. *Fundamentals of statistical signal processing: Practical algorithm development*, volume 3. Pearson Education, 2013.

A. Le Pichon, J. Guilbert, M. Vallée, J. Dessa, and M. Ulziibat. Infrasonic imaging of the Kunlun Mountains for the great 2001 China earthquake. *Geophysical Research Letters*, 30(15), 2003.

A. Le Pichon, R. Matoza, N. Brachet, and Y. Cansi. Recent enhancements of the pmcc infrasound signal detector. *Inframatics*, 26:5–8, 2010.

A. Le Pichon, J. Vergoz, N. Brachet, P. Gaillard, Y. Cansi, and J. Guilbert. A description of the infrasound data processing at the French CEA/DASE. *Proceedings of the 2011 Monitoring Research Review: Ground-Based Nuclear Explosion Monitoring Technologies*, pages 787–797, 2011.

A. Le Pichon, L. Ceranna, C. Pilger, P. Mialle, D. Brown, P. Herry, and N. Brachet. The 2013 Russian fireball largest ever detected by CTBTO infrasound sensors. *Geophysical Research Letters*, 40(14): 3732–3737, 2013.

E. Lebarbier and T. Mary-Huard. *Le critère BIC: fondements théoriques et interprétation.* PhD thesis, INRIA, 2004.

C.-C. Lee and J.-H. Lee. Robust adaptive array beamforming under steering vector errors. *IEEE Transactions on Antennas and Propagation*, 45(1):168–175, 1997. doi: 10.1109/8.554254.

D.-C. Lee, J. V. Olson, and C. A. Szuberla. Computationally robust and noise resistant numerical detector for the detection of atmospheric infrasound. *The Journal of the Acoustical Society of America*, 134(1): 862–868, 2013.

R. G. Leisure. *Acoustic Waves in Solids*, page 56–93. Cambridge University Press, 2017.

J. Li, P. Stoica, and Z. Wang. On robust Capon beamforming and diagonal loading. *IEEE Transactions on Signal Processing*, 51(7):1702–1715, 2003. doi: 10.1109/TSP.2003.812831.

J.-D. Lin, W.-H. Fang, Y.-Y. Wang, and J.-T. Chen. FSF MUSIC for joint DOA and frequency estimation and its performance analysis. *IEEE Transactions on Signal Processing*, 54(12):4529–4542, 2006.

S.-D. Lin and M. Barkat. Maximum likelihood estimation of direction-of-arrival and detection for broadband sources via dynamic programming. *IEEE transactions on antennas and propagation*, 39(8): 1213–1221, 1991.

J. F. Lingevitch, M. D. Collins, and W. L. Siegmann. Parabolic equations for gravity and acousto-gravity waves. *The Journal of the Acoustical Society of America*, 105(6):3049–3056, 1999.

C. Listowski, E. Forestier, S. Dafis, T. Farges, M. De Carlo, F. Grimaldi, A. Le Pichon, J. Vergoz, P. Heinrich, and C. Claud. Remote monitoring of mediterranean hurricanes using infrasound. *Remote Sensing*, 14(23):6162, 2022.

C. Listowski, C. Stephan, A. Le Pichon, A. Hauchecorne, Y.-H. Kim, U. Achatz, and G. Bölöni. Stratospheric gravity waves impact on infrasound transmission losses across the International Monitoring System. *Pure and Applied Geophysics*, pages 1–33, 2024.

L. Liszka and K. Waldemark. High resolution observations of infrasound generated by the supersonic flights of Concorde. *Journal of Low Frequency Noise, Vibration and Active Control*, 14(4):181–192, 1995.

I. Loshchilov and F. Hutter. CMA-ES for hyperparameter optimization of deep neural networks. *arXiv preprint arXiv:1604.07269*, 2016.

Q. Lv, X. Zhang, and Y. Jia. Blind separation combined frequency invariant beamforming and ICA for far-field broadband acoustic signals. In *International Symposium on Neural Networks*, pages 538–543. Springer, 2005.

H. Mack and E. A. Flinn. Analysis of the Spatial Coherence of Short-Period Acoustic-Gravity Waves in the Atmosphere. *Geophysical Journal International*, 26(1-4):255–269, 12 1971. ISSN 0956-540X. doi: 10.1111/j.1365-246X.1971.tb03399.x. URL https://doi.org/10.1111/j.1365-246X.1971.tb03399.x.

K. A. Macpherson, D. Fee, J. R. Coffey, and A. J. Witsil. Using local infrasound to estimate seismic velocity and earthquake magnitudes. *Bulletin of the Seismological Society of America*, 113(4):1434–1456, 2023.

E. Marchetti, M. Ripepe, G. Ulivieri, and A. Kogelnig. Infrasound array criteria for automatic detection and front velocity estimation of snow avalanches: towards a real-time early-warning system. *Natural Hazards and Earth System Sciences*, 15(11):2545–2555, 2015.

E. Marchetti, M. Ripepe, P. Campus, A. Le Pichon, J. Vergoz, G. Lacanna, P. Mialle, P. Héreil, and P. Husson. Long range infrasound monitoring of Etna volcano. *Scientific reports*, 9(1):18015, 2019.

O. Marcillo, S. Arrowsmith, P. Blom, and K. Jones. On infrasound generated by wind farms and its propagation in low-altitude tropospheric waveguides. *Journal of geophysical research: Atmospheres*, 120(19):9855–9868, 2015.

O. Marcillo, S. Arrowsmith, M. Charbit, and J. Carmichael. Infrasound signal detection: re-examining the component parts that makeup detection algorithms. In *Infrasound monitoring for atmospheric studies*, pages 249–271. Springer, 2019. doi : https://doi.org/10.1007/978-3-319-75140-5_7.

J. Marty. The IMS infrasound network: current status and technological developments. In *Infrasound monitoring for atmospheric studies*, pages 3–62. Springer, 2019. doi: 10.1007/978-3-319-75140-5_1. doi : https://doi.org/10.1007/978-3-319-75140-5_1.

R. Matoza, M. Landès, A. Le Pichon, L. Ceranna, and D. Brown. Coherent ambient infrasound recorded by the International Monitoring System. *Geophysical Research Letters*, 40(2):429–433, 2013. doi : https://doi.org/10.1029/2012GL054329.

Q. Mayyala, K. Abed-Meraim, A. Zerguine, and A. Lawal. Fast multimodulus blind deconvolution algorithms. *IEEE Transactions on Wireless Communications*, 21(11):9627–9637, 2022.

J. A. McDonald, E. Douze, and E. Herrin. The structure of atmospheric turbulence and its application to the design of pipe arrays. *Geophysical Journal International*, 26(1-4):99–109, 1971.

B. S. Melton and L. F. Bailey. Multiple signal correlators. *Geophysics*, 22(3):565–588, 07 1957. ISSN 0016-8033. doi: 10.1190/1.1438390. URL https://doi.org/10.1190/1.1438390.

L. Meng, X.-H. Li, W.-G. Zhang, and D.-Z. Liu. The application of the Capon method to the parameter estimation of infrasound signals. In *2015 4th National Conference on Electrical, Electronics and Computer Engineering*, pages 1105–1109. Atlantis Press, 2015.

B. J. Merchant. Hyperion 5113/gp infrasound sensor evaluation. Technical report, Sandia National Lab.(SNL-NM), Albuquerque, NM (United States), 2015.

B. J. Merchant and K. D. McDowell. MB3a infrasound sensor evaluation. Technical report, Sandia National Lab.(SNL-NM), Albuquerque, NM (United States), 2014.

J.-P. Métaxian, F. Biagioli, A. Trabattoni, E. Stutzmann, G. Lacanna, G. Risica, P. Bernard, Y. Capdeville, A. Mangeney, V. Monteiller, et al. Using Distributed Acoustic Sensing, seismic and infrasonic observation to track pyroclastic flows at Stromboli Volcano (Italy). Technical report, Copernicus Meetings, 2024.

M. Michele, R. Di Stefano, L. Chiaraluce, M. Cattaneo, P. De Gori, G. Monachesi, D. Latorre, S. Marzorati, L. Valoroso, C. Ladina, et al. The Amatrice 2016 seismic sequence: a preliminary look at the mainshock. *Annals of Geophysics*, 2016.

U. Mitterbauer, E. Brückl, P. Carniel, and S. Mertl. Infrasound signals generated by production blasts in a nearby quarry. Technical report, Copernicus Meetings, 2024.

D. C. Montgomery, E. A. Peck, and G. G. Vining. *Introduction to linear regression analysis*. John Wiley & Sons, 2021.

F. Mosteller and J. W. Tukey. Data analysis and regression. a second course in statistics. *Addison-Wesley series in behavioral science: quantitative methods*, 1977.

J. P. Mutschlecner and R. W. Whitaker. Infrasound from earthquakes. *Journal of Geophysical Research: Atmospheres*, 110(D1), 2005.

J. P. Mutschlecner, R. W. Whitaker, and L. H. Auer. An empirical study of infrasonic propagation. Technical report, Los Alamos National Lab.(LANL), Los Alamos, NM (United States), 1999.

A. Nouvellet, M. Charbit, F. Roueff, and A. Le Pichon. Slowness estimation from noisy time delays observed on non-planar arrays. *Geophysical Journal International*, 198(2):1199–1207, 06 2014. ISSN 0956-540X. doi: 10.1093/gji/ggu197. URL https://doi.org/10.1093/gji/ggu197. doi : https://doi.org/10.1093/gji/ggu197.

B. A. Olshausen and D. J. Field. Sparse coding with an overcomplete basis set: A strategy employed by v1? *Vision research*, 37(23):3311–3325, 1997.

S. Osher and J. A. Sethian. Fronts propagating with curvature-dependent speed: Algorithms based on hamilton-jacobi formulations. *Journal of computational physics*, 79(1):12–49, 1988.

J. Park, C. Hayward, C. Zeiler, S. Arrowsmith, and B. Stump. Assessment of infrasound detectors based on analyst review, environmental effects, and detection characteristics. *Bulletin of the Seismological Society of America*, 107(2):674–690, 2017. doi : https://doi.org/10.1785/0120160125.

E. Parzen. On Estimation of a Probability Density Function and Mode. *The Annals of Mathematical Statistics*, 33(3):1065 – 1076, 1962. doi: 10.1214/aoms/1177704472. URL https://doi.org/10.1214/aoms/1177704472.

M. Pásztor, C. Czanik, and I. Bondár. Exploiting infrasound detections to identify and track regional storms. In *EGU General Assembly Conference Abstracts*, pages EGU21–6525, 2021.

Y. C. Pati, R. Rezaiifar, and P. S. Krishnaprasad. Orthogonal matching pursuit: Recursive function approximation with applications to wavelet decomposition. In *Proceedings of 27th Asilomar conference on signals, systems and computers*, pages 40–44. IEEE, 1993.

A. Perttu, B. Taisne, S. De Angelis, J. D. Assink, D. Tailpied, and R. A. Williams. Estimates of plume height from infrasound for regional volcano monitoring. *Journal of Volcanology and Geothermal Research*, 402:106997, 2020.

M. Peruzzetto, A. Kazantsev, K. Luu, J. Metaxian, F. Huguet, and H. Chauris. Broad-band ambient noise characterization by joint use of cross-correlation and music algorithm. *Geophysical Journal International*, 215(2):760–779, 2018.

J. Peter. Huber. Robust Statistics. Wiley, 1981 (republished in paperback). 2004.

G. R. Phillips and E. M. Eyring. Comparison of conventional and robust regression in analysis of chemical data. *Analytical Chemistry*, 55(7):1134–1138, 1983.

C. Pilger, L. Ceranna, J. O. Ross, J. Vergoz, A. Le Pichon, N. Brachet, E. Blanc, J. Kero, L. Liszka, S. Gibbons, et al. The european infrasound bulletin. *Pure and Applied Geophysics*, 175:3619–3638, 2018.

C. Pilger, P. Gaebler, P. Hupe, A. Kalia, F. Schneider, A. Steinberg, H. Sudhaus, and L. Ceranna. Yield estimation of the 2020 Beirut explosion using open access waveform and remote sensing data. *Scientific reports*, 11(1):1–14, 2021a. doi : https://doi.org/10.1038/s41598-021-93690-y.

C. Pilger, P. Hupe, P. Gaebler, and L. Ceranna. 1001 rocket launches for space missions and their infrasonic signature. *Geophysical Research Letters*, 48(8):e2020GL092262, 2021b.

D. Ponceau and L. Bosca. Low-noise broadband microbarometers. *Infrasound monitoring for atmospheric studies*, pages 119–140, 2009.

B. Poste, M. Charbit, A. Janela Cameijo, A. Le Pichon, C. Listowski, F. Roueff, and J. Vergoz. The multichannel maximum-likelihood (mcml) method: towards a multisource detection and wave parameter estimations using deep learning. In *EGU General Assembly Conference Abstracts*, pages EGU–6647, 2023a.

B. Poste, M. Charbit, A. Le Pichon, C. Listowski, F. Roueff, and J. Vergoz. The multichannel maximum-likelihood (MCML) method: a new approach for infrasound detection and wave parameter estimation. *Geophysical Journal International*, 232(2):1099–1112, 2023b.

RandOpt-INRIA. CMA-ES : le logiciel d'optimisation pour la biologie, la médecine et l'ingénierie. https://www.inria.fr/fr/cma-es-logiciel-optimisation-biologie-medecine-ingenierie, (accessed: 09.07.2024).

D. O. ReVelle. On meteor-generated infrasound. *Journal of Geophysical Research*, 81(7):1217–1230, 1976.

W. J. Rey. *Introduction to robust and quasi-robust statistical methods*. Springer Science & Business Media, 2012.

J. Rogers, J. E. Ball, and A. C. Gurbuz. Robust estimation of the number of coherent radar signal sources using deep learning. *IET Radar, Sonar & Navigation*, 15(5):431–440, 2021.

M. Rosenblatt. Remarks on Some Nonparametric Estimates of a Density Function. *The Annals of Mathematical Statistics*, 27(3):832 – 837, 1956. doi: 10.1214/aoms/1177728190. URL https://doi.org/10.1214/aoms/1177728190.

P. J. Rousseeuw. Least Median of Squares Regression. *Journal of the American Statistical Association*, 79(388):871–880, 1984. doi: 10.1080/01621459.1984.10477105. URL https://www.tandfonline.com/doi/abs/10.1080/01621459.1984.10477105.

P. J. Rousseeuw. Tutorial to robust statistics. *Journal of chemometrics*, 5(1):1–20, 1991.

P. J. Rousseeuw and M. Hubert. Recent developments in progress. *Lecture Notes-Monograph Series*, pages 201–214, 1997.

P. J. Rousseeuw and A. M. Leroy. *Robust regression and outlier detection*. John wiley & sons, 2005.

P. J. Rousseeuw and K. Van Driessen. Computing lts regression for large data sets. *Data mining and knowledge discovery*, 12:29–45, 2006.

D. N. Rutledge and D. J.-R. Bouveresse. Independent components analysis with the JADE algorithm. *TrAC Trends in Analytical Chemistry*, 50:22–32, 2013.

T. P. Ryan. *Modern regression methods*, volume 655. John Wiley & Sons, 2008.

A. Sakharov. *MEMOIRS. TRANS. BY RICHARD LOURIE.* Knopf, 1990.

S. Salvador and P. Chan. Determining the number of clusters/segments in hierarchical clustering/segmentation algorithms. In *16th IEEE international conference on tools with artificial intelligence*, pages 576–584. IEEE, 2004.

V. Satopaa, J. Albrecht, D. Irwin, and B. Raghavan. Finding a" kneedle" in a haystack: Detecting knee points in system behavior. In *2011 31st international conference on distributed computing systems workshops*, pages 166–171. IEEE, 2011.

H. Sawada, R. Mukai, S. Araki, and S. Makino. A robust and precise method for solving the permutation problem of frequency-domain blind source separation. *IEEE transactions on speech and audio processing*, 12(5):530–538, 2004.

D. A. Schecter, M. E. Nicholls, J. Persing, A. J. Bedard Jr, and R. A. Pielke Sr. Infrasound emitted by tornado-like vortices: Basic theory and a numerical comparison to the acoustic radiation of a single-cell thunderstorm. *Journal of the atmospheric sciences*, 65(3):685–713, 2008.

R. Schmidt. Multiple emitter location and signal parameter estimation. *IEEE Transactions on Antennas and Propagation*, 34(3):276–280, 1986. doi: 10.1109/TAP.1986.1143830.

D. W. Scott. Kernel density estimation. *Wiley StatsRef: Statistics Reference Online*, pages 1–7, 2014.

R. Scott Harris, D. R. Hess, and J. G. Venegas. An objective analysis of the pressure-volume curve in the acute respiratory distress syndrome. *American journal of respiratory and critical care medicine*, 161(2):432–439, 2000.

C. Seligson. Comments on "high-resolution frequency-wavenumber spectrum analysis". *Proceedings of the IEEE*, 58(6):947–949, 1970. doi: 10.1109/PROC.1970.7825.

R. H. Shumway. On Detecting a Signal in N Stationarily Correlated Noise Series. *Technometrics*, 13 (3):499–519, 1971. doi: 10.1080/00401706.1971.10488814. URL https://www.tandfonline.com/doi/abs/10.1080/00401706.1971.10488814.

O. Sigaud and F. Stulp. Adaptation de la matrice de covariance pour l'apprentissage par renforcement direct. *Revue d'intelligence artificielle*, 27(2):243–263, 2013.

P. Sijtsma. CLEAN based on spatial source coherence. *International journal of aeroacoustics*, 6(4): 357–374, 2007.

E. Smart and E. A. Flinn. Fast frequency-wavenumber analysis and Fisher signal detection in real-time infrasonic array data processing. *Geophysical journal international*, 26(1-4):279–284, 1971.

P. Smets. Infrasound and the dynamical stratosphere: A new application for operational weather and climate prediction. 2018.

A. Smirnov, I. Sokolova, and V. Dubrovin. The variety of infrasound sources recorded by kazakhstani stations. *CTBT: Science and Technology, Vienna, available at: https://www. ctbto. org/fileadmin/user_ upload/SnT2015/SnT2015_ Posters*, 2, 2015.

A. Smirnov, M. De Carlo, A. Le Pichon, N. Shapiro, and S. Kulichkov. Characterizing the oceanic ambient noise as recorded by the dense seismo-acoustic Kazakh network. *Solid Earth*, 12(2):503–520, 2021. doi : https://doi.org/10.5194/se-12-503-2021.

J. V. Stone. Independent component analysis: a tutorial introduction. 2004.

G. Symons. The eruption of Krakatoa and subsequent phenomena. *Quarterly Journal of the Royal Meteorological Society*, 14(68):301–307, 1888.

C. Szuberla and J. Olson. Uncertainties associated with parameter estimation in atmospheric infrasound arrays. *The Journal of the Acoustical Society of America*, 115(1):253–258, 2004. doi : https://doi.org/10.1121/1.1635407.

H. Tang. DOA estimation based on MUSIC algorithm, 2014.

R. Tibshirani. Regression shrinkage and selection via the lasso. *Journal of the Royal Statistical Society Series B: Statistical Methodology*, 58(1):267–288, 1996.

J. J. Tiede and M. Pagano. The application of robust calibration to radioimmunoassay. *Biometrics*, pages 567–574, 1979.

L. Tong, V. Soon, Y. Huang, and R. Liu. Amuse: a new blind identification algorithm. In *IEEE international symposium on circuits and systems*, pages 1784–1787. IEEE, 1990.

L. Tong, R.-W. Liu, V. C. Soon, and Y.-F. Huang. Indeterminacy and identifiability of blind identification. *IEEE Transactions on circuits and systems*, 38(5):499–509, 1991.

US-Standard. *US standard atmosphere*. National Oceanic and Atmospheric Administration, 1976.

A. Vallage, L. Bollinger, J. Champenois, C. Duverger, A. G. Trilla, B. Hernandez, A. L. Pichon, C. Listowski, G. Mazet-Roux, M. Menager, et al. Multitechnology characterization of an unusual surface rupturing intraplate earthquake: the ML 5.4 2019 Le Teil event in France. *Geophysical Journal International*, 226(2):803–813, 2021.

K. Varelas, A. Auger, D. Brockhoff, N. Hansen, O. A. ElHara, Y. Semet, R. Kassab, and F. Barbaresco. A comparative study of large-scale variants of CMA-ES. In *International Conference on Parallel Problem Solving from Nature*, pages 3–15. Springer, 2018.

I. Vera Rodriguez, S. P. Näsholm, and A. Le Pichon. Atmospheric wind and temperature profiles inversion using infrasound: An ensemble model context. *The Journal of the Acoustical Society of America*, 148 (5):2923–2934, 2020.

J. Vergoz, A. Le Pichon, and C. Millet. The antares explosion observed by the USArray: an unprecedented collection of infrasound phases recorded from the same event. In *Infrasound monitoring for atmospheric studies*, pages 349–386. Springer, 2019. doi : https://doi.org/10.1007/978-3-319-75140-5_9.

J. Vergoz, C. Millet, and Y. Cano. Characterization of the 4 August 2020 Beirut explosion from the infrasound component of the IMS network. In *Science and Technology Conference (SnT 2021)*, 2021.

J. Vergoz, P. Hupe, C. Listowski, A. Le Pichon, M. Garcés, E. Marchetti, P. Labazuy, L. Ceranna, C. Pilger, P. Gaebler, et al. IMS observations of infrasound and acoustic-gravity waves produced by the January 2022 volcanic eruption of Hunga, Tonga: A global analysis. *Earth and Planetary Science Letters*, 591:117639, 2022.

K. T. Walker. Evaluating the opposing wave interaction hypothesis for the generation of microbaroms in the eastern North Pacific. *Journal of Geophysical Research: Oceans*, 117(C12), 2012. doi: 10.1029/2012JC008409. URL https://agupubs.onlinelibrary.wiley.com/doi/abs/10.1029/2012JC008409.

K. T. Walker, A. L. Pichon, T. S. Kim, C. de Groot-Hedlin, I.-Y. Che, and M. Garcés. An analysis of ground shaking and transmission loss from infrasound generated by the 2011 Tohoku earthquake. *Journal of Geophysical Research: Atmospheres*, 118(23):12–831, 2013.

H. Wang and M. Kaveh. Coherent signal-subspace processing for the detection and estimation of angles of arrival of multiple wide-band sources. *IEEE Transactions on Acoustics, Speech, and Signal Processing*, 33(4):823–831, 1985.

Y. Wang, J. Li, P. Stoica, M. Sheplak, and T. Nishida. Wideband RELAX and wideband CLEAN for aeroacoustic imaging. *The Journal of the Acoustical Society of America*, 115(2):757–767, 2004.

M. Wax and T. Kailath. Detection of signals by information theoretic criteria. *IEEE Transactions on acoustics, speech, and signal processing*, 33(2):387–392, 1985.

M. Wax, T.-J. Shan, and T. Kailath. Spatio-temporal spectral analysis by eigenstructure methods. *IEEE Transactions on Acoustics, Speech, and Signal Processing*, 32(4):817–827, 1984. doi: 10.1109/TASSP.1984.1164400.

R. W. Whitaker. Infrasound signals from ground motion sources. *Proceedings of the 30th Monitoring Research Review: Ground-Based Nuclear Explosion Monitoring Technologies*, pages 912–920, 2008.

P. Whittle. Hypothesis testing in time series analysis. *(No Title)*, 1951.

S. S. Wilks. The large-sample distribution of the likelihood ratio for testing composite hypotheses. *The annals of mathematical statistics*, 9(1):60–62, 1938.

C. R. Wilson. Auroral infrasonic waves. *Journal of Geophysical Research*, 74(7):1812–1836, 1969.

C. R. Wilson. Auroral infrasonic waves and poleward expansions of auroral substorms at Inuvik, NWT, Canada. *Geophysical Journal International*, 26(1-4):179–181, 1971.

C. R. Wilson, C. A. Szuberla, and J. V. Olson. High-latitude observations of infrasound from Alaska and Antarctica: mountain associated waves and geomagnetic/auroral infrasonic signals. *Infrasound Monitoring for Atmospheric Studies*, pages 415–454, 2009.

E. Wit, E. v. d. Heuvel, and J.-W. Romeijn. 'all models are wrong...': an introduction to model uncertainty. *Statistica Neerlandica*, 66(3):217–236, 2012.

R. Wu, Z. Bao, and Y. Ma. Control of peak sidelobe level in adaptive arrays. *IEEE Transactions on Antennas and Propagation*, 44(10):1341–1347, 1996. doi: 10.1109/8.537328.

K. Wyatt. Narrowband versus broadband harmonic signals. https://interferencetechnology.com/narrowband-versus-broadband-harmonic-signals/, (accessed: 30.10.2023).

J. Yang and M. Kaveh. Wideband adaptive array processing based on the approximation of coherent signal-subspace. *submitted for publication*, 1983.

Y. Yang. Can the strengths of AIC and BIC be shared? a conflict between model indentification and regression estimation. *Biometrika*, 92(4):937–950, 2005.

Y.-S. Yoon, L. Kaplan, and J. McClellan. TOPS: new DOA estimator for wideband signals. *IEEE Transactions on Signal Processing*, 54(6):1977–1989, 2006. doi: 10.1109/TSP.2006.872581.

A. Zelias, O. Gainville, and F. Coulouvrat. Complex eigenrays algorithm for infrasound propagation in a windy range dependent atmosphere. *The Journal of the Acoustical Society of America*, 151(5): 3328–3342, 2022.

S. Zhang and I. Thng. Robust presteering derivative constraints for broadband antenna arrays. *IEEE Transactions on Signal Processing*, 50(1):1–10, 2002. doi: 10.1109/78.972477.

M. Ørregaard Nielsen and M. Ksawery Popiel. A matlab program and user's guide for the fractionally cointegrated var model. 2018. URL https://github.com/jagerman/fracdist/releases.

Benjamin POSTE

TRAITEMENT STATISTIQUE DU SIGNAL POUR LA SÉPARATION DE SOURCES MULTIPLES SUR LES ANTENNES

Résumé :

Le CEA utilise, depuis la fin des années 1990, les données du Systeme de Surveillance International (SSI) pour la vérification du Traité d'Interdiction Complète des Essais nucléaires (TICE). La surveillance repose entre autre sur la détection des ondes infrasonores, grâce à un réseau de stations équipées de microbaromètres, permettant de localiser des sources acoustiques dans la bande de fréquence 0.01-4 Hz. Ces données révèlent de nombreux signaux d'origines naturelles et anthropiques (comme la houle océanique, les volcans, ou les activités industrielles).

Cette étude vise à détecter et estimer simultanément des signaux issus de sources différentes interférant la même bande de fréquence, à l'aide de méthodes statistiques robustes adaptées au traitement en temps réel. Des algorithmes de référence comme MUltiple SIgnal Classification (MUSIC) ou Minimum Variance Distortionless Response (MVDR) sont évalués. D'autres méthodes basées sur Multi-Channel Maximum Likelihood (MCML), l'Analyse en Composantes Indépendantes (ACI) ou le dictionary coding sont développées. Une évaluation sur des signaux synthétiques et réels permet de comparer la précision de ces méthodes. Deux méthodes basées sur MCML sont particulièrement prometteuses. Une d'entre elle, basée sur la soustraction itérative des signaux, autorise des calculs en temps réel.

Les estimations des paramètres du vecteur d'onde (azimut et vitesse horizontale) fournies par ces algorithmes nécessitent un post-traitement pour créer des évènements. Une nouvelle méthode de regroupement des pixels de détection dans le domaine temps-fréquence utilisant un modèle de mélange de gaussiennes (Gaussian Mixture Model (GMM)) est proposée pour la séparation de sources multiples.

Mots clés : Traitement du signal, infrasons, antennes, separation de sources

STATISTICAL SIGNAL PROCESSING FOR MULTIPLE SOURCES SEPARATION ON ANTENNAS

Abstract :

The CEA has been using the International Monitoring System (IMS) data since the late 1990s to verify compliance with the Comprehensive Nuclear Test-Ban Treaty (CTBT). The monitoring system relies on, among other things, the detection of infrasonic waves through a network of stations equipped with microbarometers, allowing the localisation of acoustic sources in the 0.01-4 Hz frequency band. This data reveals numerous signals of both natural and anthropogenic origins (such as oceanic swell, volcanoes, or industrial activities).

This study aims to simultaneously detect and estimate signals from different sources that interfere within the same frequency band, using robust statistical methods adapted for real-time processing. Reference algorithms such as MUltiple SIgnal Classification (MUSIC) or Minimum Variance Distortionless Response (MVDR) are evaluated. Other methods based on Multi-Channel Maximum Likelihood (MCML), the Independent Component Analysis (ICA), or the dictionary coding are developed. An evaluation on synthetic and real signals allows for comparison of the accuracy of these methods. Two methods based on MCML are particularly promising. One of them, based on iterative signal subtraction, enables real-time computation.

The wave vector parameter estimates (azimuth and horizontal velocity) provided by these algorithms require post-processing to create events. A new method for clustering detection pixels in the time-frequency domain using a Gaussian Mixture Model (GMM) is proposed for the separation of multiple sources.

Keywords : Signal processing, infrasound, antennas, sources separation

Laboratoire PRISME
Université d'Orléans
8 Rue Léonard de Vinci
45072 Orléans